

# Evolution of microstructure and mechanical properties of the heat affected zone in B-containing 9% chromium steels

Dissertation of

Peter Mayr

Submitted for the degree of  
Doktor der technischen Wissenschaften  
(Doctor of technical sciences)



Institute for Materials Science, Welding and Forming



Faculty of Mechanical Engineering  
Graz University of Technology, Austria

Graz, July 2007



To my family



## Preface

This dissertation is submitted for the Degree of “Doktor der technischen Wissenschaften” at the Faculty of Mechanical Engineering of the Graz University of Technology. The work was carried out between January 2004 and June 2007 under the supervision of Prof. Horst Cerjak at the Institute for Materials Science, Welding and Forming. This work was funded by the Austrian Research Promotion Agency (FFG) under the contracts Nr. 808789, Nr. 810306, Nr. 812298 and was part of the European research collaboration COST 536 “Alloy development for critical components of environmentally friendly power plants - ACCEPT”. Part of this work was performed during research stays at the Advanced Photon Source (APS) of Argonne National Laboratory, Chicago, USA and at the Heat Resistant Design Group of the National Institute for Materials Science (NIMS), Tsukuba, Japan.

To the best of my knowledge, this work is original, except where suitable references are made to previous work. Neither this, nor any substantially similar dissertation has been submitted for any degree, diploma or qualification at any other university or institution.

Part of this work has been published in:

Cerjak H and Mayr P: “Creep strength of welded joints of ferritic steels”, in Creep Resistant Steels, Woodhead Publishing, Cambridge, in print.

Mayr P, Palmer T A, Elmer J W and Cerjak H: “In situ Observation of Phase Transformation and their Effects in 9-12% Cr Steels During Welding”, *Advanced Materials Research*, 2007 **15-17**, pp. 1014 – 1019.

Cerjak H and Mayr P: “Zum Einfluss des Schweißens auf das Kriechverhalten moderner Stähle für die thermische Energieerzeugung”, *Materialwissenschaft und Werkstofftechnik*, 2007 **38(7)**, pp. 510 – 514.

Cerjak H, Dimmler G, Holzer I, Kozeschnik E, Mayr P, Pein C and Sonderegger B: “Development and Improvement of 9-12% Cr Steels by a Holistic R&D Concept”, *Materials Science Forum*, 2007 **539-543**, pp. 2954 – 2959.

Mayr P, Cerjak H, Jochum C and Pasternak J: “Long-term creep behaviour of E911 heat resistant 9%Cr steel weldments fabricated with filler metals of different creep strength”, *8<sup>th</sup> International Conference on Creep and Fatigue at Elevated Temperatures 2007*, San Antonio, 2007.

Mayr P, Holzer I, Mendez-Martin F, Kozeschnik E and Cerjak H: “Weldability of boron containing 9% chromium steels”, *7<sup>th</sup> International Charles Parsons Turbine Conference - Power Generation in an Era of Climate Change*, Glasgow, 2007, in print.

Mayr P, Cerjak H, Jochum C and Pasternak J: “Influence of weld metal creep strength on long term creep behaviour of welded joints of E911 heat resistant 9%Cr steel”, *3<sup>rd</sup> International Conference on Integrity of High Temperature Welds*, London, 2007, pp. 119 – 128.

Cerjak H, Mayr P, Hofer P and Letofsky E: “Advanced materials for thermal power generation”, *IIW Regional Congress - Welding and Related Inspection Technologies*, Stellenbosch, 2006.

Mayr P and Cerjak H: “Weldability study of a boron alloyed high-temperature resistant 9% chromium steel”, *Materials for Advanced Power Engineering 2006*, Forschungszentrum Jülich, 2006, pp. 1393 – 1400.

Baune E, Cerjak H, Caminada S, Jochum C, Mayr P and Pasternak J: “Weldability and properties of new creep resistant materials for the use in ultra supercritical coal fired power plants”, *Materials for Advanced Power Engineering 2006*, Forschungszentrum Jülich, 2006, pp. 871 – 891.

Mayr P, Schalber A, Letofsky E and Cerjak H: “Weldability of boron alloyed high-temperature resistant 9% chromium casting steel COST-CB2A”, *7<sup>th</sup> International Conference on Trends in Welding Research*, Pine Mountain, 2006, pp. 299 – 304.

Peter Mayr  
July, 2007

## Acknowledgements

I would like to thank Professor Horst Cerjak for enabling and supervising this work. This thesis would have been impossible without the help, support, and inspiration of my colleagues at the Institute for Materials Science, Welding and Forming. Especially I would like to thank Dr. Ernst Kozeschnik, Ivan Holzer, Dr. Bernhard Sonderegger, Francisca Mendez-Martin, Dr. Norbert Enzinger and Dr. Ernst Letofsky.

I wish to express my sincere thanks to Dr. John Elmer and Dr. Todd Palmer of Lawrence Livermore National Laboratory, USA for enabling X-ray diffraction work at the synchrotron of Argonne National Laboratory and their continuous support.

Further thanks to Dr. Fujio Abe and all members of the Heat Resistant Design Group at the National Institute for Materials Science (NIMS) in Japan for making an extraordinary and fruitful research stay at their institution possible.

I would like to thank Professor Christina Berger of MPA-IfW Darmstadt, Germany for acting as assessor of this dissertation.

I would also like to express my gratitude to the Austrian Research Promotion Agency (FFG) for their financial support and to all members of the European COST 536 activity for sharing their experience.

Last but not least, I would like to sincerely thank my girlfriend Maria, family and friends for their continuous support over many years.

## Abstract

Martensitic 9-12% chromium steels are favoured grades for thick-walled components in ultra-super critical thermal power plants. Welding in all its variety is the major joining and repair technology for such components.

Within the first part of this thesis, three 9% chromium steels with controlled addition of boron are investigated. The base material as well as the heat affected zone (HAZ) of the three steels are characterised by optical and advanced electron microscopic methods and mechanical testing. Characteristic heat affected zone microstructures are generated by physical simulation using a Gleeble thermo-mechanical simulator. Phase transformations during weld thermal cycles are observed applying dilatometry and in-situ X-ray diffraction using synchrotron radiation. In the second part of this work, the influence of weld metal creep strength on the overall creep strength of welded joints of steel grade E911 is determined by long-term creep testing at 600°C up to a maximum duration of 30.000 hours.

Whereas all three 9% chromium base materials show similar microstructural features, the 9Cr-3W-3Co-VNb steel variant with balanced addition of boron and nitrogen exhibits superior creep properties at 650°C. The grain structure within the heat affected zone of the three steels also differs significantly. Contrary to the common HAZ formation in two of the steels, the 9Cr-3W-3Co-VNb steel shows no formation of a fine-grained zone. The initial base material microstructure is retained despite several phase transformations during the weld thermal cycle.

Long-term creep tests reveal that the fine-grained heat affected zone is the weakest part of E911 cross-welds. Type IV cracking is the dominant failure mode at service stresses. The cross-weld creep strength is reduced significantly compared to the base material leading to premature failures. The characteristics of Type IV failures are obtained and described in detail.

According to the results of the long-term E911 cross-weld creep tests, the 9Cr-3W-3Co-VNb steel variant with balanced addition of boron and nitrogen shows high potential to avoid Type IV cracking. By elimination of a weak grain-refined region, the creep strength of the HAZ is in line with the creep strength of the base and weld metal and premature failures in the HAZ can be avoided.

# Contents

|  |           |
|--|-----------|
| <b>I. Introduction .....</b>   | <b>1</b>  |
| <b>II. Objectives.....</b>   | <b>5</b>  |
| <b>III. Literature Review .....</b>  | <b>7</b>  |
| 1 Research work on creep resistant steels at the IWS .....                       | 7         |
| 2 Microstructure evolution in the heat affected zone of 9% Cr steels.....        | 9         |
| 2.1 Heat affected zone .....   | 11        |
| 2.2 Microstructure of multilayer welds .....                                     | 13        |
| 3 The influence of delta ferrite on the properties of martensitic Cr steels..... | 15        |
| 3.1 Grain size and hardness.....   | 15        |
| 3.2 Tensile strength.....  | 15        |
| 3.3 Toughness and ductility.....   | 15        |
| 3.4 Creep rupture strength.....  | 16        |
| 3.5 Low cycle fatigue and creep fatigue.....                                     | 18        |
| 3.6 Oxidation resistance.....  | 19        |
| 4 Selected damage mechanism in creep exposed welded joints.....                  | 20        |
| 4.1 Type I and Type II cracking .....  | 20        |
| 4.2 Type III cracking - Reheat cracking .....                                    | 22        |
| 4.3 Type IV cracking - the end of life failure mechanism in 9Cr steels.....      | 23        |
| 4.4 Cracking in dissimilar welds.....  | 32        |
| 5 Physical heat affected zone simulation .....                                   | 34        |
| 6 Direct observation of phase transformations during welding.....                | 36        |
| <b>IV. Experimental.....</b>   | <b>41</b> |
| 1 Studied materials .....  | 41        |
| 1.1 CB2A - Heat 145 .....  | 41        |
| 1.2 CB2 - Heat 37514.....  | 42        |
| 1.3 NPM1.....  | 43        |

|     |  |    |
|-----|--|----|
| 1.4 | E911 – X11CrMoWVNb9-1-1 .....  | 44 |
| 1.5 | Weld filler metals.....  | 45 |
| 2   | Imaging .....  | 47 |
| 2.1 | Optical Microscopy.....  | 47 |
| 2.2 | Scanning Electron Microscopy and associated analytical methods .....     | 48 |
| 2.3 | Transmission electron microscopy and associated analytical methods ..... | 50 |
| 2.4 | Image analysis .....   | 53 |
| 2.5 | Determination of boron nitride precipitation.....                        | 53 |
| 3   | Mechanical testing.....  | 55 |
| 3.1 | Macro hardness.....  | 55 |
| 3.2 | Micro hardness .....   | 55 |
| 3.3 | Tensile properties.....  | 55 |
| 3.4 | Charpy impact testing.....   | 57 |
| 3.5 | Creep testing .....  | 58 |
| 4   | GLEEBLE weld simulation.....   | 61 |
| 4.1 | Specimen geometry.....   | 61 |
| 4.2 | Time-temperature cycles .....  | 61 |
| 5   | X-ray diffraction using synchrotron radiation.....                       | 69 |
| 5.1 | Experimental Setup.....  | 70 |
| 5.2 | Analysis of diffraction data.....  | 74 |
| 5.3 | Applied time-temperature profiles.....                                   | 79 |
| 6   | Thermodynamic prediction of phase stability.....                         | 81 |
| 7   | Dilatometry.....   | 82 |
| 7.1 | Dilatometry during Gleeble HAZ simulation.....                           | 82 |
| 7.2 | Bähr DIL-805A/D quenching dilatometer.....                               | 82 |
| 7.3 | Analysis of dilatometry data .....                                       | 83 |
| 8   | Test weld NPM1.....  | 84 |

|            |  |            |
|------------|--|------------|
| 9          | Matching Program .....   | 86         |
| 9.1        | Fabrication of E911 cross-weld samples .....                       | 87         |
| 9.2        | Creep testing.....   | 88         |
| 9.3        | Investigation of fracture location .....                           | 88         |
| <b>V.</b>  | <b>Results.....</b>  | <b>91</b>  |
| 1          | Base material characterisation .....                               | 91         |
| 1.1        | Optical microscopy .....   | 91         |
| 1.2        | Electron microscopy.....   | 93         |
| 1.3        | Detection of boron nitrides .....                                  | 101        |
| 1.4        | X-ray diffraction .....  | 107        |
| 1.5        | Thermodynamic analysis .....                                       | 108        |
| 1.6        | Mechanical properties.....   | 115        |
| 2          | Heat affected zone characterisation.....                           | 121        |
| 2.1        | Dilatometry.....   | 121        |
| 2.2        | In-situ X-ray diffraction.....                                     | 128        |
| 2.3        | Heat affected zone microstructures.....                            | 137        |
| 2.4        | Grain size evolution in the heat affected zone.....                | 151        |
| 2.5        | Hardness of heat affected zone microstructures .....               | 158        |
| 2.6        | Behaviour of retained delta ferrite in the heat affected zone..... | 163        |
| 2.7        | NPM1 test weld.....  | 170        |
| 3          | Results of the Matching Program.....                               | 176        |
| 3.1        | Cross-weld creep strength.....                                     | 176        |
| 3.2        | Investigation of failure locations.....                            | 180        |
| 3.3        | Weld metal failures.....   | 186        |
| 3.4        | Type IV failures .....   | 188        |
| <b>VI.</b> | <b>Discussion.....</b>   | <b>193</b> |
| 1          | Base material properties.....                                      | 193        |

|              |                          |            |
|--------------|--------------------------|------------|
| 2            | Heat Affected Zone ..... | 198        |
| 3            | Matching Program.....    | 203        |
| <b>VII.</b>  | <b>Summary .....</b>     | <b>207</b> |
| <b>VIII.</b> | <b>Outlook .....</b>     | <b>209</b> |
| <b>IX.</b>   | <b>References .....</b>  | <b>211</b> |
| <b>X.</b>    | <b>Appendices</b>        |            |

## Nomenclature and Abbreviations

### General

|       |   |
|-------|---|
| IWS   | Institute for Materials Science, Welding and Forming, TU Graz |
| NIMS  | National Institute for Materials Science, Tsukuba, Japan      |
| APS   | Advanced Photon Source  |
| COST  | Cooperation for Science and Technology                        |
| BN    | boron nitrides  |
| EBSD  | electron backscatter diffraction                              |
| EDX   | energy dispersive X-ray analysis                              |
| EELS  | electron energy loss spectroscopy                             |
| EFTEM | energy filtered TEM   |
| FIB   | focused ion beam  |
| QBSD  | quad backscatter detector                                     |
| SEM   | scanning electron microscopy                                  |
| SRF   | weld strength reduction factor                                |
| SSC   | sulphide stress cracking                                      |
| TEM   | transmission electron microscopy                              |
| VIM   | vacuum induction melting                                      |
| WSF   | weld strength factor  |

### Phase Transformations

|                       |  |
|-----------------------|--|
| $A_{C1}$ ( $A_{e1}$ ) | (equilibrium) temperature of the onset of austenite formation on heating                             |
| $A_{C2}$              | Curie point – transition temperature from ferromagnetism to paramagnetism in ferromagnetic materials |
| $A_{C3}$ ( $A_{e3}$ ) | (equilibrium) temperature of the completion of austenite formation on heating                        |
| $A_{C4}$ ( $A_{e4}$ ) | (equilibrium) temperature of the onset of delta ferrite formation on heating                         |
| $A_{C5}$ ( $A_{e5}$ ) | (equilibrium) temperature of the completion of delta ferrite formation on heating                    |
| $A_{rx}$              | corresponding transformation temperatures observed on cooling  |
| bcc                   | body-centred cubic   |
| bct                   | body-centred tetragonal  |
| fcc                   | face-centred cubic   |
| $M_F$                 | martensite finish temperature  |

|          |                              |
|----------|------------------------------|
| $M_s$    | martensite start temperature |
| $\alpha$ | alpha-ferrite                |
| $\gamma$ | austenite                    |
| $\delta$ | delta ferrite                |

### **Mechanical Testing**

|                               |  |
|-------------------------------|--|
| $t_u$                         | creep rupture time   |
| $\varepsilon_f$               | creep strain   |
| $\dot{\varepsilon}_f$         | creep strain rate  |
| $\dot{\varepsilon}_{f(\min)}$ | minimum creep strain rate  |
| $A_u$                         | elongation at rupture  |
| $Z_u$                         | reduction of area at rupture   |
| $R_{u/t/T}$                   | rupture strength   |
| $R_{p0.2}$                    | 0.2% proof strength  |
| $R_m$                         | tensile strength   |
| $d_0$                         | initial diameter of cross section of the parallel length of a cylindrical test piece |
| $d_u$                         | final diameter within necked region after fracture                                   |
| $\sigma$                      | stress   |
| $L_0$                         | original gauge length  |

### **Welding**

|           |   |
|-----------|---|
| $T_0$     | preheat and inter-pass temperature                  |
| $T_p$     | peak temperature                                    |
| $t_{8/5}$ | characteristic cooling time between 800°C and 500°C |
| PWHT      | post-weld heat treatment                            |
| BM        | base metal  |
| WM        | weld metal  |
| HAZ       | heat affected zone                                  |
| CGHAZ     | coarse-grained heat affected zone                   |
| FGHAZ     | fine-grained heat affected zone                     |
| ICHAZ     | intercritical heat affected zone                    |
| GTAW      | gas tungsten arc welding                            |
| GMAW      | gas metal arc welding                               |
| SMAW      | shielded metal arc welding                          |

|     |   |
|-----|---|
| MIG | metal inert gas welding                   |
| SAW | submerged arc welding                     |
| EBW | electron beam welding                     |
| LBW | laser beam welding                        |
| Q   | heat input                                |
| U   | voltage                                   |
| I   | current                                   |
| v   | welding speed                             |
| k   | thermal efficiency of the welding process |

### **X-Ray Diffraction**

|             |                                       |
|-------------|---------------------------------------|
| TRXRD       | time-resolved X-ray diffraction       |
| SRXRD       | spatially-dissolved X-ray diffraction |
| F           | structure factor                      |
| m           | multiplicity                          |
| $k_0$       | scaling factor                        |
| L           | Lorentz polarisation factor           |
| 2- $\theta$ | diffraction angle                     |
| P           | polarisation factor                   |
| M           | temperature factor                    |
| $v$         | unit cell volume                      |
| FWHM        | full width at half maximum            |



## I. Introduction

Martensitic 9-12% chromium steels are favoured grades for thick walled components in ultra-super critical thermal power plants.<sup>1-4</sup> They exhibit excellent thermo-physical properties, i.e. low coefficient of thermal expansion and low heat conductivity, and a low price compared to Ni- or Co-based Superalloys or austenitic steels by still acceptable creep strength and oxidation resistance.<sup>5,6</sup> A more detailed consideration of this topic and a table with the chemical composition and creep rupture strength of widely used creep resistant chromium steels are given in Appendix A.

Welding in all its variety is the major joining and repair technology for components in thermal power generation.<sup>7</sup> By selection of adequate welding procedures, martensitic steels are weldable without any serious problems. All types of arc welding processes are widely-used for welds in workshops or directly on-site. The heat input generated by the welding arc results in the formation of a heat affected zone (HAZ) in the base material (BM) adjacent to the weld fusion line.<sup>8</sup> Phase transformations, dissolution of strengthening precipitates and re-precipitation of particles during a post-weld heat treatment are the effect of the thermal cycle. As a result, the HAZ itself consists of several sub-regions different in micro-structure and properties, which depend on the actual thermal history of each region.

Power plant components operating at elevated temperatures in the regime of creep are mainly designed using the 100.000 hour creep rupture strength of the material at this temperature. The creep rupture strength of base material, weld metal (WM) and weldments can differ significantly. Therefore, to properly design welded components within an adequate safety margin, long-term creep rupture data of BM, WM and weldments have to be available. Long-term experience with welded components in service as well as results of creep tests of cross-weld specimens indicate reduced creep rupture strength of weldments compared to the base material and weld metal. This tendency is similar for all creep resistant chromium steels currently in service irrespective of their exact chemical composition and their exact weld fabrication parameters. At lower temperatures or higher stresses, the difference in creep strength between base metal and cross-welds is only very small.<sup>9</sup> The difference in creep strength becomes more prominent as the temperature is increased and as

the applied stress level is lowered (see Figure 1). In some cases, weldments exhibit only half the creep rupture strength of the base material.

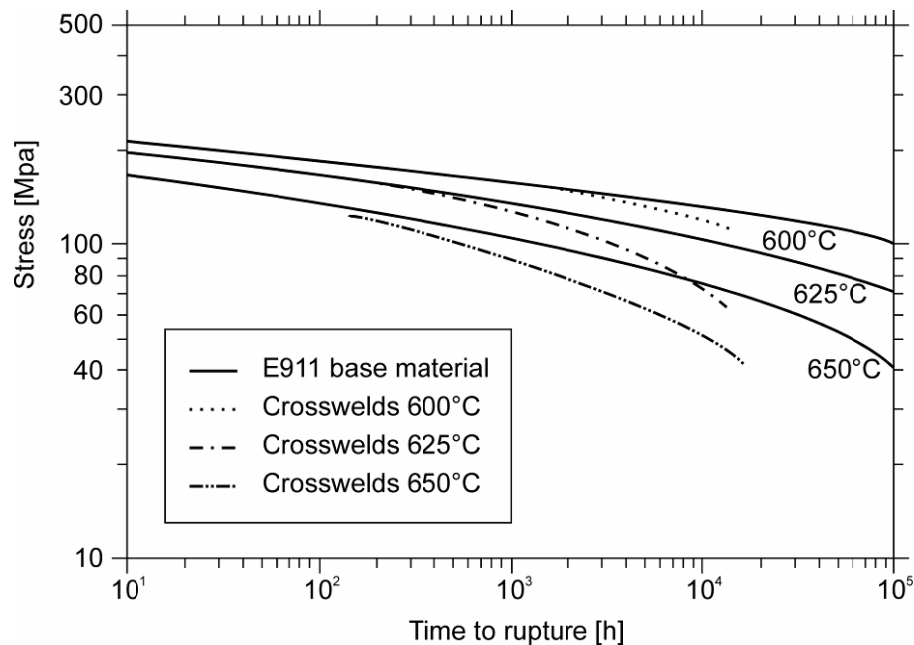


Figure 1: Comparison of cross-weld creep rupture strength to mean base material creep rupture strength of E911 steel at different temperatures.<sup>10</sup>

At this time, the mismatch in creep strength between base material and cross-welds is considered during the design stage of new components and residual life evaluation of existing structures by the implementation of a weld strength factor (WSF).<sup>11-13</sup> For nuclear power plants, these weld strength factors are already implemented in the design codes. The weld strength factor is defined as the ratio of creep rupture stress at a certain time and temperature between weldment and base material.

Up to now, often a time and temperature independent weld strength reduction factor was defined. For example, in the German AD2000-Merkblatt B0, a constant WSF of 0.8 has been given for components designed using creep rupture strength values.<sup>14</sup> Investigations by many researchers have proven that this factor cannot be assumed to be constant over temperature and stress level, but rather depends on several parameters such as material type, stress level, temperature and time and can be either higher but also significantly lower.<sup>15, 16</sup>

In Figure 2, WSF for several steel grades at different temperatures published in literature<sup>17-19</sup> are shown. A reduction of up to 50% in creep rupture strength for weldments compared to the base material emphasises the importance of further research on cross-weld creep strength and its improvement. Within this work, focus is put on the influence of weld metal creep strength on the overall creep behaviour of welded joints (“Matching Program”).

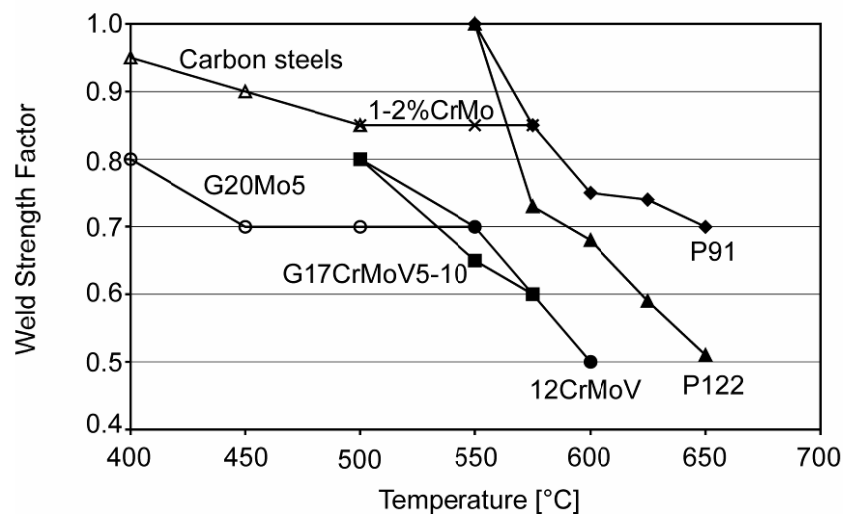


Figure 2: Weld strength factors as a function of temperature for the 100.000 hours creep rupture strength of different steel grades.

The most prominent failure mechanism in creep exposed weldments causing this mismatch in creep strength is named Type IV cracking.<sup>20</sup> Type IV cracking is limited to the fine-grained and intercritical region of the heat affected zone and seen today as the major end-of-life failure in high temperature exposed welded joints. A revolutionary 9% chromium steel with controlled addition of boron and nitrogen has been developed by Abe and co-workers<sup>21</sup> in Japan. A detailed history on the development of this steel is given in Appendix C. In this steel, the formation of a continuous fine-grained region within the HAZ is suppressed by a, so far, not clearly identified mechanism. Up to 10.000 hours, creep rupture strength of weldments at 650°C is similar to base material creep strength.

Motivation of the present work was to check this extraordinary HAZ formation behaviour using a similar steel with slight variation in boron and nitrogen content and to compare the HAZ microstructure and properties of this steel with the most promising European candidate materials.



## II. Objectives

The main objective of the first part of this work is to characterise the initial microstructures and mechanical properties of three boron containing 9% chromium steels. Two of these steel variants, CB2A and CB2, have been developed within the European research activity COST. The third steel, NPM1, has been designed by the Institute for Materials Science, Welding and Forming (IWS) of the Graz University of Technology following an approach by Japanese scientists of the National Institute for Materials Science (NIMS). Creep properties of NPM1 are assessed to allow a comparison of this new steel grade with well-known European grades.

Objective of the second part of this work is to compare the heat affected zone (HAZ) and, therefore, the influence of weld thermal cycles on the evolution of the microstructure of the three 9% chromium steels using HAZ thermal simulation. Special attention is put on the formation of delta ferrite at the highest peak temperatures and its influence on the HAZ properties. Investigations cover conventional optical microscopy as well as advanced analytical electron microscopical methods, such as energy dispersive X-ray analysis (EDX), energy filtered transmission electron microscopy (EFTEM), electron energy loss spectroscopy (EELS) and electron backscatter diffraction (EBSD). By application of in-situ X-ray diffraction using synchrotron radiation coupled with physical weld simulation new perspectives on phase transformations in martensitic steels will be obtained. Mechanical testing of weld-simulated microstructures completes the examination of the HAZ of the three different steels.

The third part of this thesis is focused on the identification of the influence of weld metal creep strength on the overall creep strength of cross-weld samples. Specimens extracted from girth welds of an E911 collector pipe welded with three weld filler materials, differing in creep rupture strength, are creep tested at 600°C at different stress levels. Fractured samples are analysed using conventional optical microscopy in combination with electron microscopy. The influence of weld metal creep strength on Type IV cracking in the fine-grained HAZ region, as the most prominent and life-limiting failure mechanism in creep exposed cross-welds, is studied.



### III. Literature Review

#### 1 Research work on creep resistant steels at the IWS

Since 1986 the Institute for Materials Science, Welding and Forming (IWS) of the Graz University of Technology is an active member of the European joint research collaboration on materials for advanced power plants within COST (CO-operation in the field of Science and Technology). A detailed historical overview on steel development within the European COST projects is given in Appendix B.

On the following pages, a table of all completed and ongoing Master and Doctoral Theses at the IWS with the focus on material development for thermal power generation is given.

**Table 1: Master and Doctoral Theses at the IWS, TU Graz, related to the present thesis.**

| <i>Completed Master Theses</i>  |  |      |
|---------------------------------|--|------|
| <b>P. Hofer</b>                 | Microstructural Evaluation of creep processes in a tungsten modified 9-10% Chromium cast steel   | 1994 |
| <b>P. Thurner</b>               | Mikrostrukturelle Untersuchung von langzeitausgelagerten Kerbschlagbiegeproben des hochwarmfesten ferritischen Chromstahles G-X12 CrMoWVNb10-1-1 | 1995 |
| <b>C. Eck</b>                   | Grundlagenuntersuchungen der Schweißignung des NF616   | 1995 |
| <b>C. Schrock</b>               | Entwicklung eines EDV-Programmes zur Auswertung von Zeitstanddaten von Stählen bei erhöhten Temperaturen   | 1995 |
| <b>J. Eisner</b>                | Gefügecharakterisierung von neu entwickelten modifiziertem 9Cr1Mo Schweißgut   | 1996 |
| <b>A. Zwenig and G. Ziegler</b> | Charakterisierung der Eigenschaften der Wärmeeinflusszone bei unterschiedlichen Streckenergien anhand des neu entwickelten Chromstahles E911     | 1997 |
| <b>A. Schalber</b>              | Charakterisierung der Schweißignung des Bor-modifizierten 9%Chromstahles CB2A  | 1998 |
| <b>T. Weidinger</b>             | Adaptierung einer Hochtemperatur-Belastungseinrichtung für die Rasterelektronenmikroskopie mit Unterstützung von Finite-Elemente-Modellierung    | 2002 |
| <b>G. Kukutschki</b>            | Sammlung und Auswertung der Materialdaten von Stählen für Gas- und Dampfturbinenrotoren anhand eines Eigenschaftsprofils                         | 2003 |

|                                  |  |      |
|----------------------------------|--|------|
| <b>P. Mayr</b>                   | Charakterisierung und Überprüfung der Schweißignung des neu entwickelten hochwarmfesten Werkstoffs P23   | 2004 |
| <b>S. W. Plimon</b>              | Simulation einer großtechnischen Wärmebehandlung und begleitende mikrostrukturelle Untersuchung an einem modernen 9-12% Cr Stahl“, Master Thesis | 2004 |
| <b>F. Méndez-Martin</b>          | Microstructural characterisation of the HAZ of new creep resistant 9% chromium steels using weld simulation technique                            | 2006 |
| <b>Completed Doctoral Theses</b> |  |      |
| <b>F. Brühl</b>                  | Verhalten des 9%-Chromstahles X10CrMoVNb9-1 und seiner Schweißverbindungen im Kurz- und Langzeitversuch  | 1989 |
| <b>F. A. Schuster</b>            | Untersuchung der Gefüge und mechanischen Eigenschaften der warmfesten Stahlgussorte G-X12CrMoWVNbN10-1-1   | 1996 |
| <b>E. Kozeschnik</b>             | Thermodynamische Berechnung der Phasengleichgewichte und der Ausscheidungskinetik in metallischen Werkstoffen                                    | 1997 |
| <b>P. Hofer</b>                  | Mikrostrukturelle Analyse als Basis für die Entwicklung neuer Kraftwerkswerkstoffe am Beispiel von G-X12CrMoWVNbN10-1-1                          | 1999 |
| <b>B. Schaffernak</b>            | Charakterisierung von 9-12% Cr Stählen mittels thermodynamischer Modellrechnungen  | 2000 |
| <b>E. Letofsky</b>               | Das Verhalten von Schweißverbindungen moderner Kraftwerkswerkstoffe  | 2001 |
| <b>P. Weinert</b>                | Modellierung des Kriechverhaltens von ferritisch/martensitischen 9-12% Cr Stählen auf mikrostruktureller Basis                                   | 2001 |
| <b>G. Dimmler</b>                | Quantifizierung der Kriech- und Zeitstandfestigkeit von 9-12%Cr Stählen auf mikrostruktureller Basis   | 2003 |
| <b>B. Sonderegger</b>            | Charakterisierung der Substruktur in modernen 9-12% Cr Stählen mittels der EBSD Methode  | 2005 |
| <b>J. Rajek</b>                  | Computer simulation of precipitation kinetics in solid metals and application to the complex power plant steel CB8                               | 2006 |
| <b>Current Projects</b>          |  |      |
| <b>I. Holzer</b>                 | Kinetic Simulation of microstructural evolution of 9-12% Cr steels   | -    |
| <b>C. Pein</b>                   | Modellierung der lokalen Mikrostruktur in modernen 9-12% Cr Stählen  | -    |
| <b>F. Méndez-Martin</b>          | Experimentelle und theoretische Untersuchung der Ausscheidungskinetik im kriechfesten 12% Cr - Stahl VM12  | -    |

## 2 Microstructure evolution in the heat affected zone of 9% Cr steels

Fusion welding, as the most important joining process in power plant construction works, strongly affects the component properties.<sup>7</sup> Not only a new type of material, the weld metal, is deposited in between the connected parts but also the base material is altered by a local and very inhomogeneous heat treatment as a result of the weld thermal cycle. Good overviews on welding metallurgy are given by K. Easterling<sup>8</sup>, H. Granjon<sup>22</sup> and G. Schulze<sup>23</sup>. This chapter focuses on phase transformations taking place within the weld heat affected zone (HAZ) of ferritic heat resistant steels, strongly influencing the final mechanical properties of the weldment.

The optimised base materials microstructure and properties, set through accurate melting techniques, exact production process control and proper heat treatment by the base metal manufacturer are changed completely within the HAZ by the applied weld thermal cycle. In addition, internal stresses generated during rapid cooling, which are in the order of the yield strength of the material, sum up with external stresses later on in service.

In Figure 3, the basic influences of the welding process on the metallurgy in the HAZ are shown and compared to the calculated equilibrium phase diagram of X10CrMoVNb9-1 (P91) steel. Depending on the selected welding process, the base material microstructure within the HAZ is changed. The resulting microstructure is governed by the heating rate of the weld thermal cycle, the peak temperature ( $T_p$ ), the dwell time, the cooling rate, effects of multilayer welding and, finally, by the post-weld heat treatment (PWHT).

The heating rates in arc welding processes can be as high as hundreds of  $K s^{-1}$ . As a result, transformation temperatures are shifted to significantly higher temperatures than predicted in the equilibrium phase diagram ( $T_0$ ). For example, the ferrite ( $\alpha$ ) to austenite ( $\gamma$ ) phase transformation can occur about  $100^\circ C$  higher at a heating rate of  $100 K s^{-1}$  than the calculated  $T_0$ , resulting in considerable superheating of the ferrite before transformation. Other parameters affected by the heating rate are: recrystallisation temperature, solution temperature of carbides and nitrides and grain growth.

By higher heating rates, not only phase transformations but also solution temperatures of precipitates are shifted to higher temperatures. In most cases equilibrium is not reached at high heating rates and short dwell times and superheating occurs. It is of great impor-

tance to estimate how this can affect the microstructural evolution, especially the grain growth behaviour, which is strongly influenced by grain boundary pinning. When welding precipitation strengthened creep resistant steels, three scenarios should be considered:

- Peak temperature is too low to have any noticeable effect on the precipitates;
- Particles only partially dissolve during weld thermal cycle, but eventually coarsening of favoured particles occurs;
- Particles dissolve completely during the thermal cycle and omission of grain boundary pinning causes excessive grain growth.

Apart from precipitation strengthening, grain size control is of major importance, being a key factor for good mechanical properties and the susceptibility of the alloy to several damage mechanisms e.g. cold cracking, reheat cracking or Type IV cracking.

Excessive grain growth can take place in regions where most of the precipitates have been dissolved by the weld thermal cycle. After completion of  $\alpha/\gamma$  transformation, the stability of newly formed grains is far from equilibrium. With increasing peak temperature, crystallographically favoured grains begin to grow at the expense of smaller grains. The resulting coarse-grained microstructure generally shows low toughness characteristics.

In 9-12% Cr steels, according to the equilibrium phase diagram, austenite starts to transform to delta ferrite ( $\delta$ ) at highest peak temperatures. The nucleation of delta ferrite grains at austenite grain boundaries reduces the grain size again. Whereas the lower solubility of carbon and other austenite stabilising elements in ferrite results in an escape of these elements out of the delta ferrite into remaining austenite regions, ferrite formers, such as chromium, are enriched in ferritic regions. Therefore, segregated regions differ locally in chemical composition and austenite transformation on cooling can be incomplete, resulting in retained delta ferrite or retained austenite.

Moreover, high cooling rates, predominant for low heat input welding processes such as electron beam- (EB), laser- and gas tungsten arc welding (GTAW), in combination with thick walled components, can result in an incomplete reverse-transformation of delta ferrite back to austenite. Small amounts of delta ferrite can be present in the microstructure even at room temperature. Multilayer welding techniques offer more time for diffusion to compensate segregational processes and result in a complete and homogeneous re-transformation of delta ferrite to austenite.<sup>24</sup>

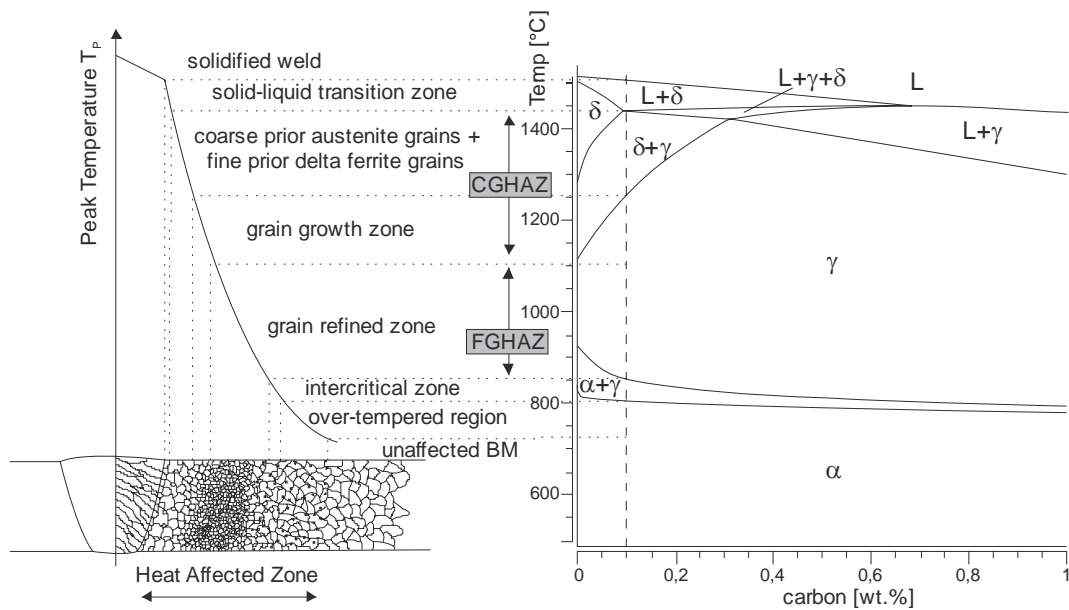


Figure 3: Schematic of the sub-zones of the HAZ and relation to the calculated equilibrium phase diagram of X10CrMoVNb9-1 (P91-type) steel.

In the following paragraphs, the HAZ of creep resistant chromium steels and their sub-regions are described in more detail:

## 2.1 Heat affected zone

As pointed out above, the welding process strongly influences the microstructure and properties of the base material. As a result of the severe thermal cycle caused by the welding process, the original microstructure is altered and a so-called heat affected zone (HAZ) is formed. The HAZ can be divided into a number of sub-zones. No distinct borderline between the different regions is recognisable. It can be seen more as a continuous gradient from the weld fusion line to the unaffected base material. Each sub-zone is represented by its characteristic microstructure and properties.

### Grain growth zone ( $T_p \gg A_{C3}$ )

This zone adjacent to the fusion line experiences temperatures well above the  $A_{C3}$ -transformation temperature. Any precipitates, which obstruct growth of austenite grains at lower temperatures, dissolve, resulting in coarse grains of austenite. In 9-12% Cr steels, delta ferrite grains can nucleate at highest peak temperatures ( $T_p > 1250^\circ\text{C}$ ) causing the overall grain size to decrease. On cooling, 9-12% Cr steels form a martensitic micro-

structure. The coarse-grained zone (CGHAZ) features the highest hardness, and, generally, low toughness values are expected.

#### **Grain-refined zone ( $T_P > A_{C3}$ )**

Lower peak temperatures of about 1100°C, just above  $A_{C3}$ , give rise to the formation of small grains of austenite (FGHAZ). In addition, peak temperature is not sufficiently high to completely dissolve precipitates, thus limiting grain growth by pinning austenite grain boundaries. On cooling, a martensitic microstructure forms. The fine-grained region of the HAZ is regarded as the weakest zone in weldments during creep loaded service. At longer service times and lower stress levels, most of the weldments of creep resistant ferritic steels fail within this region by the, so called, Type IV mechanism.

#### **Partially transformed zone – Intercritical HAZ ( $A_{C1} < T_P < A_{C3}$ )**

Peak temperatures lying between the  $A_{C1}$  and  $A_{C3}$  transformation temperatures result in a partial transformation of  $\alpha$  into  $\gamma$  on heating. Whereas new austenite grains nucleate at favoured positions, such as prior austenite grain boundaries or martensite lath boundaries, the untransformed tempered martensitic microstructure is simply tempered for a second time by this weld thermal cycle. Partial dissolution of precipitates can be experienced in this part of the HAZ and coarsening of undissolved precipitates can occur, especially during subsequent PWHT. After cooling, a microstructure consisting of newly formed virgin martensite and the tempered original microstructure exists. The intercritical HAZ (ICHAZ) is characterised by a small grain size and, generally, exhibits the lowest hardness values. This sub-zone of the HAZ shows similar susceptibility to Type IV cracking as the grain-refined zone.

#### **Over-tempered region**

With peak temperatures below  $A_{C1}$ , the microstructure does not undergo any phase transformations but the original microstructure is locally tempered at higher temperatures compared to that of the post-weld heat treated base material. As a result, coarsening of precipitates might be enhanced by a higher coefficient of diffusion at this temperature.

#### **Zone of unchanged base material**

The zone of unchanged base material concerns temperatures up to ca. 700°C, in which no visible changes in morphology of constituents occur.

## 2.2 Microstructure of multilayer welds

The above described straight forward characterisation of HAZ sub-zones is only representative for single layer welds. In multilayer welds, multiple thermal influences on the microstructure make identification of different microstructural sub-zones far more complicated. Therefore, special attention has to be paid on multilayer welding techniques. Multilayer welds are formed by subsequent deposition of weld beads on solidified former deposited runs. Significant changes in the microstructure of multilayer welds compared to single layer welds are the result of this additional heat input into the weld metal. The HAZ is strongly affected by this process as well. Reed and Bhadeshia<sup>25</sup> as well as Cerjak et al.<sup>26</sup> characterised the HAZ of multilayer welds by mathematical modelling.

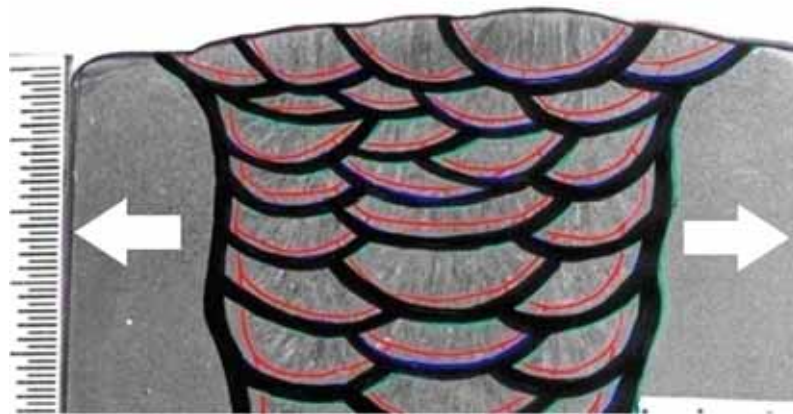


**Figure 4: Multilayer weld of E911 base material with matching filler material. Areas exposed to peak temperatures between  $A_{C1}$  and  $A_{C3}$  transformation temperatures (Intercritical HAZ) are marked black. The loading direction is indicated by arrows.<sup>10</sup>**

The “multilayer” effect is not only active in the HAZ of base material but also regions with varying microstructure can be formed within the weld metal. In Figure 4, intercritically heated areas within a cross-weld of E911 base material are marked in black, whereas the fusion lines are marked by red lines.<sup>10</sup> Whereas a continuous region of intercritically heated material forms within the HAZ of the base material parallel to the fusion line, the HAZ within the weld metal is discontinuous related to the loading direction. If subsequent weld beads are deposited symmetrically to the weld centreline (see Figure 5), a continuous layer of intercritically heated material is also formed within the weld deposit.<sup>27</sup> The heat affected regions within the weld metal can exhibit the same susceptibility to certain cracking

mechanism, e.g. reheat cracking, Type IV cracking, as prominent in the HAZ of base material. Therefore, in multilayer welds, special attention has to be paid on the welding parameters, especially heat input, joint geometry and weld layer structure.



Figure 5: Creep exposed  $2\frac{1}{4}\text{Cr-1Mo}$  SAW weld with symmetrically deposited weld beads showing cracking in the refined weld metal at the weld centerline (Picture courtesy of C. D. Lundin).<sup>27</sup>

### 3 The influence of delta ferrite on the properties of martensitic Cr steels

#### 3.1 Grain size and hardness

Delta ferrite formation in high chromium ferritic weld metal and the HAZ of martensitic chromium steels formed at highest peak temperatures has been observed by several authors.<sup>28-37</sup> Nucleation of delta ferrite grains favourably takes place at prior austenite grain boundaries and restricts austenite grain growth, resulting in a finer prior austenite grain size in regions exposed to peak temperatures higher than 1200°C. It is also without controversy that the presence of relatively soft retained delta ferrite in a tempered martensitic microstructure generally reduces the overall hardness of the microstructure.<sup>30, 32</sup>

#### 3.2 Tensile strength

In 9Cr-1Mo-2.7W material, Park et al.<sup>38</sup> could not detect any influence of soft delta ferrite grains on the strength of the material. He concluded that the volume fraction of delta ferrite of 8% is not high enough to affect the overall strength of the steel. Other authors clearly claim a deteriorating effect of delta ferrite in a martensitic matrix on the overall strength.<sup>39</sup>

#### 3.3 Toughness and ductility

The role of retained delta ferrite on toughness of martensitic steels is not described consistently in literature. Whereas most authors<sup>28, 30, 31, 40</sup> attribute increased toughness to a certain amount of retained delta ferrite, others<sup>24, 41</sup> emphasise the negative influence of retained delta ferrite on the toughness behaviour of the microstructure. According to Schäfer<sup>39</sup>, the reduced toughness in martensitic 9-14% Cr steels with a certain amount of delta ferrite is caused by a combined effect of delta ferrite and “dendritic” carbides which encapsulate the delta ferrite. Whereas pure delta ferrite increases the ductility and toughness of the steel, delta ferrite in combination with brittle “dendritic” carbides lower the toughness significantly. A summary of his results on the influence of delta ferrite and massive “dendritic” carbides on the mechanical properties of 9-14%Cr steels is given in Table 2.

**Table 2: Influence of delta ferrite and massive dendritic carbides, separately and in combination, on the mechanical properties of six martensitic chromium steels (9-14 wt.% Cr).<sup>39</sup>**

|  | Strength       |                |                   | Ductility      |      |                | Toughness      |                 |                               |
|--|----------------|----------------|-------------------|----------------|------|----------------|----------------|-----------------|-------------------------------|
|  | F <sub>m</sub> | R <sub>m</sub> | R <sub>p0.2</sub> | S <sub>u</sub> | A    | A <sub>g</sub> | A <sub>v</sub> | AR <sub>m</sub> | A <sub>g</sub> R <sub>m</sub> |
| <b>Delta ferrite</b>                     | -              | -              | --                | +              | +    | ++             | +(+)           | -               | +(+)                          |
| <b>Carbide dendrites</b>                 | +              | -              | -                 | --             | -(-) | +              | --             | -               | 0(-)                          |
| <b>Delta ferrite + carbide dendrites</b> | -              | -(-)           | --                | -              | -    | ++             | -(-)           | --              | +                             |

F<sub>m</sub>=maximum force; S<sub>u</sub>=bending at brittle fracture; A=total elongation; A<sub>g</sub>=uniform elongation;

### 3.4 Creep rupture strength

Delta ferrite is regarded to have a negative influence on long term creep behaviour of martensitic steels.<sup>42-44</sup> Kimura et al.<sup>45</sup> studied the long-term creep and degradation behaviour of ASME Grade 122 steels. Whereas KA-SUS410J3TB (see Table 3) shows a tempered martensitic microstructure in as-received condition, KA-SUS410J3DTB shows a dual phase microstructure consisting of tempered martensite with about 5 vol.% of delta ferrite due to the higher chromium content. Creep rupture strength and microstructural changes during creep exposure have been investigated, especially concerning the influence of delta ferrite.

**Table 3: Chemical composition (wt. %) of Japanese KA-SUS410J3 steels corresponding to ASME Grade 122 steels.**

| Steels                              | C    | Si   | Mn   | Cr    | Mo   | W    | Cu   | V    | Nb   | N     | B      | Al    |
|-------------------------------------|------|------|------|-------|------|------|------|------|------|-------|--------|-------|
| <b>KA-SUS410J3TB (single phase)</b> | 0.13 | 0.31 | 0.60 | 10.65 | 0.33 | 1.87 | 0.86 | 0.19 | 0.05 | 0.057 | 0.0024 | 0.007 |
| <b>KA-SUS410J3DTB (dual phase)</b>  | 0.11 | 0.27 | 0.59 | 12.10 | 0.34 | 1.82 | 0.82 | 0.19 | 0.06 | 0.066 | 0.0030 | 0.012 |

Results of creep tests show that short-term creep rupture strength is almost the same for both steels. However, with increasing testing duration, the slope of the stress vs. time to rupture curve of the dual phase steel becomes much steeper compared to that of the single phase steel. The long-term creep rupture strength of the dual phase steel is significantly lower than that of the single phase steel (Figure 6). Microstructural examinations of

creep exposed samples showed increased coarsening of precipitates especially along delta-ferrite and tempered martensite boundaries in the dual phase steel.

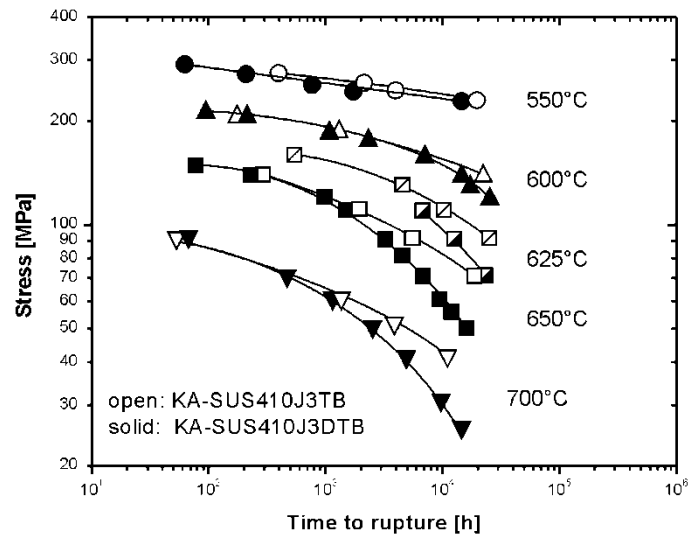


Figure 6: Comparison of creep rupture strength of single phase and dual phase Grade 122 steel.<sup>45</sup>

Recovery of tempered martensitic microstructure was also more pronounced in the dual phase steel, especially in the vicinity of delta ferrite and tempered martensite boundaries. Decrease in long-term creep strength was assumed to be caused by segregation of ferrite- and austenite stabilising alloying elements which, during long-term creep exposure, enhances coarsening of precipitates and promotes recovery of tempered martensitic microstructure.

Sawada et al.<sup>42</sup> investigated the same creep exposed samples of P122 steel regarding Z-phase precipitation. In 600°C creep exposed samples of both steels, Z-phase was found at prior austenite grain boundaries and packet boundaries. In dual phase P122 steel, a large number of Z-phase particles was found in the vicinity of delta ferrite regions, whereas these regions were depleted of MX particles. The mean diameter of Z-phase particles in P122 steel with delta ferrite is relatively large compared to particles observed in the single phase steel. There was no difference in metallic composition of Z-phase particles related to their precipitation site such as prior austenite grain boundaries or delta ferrite regions. The abrupt decrease in creep strength of dual phase P122 steel was directly associated with the excessive precipitation of Z-phase and depletion of MX particles.

Igarashi et al.<sup>43</sup> attributed the inferior creep behaviour of dual phase P122 steel to heterogeneous creep deformation at lower stress level, with an early transition to the acceleration creep stage at a very small creep strain. Recovery of martensitic microstructure was accelerated in the vicinity of delta ferrite regions and resulted in sub-grain formation preferentially along delta ferrite/tempered martensite boundaries. Liu et al.<sup>44</sup> observed this accelerated recovery near delta ferrite grains in a 13 wt.% Cr steel with about 2% delta ferrite and attributed it to the depletion of alloying elements such as Mo, W and Cr by the formation of coarse  $M_{23}C_6$ .

### 3.5 Low cycle fatigue and creep fatigue

The influence of delta ferrite in W-alloyed 9% Cr steel on low cycle fatigue (LCF) properties was studied by Park et al.<sup>38</sup> Alloying of 9Cr1Mo steel with 2.7% W resulted in a dual phase microstructure of martensite and about 8% delta ferrite. LCF properties of the steel have been deteriorated by the delta ferrite grains, which acted as a preferential crack initiation site during cyclic loading.

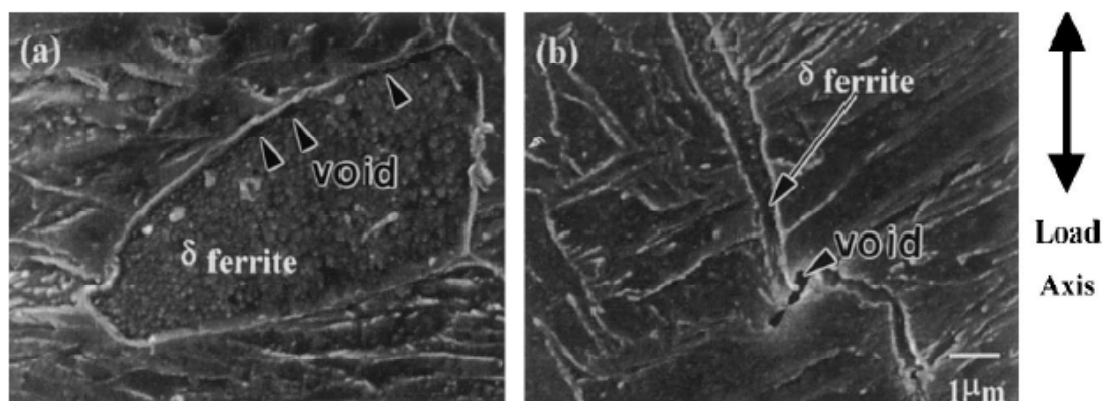


Figure 7: SEM micrograph showing the crack initiation site in 9Cr-1Mo-2.7W alloy with delta ferrite oriented (a) perpendicular and (b) parallel to the tensile axis.<sup>38</sup>

Baek et al.<sup>46</sup> studied long-term fatigue properties of P92 steel. The microstructure of this melt consisted of tempered martensite with a few percent of delta ferrite. After aging at 650°C for 1,000 hours Laves phase was preferably precipitated inside delta ferrite grains. Laves phase formation and growth was due to the difference in W solubility between delta ferrite and martensite. Aged P92 steel exhibited a decrease in fatigue and creep-fatigue life

under all test conditions. Cavities and fatigue cracks were mainly observed at the boundaries between delta ferrite and martensite. They concluded that Laves phase plays an important role on cavity formation during fatigue testing. Delta ferrite accelerates the growth of Laves phase and, therefore, reduces the fatigue life of dual phase P92 steel.

### **3.6 Oxidation resistance**

Hara et al.<sup>47</sup> studied the influence of delta ferrite in a 13 wt.% Cr steel on sulphide stress cracking (SSC) resistance in mild sour environments. The appearance of SSC was directly related to the presence of delta ferrite in the steel. The initiation of SSC did not depend on the shape of delta ferrite. The difference in corrosion potential with and without delta ferrite is attributed to the existence of chromium depleted zones, which were formed adjacent to delta ferrite regions as a result of chromium carbide and nitride precipitation at delta ferrite grain boundaries.

## 4 Selected damage mechanism in creep exposed welded joints

In 1974, Schüller et al.<sup>48</sup> categorised the types of cracking observed in weldments of heat resistant steels by a simple scheme (see Figure 8). Cracks were classified depending on their location and orientation within the weldments. Cracks in the deposited weld metal correspond to Type I and Type II. They form in the weld metal and develop either in longitudinal or transversal direction. Whereas Type I cracks get arrested in the weld metal, Type II cracks can propagate into the HAZ or even into the base material. The other types of cracks develop within the HAZ of weldments. Type III cracks form in the coarse-grained part of the HAZ close to the fusion line and can prolong in this zone as well as into the base material. Cracks of Type IV are restricted to the fine or intercritical zone adjacent to the unaffected base material. Brett<sup>49</sup> added the term of Type IIIa cracking to this scheme for a failure mechanism taking place close to the fusion line (Type III) but in a fully refined HAZ structure with higher fracture ductility.

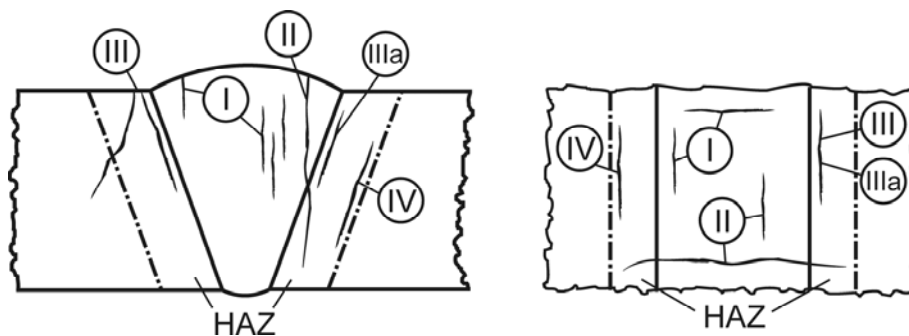


Figure 8: Modified schematic of cracking modes in weldments of heat resistant steels (Original by Schüller et al.)

### 4.1 Type I and Type II cracking

Defects in the weld metal are commonly associated with the welding process itself or stress relieving during PWHT. Less frequently, weld metal cracks can be related to creep damage during high temperature service.<sup>50, 51</sup>

Cracks in the weld metal are mostly in transversal direction, although also longitudinal failures are reported. Previously reported cracks are almost inter-crystalline and appeared as hot cracks formed during solidification of the weld metal. Since weld metal development has improved and the cleanliness of weld deposit was increased in the last decades, the

significance of solidification cracks in ferritic steels has diminished. They are still of great concern in austenitic and Ni-based weld metals.

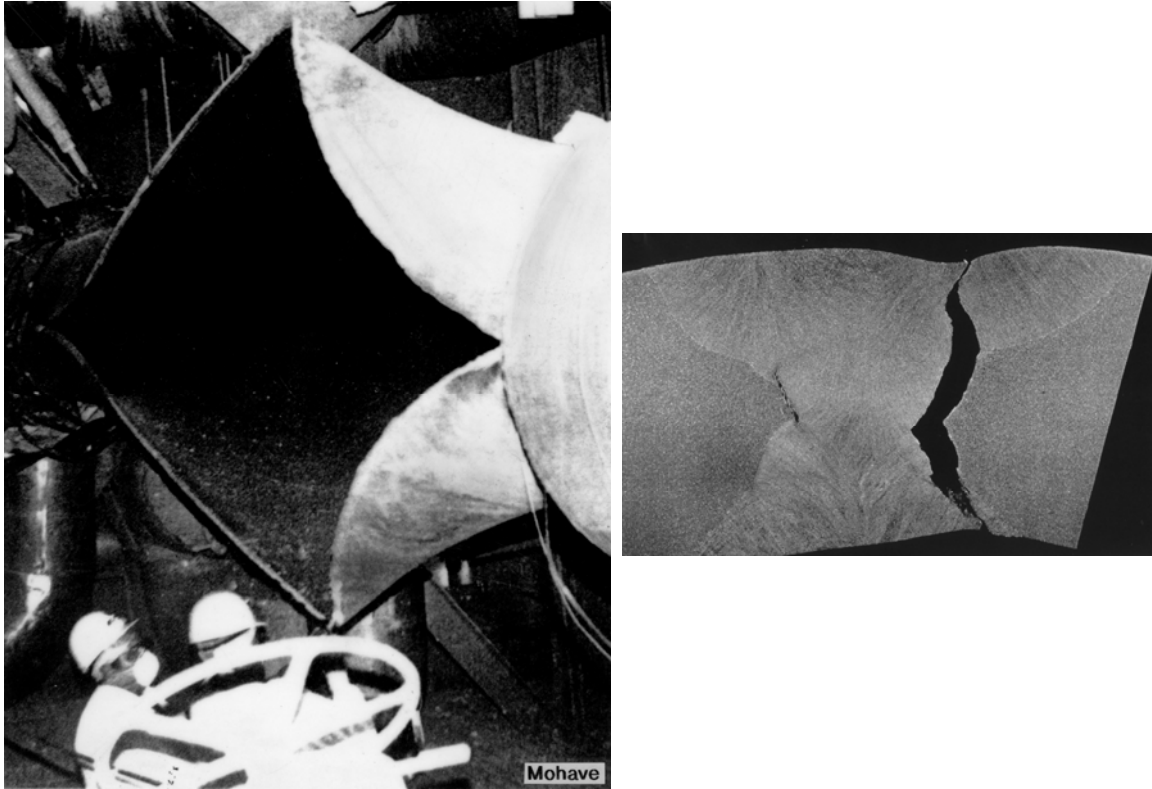


**Figure 9: Failed seam welded hot reheat pipe of grade 11 material (1.25Cr-0.5Mo) after 87,000 hours in service at 540°C causing 6 deaths and 10 injured. Crack formed by weld metal cavitation and cracking along the fusion boundary with the weld in the normalized and tempered condition. High oxygen content due to the submerged arc welding (SAW) acid flux resulted in myriads of inclusions which were the initiators of creep cavitation. (Courtesy of C. Lundin)**

As described above, weld metal deposit produced by multilayer welding technique followed by a sub-critical tempering does not exhibit a uniform microstructure. By multilayer welding, solidified weld beads beneath experience a significant thermal influence by subsequent weld thermal cycles. Therefore, in multilayer weld metal, similar zones compared to that of the HAZ of base metal develop. These zones within the weld metal can become susceptible to different forms of creep damage. Whereas coarse-grained areas in the weld deposit might show a susceptibility to reheat cracking, fine-grained regions might fail by Type IV cracking with the same mechanisms active as in the analogous part of the HAZ of the base metal. Both failure mechanisms will be described in more detail in the following paragraphs.

## 4.2 Type III cracking - Reheat cracking

Reheat or stress relief cracking is defined as an intergranular cracking in the HAZ or the weld metal that occurs during exposure of welded structures to elevated temperatures produced by PWHT or high temperature service up to about 20,000 hours. This type of cracking in welded structures of creep resistant, precipitation strengthened alloys has received considerable attention since the mid-1950's.<sup>52</sup> Initial work was concerned primarily with cracking problems in austenitic steels (18Cr-12Ni-1Nb) used for power generating equipment, especially high temperature steam piping. Reheat cracking was also reported in some Ni-base superalloys.<sup>53</sup>

In the early 1960's, similar cracking problems during stress relief heat treatments and high temperature service were again observed in power generating constructions where the ferritic creep resisting 2CrMo and CrMoV weldments in steam pipework and valve assemblies were found to exhibit occasional cracking. Whereas high alloyed 9-12% chromium steels show almost no susceptibility to reheat cracking, new developed low alloyed 2¼ % chromium steels can exhibit significant susceptibility depending on their alloying concept.

The mechanism of reheat cracking is generally understood although details of the controlling parameters and their mechanistic interpretation remain still a subject for discussion. In general terms, cracking results when the relaxation strains, occurring with stress relief of residual stresses during PWHT or high temperature service, exceed the local ductility of the material. Factors affecting the susceptibility of welded structures to reheat cracking include the chemical composition, the microstructure resulting from the welding process, and the stress state. The significance of segregation of alloying elements such as Al, B, Mn and impurity elements such as P, S, As, Sb, Sn, etc. is under discussion in literature. Some authors state a strong influence of elements segregated at the PAGB in lowering the cohesive strength of the boundaries, whilst others find no interaction between segregations and stress relief cracking failures.<sup>52-54</sup> It is evident that all mechanisms weakening or embrittling grain boundaries enhance the susceptibility to reheat cracking.

In the CGHAZ, almost all precipitates are dissolved during the weld thermal cycle. During PWHT and high temperature service, re-precipitation takes place at the grain boundaries as well as inside the grains. The grain interior gets strengthened by precipitation of finely dispersed, mainly coherent carbonitrides whereas prior austenite grain boundaries are energetically favourable for precipitation of incoherent carbides such as Fe<sub>3</sub>C, M<sub>23</sub>C<sub>6</sub>,

$M_6C$ . Highly diffusive grain boundaries enhance the coarsening process of the latter and result in the depletion of solid solution strengthening elements and the dissolution of MX particles in the vicinity of prior austenite grain boundaries (PAGB).

As a result of these microstructural changes, precipitation strengthened grain interiors are surrounded by weak grain boundary areas. Hence, reduction of welding residual stresses is mainly proceeding by deformation concentrated at the grain boundaries. Therefore, stress relief cracking appears macroscopically as intergranular cracks along PAGB with low rupture ductility (Figure 10).

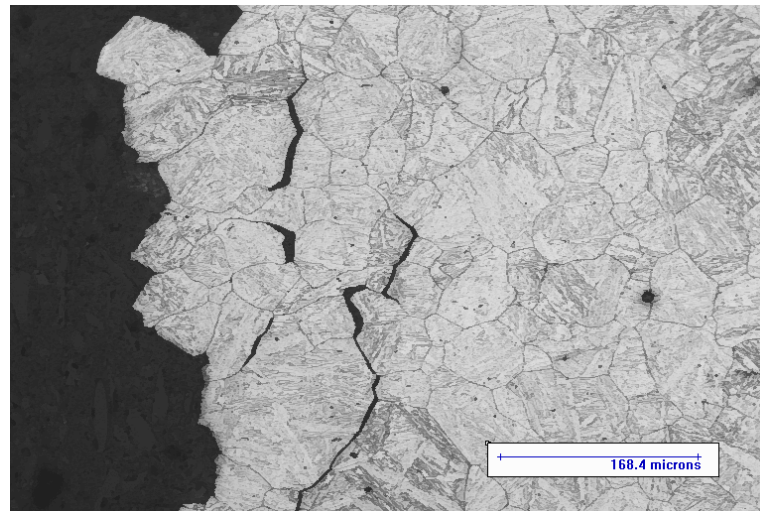


**Figure 10: Intergranular cracking in the coarse-grained HAZ of P23 steel.<sup>55</sup>**

Examination has shown that damage caused by stress relief cracking forms at the boundaries of large prior austenite grains by a mechanism of creep cavitation.<sup>56</sup> Cavities nucleate primarily on PAGB at incoherent precipitates, acting as stress concentrators. Susceptibility to reheat cracking is a function of precipitation strengthening in the grain interior, strengthening and weakening behaviour of grain boundaries and relaxation of residual stresses.

#### **4.3 Type IV cracking - the end of life failure mechanism in 9Cr steels**

Type IV cracking is defined as the formation and propagation of failures in the fine-grained HAZ and the intercritically heated region of the HAZ. A strict differentiation between ICHAZ and FGHAZ is generally difficult because of very similar microstructural

features in both regions. Currently, Type IV cracking is considered as the major “end of life” failure mechanism for ferritic creep resistant steel weldments in power generating industry. Therefore, this failure mechanism is of great interest and many researchers have investigated this life limiting phenomenon in welded components. Type IV cracking has been observed in low alloy ferritic/bainitic steels ( $\frac{1}{2}\text{Cr}\frac{1}{2}\text{Mo}\frac{1}{4}\text{V}$ , 1CrMo, 1CrMoV,  $1\frac{1}{4}\text{Cr}\frac{1}{2}\text{Mo}$ , 2CrMo, T/P22, T/P23, T/P24), as well as in ferritic/martensitic 9-12%Cr steels (P91, X20CrMoV121, P92, P122, E911).<sup>57-68</sup>

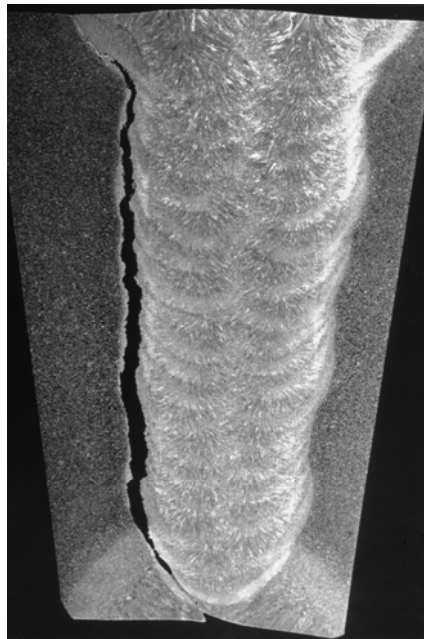


**Figure 11: Type IV cracking observed in a low alloyed 1Cr-0.5Mo pipe (wall thickness 86 mm), after 200.000 hours in service at 540°C and 18 MPa.<sup>69</sup>**

Time to rupture for failures in the Type IV region is sensitive to the stress state and the applied loading direction. Cracking was observed in seam welds as well as in girth welds. Whereas girth welds, loaded by system axial stresses, tend to fail by a “leak before break” mechanism, failures in seam welds, loaded by the hoop stress, can be catastrophic.<sup>70</sup> Review papers on Type IV cracking have been written by Middleton and Metcalfe (1990)<sup>62</sup>, Ellis and Viswanathan (1998)<sup>70</sup> and Francis et al. (2006)<sup>20</sup>.

Creep failures in ferritic weldments at high stress levels take place randomly either in BM, WM or the HAZ, whereas fracture location of weldments exposed to lower stress levels is shifted into the very narrow FGHAZ or intercritical HAZ region.

Generally, Type IV cracking can be seen as the result of a microstructural zone of material weak in creep strength surrounded by material that is stronger in creep. This mismatch in creep properties leads to highly complex material behaviour.<sup>57</sup>



Figure 12: Cracking found on a grade 91 header after operation for 58,000 hours at 580°C. Fracture mode identified as Type IV on the header side toe of a large header to stub weld.<sup>71</sup>

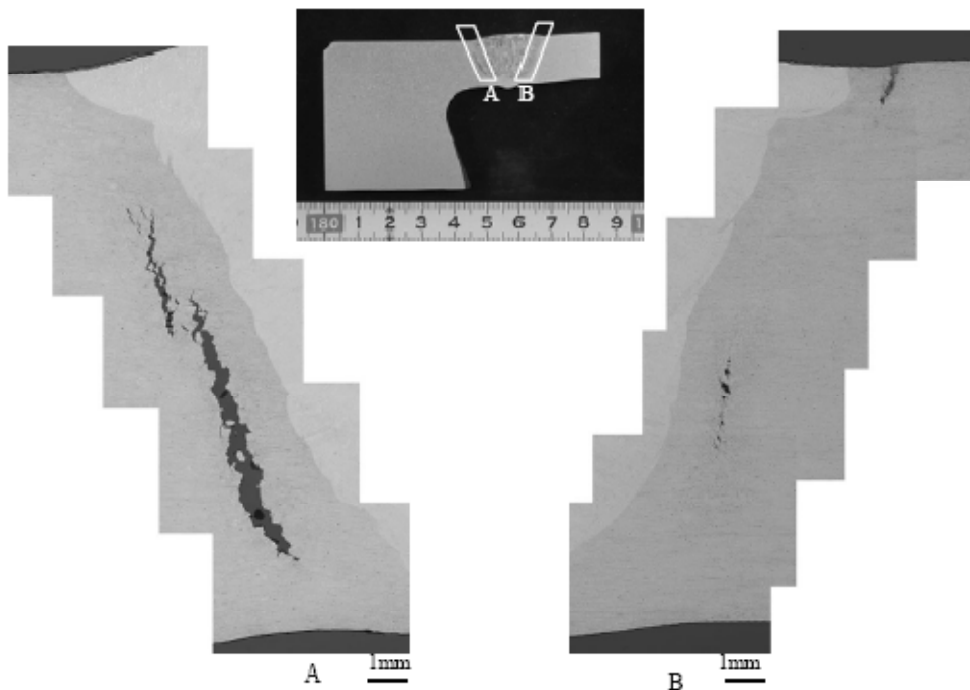
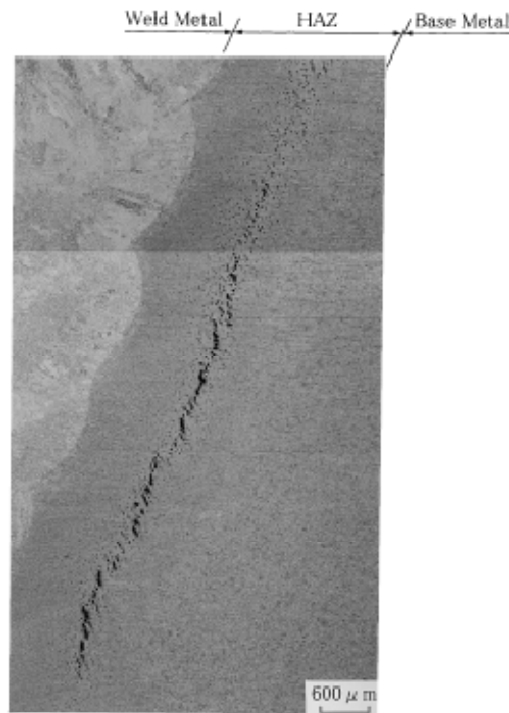


Figure 13: Type IV failure in P122 header end cap weld.<sup>72</sup>

Most fractures have a macroscopic appearance typical of a low ductility failure. Figure 13 shows a Type IV failure in a P122 header end cap weld. Cracks were observed on both sides of the FGHAZ of the weldment. Calculation of the failure strain using the overall gauge length results in very low strain values, typically below 10%. This leads to the assumption that the fracture mode is relatively brittle. However, significant creep deformation can be measured in a narrow part of the HAZ close to the unaffected base material as investigated by Parker.<sup>64</sup> This fact indicates a strong strain localisation. Parker estimated the longitudinal strain of uniaxial specimens after creep exposure from measurements of the grain dimensions present in the fractured region. Changes in grain shape suggest a localised strain of about 20-30% and, therefore, the failures are in fact locally highly ductile in nature. The failure mechanism of Type IV cracking is governed by creep cavitation. Creep voids generally initiate sub-surface and grow by a diffusive mechanism. Figure 14 shows a replica taken from a P122 weldment, creep tested at 675°C and 70 MPa until fracture after 689 hours occurred. A very narrow band of voids in the outer region of the HAZ, 1 mm away from the fusion line, was observed. Micro-cracks were formed by coalescence of voids in the specimen interior.



**Figure 14: Microstructure of P122 cross-weld creep tested at 675°C and 70 MPa for 689 hours. Creep void nucleation and formation of micro-cracks was observed in the outer region of the HAZ.<sup>73</sup>**

Preferred nucleation sites for voids are particle/matrix interfaces associated with inclusions or second phase particles.<sup>74</sup> In the IC/FGHAZ region of weldments, carbides are only partially dissolved by the applied weld thermal cycle. Precipitation on retained large particles, such as  $M_{23}C_6$ , is favoured instead of fine re-precipitation on grain boundaries in order to decrease the interfacial energy of the microstructure.<sup>75</sup> Therefore, retained carbides coarsen more rapidly than those in the base material or weld metal during PWHT and are preferred nucleation sites for creep voids. Letofsky<sup>76</sup> compared the evolution of precipitates at different stages of creep testing in the ICHAZ of G-X12CrMoWVNbN10.1.1 steel with that of the unaffected base material and matching weld metal using energy filtering transmission electron microscopy (EFTEM). His work is in good agreement with other research showing that kinetics of microstructural changes, e.g. coarsening of precipitates and formation of Laves and Z-phase are significantly faster in the ICHAZ than in all other regions of the weld (Figure 15).<sup>65, 77-82</sup>

### G-X12 CrMoWVNbN 10.1.1, ICHAZ

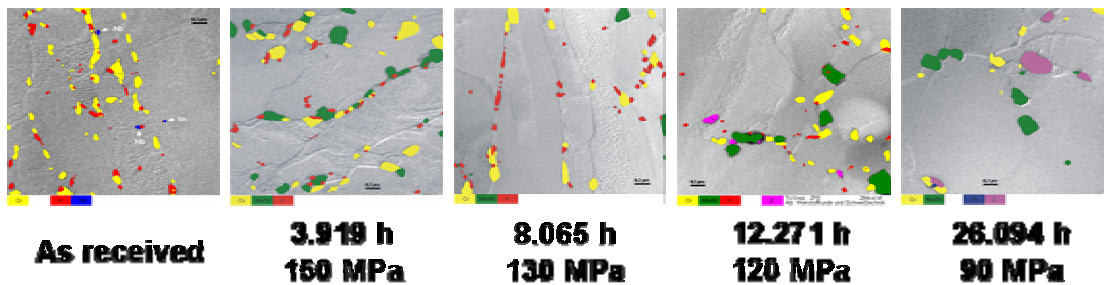


Figure 15: Evolution of precipitates in the ICHAZ of creep exposed cross-weld samples of G-X12CrMoWVNbN10.1.1 steel.<sup>82</sup>

General agreement also prevails concerning other microstructural features of the IC-/FGHAZ. Both regions susceptible for Type IV cracking consist of fine equiaxed sub grains. A lath-type structure as generally observed in all other parts of weldments is missing.<sup>75</sup> During creep exposure the sub-grain microstructure tends to coarsen significantly.<sup>83, 84</sup> TEM investigations also revealed a significantly lower dislocation density in the vicinity of the FGHAZ compared to the other areas in welded joints. Further recovery of excess dislocations takes place during high temperature service.<sup>81</sup> All these microstructural changes take place at higher velocity in the IC/FGHAZ and contribute to the continuous weakening of this specific region, finally leading to the breakdown of creep strength. The formation of a “soft zone” with low hardness is not always directly related to low creep rupture stress. Whereas, in some investigations, the location of final fracture corresponds with that of the soft zone,<sup>10, 70, 80, 85</sup> other researchers clearly distinguish between softened regions and regions with low creep rupture strength.<sup>75, 77, 81</sup>

#### 4.3.1 The role of constraint

The role of constraint on the creep weak IC/FGHAZ region from adjacent stronger CGHAZ and BM is a key factor for clarification of Type IV cracking mechanism. By plain tensile loading of the dissimilar regions of the HAZ in series, the weakest part tries to deform transversely under high strains. If this region is sufficiently thin, it is constrained from doing so by the adjacent stronger material. As a result, a triaxial stress state predominates and prevents the weaker region from yielding.

Under the regime of creep, the situation is more diverse and discussed intensively in literature.<sup>86</sup>

Li<sup>87</sup> simulated creep behaviour of P122 cross-welds using a FEM model based on Norton's law representing four regions with different creep properties. He concluded that the FGHAZ has the highest equivalent strain, high first principal stress and hydrostatic pressure. The constraining effect of BM and CGHAZ prevent creep deformation in the FGHAZ. Therefore, a narrow FGHAZ is calculated to decrease the equivalent strain in the FGHAZ and is considered to be beneficial in decreasing the occurrence of creep voids. Experimental validation is provided by Japanese researchers reducing the HAZ width of P122 steel by electron beam welding (EBW). Creep rupture strength of EB weldments was improved by a factor of 2 compared to weldments produced by GTAW process, although EBW specimens still failed by Type IV mechanism.<sup>88</sup> Crack initiation was at lower creep strain in the EB joint because of larger local multi-axiality compared to the GTAW joint.

Abe et al.<sup>89</sup> simulated Type IV creep crack growth behaviour in P122 weldments using a three-dimensional FE model taking the diffusive growth of creep voids into account. As a result, creep cracks grow faster in the center of specimen thickness than in the perimeter of the specimen. Higher multiaxiality in the center of specimen thickness leads to higher vacancy concentration, which is consistent with experimental observation of initial creep voids in the center region. This is supported by the acceleration of vacancy diffusion, formation and growth of creep voids under multi-axial conditions for welded joint specimen and, as a result, the enhancement of damage accumulation by multiaxial stress states.<sup>90</sup> Moreover, no mechanical constraint throughout simulated HAZ creep specimen resulted in no void formation.<sup>91</sup>

An alternative approach to modelling Type IV damage was introduced by Kimmins and Smith<sup>92</sup>, who suggested that constraint is relaxed by grain boundary sliding. Their experimental results put forward that additional grain boundary sliding results in a greater number of cavities. Once sliding is accommodated the failure time for both cross-weld and simulated Type IV samples was similar. Therefore, they concluded that material weak in creep deforms independently of adjacent stronger material and rather than using conventional continuum damage models in FE analysis, alternative models involving the mechanism of grain boundary sliding require development.<sup>57</sup>

#### 4.3.2 Detectability

As mentioned earlier, Type IV damage initiates as creep cavitation subsurface at about halftime of the expected life of the weldments.<sup>83</sup> However, cracks can form relatively late in

life and crack growth once initiated can, however, be very rapid.<sup>93</sup> Remaining life for propagation throughout the wall can be less than 10,000 hours.<sup>62</sup> Surface bearing cracks do not appear until late in life. Therefore, surface examination of creep exposed weldments only by replication techniques, penetration testing or eddy current testing can be misleading and severe damage in subsurface regions can be overlooked.<sup>69</sup> A sound residual life investigation on weldments can only be performed by advanced ultrasonic (UT) inspections or highly sophisticated volumetric methods such as time of flight diffraction (TOFD) with which creep voids and micro-cracks can be detected even at a life ratio ( $t/t_r$ ) of 0.5. In any case, life assessment methods for weldments vulnerable to Type IV cracking have to include a qualitative damage classification scheme and a cavity density based model.<sup>70, 94, 95</sup>

#### 4.3.3 Solutions for preventing Type IV cracking

The enforcement of a full quality heat treatment consisting of austenitising and tempering on welded structures results in the reconstitution of a homogeneous microstructure. The erasure of the graded microstructure in the heat affected zone results in a complete insensitivity to all types of HAZ cracking mentioned before. A full quality heat treatment on all welded structures is on one hand financially unfeasible and on the other hand just impossible, considering the size of power plant components and the necessity of on-site weldings.

Recently, at the National Institute for Materials Science (NIMS) in Japan, revolutionary 9Cr-3W-3Co steel with reduced nitrogen level and controlled addition of boron was developed. Contrary to all present creep resistant steels, this steel did not show the formation of a fine-grained region within the HAZ. Figure 16 shows results of an electron backscatter diffraction pattern (EBSP) analysis of the grain size, as a function of distance from the fusion line, of conventional P92 steel versus the new 9Cr-3W-3Co material.<sup>96</sup> By the elimination of fine grains in the HAZ, which is limited to a certain compositional range of boron and nitrogen (Figure 17b), the formation of creep damage by Type IV mechanism could be avoided. Up to a duration of 10,000 hours, creep tests at 650°C are very promising and no difference in creep strength between cross-weld specimen and base material is shown (Figure 17a). It is believed that the underlying mechanism is based on the austenite memory effect found in earlier work on 1Cr-1Mo-0.75V(Ti, B) steel.<sup>97</sup> Although the

mechanisms active in this steel are up to now not fully understood, this might be a possible approach for the prevention of Type IV cracking in ferritic creep resistant steels.

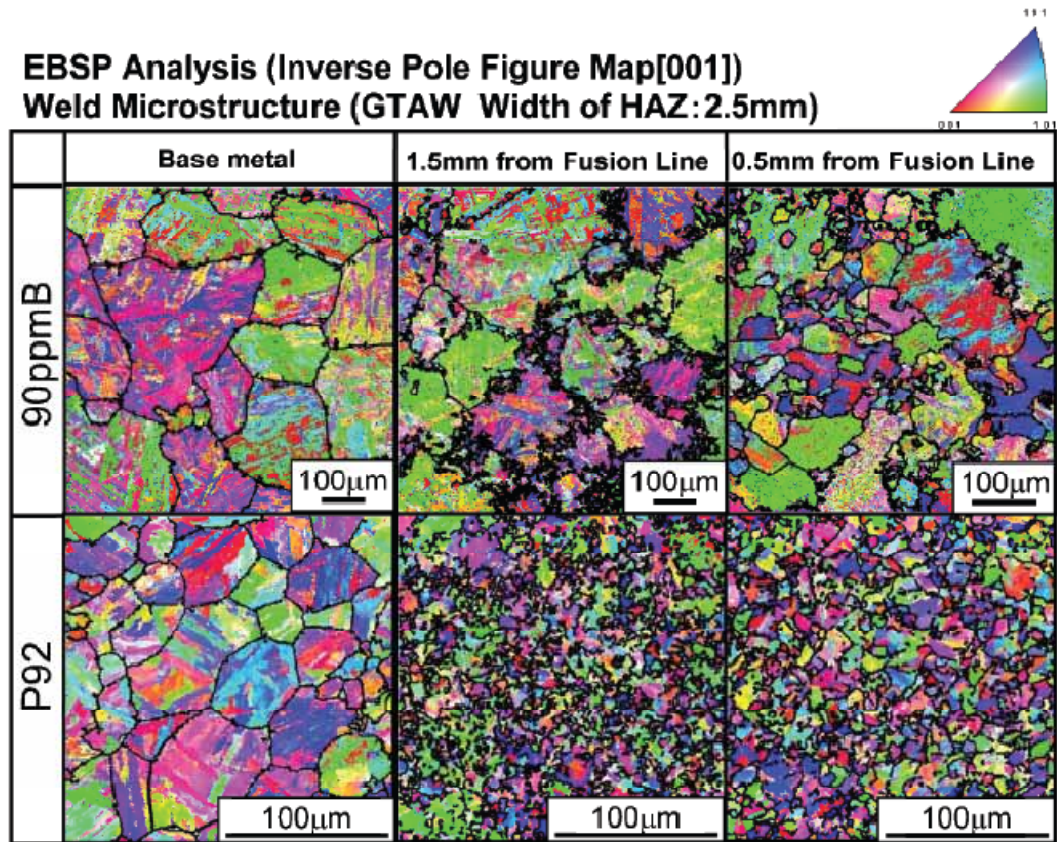


Figure 16: Electron backscatter diffraction pattern (EBSP) analysis results for 9Cr-3W-3CoNB steel and P92 steel HAZ microstructures.<sup>96</sup>

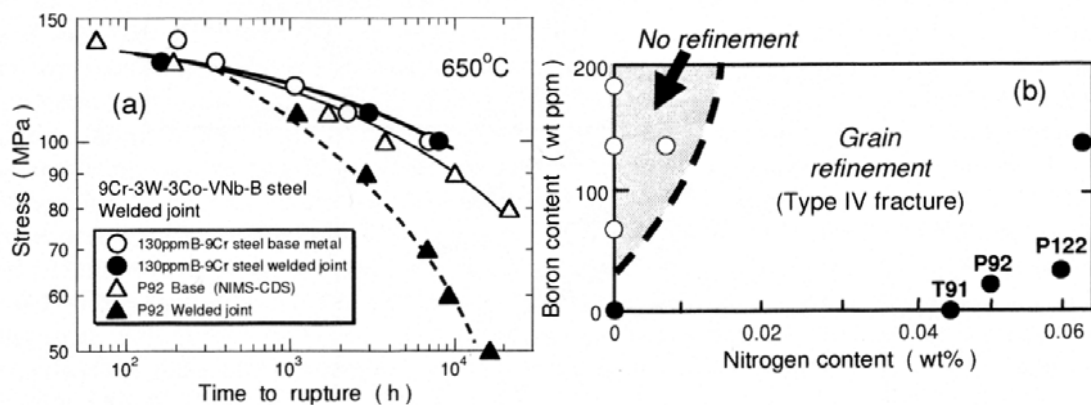


Figure 17: (a) Creep rupture data obtained at 650°C for welded joints and base material of 9Cr-3W-3Co-VNb steel with 130 ppm boron compared to P92 data.<sup>91</sup> (b) Grain refinement in 9 to 12% Cr steels during heating to temperatures between 900°C and 1100°C.<sup>98</sup>

#### 4.4 Cracking in dissimilar welds

For the sake of completeness, cracking in dissimilar welds is mentioned in this chapter. A multitude of different types of dissimilar welds exists, depending on the steel grades and welding consumables used. In thermal power stations, dissimilar welded joints between ferritic and austenitic steels and high alloyed martensitic and low alloyed ferritic/bainitic steels are commonly in use. Weldments, joining different alloys, are sometimes characterised by a very sharp transition in microstructure, physical properties, chemical potential and, as a result, in mechanical properties. Due to the diversity of different types of joints, this chapter numerates only basic mechanisms relevant for creep damage in heat resistant weldments. Two major mechanisms are:

- mismatch in physical properties
- decarburisation / carburisation (gradient in chemical composition and potential)<sup>99</sup>

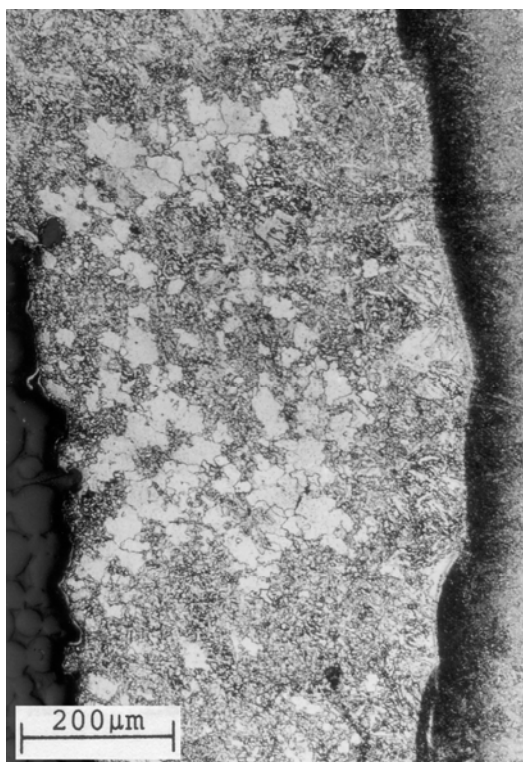


Figure 18: Cross-weld creep sample of 1%CrMoV cast welded with 12%CrMoV filler fractured after 806 hours at 180MPa at 550°C in the decarburised CGHAZ of the 1%CrMoV steel.<sup>40</sup> Fracture surface on the left with decarburised (bright appearance) areas.

Firstly, additional stresses can arise from a mismatch in physical properties. Different coefficients of thermal expansion and heat conductivity introduce thermal stresses adding up with system stresses. This results in an additional localised loading due to the combination of creep and fatigue close to the fusion line leading to premature failures.

The more potent mechanisms influencing the time to rupture and failure location in creep exposed dissimilar welds are variations within the microstructure due to gradients in chemical composition.

Formation of localised zones with inferior creep properties can be the result of diffusion of alloying elements across the interface either initially during PWHT or during service at elevated temperature.<sup>100</sup> Investigating welds between a 1%CrMoV cast and a 12%CrMoV forged pipe (X20CrMoV12-1) utilising a 12%CrMoV filler material, Witwer<sup>101</sup> showed the formation of a carbide seam in the fusion line area of the high alloyed weld material. In the low alloyed material, as a result, a carbon depleted soft region had formed. The width of carbide seam and carbon depleted region is strongly influenced by PWHT and service parameters.<sup>102</sup> Regarding creep rupture properties, this narrow zone weak in creep is surrounded by zones of higher creep strength, leading to localised, premature damage in the decarburised HAZ region of the low alloyed steel (Figure 18).

## 5 Physical heat affected zone simulation

The problem of conducting basic investigations on HAZ microstructures in actual welds is the presence of extremely small and inhomogeneous sub-zones (see Figure 3).

Physical HAZ simulation allows the generation of larger volumes of material with uniform microstructure and properties which represent one specific point within the HAZ. This homogeneous microstructure can be used for metallographic investigations as well as tested by applying common standardised mechanical testing procedures such as tensile tests, creep and fatigue tests and impact tests.

Physical weld HAZ simulation requires a time-temperature profile characteristic for a specific welding procedure as input data. The time-temperature profile can either be measured from real welds, be derived from analytical solutions of the heat conduction equation (Rosenthal<sup>103</sup>, Rykalin<sup>104</sup>) or by using more sophisticated numerical thermal heat source models like that set up by Goldak<sup>105</sup>.

Currently, different techniques for the physical HAZ simulation can be used, namely:

- heating in a hot salt bath until the peak temperature is reached, immediately followed by cooling in a moderated tempered salt bath.
- induction heating with subsequent quenching in an oil bath.
- heating in a furnace to peak temperature, followed by cooling in air or an oil bath.
- controlled resistance heating in the specimen using a weld simulator (GLEEBLE<sup>TM</sup>, Smitweld<sup>TM</sup>)
- controlled induction heating and cooling using a quenching dilatometer.

Each physical simulation process has its own characteristic advantages and disadvantages and the appropriate process has to be chosen individually. In Table 4 characteristics of different physical HAZ simulation methods are listed.

Table 4: Comparison of different HAZ simulation techniques (modified from Buchmayr<sup>106</sup>).

| Feature                               | Gleeble simulation                         | Induction heating + oil quenching          | Salt bath heating + salt bath cooling               | Furnace heating + cooling      |
|---------------------------------------|--|--|---|--------------------------------|
| heating rate                          | high, as in HAZ                            | slower as in HAZ                           | slower as in HAZ                                    | slower as in HAZ               |
| peak temperature                      | exact programmable                         | exact controllable                         | exact when using thermocouples                      | exact when using thermocouples |
| holding time at $T_p$                 | rounded T-t curve as numerically predicted | some seconds                               | none  | none                           |
| cooling rate                          | programmable                               | limited by oil temperature and sample size | determined by salt bath temperature and sample size |                                |
| homogeneity of microstructure         | limited length of about 10mm               | whole sample length                        | whole sample length                                 | whole sample length            |
| gauge length                          | reduced (~10mm)                            | user-defined                               | user-defined  | user-defined                   |
| reproducibility                       | high                                       | moderate                                   | moderate  | moderate                       |
| agreement with distinct HAZ structure | excellent                                  | good                                       | good  | good                           |
| consideration of constraint effects   | possible by applying mechanical loading    | not done                                   | impossible  | impossible                     |
| additional data measurable            | dilatation                                 | none                                       | none  | dilatation                     |
| simulation costs and duration         | high                                       | low  | low   | low cost but time consuming    |

HAZ simulation using a quenching dilatometer has not been added to the table above as only small specimens can be processed which are not suitable for mechanical testing. The process itself is highly recommended, as it allows highest heating and cooling rates, exact controllable time-temperature profiles, determination of phase transformations and good reproducibility.

## 6 Direct observation of phase transformations during welding

With conventional characterisation techniques, such as metallography or dilatometry, phase transformations in the HAZ during welding cannot be directly monitored. X-ray diffraction using high-energy synchrotron radiation can provide this information through the in-situ monitoring of phase transformations in real time. This experimental method has been established by J. W. Elmer of Lawrence Livermore National Laboratory and provides new insights into phase transformations in the HAZ during welding. Two different methods of in-situ XRD are established. *Spatially-Resolved X-Ray Diffraction (SRXRD)* experiments are performed during GTAW to obtain diffraction patterns at discrete locations across the width of the HAZ. Several SRXRD scans have to be made, starting from a location near the weld pool and proceeding outwards across the entire HAZ area. Figure 19 shows the experimental setup of SRXRD measurements during the GTAW process.

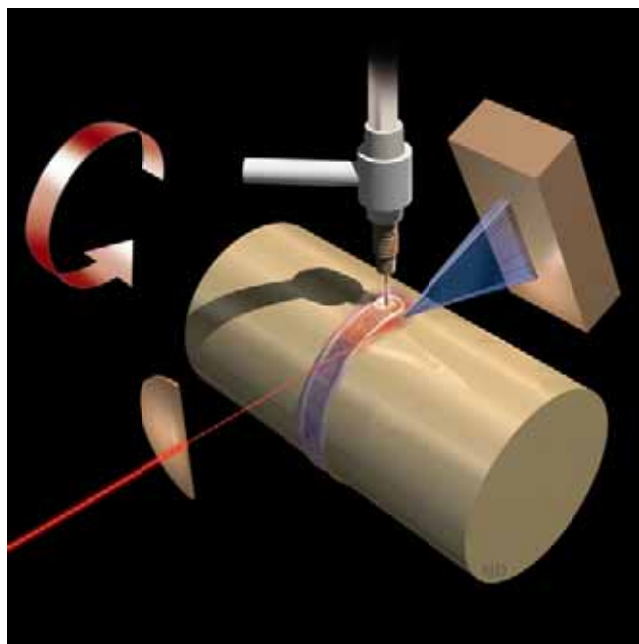


**Figure 19: Experimental setup of Spatially Resolved X-Ray Diffraction (SRXRD) during welding using synchrotron radiation. The beam is positioned in the HAZ and diffraction patterns are recorded by a detector behind. (Picture courtesy of J.W. Elmer)**

The recorded XRD patterns can then be analysed in order to determine the degree to which a phase transformation has proceeded or to monitor changes in the characteristics of each phase. Based on these results, the kinetics of the prominent phase transformation

taking place in each materials system can be experimentally measured and the results integrated into phase transformation models. So far, SRXRD experiments have been performed on commercially pure titanium, Ti-6Al-4V, 1005 steel, 1045 steel, and 2205 DSS (Duplex Stainless Steel). By this method, a map of phases present in the HAZ can be constructed for a single set of welding conditions. Palmer et al.<sup>107</sup> acquired a complete phase map of a duplex stainless steel weldment based on SRXRD observations (Figure 20). Three phase regions, the liquid, a single  $\delta$ -Fe (bcc) phase, and a two phase  $\delta$ -Fe (bcc) +  $\gamma$ -Fe (fcc) region are included. Semi-quantitative  $\delta$  volume fractions are superimposed over the calculated liquidus (1443°C) and the  $\delta/\gamma$  solvus (1316°C) isotherms. Adjacent to the liquid phase, single  $\delta$ -phase region is observed. As the distance from the weld centreline increases, two phase  $\delta/\gamma$  regions are observed adjacent to the single  $\delta$ -phase regions and extend in all directions. This map provides information concerning the effects of the welding process on the  $\delta/\gamma$  phase balance across all of the regions surrounding the weld pool and allows tracking  $\delta$ - $\gamma$  transformation with respect to the progress of the weld.

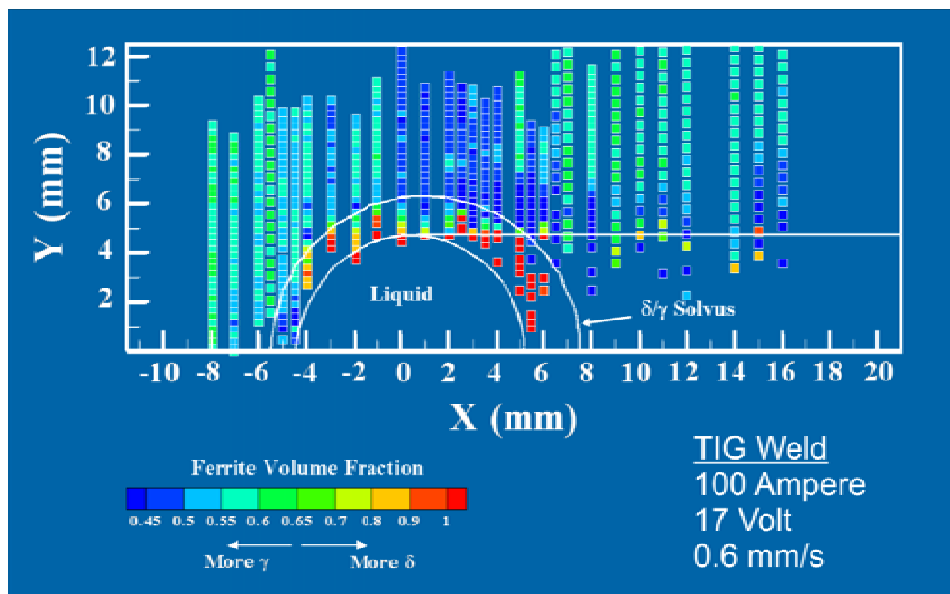
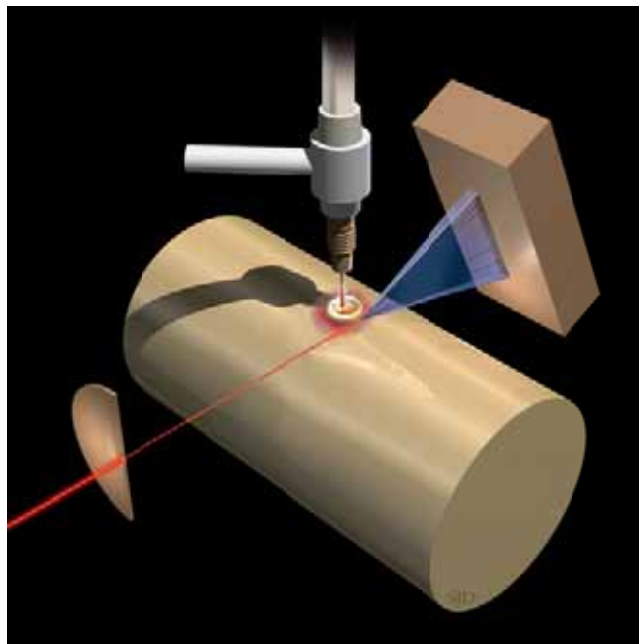


Figure 20: Complete phase map of 2205 Duplex Stainless Steel weldment calculated from in-situ SRXRD patterns showing delta ferrite volume fractions.<sup>107</sup>

In-situ *Time-Resolved X-Ray Diffraction (TRXRD)* experiments during welding allow visualising phase transformations in the HAZ under rapid heating and cooling conditions. The X-ray beam is positioned at different locations relative to the center of the weld. A GTA spot weld is made by striking a stationary arc, maintaining this arc for a fixed amount

of time, and then extinguishing the arc to let the weld cool. TRXRD data are gathered over a period of time during welding, allowing both the heating and the cooling cycles to be observed during one weld. By positioning the beam close to the center of the weld, melting and re-solidification can be studied. Positioning the beam farther away from the center of the weld allows transformations in the HAZ to be studied.



**Figure 21: Experimental setup of Time Resolved X-Ray Diffraction (TRXRD) during welding using synchrotron radiation. (Picture courtesy of J.W. Elmer)**

Analysis of TRXRD data allows calculating relative volume fractions of present phases, their lattice parameters, and the widths of their diffraction peaks as a function of weld heating and cooling time. Included in these results is information related to the kinetics and types of phase transformations occurring in the HAZ during welding. Modelling of the experimentally measured transformation rates will be used for better understanding of mechanism behind each transformation and for determining parameters useful in the prediction of phase transformations. So far, TRXRD measurements have been performed on 1005 steel, 1045 steel, 2205 DSS, 304 stainless steel, and Ti-6Al-4V.

Babu et al.<sup>108</sup> studied the primary weld solidification in Fe-C-Al-Mn steel welds with different weld cooling rates using in-situ TRXRD. The primary solidification phase under rapid- and slow-cooling rate conditions was examined. The results showed non-equilibrium austenite solidification during rapid cooling in contrast to equilibrium  $\delta$ -ferrite solidifica-

tion that took place under slow cooling conditions. This observed change in solidification sequence from primary delta ferritic to primary austenitic solidification was then mathematically predicted with increasing solid-liquid interface velocity using interface response function calculations.

In both XRD experimental techniques described above, the temperature cycle produced by the welding arc is not well controlled and temperatures are not directly measured. Useful kinetic information from these data could only be obtained by coupling XRD measurements with a thermal-fluids numerical simulation. This code enables the temperatures in the HAZ and fusion zones to be calculated and is accurate enough to determine heating rates, cooling rates and approximate temperatures where phase transformations are observed. However, some of the finer details of phase transformations cannot be measured with confidence due to the uncontrolled weld thermal cycle and some uncertainties about the actual temperature of the weld. Therefore, a special experimental setup was created to investigate phase transformations under more controlled conditions (Figure 22).

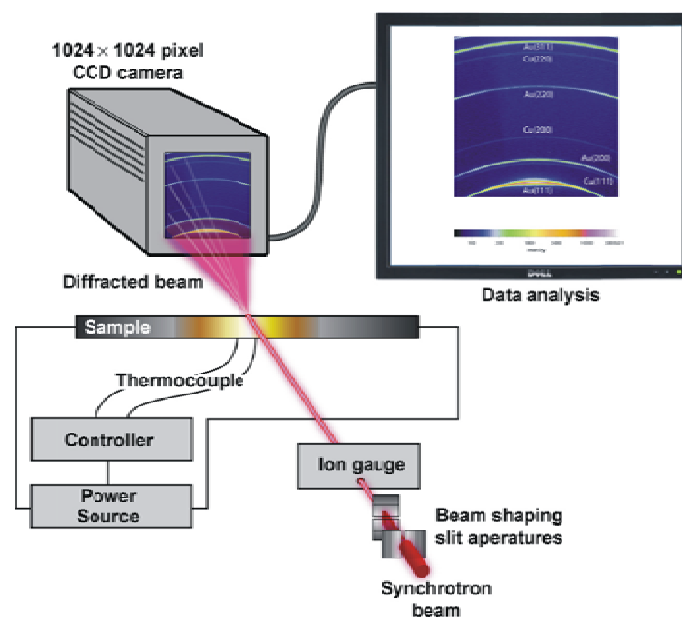


Figure 22: Schematic of in-situ XRD measurements during controlled heating and cooling.

In this setup, in-situ XRD measurements are performed during rapid heating and cooling of specimens using direct resistance heating and water cooled grips. The temperature of the samples is monitored and recorded using thermocouples spot welded to the back side of the sample directly below the X-ray impingement point. The entire assembly is

covered with a canister in which pure helium is introduced to minimise oxidation of the sample during high temperature runs. This experimental setup allows obtaining high quality XRD patterns during controlled programmed thermal cycles. Analysis of in-situ XRD data allows calculation of relative volume fractions of present phases, their lattice parameters, and the widths of their diffraction peaks as a function of time and temperature.

## IV. Experimental

### 1 Studied materials

Within this work, four different martensitic steels are investigated. All steels are within the group of 9 wt. % chromium steels and have been melted with controlled additions of boron and nitrogen. Two steels are cast materials, designated as CB2A and CB2, and have been developed within the European COST activities. Of these, CB2A material is part of a 100 kg test melt produced by voestalpine Gießerei Linz, Austria and CB2 material is part of a 4.3 ton pilot valve body produced by PHB Stahlguss International, Germany. The third steel, NPM1, is a 20 kg test melt particularly produced for this investigation.

For long-term creep testing of cross-welds, specimens have been extracted from a butt-welded collector pipe of commercially available steel grade E911, welded with three different types of filler materials. This task is incorporated within the European COST activities under the title “Matching Program”.

#### 1.1 CB2A - Heat 145

The investigated CB2A material originates from a 100 kg test melt (Heat 145) produced by voestalpine Gießerei Linz, Austria. This heat has been already under investigation in a Master Thesis by Schalber<sup>113</sup> in 1998 and Doctoral Thesis by Letofsky<sup>10</sup> in 2001. Results, relevant for this work, are summarised in Appendix B. CB2A is a modified 9Cr-1Mo steel with a relatively high carbon content of 0.168 wt. %, about 100 ppm boron and 160 ppm nitrogen. The chemical composition of heat 145 is listed in Table 5.

**Table 5: Chemical composition of CB2A - Heat 145 in wt. %.**

| Analysis   | C     | Si   | Mn   | P         | S        | Al       | Cr   | Mo   | Ni   | V    |
|------------|-------|------|------|-----------|----------|----------|------|------|------|------|
| CB2A (145) | 0.168 | 0.23 | 0.22 | 0.008     | 0.004    | 0.003    | 8.85 | 1.54 | 0.18 | 0.29 |
|            |       |      |      | <b>Nb</b> | <b>B</b> | <b>N</b> |      |      |      |      |
|            |       |      |      | 0.057     | 0.0092   | 0.0160   |      |      |      |      |

The test melt has been subjected to a heat treatment similar to the one applied for large cast components (Table 6). The heat treatment consists of austenitising at 1100°C for 8 hours with subsequent air cooling. Tempering is performed at 730°C for 10 hours followed by air cooling. An additional stress relieving at 730°C for 24 hours with subsequent air cooling is performed to simulate PWHT after fabrication welding of casting defects.

Within this study, CB2A material is used for physical HAZ simulation to study the formation of delta ferrite in the HAZ of simulated high energy welds.

**Table 6: Quality heat treatment of test melt CB2A (Heat 145) at voestalpine Gießerei Linz.**

|                         | Heating rate | Temperature | Duration | Cooling media |
|-------------------------|--------------|-------------|----------|---------------|
| <b>Austenitising</b>    | n.a.         | 1100°C      | 8 h      | air           |
| <b>Tempering</b>        | n.a.         | 730°C       | 10 h     | air           |
| <b>Stress relieving</b> | n.a.         | 730°C       | 24 h     | air           |

n.a. ... not available

## 1.2 CB2 - Heat 37514

CB2 material has been produced by PHB Stahlguss International, Germany. After melting in a combined arc furnace/converter process, a 4.3 ton pilot valve body has been cast. The chemical composition of CB2 - Heat 37514 is shown in Table 7 and is reported with heat treatment specifications and basic mechanical properties in material certificate number 49.0840.

**Table 7: Chemical composition of CB2 Heat 37514 in wt. %.**

| Analysis           | C    | Si   | Mn       | P         | S         | Al       | Cr       | Mo   | Ni   | Co   |
|--------------------|------|------|----------|-----------|-----------|----------|----------|------|------|------|
| <b>CB2 (37514)</b> | 0.11 | 0.28 | 0.86     | 0.013     | 0.006     | 0.007    | 9.12     | 1.46 | 0.22 | 1.02 |
|                    |      |      | <b>V</b> | <b>Nb</b> | <b>Ti</b> | <b>B</b> | <b>N</b> |      |      |      |
|                    |      |      | 0.19     | 0.060     | 0.001     | 0.0115   | 0.0211   |      |      |      |

The heat treatment at PHB Stahlguss International consists of austenitising at 1100°C for 9 hours and tempering at 730°C for 10 hours. The heat treatment parameters are summarised in Table 8. The base material properties of this heat have already been evaluated in

previous work within COST 522 and COST 536. A summary of results, relevant for this study, is given in Appendix B. A block of 70kg of this melt has been sent to TU Graz for heat affected zone simulations.

**Table 8: Heat treatment parameters of 4.3 ton CB2 pilot valve at PHB Stahlguss International, Germany.**

|                      | Heating rate           | Temperature | Duration | Cooling media |
|----------------------|------------------------|-------------|----------|---------------|
| <b>Austenitising</b> | <100°C h <sup>-1</sup> | 1100°C      | 9 h      | air           |
| <b>Tempering</b>     | <70°C h <sup>-1</sup>  | 730°C       | 10 h     | air           |

CB2 material is used for physical HAZ simulation, simulating welding processes with different heat inputs, ranging from 3.7 kJ cm<sup>-1</sup> to 84.2 kJ cm<sup>-1</sup>.

### 1.3 NPM1

A 20 kg test melt of a boron-nitrogen balanced 9Cr-3W-3Co steel has been produced by vacuum induction melting (VIM) at the University of Leoben. The alloying concept for this test melt follows published Japanese research work at the National Institute for Materials Science (see Appendix C). An ingot with dimensions 110 x 110 mm and a length of 170 mm has been cast (Figure 23).



**Figure 23: Casting of test melt NPM1 at University Leoben in a vacuum induction furnace (left) and moulded ingot (right).**

For homogenisation of the material, the block has been forged to the final dimensions of 50 x 50 mm and a resulting length of 800 mm at Böhler Schmiedetechnik, Kapfenberg, Austria. The temperature window for the forging process is defined by a maximum forging temperature of 1150°C and a minimum temperature of 950°C.

**Table 9: Chemical composition of test melt NPM1 in wt. %.**

| Analysis    | C     | Si   | Mn       | P         | S         | Al       | Cr       | Ni   | W    | Co   |
|-------------|-------|------|----------|-----------|-----------|----------|----------|------|------|------|
| <b>NPM1</b> | 0.074 | 0.29 | 0.44     | 0.009     | 0.004     | <0.005   | 9.26     | 0.06 | 2.84 | 2.95 |
|             |       |      | <b>V</b> | <b>Nb</b> | <b>Ti</b> | <b>B</b> | <b>N</b> |      |      |      |
|             |       |      | 0.21     | 0.056     | <0.005    | 0.0120   | 0.0130   |      |      |      |

The forged block is subjected to a quality heat treatment consisting of austenitising at 1150°C for 1 hour with subsequent air cooling, followed by tempering at 770°C for 4 hours with ensuing air cooling. The final chemical composition of the test melt is determined after quality heat treatment and is listed in Table 9. Heat treatment parameters are summarised in Table 10.

**Table 10: Heat treatment parameters of test melt NPM1.**

|                      | Heating rate          | Temperature | Duration | Cooling media |
|----------------------|-----------------------|-------------|----------|---------------|
| <b>Austenitising</b> | 250°C h <sup>-1</sup> | 1150°C      | 1 h      | air           |
| <b>Tempering</b>     | 250°C h <sup>-1</sup> | 770°C       | 4h       | air           |

NPM1 material is used for physical HAZ simulation. Heat input is kept constant at 10.8 kJ cm<sup>-1</sup> and peak temperatures varied from 800°C to 1300°C. For comparison, a real weld using the same heat input and Ni-base weld metal is fabricated.

#### 1.4 E911 – X11CrMoWVNb9-1-1

The investigated E911 material is part of a commercially produced pipe by Vallourec and Mannesmann with an outside diameter of 355 mm and a wall thickness of 43 mm. The

compositional range according European standard EN-10302 (05/2002) for X11CrMoWVNb9-1-1 is listed in Table 11.

**Table 11: Compositional range of steel grade X11CrMoWVNb9-1-1 (E911, 1.4905) in wt. %.**

| Analysis | C    | Si    | Mn   | Cr   | Ni   | Mo   | V    | W    | Nb   | N    | B    |        |
|----------|------|-------|------|------|------|------|------|------|------|------|------|--------|
| E911     | min. | 0.090 | 0.10 | 0.30 | 8.50 | 0.10 | 0.90 | 0.18 | 0.90 | 0.06 | 0.05 | 0.0005 |
|          | max. | 0.130 | 0.50 | 0.60 | 9.50 | 0.40 | 1.10 | 0.25 | 1.10 | 0.10 | 0.09 | 0.0050 |

### 1.5 Weld filler metals

The scope of this doctoral thesis comprises the investigation of three butt welds of an E911 collector pipe using three different weld metals and one demonstration weld of NPM1 material utilising Ni-base weld metal.

Weld filler metals utilised for the fabrication of the E911 collector butt welds have been supplied by Böhler Thyssen Welding, Germany. The chemical composition of the filler metals according Böhler Thyssen Welding product catalogue is listed in Table 12

**Table 12: Chemical composition of weld metals in wt. % according to Böhler Thyssen Welding product catalogue.**

|                   | C    | Si   | Mn  | Cr  | Mo  | Ni  | W   | V   | Nb   | N    |
|-------------------|------|------|-----|-----|-----|-----|-----|-----|------|------|
| Thyssen Chromo 9V | 0.09 | 0.2  | 0.6 | 9.0 | 1.1 | 0.8 | -   | 0.2 | 0.05 | 0.04 |
| Thermanit MTS 911 | 0.11 | 0.25 | 0.6 | 8.8 | 1.0 | 0.7 | 1.0 | 0.2 | 0.05 | 0.05 |
| Thermanit MTS 616 | 0.11 | 0.2  | 0.6 | 8.8 | 0.5 | 0.7 | 1.6 | 0.2 | 0.05 | 0.05 |

For fabrication of cross-weld specimens of NPM1 material Ni-base filler metal Böhler *Nibas 70/2-IG* (AWS NiCr-3) was utilised. Ni-base filler metal was chosen as further research work comprises creep testing of cross-weld samples to study the HAZ of NPM1 steel under creep loading. At the moment, there is no martensitic weld metal available with creep rupture properties comparable to the expected NPM1 base material creep rupture strength. To avoid failures in a weak weld metal, *Nibas* weld metal with high creep resistance has been chosen. The chemical composition of *Nibas 70/20-IG* GTAW wire is listed in Table 13.

**Table 13: Chemical composition of Ni-base filler Nibas 70/20-IG in wt. % according to Böhler Thyssen Welding product catalogue.**

| Analysis                 | C     | Si   | Mn   | P     | S     | Al     | Cr   | Ni   | W    | Co   |
|--------------------------|-------|------|------|-------|-------|--------|------|------|------|------|
| Böhler<br>Nibas 70/20-IG | 0.074 | 0.29 | 0.44 | 0.009 | 0.004 | <0.005 | 9.26 | 0.06 | 2.84 | 2.95 |

## 2 Imaging

### 2.1 Optical Microscopy

To reveal the microstructure of base metals, HAZ simulated material, cross-welds, and creep exposed material, specimens are cut to an appropriate size and for further processing embedded either in Epovit (epoxy for hot mounting) or using cold-curing resin. The surface to be investigated is subsequently ground using SiC paper down to grit 4000 and polished in two steps using a cloth coated with 3 and 1  $\mu\text{m}$  diamond suspension. For the investigation of fracture locations of cross-weld creep specimens, a final vibration polishing step is performed down to a surface roughness of 0.02  $\mu\text{m}$  using a Bühler Vibromet 2 with a 0.02  $\mu\text{m}$  alumina suspension. The polished samples are finally etched using appropriate etchants. A short description of different etchants used in this work is shown in Table 14. The utilisation of different etchants is necessary to highlight special features and phases in the material.

**Table 14: Composition, condition of use, and characteristic field of application of utilised etchants within this work.**

| Name                     | Composition  | Etching procedure                               | Characteristic  |
|--------------------------|--|---|---|
| <b>Adler</b>             | 25 ml distilled water<br>50 ml hydrochloric acid<br>15 g iron(III) chloride<br>3 g ammonium tetrachlorocuperate II | wiping of specimen surface with drenched cotton | Macro etchant, reveals HAZ of cross-weld samples  |
| <b>Modified LBII</b>     | 100 ml distilled water<br>0.75 g ammonium hydrogen fluoride<br>0.90 g potassium disulfide                          | Immersion of sample until sample gets bluish    | Colour etchant, reveals martensitic lath structure, prior austenite grain boundaries and precipitates |
| <b>Picric Acid + HCl</b> | 100 ml ethanol<br>10 g picric acid<br>2 ml hydrochloric acid   | Immersion of sample for ca. 1.5 minutes         | Reveals prior austenite grain boundaries and martensite lath structure                                |

Images are taken using either a Nikon SMZ-U stereo microscope for macroscopic photos up to a magnification of 10 or a Reichert MeF3 optical microscope for higher magnifications.

## 2.2 Scanning Electron Microscopy and associated analytical methods

### 2.2.1 Secondary Electron Mode

Fracture surfaces of Charpy specimens and numerous etched cross-sectional samples (etchants see Table 14) are observed using a LEO 1450 VP Scanning Electron Microscope (SEM) at the IWS. In the secondary electron (SE) mode, the machine is operated at an accelerating voltage of 15 kV. The working distance is adjusted according to the purpose of the study. Larger working distance results in higher depth of focus, whereas less working distance results in higher resolution. Working parameters of the SEM are documented in the footer of each image.

For the investigation of grain size in the HAZ of “Matching Program” specimens, at NIMS, a HITACHI S4700 field emission scanning electron microscope (FESEM) is used. The FESEM is operated using an acceleration voltage of 10 or 15 kV and the working distance is varied from 8 to 13 mm. Operating parameters of the FESEM are documented in the footer of each image.

### 2.2.2 Quad Backscatter Detection (QBSD)

LEO 1450 VP SEM at IWS is equipped with an Everhard-Thornley 4-quadrant backscatter detector. This detector allows generating images of the backscattered electrons emitted from the sample. The image contrast is only governed by the difference in atomic number  $Z$  of elements in the area investigated. Regions comprising of light elements emit less backscattered electrons than regions consisting of elements with higher  $Z$ -values, e.g.  $\text{Fe}_2\text{W}$  Laves phase, therefore, the latter appear brighter in the QBSD image.

### 2.2.3 Electron Backscatter Diffraction (EBSD)

Electron Backscatter Diffraction is a technique, which allows crystallographic information to be obtained from samples observed in the SEM. For EBSD measurements, a stationary electron beam strikes a tilted sample and diffracted electrons are recorded by a detector. The recorded pattern is characteristic for the crystal structure and orientation of the sample region from which it is generated. The diffraction pattern can be used to measure crystal orientations, grain boundary misorientations, distinguish between different phases, and provide information about local crystalline perfection. When the beam is scanned in a grid across a polycrystalline sample and the crystal orientation is measured at each point, the resulting map reveals the constituent grain morphology, orientations, and

boundaries. These data can be used to show preferred crystal orientations (texture) in the material.<sup>109</sup>

In this work, the EBSD method is used to compare prior austenite grain size and martensite lath structure in the base material and the heat affected zone of weldments.

### **Analysis of EBSD data**

During measurement, the EBSD software identifies and assigns the diffraction pattern of the analysed point, as well as identifies phases and orientations. Areas of similar orientation can then be merged together to show grains, subgrains and martensite laths.

The EBSD method can also measure the misorientation between neighbouring points. By analysing the misorientation (Rodriguez Angle), small angle and large angle grain boundaries can be distinguished. Statistical scattering can be filtered applying a method developed by B. Sonderegger.<sup>109</sup>

Whereas small misorientation angles (1-20°) are characteristic for small angle grain boundaries, boundaries with misorientation larger than 50° are typically martensite lath boundaries.<sup>110, 111</sup> Measured points with misorientation from 20 to 50° can be attributed to prior austenite grain boundaries.<sup>112</sup> After filtering EBSD data, small angle grain boundaries (1 – 20°), martensite lath boundaries (50 – 63°) and prior austenite grain boundaries (20 – 50°) can be separated from each other and plotted into the form of orientation maps.

#### **2.2.4 Energy Dispersive X-Ray Spectroscopy (EDX)**

Energy dispersive X-ray spectroscopy is an analytical tool for the chemical characterisation of a sample. By analysing X-rays emitted from the specimen, a qualitative and, with some restrictions, quantitative analysis can be obtained. The LEO 1450 VP SEM at IWS is equipped with a Röntec EDX unit. Apart from area analysis and spot analysis, line scans are conducted to identify modifications in chemical composition along a defined line across the sample surface. The spectra are analysed using the software package Röntec-Edwin.

#### **2.2.5 Focused Ion Beam Technique (FIB)**

Focused Ion Beam (FIB) technology has become a very powerful tool for TEM sample preparation in steel metallography. The preparation of TEM samples of well localised sites allows to directly investigate special points of interest for example grain boundaries. The FIB system uses a Ga<sup>+</sup> ion beam to raster over the surface of a sample in a similar way

as the electron beam in a scanning electron microscope does. The high energy ion beam allows the milling of small ditches in the sample at well localised sites, so that samples, sufficiently thin for TEM investigation, can be cut out of the bulk material. For this investigation, an FEI dual beam UHR FEG-SEM/FIB is used. Figure 24 shows TEM sample preparation using FIB technology on NPM1 base material.

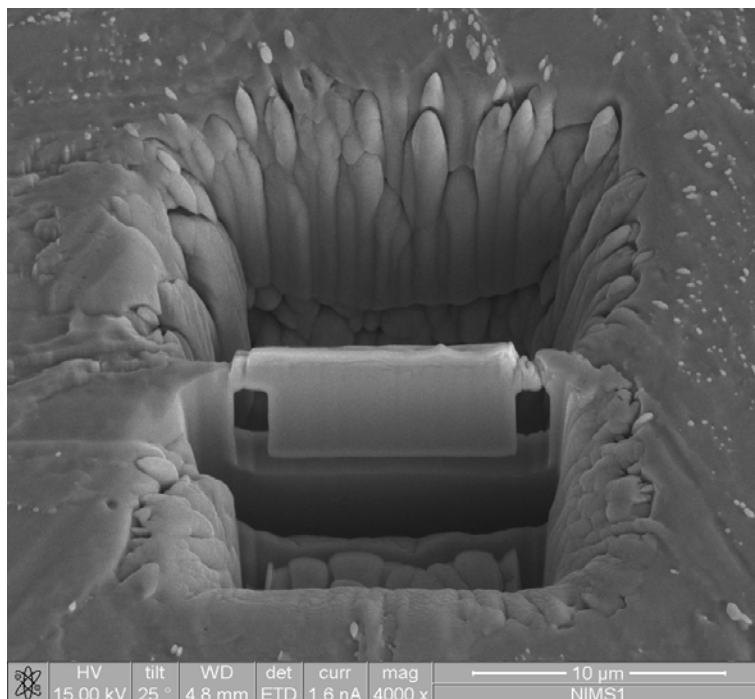


Figure 24: TEM specimen preparation using FIB technology on NPM1 base material.

## 2.3 Transmission electron microscopy and associated analytical methods

### 2.3.1 Bright Field Imaging

Most transmission electron microscopy (TEM) work has been performed using a Philips CM20 TEM at the Research Institute for Electron Microscopy and Fine Structure Research (FELMI) of Graz University of Technology. The TEM with a LaB<sub>6</sub> cathode is operated at an acceleration voltage of 200 kV. The maximum lateral resolution, according to the manufacturer, is 0.27 nm. Preparation of all TEM samples, if not otherwise mentioned (FIB technique), comprised of mechanically cutting disks of 3 mm diameter and of 100 to 300 µm thickness. By mechanical dimpling, the specimen thickness in the center region is reduced below 100 µm. The final step in sample preparation is electrolytic thin-

ning using Ar-ions until a hole in the center is formed. The area next to the hole is sufficiently thin (<100 nm) to perform TEM investigations.

### 2.3.2 Energy Dispersive X-Ray Spectroscopy (EDX)

Energy dispersive X-ray analysis is used to quantify the chemical composition of a small specimen area. The advantage of an EDX system, compared to electron energy loss spectroscopy (EELS), is a significantly higher accuracy in the quantification of elemental content. Philips CM20 TEM is equipped with an HPGGe EDXS detector. A characteristic EDX spectrum of a chromium carbide is shown in Figure 25.

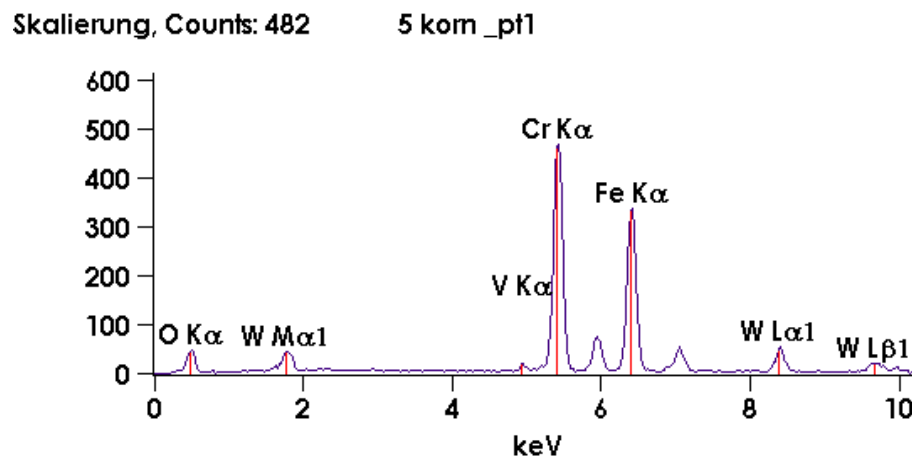


Figure 25: EDX spectrum of a chromium carbide showing peaks of W, V and Cr.

For the analysis of retained delta ferrite in the simulated HAZ of CB2A steel, a JEOL JEM-2010F operated in scanning TEM (STEM) mode with aligned JEOL JED-2300 PREMIUM EDX unit has been used at NIMS, Japan. This EDX system has a minimum energy resolution of 128 eV and can detect elements of the periodic table starting from boron. Apart from conventional spot and line scans, mappings of the sample surface are obtained.

### 2.3.3 Electron Energy Loss Spectroscopy (EELS)

Electron energy loss spectroscopy is an analytical technique in TEM for analysis of elemental composition of small specimen areas. EELS has a very high efficiency in detecting elements of low Z-values, such as boron. For this investigation, a Gatan 678 Imaging Filter (GIF) aligned to the course of the electron beam of Philips CM20 TEM has been

used. The imaging filter analyses electrons passing through and a corresponding energy loss spectrum is obtained. A schematic of EEL spectra features is shown in Figure 26. By identifying elemental peaks within the spectrum, elemental composition of investigated areas can be obtained.

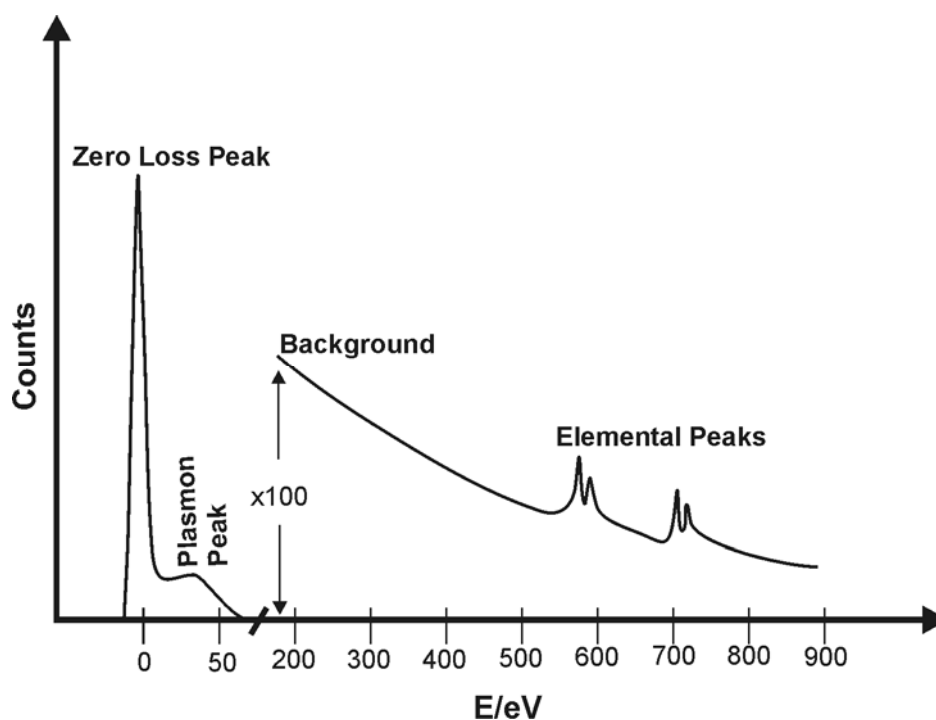


Figure 26: Schematic of EELS spectral features.<sup>109</sup>

#### 2.3.4 Energy Filtered Transmission Electron Microscopy (EFTEM)

By energy filtered transmission electron microscopy, elemental distributions within the specimen can be visualised and different phases visually separated. For this investigation, a Gatan 678 Imaging Filter (GIF) aligned to the course of the electron beam of Philips CM20 TEM is used. Using this method, it is possible to filter electrons, which have suffered a characteristic energy loss on passing through the sample by inelastic interaction and generate an image based only on these electrons. By selection of suitable energy windows, images of elemental distribution of selected elements can be shown.

## 2.4 Image analysis

The image analysis software package Zeiss KS-400 is used for the quantification of the volume fraction of delta ferrite in weld-simulated specimens of CB2A material. The following procedure is used: A series of digital micrographs obtained from optical microscopy is taken from representative areas of the specimens at a magnification of 62.5. A special delta ferrite recognition routine is applied to two or three pictures per sample and allows measurement of the area fraction of delta ferrite. For satisfactory results using the image analysis technique, all pictures have to be taken under the same conditions of brightness and contrast. Best results are obtained if the delta ferrite has the same range of intensity throughout the image. This part of the work is very crucial, as different weld-simulated microstructures reacted differently to the etching procedure and a homogeneous response is not always obtained. In reality, delta ferrite regions had sometimes to be identified by manually marking and encircling them. Another fact limiting the quality of this evaluation method is that delta ferrite is present in two different manifestations. Whereas large delta ferrite grains, visible at low magnifications, are placed along prior austenite grain boundaries, narrow delta ferrite laths, only visible at highest magnification, are present in between martensite laths. For the determination of delta ferrite content in weld-simulated specimens, only the large delta ferrite grains are taken into account. It is not possible to consider both small and large delta ferrite areas at the same time. As a result, this evaluation is afflicted with a not specified error. Moreover, qualitative assessment is possible.

## 2.5 Determination of boron nitride precipitation

The detection of boron nitrides (BN) is performed on fractured samples of CB2A, CB2 and NPM1 base material. The surfaces of two fractured samples of each steel grade are investigated using a scanning electron microscope (SEM). Inclusions are analysed by an aligned EDX unit.

Specimens of the base materials in as-received condition with a diameter of 3.6 mm and 50 mm in length are machined. The specimens are fractured at a 90° notch. A sketch of the specimen geometry is shown in Figure 27.

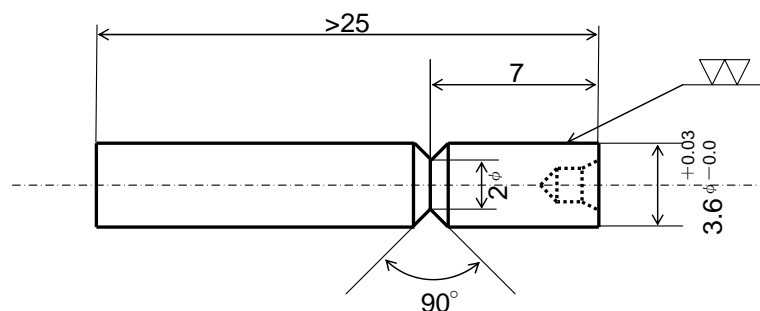


Figure 27: Sketch of specimen preparation for detection of BN precipitation (all measures in mm).

The specimens are fractured at the notch by manually bending with an attached lever. The shorter parts of the broken samples, 7 mm in length, are mounted in a specimen holder and investigated immediately by SEM to avoid contamination of the fracture surface.

A JEOL JSM-5400 SEM with an attached JEOL JED-2140 energy dispersive X-ray analyzer is used. The acceleration voltage of 15 keV and working distance of 20 mm are kept constant for all samples investigated. The smallest size of particles detectable and identifiable by this EDX unit is 0.2  $\mu\text{m}$ . Pictures of all investigated particles are taken with an attached Polaroid camera and EDX spectra are recorded with a connected PC workstation. The determination of the chemical composition of particles especially containing light elements such as boron and nitrogen using EDX is afflicted with several sources of error. Therefore, the measured chemical composition of analysed particles provides only qualitative not quantitative information.

### **3 Mechanical testing**

#### **3.1 Macro hardness**

Vickers macro hardness measurements are made using a Reicherter Briviskop testing machine using a load of 10 kg (HV 10). Tests are performed on flat cross-sectional specimens according to DIN EN ISO 6507-1(2006-03). Macro hardness values are averaged from at least three single indentations.

#### **3.2 Micro hardness**

For hardness measurements of small specimen areas, e.g. delta ferrite grains, Vickers micro hardness is obtained using a PAAR MHT4 testing machine with variable force ranging from 0.0005 – 2 N. For the study of delta ferrite micro hardness, a load of 0.01 kg (HV 0.01) is applied. Hardness traverses across the heat affected zone of weldments are obtained using a load of 0.1 kg (HV 0.1).

#### **3.3 Tensile properties**

##### **3.3.1 Tensile properties at ambient temperature**

Tensile properties at ambient temperature of CB2A and NPM1 base materials are obtained using a Zwick Universal tension/compression testing machine with a maximum force of 100 kN. Testing at ambient temperature is performed according to DIN EN 10002-1 (2001-12) on standard tensile specimens according to DIN 50125 (2004-01). Specimen geometry is shown in Figure 28.

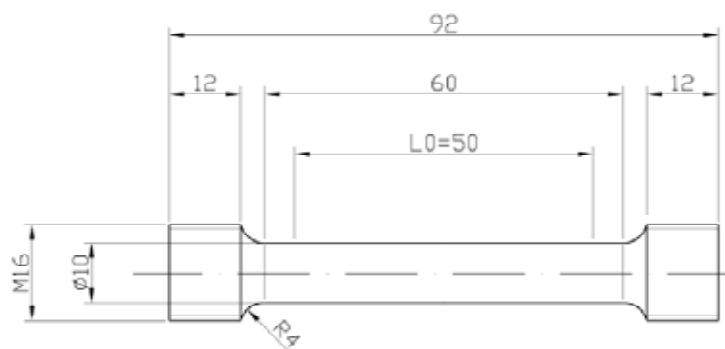


Figure 28: Geometry of tensile specimens according to DIN 50125 (2004-01).

### 3.3.2 Tensile properties at elevated temperatures

Within base material characterisation of NPM1 steel, tensile properties at elevated temperatures are obtained according to DIN EN 10002-5 (1992-02) using a Zwick Universal tension/compression testing machine with a maximum force of 100 kN with an attached furnace chamber. Tests are performed using a constant strain rate of  $1 \text{ mm min}^{-1}$ . For strain measurement, an extensometer is attached to the specimen. Therefore, the specimen geometry is adapted and ridged specimens have been fabricated. Specimen geometry is shown in Figure 29.

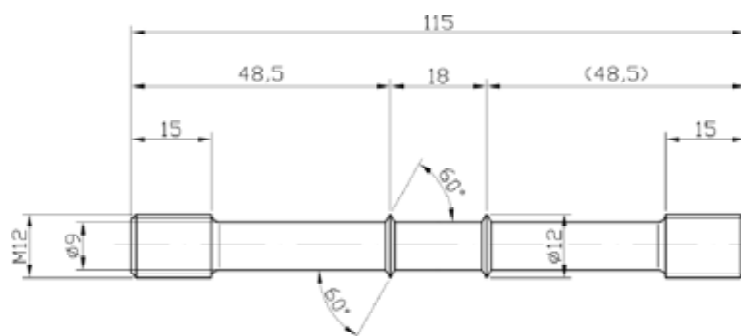


Figure 29: Specimen geometry for tensile tests at elevated temperatures.

Tensile tests are performed at 6 different temperatures ranging from  $300^\circ\text{C}$  to  $700^\circ\text{C}$ . Testing temperatures and specimen codes are listed in Table 15.

Table 15: Specimen codes and testing temperatures for hot tensile testing of NPM1 base material.

| Specimen | Testing Temperature |
|----------|---------------------|
| N2-3     | 300°C               |
| N2-4     | 500°C               |
| N2-5     | 550°C               |
| N2-6     | 600°C               |
| N2-7     | 650°C               |
| N2-8     | 700°C               |

The Young's Modulus  $E$  [GPa] is derived graphically from the inclination of the linear-elastic region of the stress strain curve. The 0.2% yield strength  $R_{p0.2}$  [MPa] is determined by the intersection of a line offset from the linear region by 0.2% strain. Tensile strength, reduction of area and fracture elongation are calculated according to:

$$\text{Tensile Strength [MPa]} \quad T_m = \frac{F_{\max}}{S_0}$$

$$\text{Reduction of Area [%]} \quad Z = \frac{S_0 - S_u}{S_0} \times 100$$

$$\text{Fracture Elongation [%]} \quad A = \frac{L_0 - L_u}{L_0} \times 100$$

### 3.4 Charpy impact testing

To obtain impact toughness values of different microstructures, Charpy-V impact testing according to DIN EN 10045-1 (1991-04) is performed at ambient temperature. A standardised sample of 10 mm square section x 55 mm with a 2 mm deep V-notch positioned at the middle of the specimen is fractured using a 300 Joule pendulum hammer.

### 3.5 Creep testing

Constant load uniaxial creep testing in tension of NPM1 base material and E911 cross-weld samples are performed in the creep laboratory of IWS. Creep testing conditions are in accordance with DIN EN 10291 (2001-01). Two different types of creep furnaces are utilised:

- Single specimen furnaces with continuous strain measurement
- Single line, multi-specimen furnaces with interrupted strain measurement

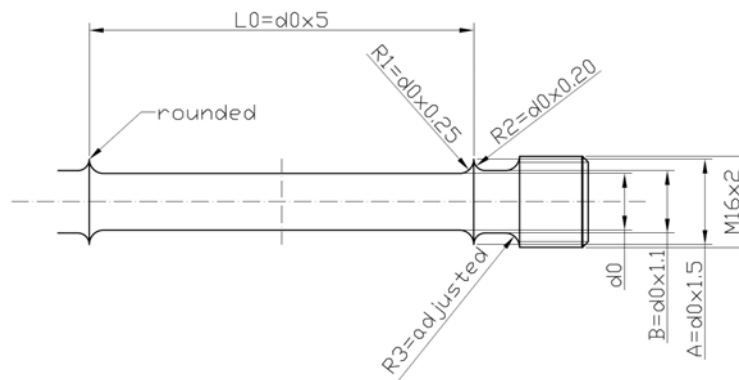


Figure 30: Parametric drawing of creep test specimen for continuous and interrupted strain measurement. Reference length ( $L_0$ ) and diameters are adjusted according the applied force.

Reduction of area after rupture ( $Z_u$ ), rupture elongation ( $A_u$ ) and creep strain ( $\epsilon$ ) are calculated according to:

$$\text{Reduction of Area after Rupture [\%]} \quad Z_u = \frac{S_0 - S_u}{S_0} \times 100$$

$$\text{Rupture Elongation [\%]} \quad A_u = \frac{L_{ru} - L_{r0}}{L_{r0}} \times 100$$

$$\text{Total Creep Strain [-]} \quad \epsilon = \frac{\Delta L_{rt}}{L_{r0}}$$

Creep Strain Rate [ $\text{h}^{-1}$ ]

$$\varepsilon_f = \frac{\partial \varepsilon}{\partial t}$$

with:

$S_0$  ... initial cross section area at gauge       $L_{r0}$  ... initial reference length  
 $S_u$  ... cross section area after fracture       $L_{ru}$  ... reference length after fracture  
 $\Delta L_{rt}$  ... change in reference length

To calculate the creep strain rate ( $\varepsilon_f$ ), a parametric equation is fitted to the measured strain-time curve using software Table Curve\* and derived with respect to time.

### 3.5.1 Single specimen furnace with continuous strain measurement

Creep tests of NPM1 base material are conducted at 650°C and two different stress levels, i.e. 130 and 100 MPa. Strain data for both specimens are continuously recorded by attached strain gauges and stored by a PC.

**Table 16: Specimen designation and stress level for creep testing of NPM1 base material.**

| Specimen | Stress [MPa] |
|----------|--------------|
| NPM11    | 130          |
| NPM12    | 100          |

### 3.5.2 Single line, multi-specimen furnace

Interrupted creep testing is performed using single line, multi specimen furnaces. To measure the creep strain, the specimen string is removed from the furnace after releasing the applied force. After cooling to room temperature, elongation of each sample is measured and documented. The specimen string is inserted into the furnace again and, after reaching the testing temperature, the force is applied again. This method allows using one furnace to test several specimens at the same time. Interrupted strain measurement is a compromise, as strain data can only be acquired after discrete time-steps and total testing time is extended because of the time consuming mounting and dismounting procedure.

\* Table Curve 2D Ver.5, AISN Software, 2000.

Specimens of the Matching Program are tested at 600°C and stresses ranging from 70 to 150 MPa. The specimen codes and parameters are given in Chapter IV.9.2. Within the gauge length of cross-weld samples, different microstructures, i.e. WM, HAZ and BM are present. Therefore, the measured strain for cross-weld specimens is a composite of the strains of these individual sub-zones.

## 4 GLEEBLE weld simulation

A thermo-mechanical simulator Gleeble 1500 has been used for the physical simulation of the heat affected zone. Specimens mounted between water cooled copper grips are heated by resistance heating. The actual temperature is measured by thermocouples (type K) attached to the specimen surface at the center. Measured and programmed temperatures are compared in a loop of the control PC.

To prevent oxidation of the specimen surface, the chamber can be flooded with inert argon gas.

### 4.1 Specimen geometry

Two different sample geometries are used for the HAZ simulation. For impact testing of CB2A HAZ microstructure, square specimens with a cross section of 10 x 10 mm and 100 mm in length are used. For metallographic investigations of CB2A, CB2 and NPM1 HAZ simulated microstructures, cylindrical specimens with a diameter of 12 mm are used.

### 4.2 Time-temperature cycles

Time-temperature cycles are generated using the Tempcycle software. This software has been developed at the IWS and used in many previous works to calculate weld temperature cycles. Basically, Tempcycle calculates time-temperature curves, as a function of temperature dependent material properties ( $c_p$ ,  $\lambda$ ), weld parameters ( $T_p$ ,  $V$ ,  $A$ ,  $v$ ) and weld geometry (thickness) by analytically solving the heat conduction equations. Welding parameters are selected according to established welding procedures in industry. The process of generating weld time-temperature cycles is described in detail in the PhD thesis of E. Letofsky, IWS (2001).<sup>10</sup>

#### 4.2.1 CB2A

To allow comparison of results obtained in earlier work by Schalber<sup>113</sup> and Letofsky<sup>10</sup> with results of this work, the same time-temperature cycles for the HAZ simulation are applied. Specimens are simulated with different peak temperatures and a constant cooling time of  $t_{8/5}$  of 40 seconds.

Table 17: Simulation parameters for HAZ simulation of CB2A material used in this work.

| Peak Temperature<br>$T_p$ | Cooling Time<br>$t_{8/5}$ |
|---------------------------|---------------------------|
| 1300°C                    | 40 s                      |
| 1200°C                    | 40 s                      |
| 1100°C                    | 40 s                      |
| 1000°C                    | 40 s                      |
| 950°C                     | 40 s                      |

After weld simulation, some specimens are subjected to a post-weld heat treatment for 12 hours at 730°C.

#### 4.2.2 CB2

CB2 material is simulated using several heat inputs to cover different welding processes with a wide range of heat input. The underlying welding parameters as well as the calculated heat input and the resulting characteristic cooling times are summarised in Table 18. Weld simulation covers the range from the low heat input GTAW process with 3.7 kJ cm<sup>-1</sup> to the high energy SAW process with 84.2 kJ cm<sup>-1</sup>.

Table 18: Input data for Gleeble weld simulation of CB2 material

| Process  | Preheat Temp. [°C] | Current [A] | Voltage [V] | Welding Speed [cm min <sup>-1</sup> ] | k   | HC | Heat Input Q [kJ cm <sup>-1</sup> ] | $t_{8/5}$ [s] |
|----------|--------------------|-------------|-------------|---------------------------------------|-----|----|-------------------------------------|---------------|
| GTAW (1) | 200                | 40          | 13          | 5                                     | 0.6 | 3D | 3.7                                 | 6             |
| GTAW (2) | 200                | 50          | 15          | 5                                     | 0.6 | 3D | 5.4                                 | 9             |
| SMAW     | 200                | 100         | 26          | 11                                    | 0.8 | 3D | 11.3                                | 18            |
| MIG      | 200                | 350         | 30          | 22                                    | 0.8 | 3D | 22.9                                | 37            |
| SAW (1)  | 200                | 900         | 33          | 38                                    | 1   | 3D | 46.9                                | 75            |
| SAW (2)  | 200                | 975         | 36          | 25                                    | 1   | 3D | 84.2                                | 137           |

k ... process efficiency  
 $t_{8/5}$  ... characteristic cooling time  
 HC ... heat conduction  
 3D ... 3 dimensional

Three peak temperatures have been chosen for each heat input. The highest peak temperature of 1300°C is selected to simulate the coarse-grained HAZ. 1100°C is selected to simulate the fine-grained HAZ and the lowest peak temperature, lying in between  $A_{C1}$  and  $A_{C3}$ , to simulate the intercritical HAZ region. Detailed simulation parameters are given in Table 19.

**Table 19: Specimen codes and simulated peak temperatures of CB2 Gleeble simulation.**

| Specimen   | Welding Process | Peak Temperature $T_p$<br>[°C] |
|------------|-----------------|--------------------------------|
| <b>C2</b>  | GTAW (1)        | 1300                           |
| <b>C2</b>  | GTAW (2)        | 1300                           |
| <b>C3</b>  | SMAW            | 1300                           |
| <b>C4</b>  | MIG             | 1300                           |
| <b>C5</b>  | SAW (1)         | 1300                           |
| <b>C6</b>  | SAW (2)         | 1300                           |
| <b>C7</b>  | GTAW (1)        | 1100                           |
| <b>C8</b>  | GTAW (2)        | 1100                           |
| <b>C9</b>  | SMAW            | 1100                           |
| <b>C10</b> | MIG             | 1100                           |
| <b>C11</b> | SAW (1)         | 1100                           |
| <b>C12</b> | SAW (2)         | 1100                           |
| <b>C13</b> | GTAW (1)        | 960                            |
| <b>C14</b> | GTAW (2)        | 960                            |
| <b>C15</b> | SMAW            | 950                            |
| <b>C16</b> | MIG             | 950                            |
| <b>C17</b> | SAW (1)         | 920                            |
| <b>C18</b> | SAW (2)         | 920                            |

Plots of the calculated time-temperature profiles for CB2 HAZ simulation are shown in Figure 31.

After simulation, the specimens are cut along the symmetry axis where the thermocouples have been attached. Half of the specimens are investigated in the as-simulated condition and half are subjected to a PWHT for 24 hours at 730°C in an inert gas atmosphere (argon) applying a heating rate of 50°C per hour and furnace cooling.

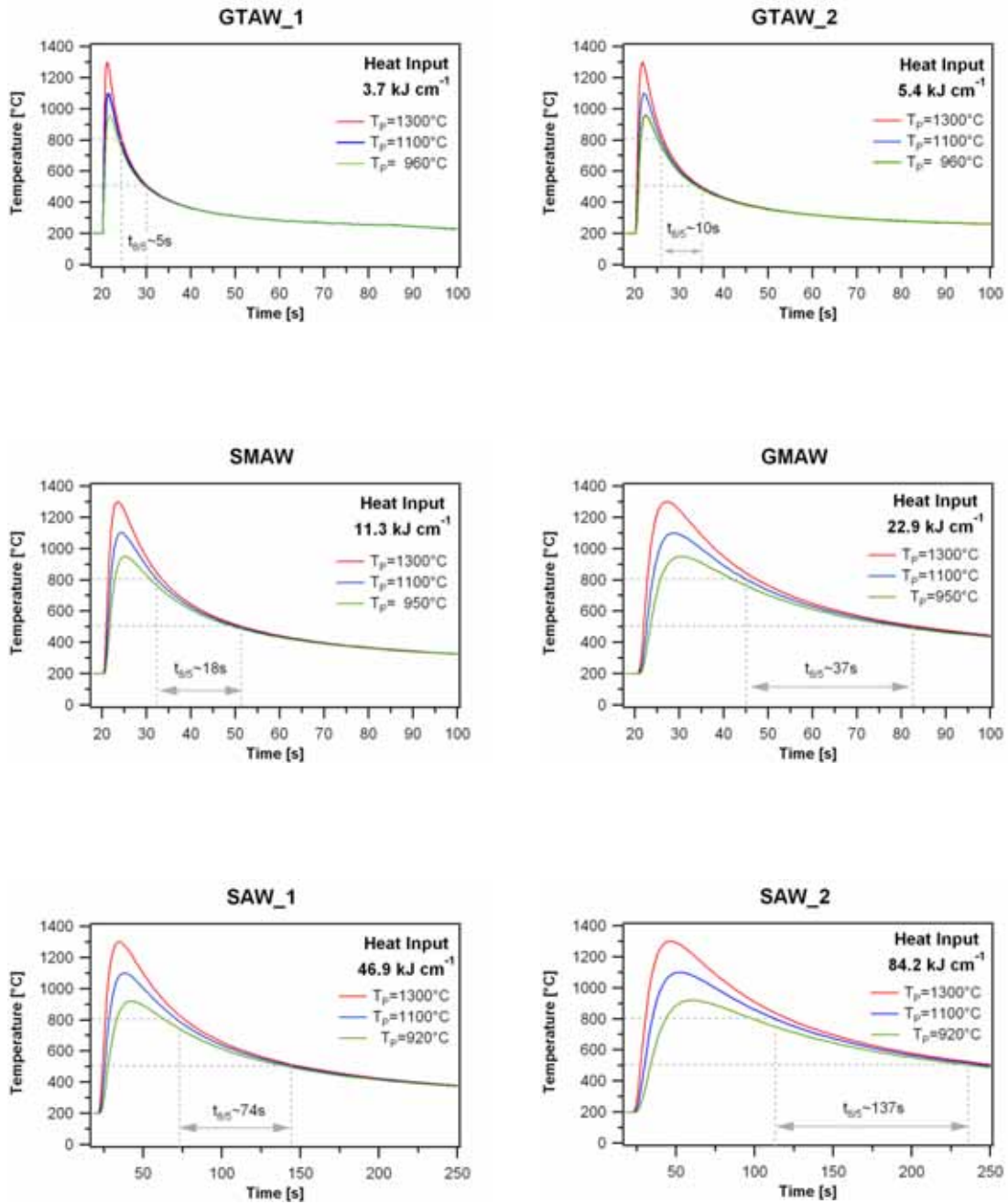


Figure 31: Calculated weld time-temperature cycles for Gleeble HAZ simulation of CB2 steel. Heat input ranging from  $3.7 \text{ kJ cm}^{-1}$  to  $84.2 \text{ kJ cm}^{-1}$  resulted in characteristic cooling times from 5 to 137 seconds. Peak temperatures are selected to simulate CGHAZ ( $1300^\circ\text{C}$ ), FGHAZ ( $1100^\circ\text{C}$ ) and ICHAZ ( $960^\circ\text{C}$ ,  $950^\circ\text{C}$ ,  $920^\circ\text{C}$ ).

## 4.2.3 NPM1

NPM1 HAZ simulation covers a GTAW process with a heat input of  $10.8 \text{ kJ cm}^{-1}$  and a characteristic cooling time of 19 seconds. Welding parameters, calculated heat input and resulting characteristic cooling time are listed in Table 20.

Table 20: Input data for Gleeble weld simulation of NPM1 material.

| Process | Preheat Temp. [°C] | Current [A] | Voltage [V] | Welding Speed [cm min <sup>-1</sup> ] | k   | HC | Heat Input [kJ cm <sup>-1</sup> ] | t <sub>8/5</sub> [s] |
|---------|--------------------|-------------|-------------|---------------------------------------|-----|----|-----------------------------------|----------------------|
| GTAW    | 200                | 160         | 15          | 8                                     | 0.6 | 3D | 10.8                              | 19                   |

k ... process efficiency  
t<sub>8/5</sub> ... characteristic cooling time

HC ... heat conduction  
3D ... 3 dimensional

For single weld cycle simulation, 12 different peak temperatures ranging from 800°C to 1300°C are selected. Plots of the calculated time-temperature profiles are shown in Figure 32.

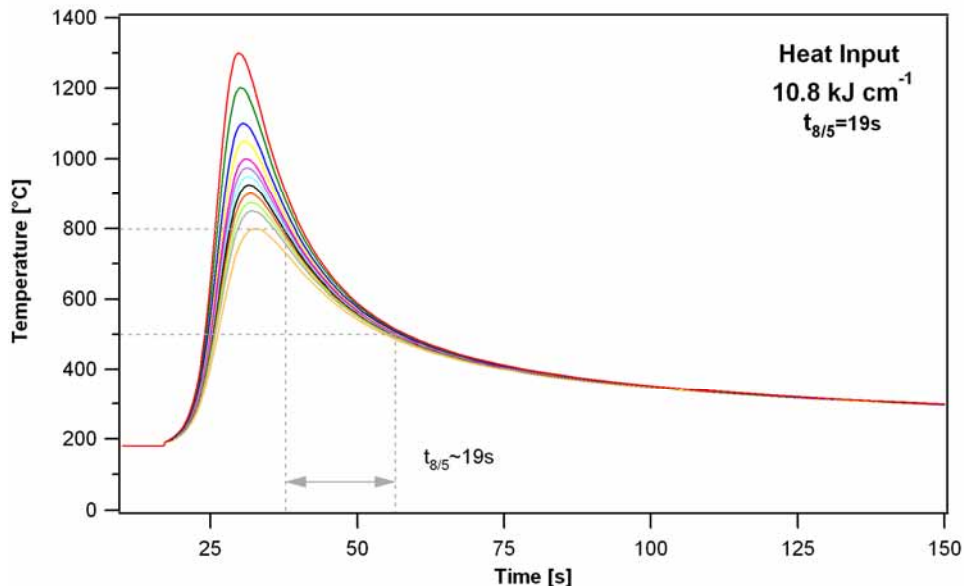


Figure 32: Calculated weld time-temperature cycles for Gleeble HAZ simulation of NPM1 steel. Peak temperatures ranging from 800°C to 1300°C and constant characteristic cooling time of 19 seconds.

In addition to the single weld cycle, some double weld thermal cycles are simulated. The peak temperatures are chosen to simulate CG/FGHAZ ( $1300^{\circ}\text{C}/1100^{\circ}\text{C}$ ),

CG/ICHAZ (1300°C/950°C), FG/ICHAZ (1100°C/950°C) and ICHAZ (975°C) followed by an over-tempering at 850°C. The characteristic cooling time for each individual weld thermal cycle is kept constant at 19 seconds. Table 21 summarises the performed HAZ simulations.

**Table 21: Specimen codes and simulated peak temperatures for NPM1 HAZ simulation.**

| Specimen | Welding Process | Peak Temperature T <sub>p</sub><br>[°C] |
|----------|-----------------|---|
| N112     | GTAW            | 800                                     |
| N111     | GTAW            | 850                                     |
| N110     | GTAW            | 875                                     |
| N19      | GTAW            | 900                                     |
| N18      | GTAW            | 925                                     |
| N17      | GTAW            | 950                                     |
| N16      | GTAW            | 975                                     |
| N15      | GTAW            | 1000                                    |
| N14      | GTAW            | 1050                                    |
| N13      | GTAW            | 1100                                    |
| N12      | GTAW            | 1200                                    |
| N11      | GTAW            | 1300                                    |
| N3-1*#   | GTAW            | 1300/1100                               |
| N3-2*    | GTAW            | 1300/1100                               |
| N3-3*#   | GTAW            | 1300/950                                |
| N3-4*    | GTAW            | 1300/950                                |
| N3-5*#   | GTAW            | 1100/950                                |
| N3-6*    | GTAW            | 1100/950                                |
| N3-7*#   | GTAW            | 975/850                                 |
| N3-8*    | GTAW            | 975/850                                 |

\* ... simulated weld double cycles

# ... specimens for PWHT

After cutting, half of the specimens are again investigated in the as-simulated condition and half is subjected to a PWHT for 740°C for 4 hours in an argon atmosphere applying a heating rate of 100°C per hour and furnace cooling.

## 5 X-ray diffraction using synchrotron radiation

Since the method of acquiring X-ray diffraction (XRD) patterns in-situ during physical weld simulation is quite new in material science, this experimental technique is described in more detail. In-situ X-ray diffraction experiments are performed at the Advanced Photon Source (APS) at the Argonne National Laboratory, USA. An aerial view of the synchrotron site is shown in Figure 33.



**Figure 33: Aerial view of the Advanced Photon Source (APS) at Argonne National Laboratory, Chicago, Illinois, USA (Courtesy of APS, Argonne)**

In-situ X-ray diffraction experiments are performed using the UNICAT beamline BM-33-C (Figure 34). A beam energy of 30 keV from a ring current of 100 mA is used in these experiments. Prior to the beam coming in contact with the sample, it first passes through a water cooled Si (111) monochromator and is then focused and sized to dimensions of 1 mm wide by 0.25 mm high using a dynamically bent Si crystal and collimator slits.

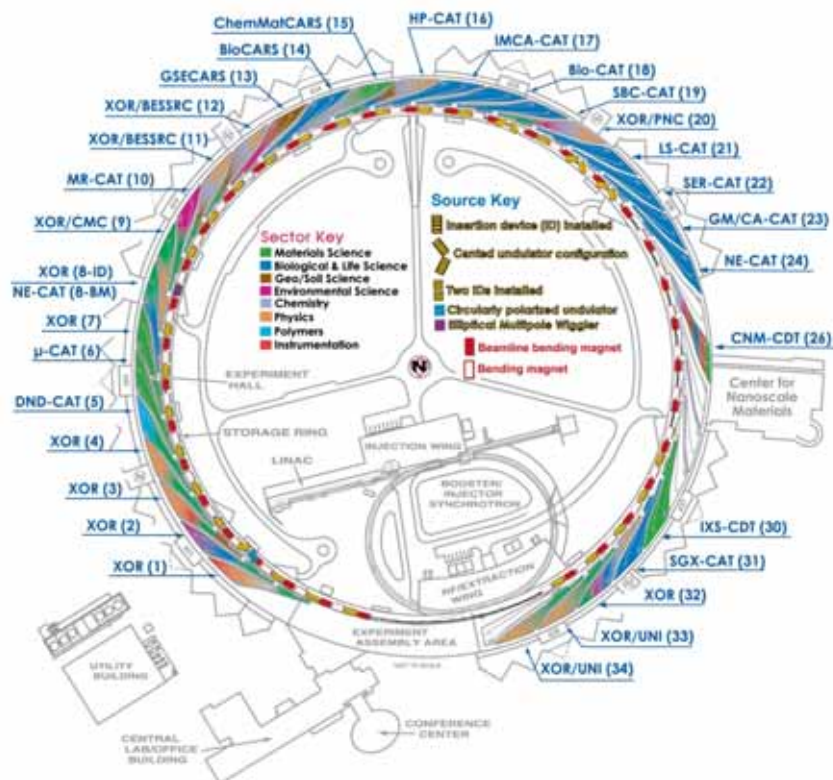


Figure 34: Sectors of the Advanced Photon Source (APS). Experiments are performed at the UNI-CAT beamline BM-33-C. (Courtesy of APS, Argonne)

## 5.1 Experimental Setup

In situ X-ray diffraction experiments are performed during direct resistance heating of test coupons measuring 100 mm long by 4.75 mm wide by 2 mm thick. These samples are machined from the different melts of base material. The surface area, where the X-ray impinges is polished to a 1  $\mu\text{m}$  finish in preparation for the X-ray diffraction experiments. In these experiments, the X-ray beam impinges on the top surface of the sample at a  $5^\circ$  angle of incidence. The 528  $\mu\text{m}$  X-ray absorption length provides a penetration depth of at least 23  $\mu\text{m}$ , which can become larger at higher Bragg angles. A schematic diagram of the experimental setup is shown in Figure 35.

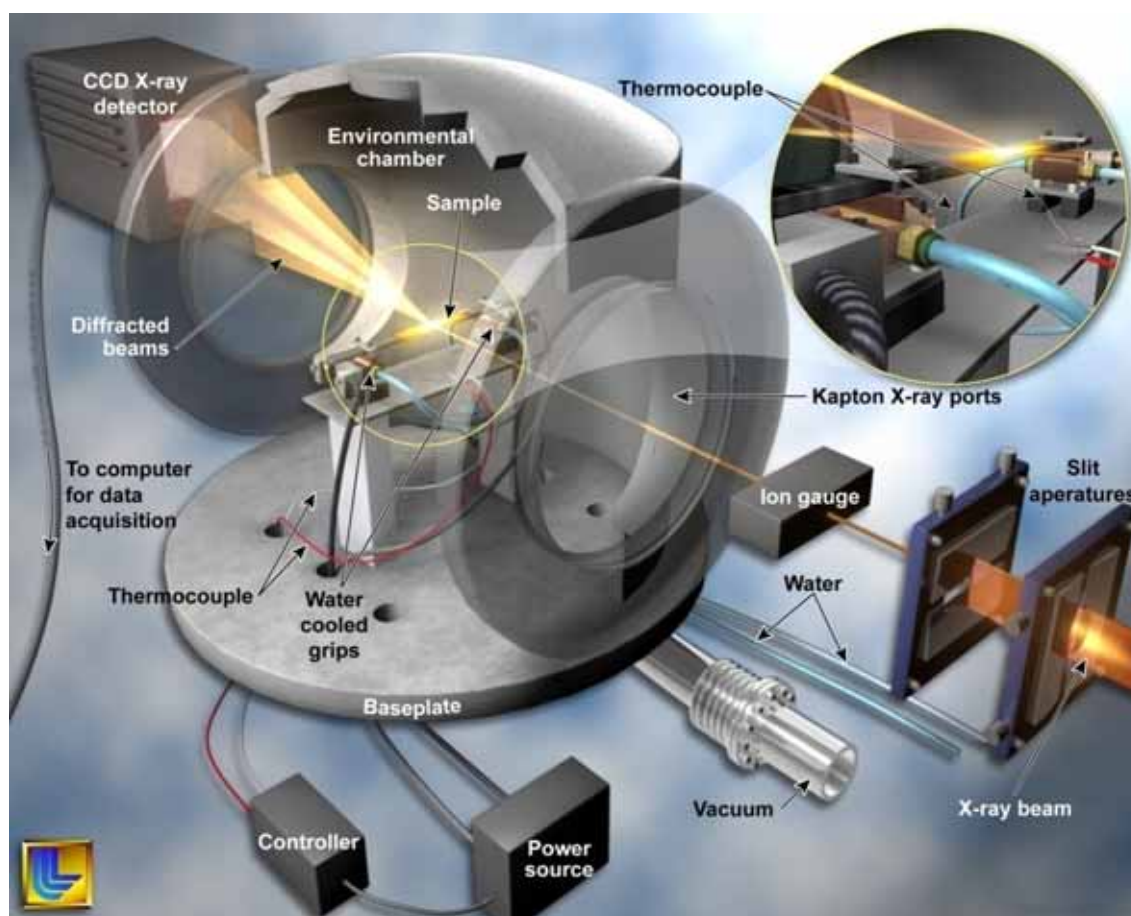


Figure 35: Setup for the XRD experiments used for in-situ observations of phase transformations under controlled heating and cooling conditions. (Courtesy of J. W. Elmer)

Direct resistance heating of the samples is used for rapid heating, while water cooled grips allow rapid cooling of the samples. The temperature of the sample is monitored and recorded using type-S (Pt/Pt-10%Rh) thermocouples, which are spot welded on the back side of the sample directly below the X-ray impingement point. A Eurotherm 818 temperature controller, a Eurotherm 425A power thyristor, and a Trindl RT300 transformer are used to control the AC current passing through the sample so that pre-programmed thermal cycles can be executed in a controlled manner. The heating power supply is capable of producing 300A at 6V and can heat the sample up to temperatures as high as 1400°C. The sample, along with the heating and cooling stage assembly, is placed inside a vacuum chamber in order to mitigate any potential oxidation and atmospheric contamination dur-

ing the prolonged heating cycles. Prior to each experiment, the chamber is evacuated and maintained under vacuum during the entire experiment.

The diffracted beams are collected using a CCD detector manufactured by Roper Scientific (A99k401, RS/Photometrics) and placed 330 mm behind the sample. This detector uses a  $6.1 \times 6.1 \text{ cm}^2$  array of  $1024 \times 1024$  pixels spaced  $60 \mu\text{m}$  apart to capture the diffraction patterns produced on a scintillating screen, which is connected to the CCD array using a fibre optic bundle. The detector captures the X-ray data by integrating the diffracted beams over a one second exposure. Another two seconds are required to clear the data from the CCD detector and transfer it to the computer. Thus, it is possible to capture a complete diffraction pattern approximately every 3 seconds. An advantage of the 2D detector is that a larger number of grains satisfy the diffraction condition compared to a conventional  $\theta/2\theta$  scan, such that statistically valid diffraction data can be collected for more coarse-grained samples. A sample of an X-ray diffraction pattern obtained on an as-received CB2A sample at  $299^\circ\text{C}$  is shown in Figure 36 (a). In this figure, the Debye arcs of the diffracted beam are shown for a d-spacing range from approximately 1.1 to  $2.4 \text{ \AA}$ .

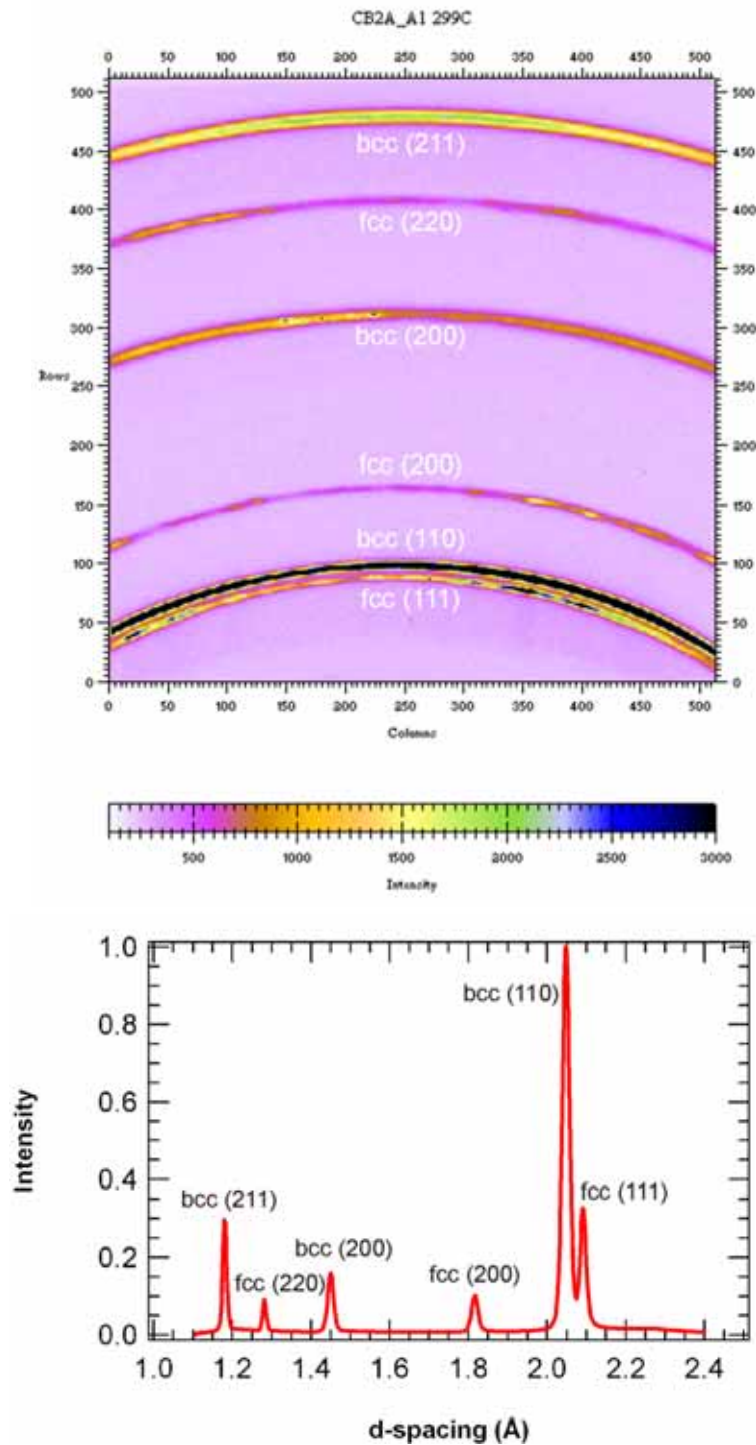


Figure 36: Diffraction pattern of CB2A sample at 299°C on cooling. a) Debye arcs as imaged on the CCD areal X-ray detector, b) shows this same data converted into an intensity versus d-spacing plot.

## 5.2 Analysis of diffraction data

To calibrate the X-ray detector, the room temperature lattice parameters of the base metal are measured first using a conventional  $\text{CuK}\alpha$  X-ray diffraction system. A room temperature pattern is then collected using the CCD with synchrotron radiation.

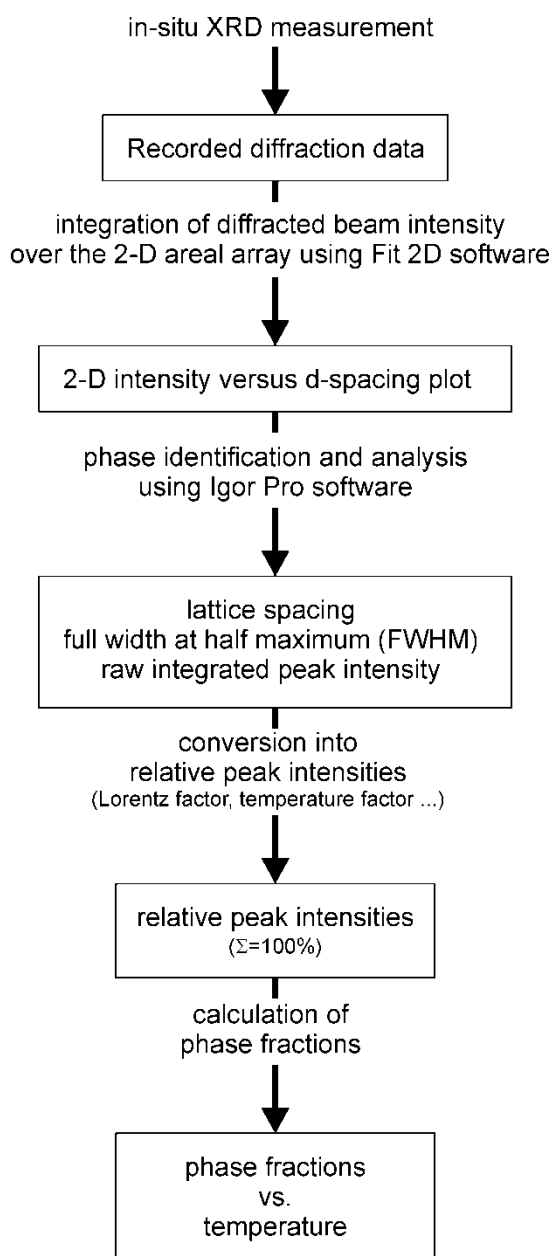


Figure 37: Schematic of XRD data analysis to obtain phase fractions versus temperature plot.

Five points are selected along each of three Debye arcs. Finally, the sample-detector distance, the position of the centre of the arcs on the detector, and the magnitude and ori-

entation of the detector tilt are varied to minimize the difference between the d-spacing at the selected points as calculated from these detector patterns and that calculated from the lattice parameters. Using this calibration, the Debye arcs are converted into a two dimensional plot showing diffracted beam intensity versus d-spacing using the FIT2D software<sup>†</sup>. This software integrates the diffracted beam intensity for each arc over the entire two dimensional areal array, providing the data used to create the diffraction patterns used in the following analysis. An integrated intensity versus d-spacing plot for a diffraction pattern of CB2A steel is shown in Figure 36 (b). As a next step, the amounts of  $\alpha$  and  $\gamma$  phases present at each time increment are calculated by performing an analysis of the peaks present in each diffraction pattern. The lattice spacing, full width at half maximum (FWHM) value and integrated intensity of each peak are determined using a semi-automated curve-fitting routine developed in Igor Pro®, Version 4.0. In this routine, developed by Babu, a sum of one or more Gaussian peak profile fitting functions is applied to each peak and the values of these fitted peaks are then reported. Figure 38 shows the method of peak fitting using the routine programmed by Babu in the Igor Pro software.

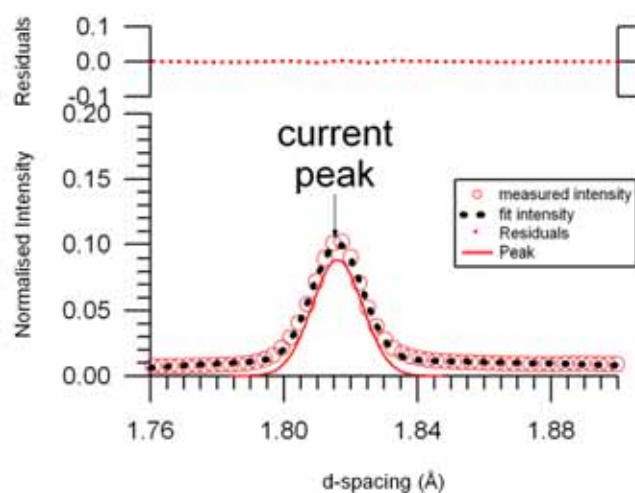


Figure 38: Fitted intensity peak using the Igor Pro software.

As a result, d-spacing, peak intensity, FWHM value and peak area of the fitted peak are calculated.

Table 22 shows the output values of the fitted peak displayed in Figure 38.

---

<sup>†</sup> FIT2D, V9.32, Andy Hammersley, ESRF, BP 220, 38043 Grenoble, France

Table 22: Results of XRD peak analysis on peak shown in Figure 38.

| XRD Image<br>Nr. | Time<br>[s] | Temperature<br>[°C] | d-spacing<br>[Å] | Peak<br>Intensity | FWHM     | Peak<br>Area |
|------------------|-------------|---------------------|------------------|-------------------|----------|--------------|
| 116              | 198         | 299.1               | 1.81596          | 0.0889158         | 0.010698 | 0.001686     |

The integrated intensity values measured from the peaks present in each diffraction pattern are then converted into relative peak intensities. This conversion takes into account the structure factors for the bcc and fcc crystal structures of the ferrite and austenite phase, respectively, the multiplicity for each peak, and the Lorentz polarization factor. Based on these considerations, the raw intensity of each peak is proportional to the relationship given below:

$$k_0 = \frac{F^2}{v^2} m \times L \times P \times e^{-2M}$$

Where  $F$  is the structure factor,  $v$  is the unit cell volume,  $m$  is the multiplicity,  $L$  is the Lorentz factor, defined in the following relationship,  $P$  is the polarization factor, and  $M$  is the temperature factor. The expression for the temperature factor is strictly valid only for cubic, monatomic crystals. Values for the unit cell volume for each phase, along with the structure factor and multiplicity values for each peak are provided in Table 23. Structure factor and multiplicity values are calculated using Crystallographica (Oxford Cryosystems, 1999). The Lorentz factor is a function of diffraction angle and it is calculated as:

$$L = \frac{1}{\sin \theta \times \sin 2\theta}$$

Where  $\theta$  is the diffraction angle for each peak, which are for the ferrite, and austenite peaks listed in Table 24.

**Table 23: Unit cell volume for each phase, structure factor and multiplicity values along with the calculated scaling factor for each fcc and bcc peak.**

|                      | Structure Factor<br>$F^2$ | Unit Cell Volume<br>$V [\text{\AA}^3]$ | Multiplicity<br>$m$ | Scaling Factor<br>$k_0$ |
|----------------------|---------------------------|--|---------------------|-------------------------|
| <b>FCC<br/>(111)</b> | 4876.2289                 | 43.76                                  | 8                   | 940.6182864             |
| <b>FCC<br/>(200)</b> | 4126.7776                 | 43.76                                  | 6                   | 448.640783              |
| <b>FCC<br/>(220)</b> | 2395.1236                 | 43.76                                  | 12                  | 262.3213551             |
| <b>BCC<br/>(110)</b> | 1257.4116                 | 23.55                                  | 12                  | 1333.654628             |
| <b>BCC<br/>(200)</b> | 809.9716                  | 23.55                                  | 6                   | 215.8879843             |
| <b>BCC<br/>(211)</b> | 580.81                    | 23.55                                  | 24                  | 415.0306013             |

Several simplifying assumptions have been made in the conversion of the raw peak intensity values. In particular, the polarization factor is set equal to unity ( $P=1$ ) because the synchrotron radiation used in the experiments is, to a good approximation, horizontally polarized. The more common expressions for the polarization factor are for unpolarised laboratory X-ray sources. Debye temperatures of austenite and ferrite are the same within the large experimental uncertainty, so it is assumed that the temperature factors are the same for each phase, which then cancels out the temperature effects in the conversion of the raw peak intensities.

**Table 24: Diffraction angles of fcc and bcc peaks in radians and calculated Lorentz factor.**

|                      | Diffraction Angle<br>$2-\theta$<br>[rad] | Lorentz Factor<br>$L$ |
|----------------------|--|-----------------------|
| <b>FCC<br/>(111)</b> | 0.209072991                              | 46.17362517           |
| <b>FCC<br/>(200)</b> | 0.241553568                              | 34.69693094           |
| <b>FCC<br/>(220)</b> | 0.342451053                              | 17.47749142           |
| <b>BCC<br/>(110)</b> | 0.202859619                              | 49.01923064           |
| <b>BCC<br/>(200)</b> | 0.287385915                              | 24.63708107           |
| <b>BCC<br/>(211)</b> | 0.352573962                              | 16.51264391           |

Finally, the relative peak intensities are calculated according to:

$$\text{relative peak intensity} = \frac{\text{measured peak intensity}}{\text{scaling factor } k_0}$$

The volume fractions of the ferrite and austenite phases are then determined by summing the integrated intensity values for the peaks from each phase and dividing this value by the sum of the integrated intensity values for all of the peaks observed in each diffraction pattern.

### 5.3 Applied time-temperature profiles

Two different time-temperature profiles are used as input for in-situ XRD measurements. One is a fast weld temperature cycle similar to the temperature cycle applied for Gleeble HAZ simulation (Chapter IV.4.2.1) and dilatometry experiments (see Chapter IV.7.2) of CB2A material. The peak temperature is set to 1300°C and a heating rate of 100K s<sup>-1</sup> is programmed. Air cooling results in a characteristic cooling time of  $t_{8/5} \sim 40$  s (Figure 39).

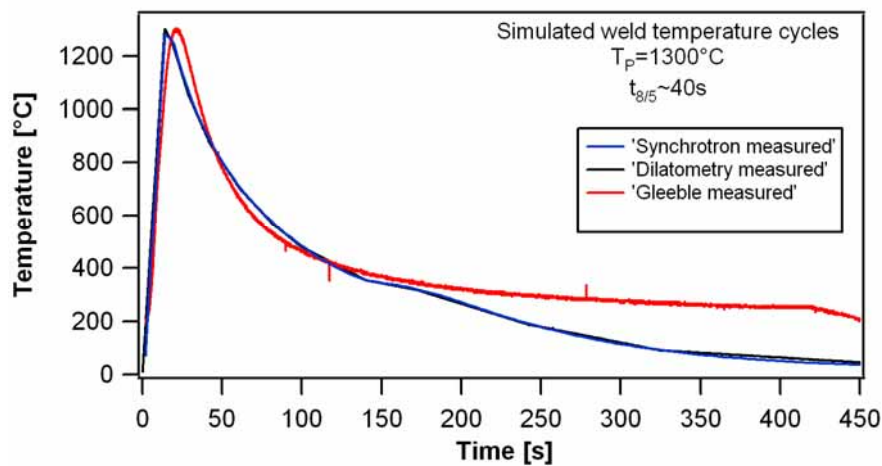


Figure 39: Comparison of simulated weld temperature cycles for in-situ XRD experiments with dilatometry and Gleeble temperature cycles.

An additional, slower heating cycle with a heating rate of 10K s<sup>-1</sup> is employed on samples of each material grade. Air cooling results again in a characteristic cooling time of  $t_{8/5} \sim 40$  s. This temperature cycle allows observation of phase transformations during heating in more detail as more diffraction patterns can be recorded.

Table 25: Specimen codes and parameters of the thermal cycles for in-situ XRD experiments.

| Steel Grade<br>(Specimen) | Peak temperature<br>[°C] | Heating rate<br>[K s <sup>-1</sup> ] | Cooling time<br>t <sub>8/5</sub> [s] | Description                        |
|---------------------------|--------------------------|--------------------------------------|--------------------------------------|------------------------------------|
| CB2A (A8)                 | 1300                     | 100                                  | 43                                   | Welding cycle                      |
| CB2A (A1)                 | 1300                     | 100                                  | 43                                   | Welding cycle                      |
| CB2A (A2)                 | 1300                     | 10                                   |                                      | Slow cycle                         |
| CB2A (A4)                 | 1300                     | 10                                   |                                      | Slow cycle                         |
| CB2 (C3)                  | 1300                     | 100                                  | 43                                   | Welding cycle                      |
| NPM1 (N1)                 | 1300                     | 100                                  | 43                                   | Welding cycle                      |
| NPM1 (N1Q)                | -                        | -                                    |                                      | Quenching of N1 in LN <sub>2</sub> |
| NPM1 (N7)                 | 1300                     | 100                                  | 43                                   | Welding cycle                      |
| NPM1 (N5)                 | 1300                     | 10                                   |                                      | Slow cycle                         |

## 6 Thermodynamic prediction of phase stability

Equilibrium phase diagrams and phase fraction diagrams are calculated using the software package Matcalc<sup>114-117</sup> developed at the IWS. Matcalc is a very powerful multi-component, multi-phase, multi-particle kinetic simulation tool to simulate kinetic processes, e.g. nucleation, coarsening, dissolution of precipitates during production and service. Beside kinetic simulations, also basic equilibrium calculations e.g. phase diagrams and phase fraction diagrams can be calculated. For all calculations, Version 5.13 of Matcalc is used in combination with the thermodynamic database TCFE3 (modified for chromium steels). The chemical composition, acting as input data, is set identical to the actual chemical composition of the three alloys investigated, CB2A, CB2 and NPM1, as given in Chapter IV.1.

Phase diagrams are calculated as a function of the chromium content varying from 6 to 16 wt. %. Although all emerging phases are considered within this calculation, only the bcc and fcc matrix phases are incorporated in the plotted phase diagrams for reasons of clarity. Equilibrium phase transformation temperatures  $A_{e1}$ ,  $A_{e3}$ ,  $A_{e4}$  and  $A_{e5}$  are derived from this calculation.

Phase fractions of secondary phases as a function of temperature are derived from stepped equilibrium calculations in a temperature range of 400°C to 1600°C. The range of thermal stability of each phase is summarised in a table.

## 7 Dilatometry

Two types of dilatometers are used in the present work. During heat affected zone simulation using a Gleeble 1500 thermo-mechanical simulator, expansion is recorded with an attached dilatometer. This method is employed to determine transformation temperatures for all HAZ simulated specimens.

For the investigation of delta ferrite formation in steel CB2A, a Bähr DIL-805A/D dilatometer at the University of Leoben is used. This dilatometer allows, while recording the expansion, to quench samples at a defined temperature by a helium jet. With this method, the microstructure present at this temperature can be frozen.

### 7.1 Dilatometry during Gleeble HAZ simulation

During Gleeble HAZ simulation, expansion of the sample is recorded by an attached dilatometer. The dilatometer is placed in the same plane as the attached thermocouples ensuring the right correlation between measured temperature and expansion. Recorded data is analysed as described in Chapter IV.7.3.

### 7.2 Bähr DIL-805A/D quenching dilatometer

Dilatometric measurements on steel CB2A are performed at the University of Leoben. A Bähr DIL-805A/D horizontal dilatometer is used to record phase transformations during a characteristic weld thermal cycle.

#### 7.2.1 Experimental setup

Cylindrical hollow specimens of material CB2A with an outer diameter of 5 mm, a wall thickness of 1.5 mm and 10 mm in length are used. The specimens are placed between two quartz tubes and heated by inductive heating after evacuation of the specimen chamber. The programmed temperature cycle is controlled by attached Type-S thermocouples. The sample elongation is recorded continuously by the control PC. The programmed thermal cycle is equivalent to one of the temperature cycles used for in-situ XRD experiments at APS and Gleeble HAZ simulation of CB2A (Figure 39). The temperature cycle is characterised by a peak temperature of  $T_p=1300^\circ\text{C}$  and a characteristic cooling of  $t_{8/5}\sim 40\text{s}$ .

To determine the microstructure of CB2A at elevated temperature, samples are quenched at defined positions during the thermal cycle using a helium jet. Specimen codes and quenching temperatures are shown in Table 26.

**Table 26: Sample codes and quenching temperatures for dilatometry experiments on CB2A material.**

| Sample number | Quenching Temperature       |        |
|---------------|-----------------------------|--------|
| 14            | Quenching on heating        | 1088°C |
| 13            |                             | 1188°C |
| 12            |                             | 1279°C |
| 10            |                             | 1300°C |
| 9             | Quenching on cooling        | 1268°C |
| 8             |                             | 1244°C |
| 7             |                             | 1198°C |
| 6             |                             | 1156°C |
| 5             |                             | 1050°C |
| 4             |                             | 479°C  |
| 2             | completed temperature cycle |        |

To study the influence of holding at peak temperature on the microstructure, one sample is exposed to a different thermal cycle. Sample 11 is heated to the peak temperature of 1300°C applying the standard heating rate of 100K s<sup>-1</sup> but kept at peak temperature for 60 seconds before quenching.

### 7.3 Analysis of dilatometry data

Transformation temperatures are determined by the tangent method. Therefore, the relative expansion is plotted versus temperature. A tangent is drawn following the straight part of the recorded dilatometric data. The transformation temperature is defined as the temperature at the point where measured data deviates from the tangent. This procedure is applied to determine  $A_{C1}$ ,  $A_{C2}$ ,  $A_{C3}$ ,  $A_{C4}$ ,  $A_{C5}$ ,  $M_S$  and  $M_F$  transformation temperatures.

## 8 Test weld NPM1

For verification of the results of physical HAZ simulation, a multi-layer GTAW test weld of NPM1 material using Ni-base Nibas 70/20-IG filler metal is produced at Böhler Thyssen Schweißtechnik, Austria. Two plates 120 mm in length, 50 mm wide with a thickness of 25 mm are fabricated from NPM1 test bar material. Butt weld joint geometry is a single V – double bevel 30° with a root face of 2 mm. Preheat temperature and interpass temperature are set to 140°C and controlled by attached thermocouples. For the first three beads, a 2.0 mm wire and for subsequent beads a 2.4 mm wire was used. Details of the GTAW process parameters are listed in Table 27. The heat input  $Q$  is calculated according to DIN EN 1011-1:1998:

$$Q \left[ \frac{kJ}{cm} \right] = \frac{U[V] \times I[A] \times 60}{v \left[ \frac{cm}{min} \right] \times 1000} \times k$$

with voltage ( $U$ ), current ( $I$ ), welding speed ( $v$ ) and an efficiency ( $k$ ) of GTAW process of 0.6 to 9.5 kJ cm<sup>-1</sup>.

**Table 27: Welding parameters employed for GTAW process of NPM1 plate material.**

| Run    | Welding process | Diameter of Filler Material [mm] | Current [A] | Voltage [V] | Welding Speed [cm min <sup>-1</sup> ] | Type of current/ Polarity |
|--------|-----------------|----------------------------------|-------------|-------------|---------------------------------------|---------------------------|
| 1      | GTAW 141        | 2.0                              | 100         | 11          | 8.0                                   | DC <sup>+</sup> -“        |
| 2 ÷ 3  | GTAW 141        | 2.0                              | 165 - 180   | 12.5 – 13.5 | 8.0 - 12.0                            | DC <sup>+</sup> -“        |
| 4 ÷ 32 | GTAW 141        | 2.4                              | 180 - 190   | 12.0 – 13.5 | 8.0 – 12.0                            | DC <sup>+</sup> -“        |

A sketch of the welding sequence for the NPM1 test weld is shown in Figure 40.

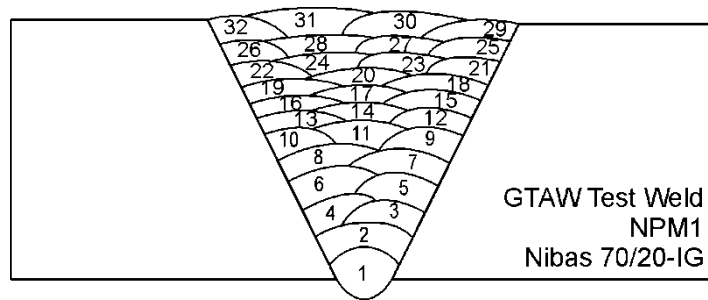


**Figure 40: Schematic of welding sequence for the NPM1 test weld using Nibas 70/20-IG filler metal. Plate thickness is 25 mm.**

One cross-sectional cut is investigated in the as-welded condition. The rest of the plate is subjected to a PWHT at 740°C for 4 hours with a heating rate of 100°C h<sup>-1</sup> and furnace cooling.

## 9 Matching Program

Within the COST 522 program, an extensive research program on the influence of weld metal creep strength on the overall creep strength of welded joints has been started. The program includes the welding of an X11CrMoWVNb9-1-1 (E911) collector pipe with an outside diameter of 355 mm and a wall thickness of 43 mm using three welding consumables with different level of creep strength compared to the base material:

- Under-Matching: Thermanit MTS 3 for GTAW, Thermanit Chromo 9V for SMAW (P91 type filler metal)
- Matching: Thermanit MTS 911 for GTAW and SMAW (E911 type filler metal)
- Over-Matching: Thermanit MTS 616 for GTAW and SMAW (P92 type filler metal)

The welding consumables have been provided by Böhler Thyssen Welding and the pipe material has been provided by Vallourec & Mannesmann Tubes. The chemical compositions of the pipe material and weld metals are listed in the materials section of this chapter.

Three pipe sections have been welded in the fixed horizontal position by Rafako SA Boiler Engineering Company in Poland. Figure 41 shows a schematic of the experimental setup with an included sketch of weld geometry.

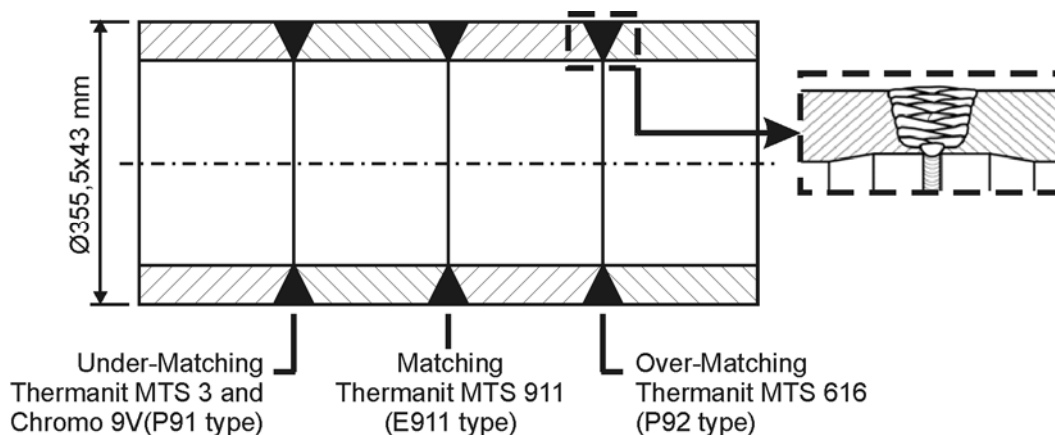


Figure 41: Experimental setup for butt welded E911 collector pipe.

### 9.1 Fabrication of E911 cross-weld samples

The root pass of all three welded joints is made by gas tungsten arc welding (GTAW) using  $\text{Ø}2.4$  mm wire. For the GTAW process, direct current of straight polarity is used. Shielded metal arc welding (SMAW) is used for subsequent passes using electrode diameters ranging from 2.5 to 4.0 mm. For SMAW welds, direct current of reverse polarity is used. A drawing of weld preparation and weld layer sequence is shown in Figure 42. Welding parameters, provided by Rafako, are summarised in Table 28.

For all three welds, a preheat temperature in the range of 200 to 250°C is chosen. Interpass temperature is kept at 250 to 350°C all time during welding.

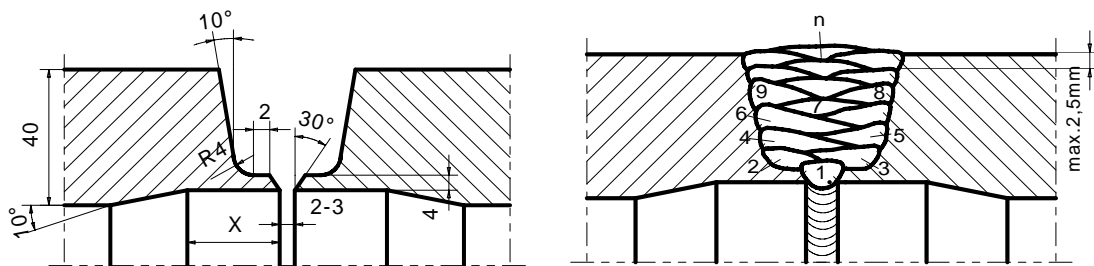


Figure 42: Sketch of welding preparation for E911 pipe butt welds (left) and weld layer sequence (right)

Table 28: Details of welding procedure, wire and electrode diameters and applied welding parameters for butt welded joints on E911 pipe according to Rafako SA.

| Run   | Welding process | Diameter of Filler Material [mm] | Current [ A ] | Voltage [ V ] | Type of current/ Polarity |
|-------|-----------------|----------------------------------|---------------|---------------|---------------------------|
| 1     | GTAW<br>141     | 2.4                              | 90 ÷ 100      | -             | DC”-“                     |
| 2 ÷ 3 | SMAW<br>111     | 2.5                              | 70 ÷ 100      | -             | DC”+“                     |
| 4 ÷ 5 | SMAW<br>111     | 3.2                              | 90 ÷ 140      | -             | DC”+“                     |
| 8 ÷ n | SMAW<br>111     | 4.0                              | 130 ÷ 180     | -             | DC”+“                     |

Max. thickness of each bead, layer: 2.5 mm

All three welds are subjected to a PWHT of 760°C for 2 hours. After PWHT, cross-weld samples 18 mm in diameter are machined out of the welded pipe parallel to the pipe axis and sent to TU Graz for creep testing.

## 9.2 Creep testing

Cross-weld specimens are machined to final dimensions at the Graz University of Technology. A sketch of the creep specimen geometry is shown in the experimental section of this work. The specimens are creep tested at 600°C at eight stress levels ranging from 70 to 150 MPa. The test matrix for the investigation on cross-weld creep rupture strength is shown in Table 29. Creep testing is interrupted to measure the elongation of the samples and, thus, to determine actual creep strain.

After fracture, time to rupture, reduction of area, ultimate fracture strain, and strain vs. time are evaluated for all specimens.

## 9.3 Investigation of fracture location

Fractured specimens of the Matching Program are investigated by conventional optical microscopy as well as advanced electron microscopic methods. To reveal possible creep void formation, cross-sectional cuts of the specimens are prepared and vibration polished. This preparation method guarantees that surface stresses introduced by the polishing process are reduced to a minimum and that creep voids are not closed by the polishing process. Details of specimen preparation and metallographic investigation methods can be found in Chapter IV.2 “Imaging”.

Table 29: Specimen codes, dimensions and testing parameters for the Matching program.

| Weld           | Sample Nr. | Force [N] | Diameter [mm] | Stress [MPa] | Gauge length [mm] |
|----------------|------------|-----------|---------------|--------------|-------------------|
| Under-Matching | UM8        | 8240      | 8.36          | 150          | 41.87             |
|                | UM1        | 8240      | 8.98          | 130          | 44.90             |
|                | UM2        | 8240      | 9.35          | 120          | 46.75             |
|                | UM3        | 8240      | 9.77          | 110          | 48.85             |
|                | UM4        | 3924      | 7.07          | 100          | 35.35             |
|                | UM5        | 3924      | 7.45          | 90           | 37.25             |
|                | UM6        | 3924      | 7.90          | 80           | 39.50             |
|                | UM7        | 3924      | 8.45          | 70           | 42.25             |
| Matching       | M8         | 8240      | 8.36          | 150          | 41.87             |
|                | M1         | 8240      | 8.98          | 130          | 44.90             |
|                | M2         | 8240      | 9.35          | 120          | 46.75             |
|                | M3         | 8240      | 9.77          | 110          | 48.85             |
|                | M4         | 3924      | 7.07          | 100          | 35.35             |
|                | M5         | 3924      | 7.45          | 90           | 37.25             |
|                | M6         | 3924      | 7.90          | 80           | 39.50             |
|                | M7         | 3924      | 8.45          | 70           | 42.25             |
| Over-Matching  | OM 8       | 8240      | 8.36          | 150          | 41.87             |
|                | OM1        | 8240      | 8.98          | 130          | 44.90             |
|                | OM2        | 8240      | 9.35          | 120          | 46.75             |
|                | OM3        | 8240      | 9.77          | 110          | 48.85             |
|                | OM4        | 3924      | 7.07          | 100          | 35.35             |
|                | OM5        | 3924      | 7.45          | 90           | 37.25             |
|                | OM6        | 3924      | 7.90          | 80           | 39.50             |
|                | OM7        | 3924      | 8.45          | 70           | 42.25             |



## V. Results

### 1 Base material characterisation

As all investigated materials differ in chemical composition, heat treatment and mechanical treatments, it is important to characterise their as-received state before investigating their HAZ microstructure. Additionally, as NPM1 is an experimental test melt and only little information has been published by Japanese colleagues, basic material characterisation is of great interest.

#### 1.1 Optical microscopy

The results of base material investigations obtained by optical microscopy are summarised on the following pages. Further images can be found in Appendix D.

Optical micrographs of the initial microstructures of the materials are shown in Figure 43. All base materials show a tempered martensitic microstructure in the as-received condition with no evidence of delta ferrite. As NPM1 is a forged material, it has a much finer and more homogeneous prior austenite grain size compared to the cast steel variants CB2A and CB2. Martensitic lath structure appears to be finer in the cast steels compared to the forged steel NPM1.

The cast steels show irregular shaped prior austenite grains with sizes ranging from few hundred microns to several millimetres. NPM1 features a homogeneous polygon prior austenite grain structure with an average grain size of 255  $\mu\text{m}$  (see Figure 44). Optical micrographs of the etched NPM1 base material specimen reveal an uncommon bright zone in the vicinity of the prior austenite grain boundaries.

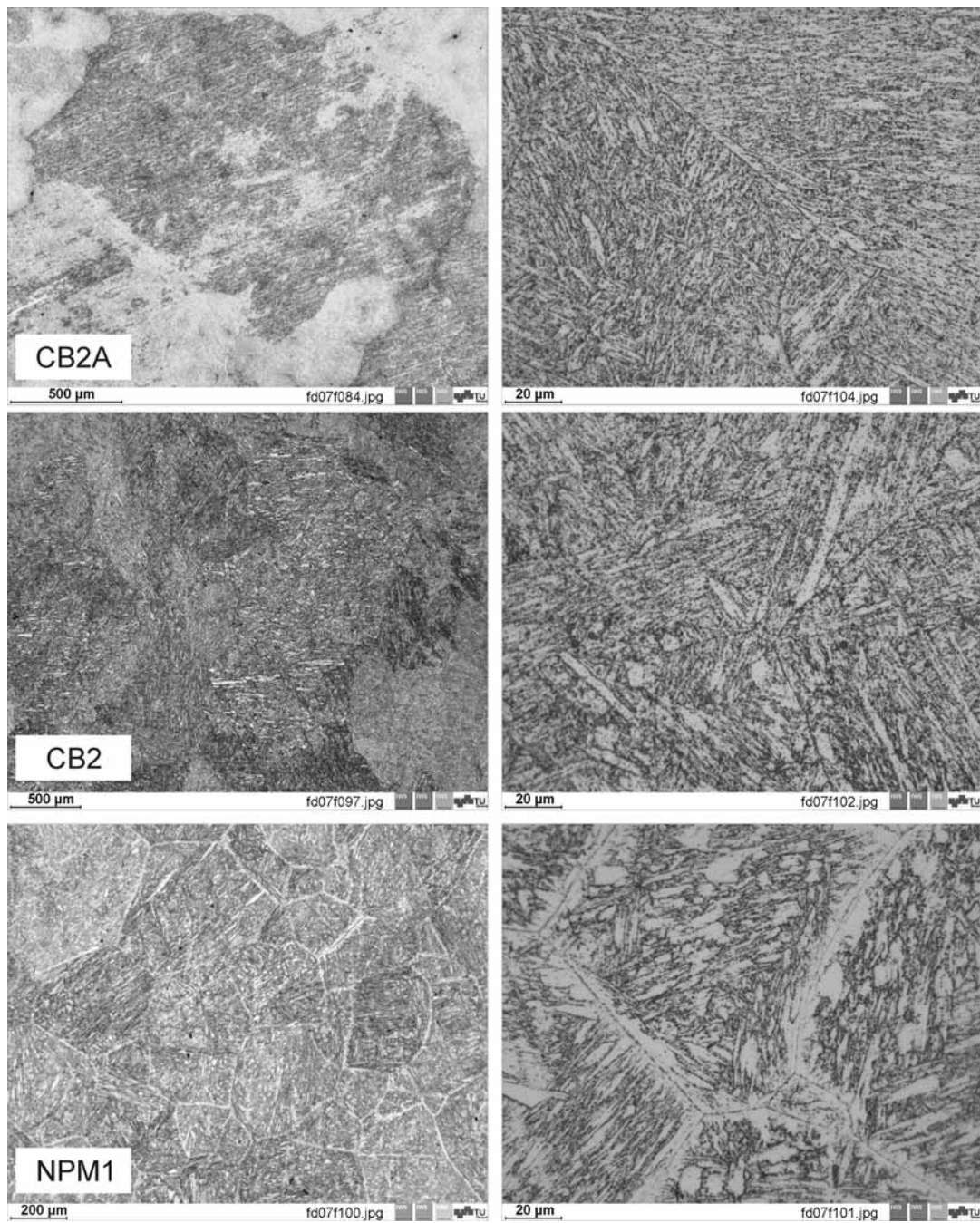


Figure 43: Optical micrographs of initial base materials microstructures showing prior austenite grain size (left) and tempered martensitic lath structure (right).

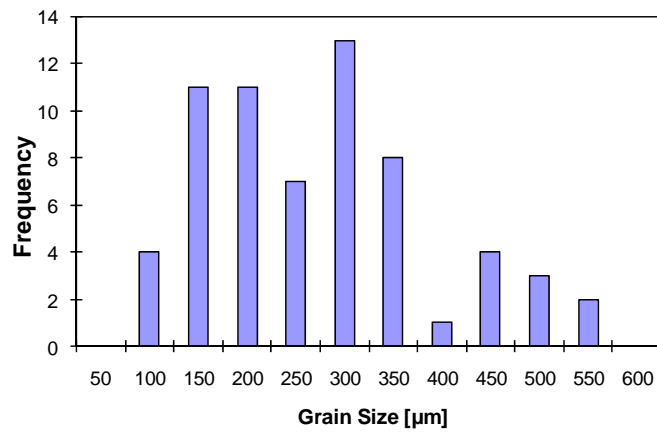


Figure 44: Size distribution of 65 randomly analysed prior austenite grains in NPM1 base material.

## 1.2 Electron microscopy

On the following pages, the results of base material investigations obtained by electron microscopy are summarised. Additional images can be found in Appendix D.

Figure 45 shows an inverse pole figure map of NPM1 base material obtained by EBSD method. Martensite laths and lath packages are clearly visible. Prior austenite grain boundaries are filtered and marked black.

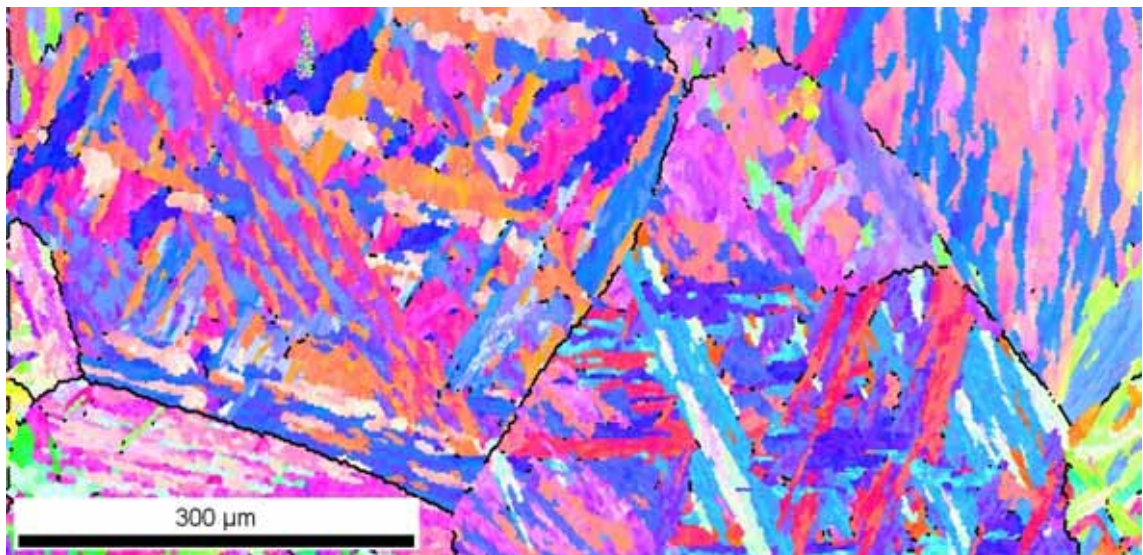


Figure 45: EBSD image of NPM1 base material. Pixels with misorientation satisfying prior austenite grain boundaries are filtered and set to black color.

Precipitate distribution in all three steels is observed on etched specimens by scanning electron microscopy (Figure 46). Figure 47 shows finely dispersed precipitates in all three steel variants. Precipitates are mainly aligned along the prior austenite grain and the martensitic lath boundaries. Some finer precipitates can be observed inside the martensitic laths. In NPM1, a precipitate free zone adjacent the PAGB is visible. This correlates well with the different etching response this material shows close to the grain boundary in the optical micrographs. The precipitate free zones are also clearly visible at lower magnifications (see Figure 46) making identification of prior austenite grain boundaries easy.

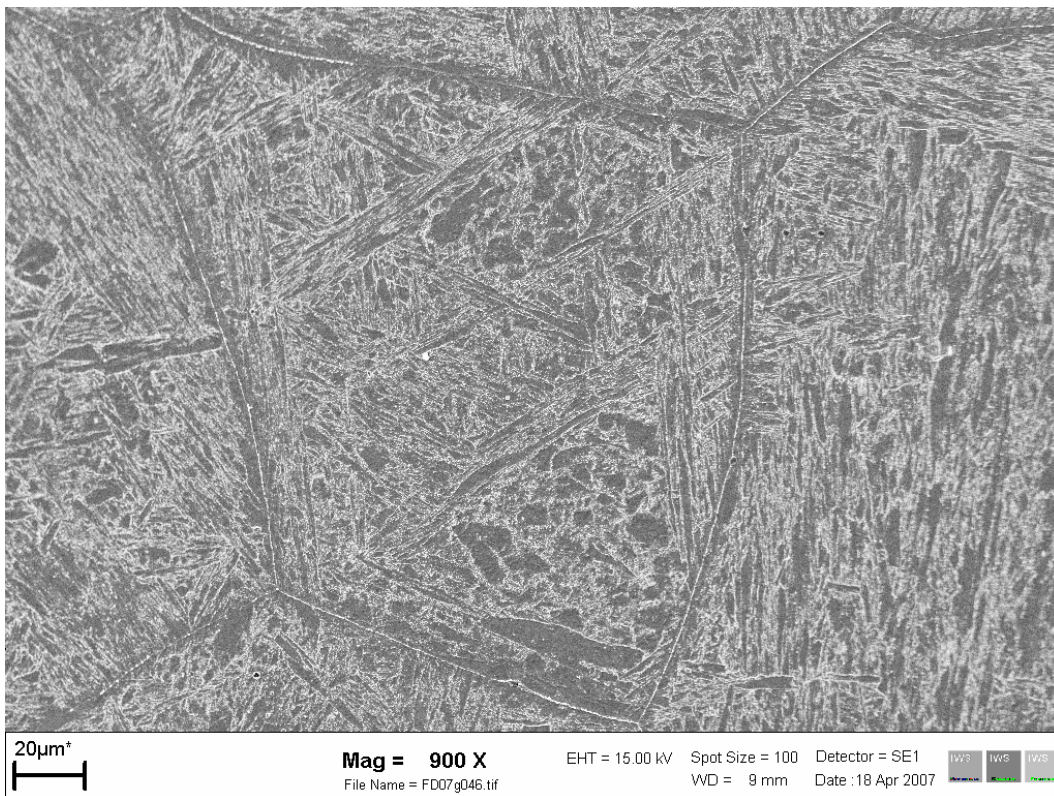


Figure 46: Precipitation structure in NPM1 base material revealing precipitate free zones along prior austenite grain boundaries (see also Figure 47 bottom).

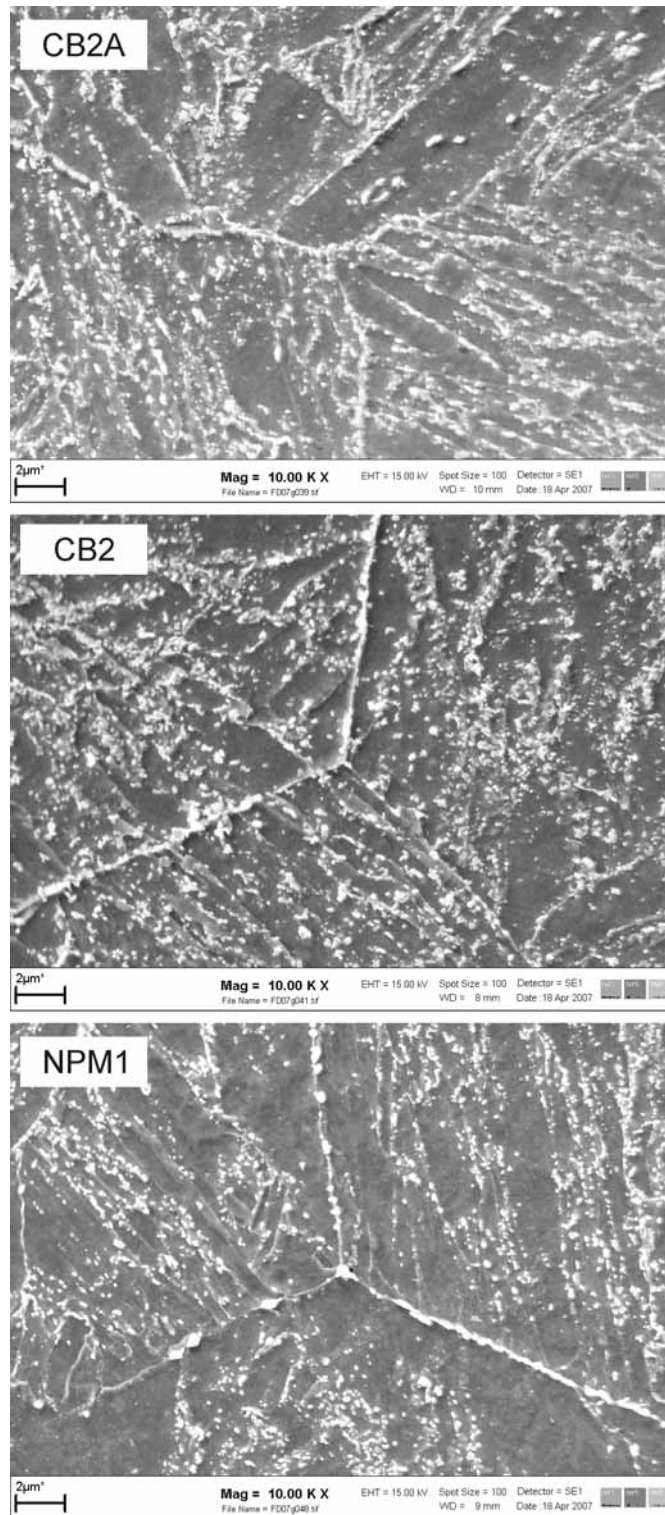


Figure 47: SEM images of precipitate distribution in base materials CB2A (top), CB2 (middle) and NPM1 (bottom) in as-received condition.

For identification of precipitates in CB2A and NPM1 base materials, analytical transmission electron microscopy examinations are performed.

### 1.2.1 CB2A

In CB2A, carbides, nitrides and carbonitrides are detected. Carbides are either rich in chromium (CrC) or niobium (NbC). Nitrides are identified as vanadium nitrides (VN) (Figure 48). Also carbonitrides enriched in vanadium and niobium ((V,Nb)(C,N)) are detected within CB2A base material. Figure 49 shows characteristic EDX and EELS spectra of the detected chromium carbides and (V,Nb)(C,N). Figure 50 shows some chromium carbides with an approximate size of 300 nm aligned along a grain boundary.

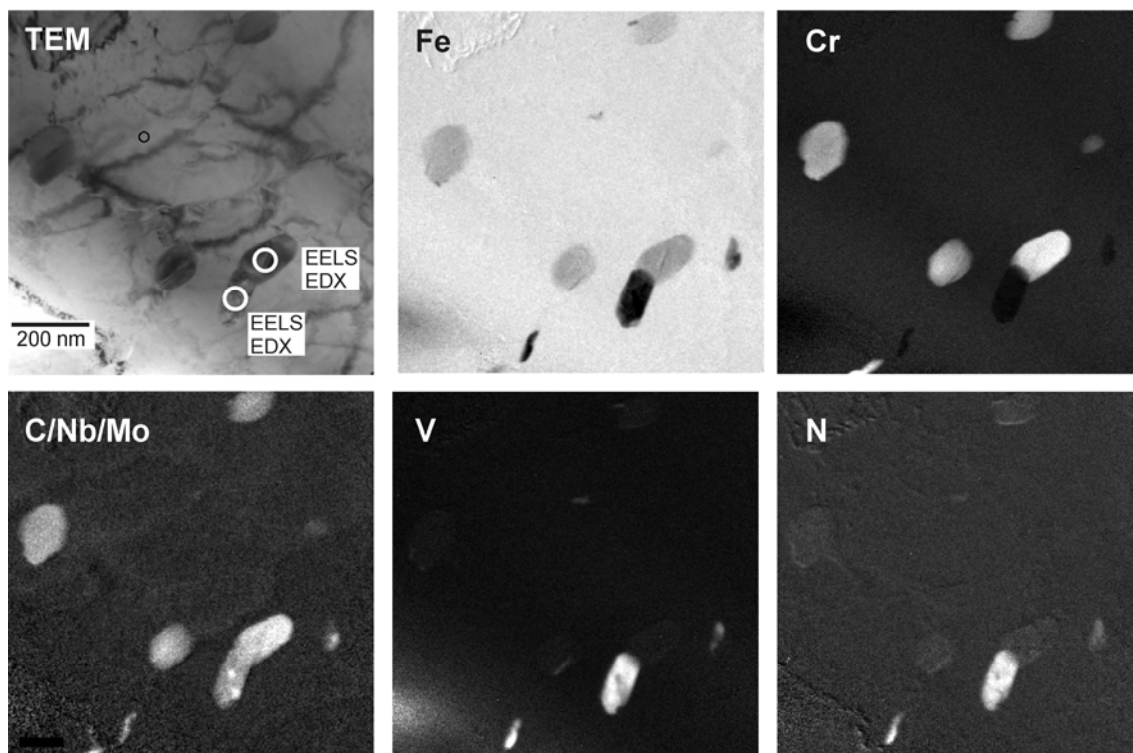


Figure 48: Bright field TEM image and corresponding EFTEM elemental maps of precipitates in CB2A base material.

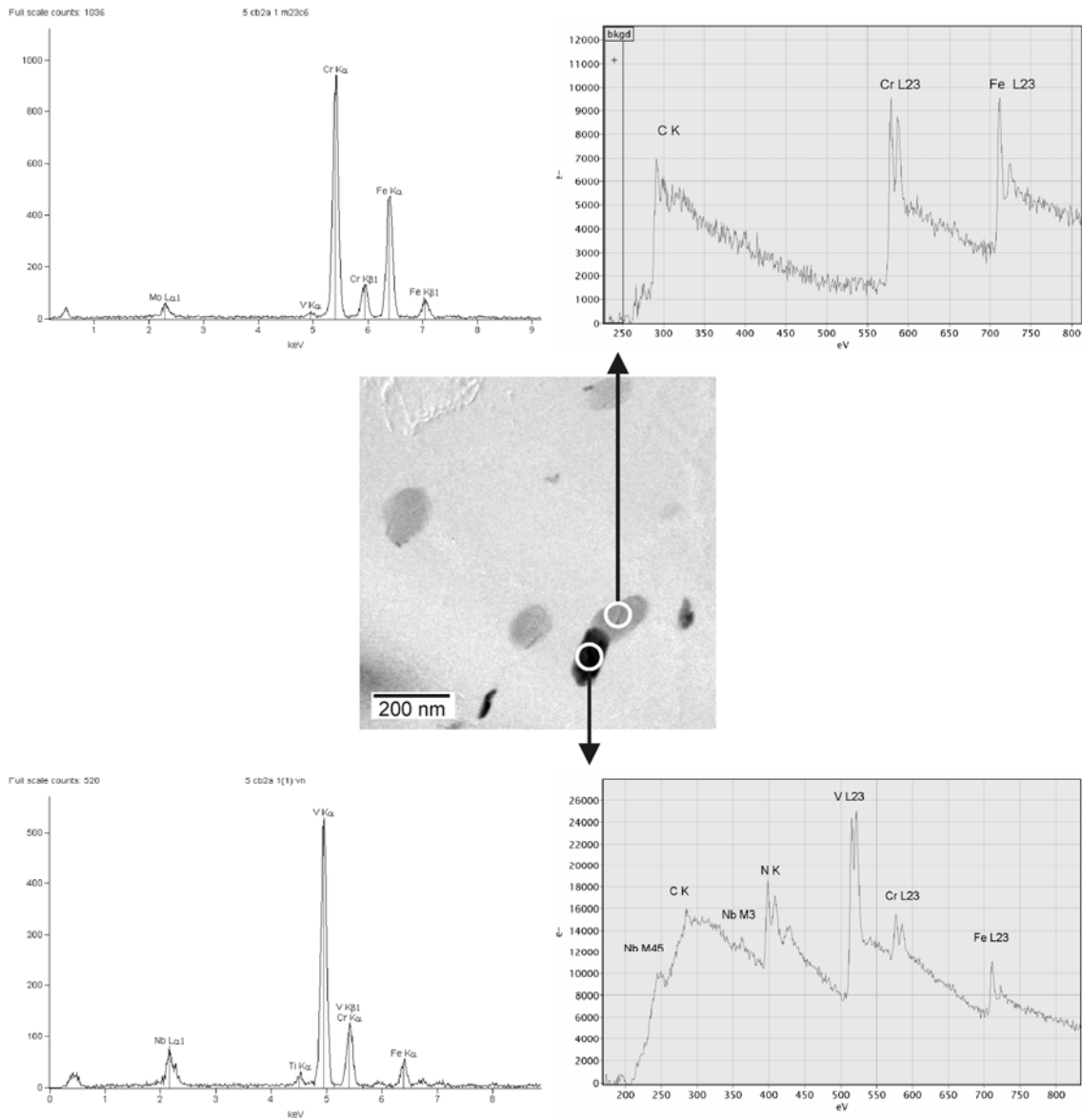


Figure 49: Identification of precipitates in CB2A base material by EELS and EDX. A chromium carbide (top) is positioned beside a carbonitride (V,Nb)(C,N) (bottom).

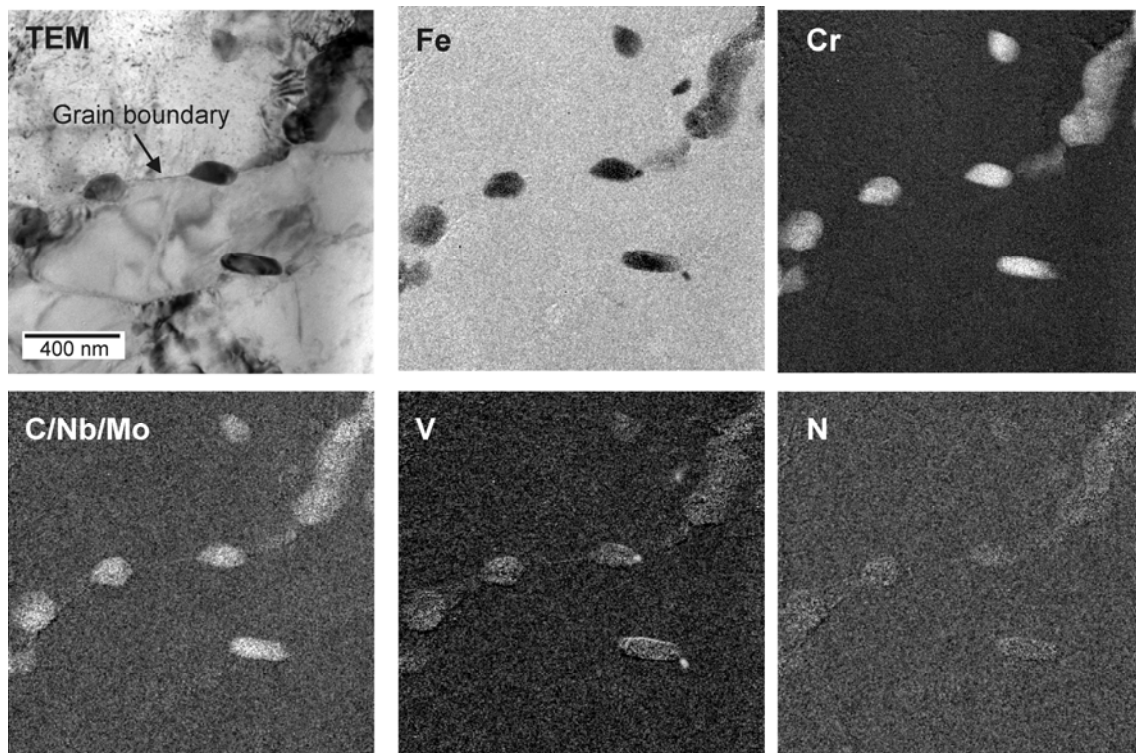


Figure 50: Chromium carbides positioned along a grain boundary in CB2A base material identified by EFTEM.

### 1.2.2 NPM1

To observe precipitate distribution in NPM1 material, specifically along the prior austenite grain boundaries, a TEM specimen is prepared using the focused ion beam (FIB) technique. Figure 51 (left) shows the position of specimen extraction in the vicinity of a triple point. A deposited Si layer protects the microstructure beneath from the high energy ion beam during sample preparation. Figure 51 (right) shows the obtained TEM specimen with two grain boundaries inside the specimen. TEM investigation shows that only a small number of precipitates are present in the specimen. Chromium carbides with a diameter of approximately 300 nm are aligned along a grain boundary. Also very fine VN particles only few nm in size are distributed along the boundary. A larger particle visible in the centre of Figure 53 is identified as a boride using EELS. In a second TEM specimen prepared from a random position by conventional sample preparation technique, (V,Nb)(C,N) carbonitrides are observed. These are similar in size to the ones observed in CB2A base material. Corresponding images and EDX and EEL spectra are given in Appendix D.

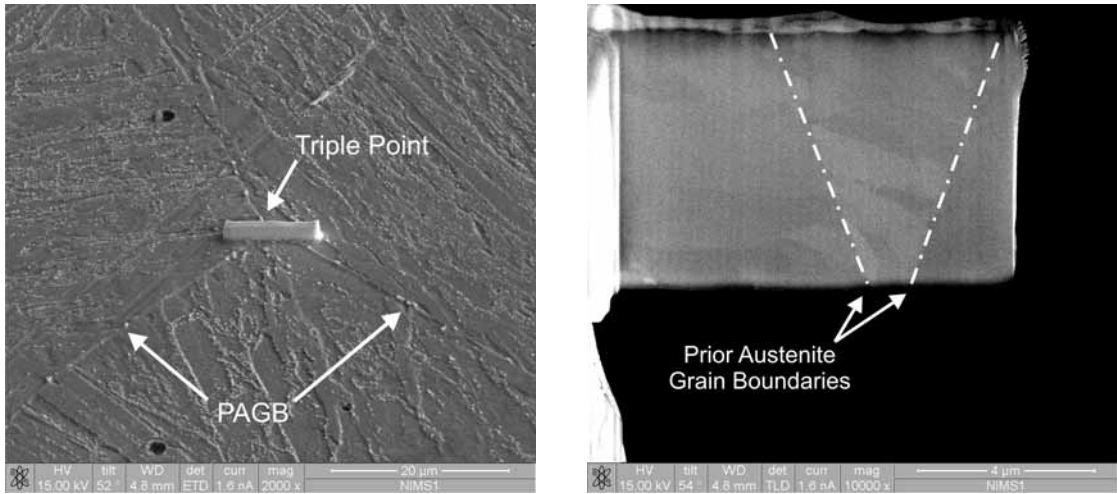


Figure 51: Location of FIB sample extraction from NPM1 base material at a PAGB triple point (left) and obtained TEM sample comprising two prior austenite grain boundaries.

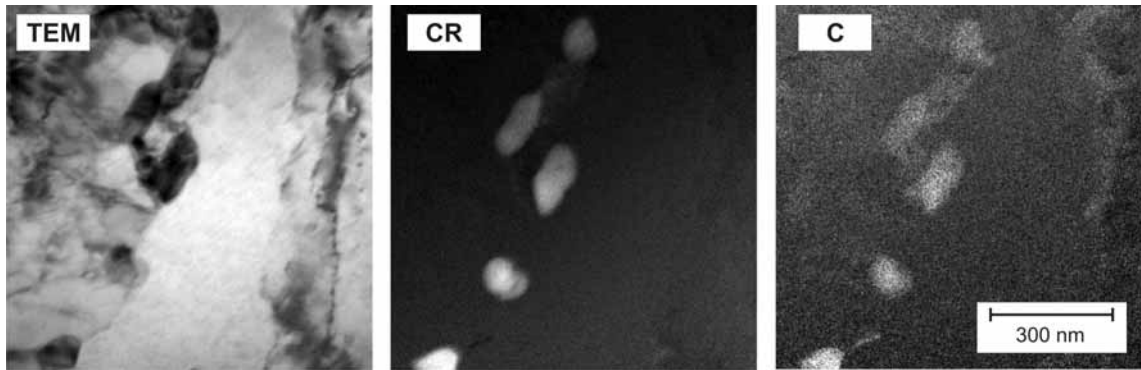


Figure 52: TEM and EFTEM images of prior austenite grain boundary region in NPM1 base material showing aligned chromium carbides.

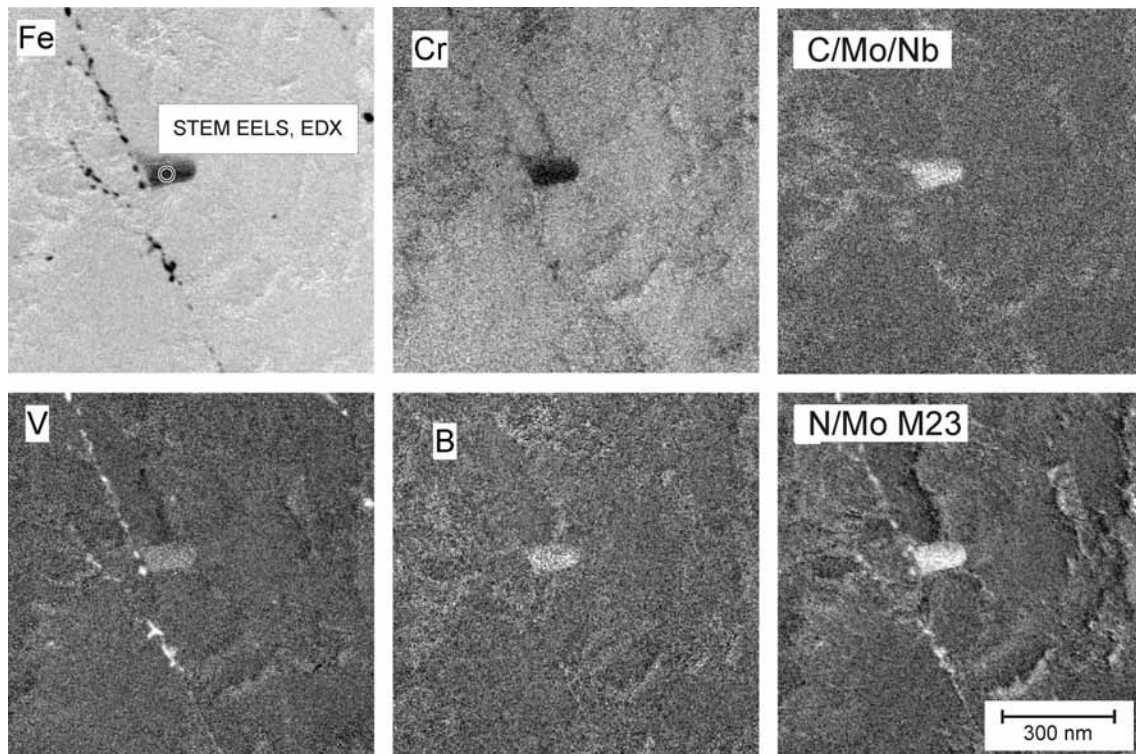


Figure 53: Very fine VN precipitates along grain boundary in NPM1 base material. The larger particle in the center of the specimen is identified as boride.

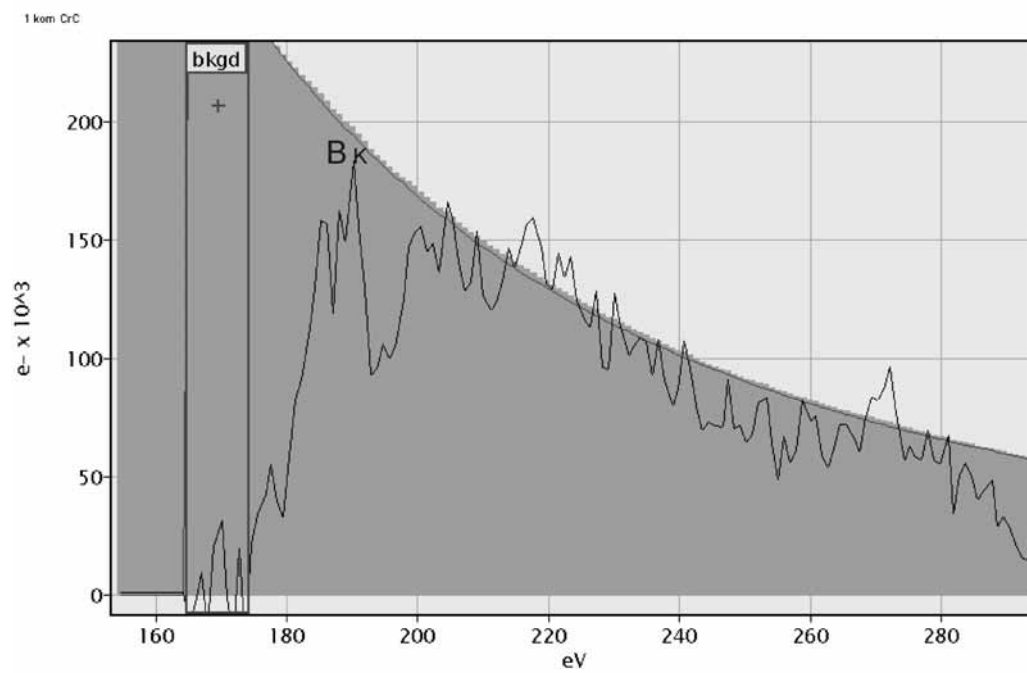


Figure 54: Corresponding EEL spectrum of large particle shown in center of Figure 53 revealing a boron peak.

### 1.3 Detection of boron nitrides

As boron is believed to have a significant influence on the creep strength of martensitic steels, possible boron nitride (BN) precipitation is investigated for all three steel variants. Figure 55 shows typical fracture surfaces of the investigated specimens.

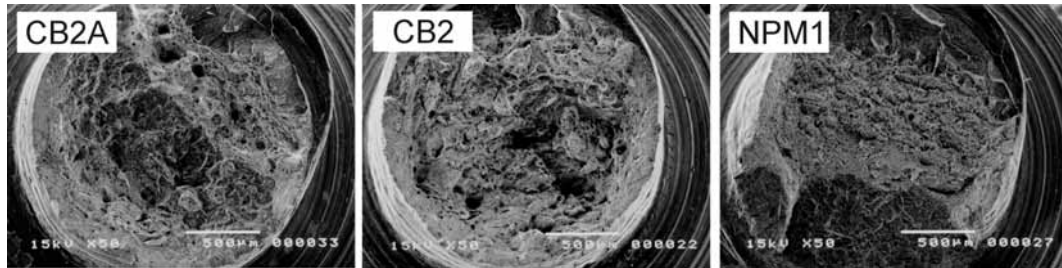


Figure 55: Fracture surfaces of CB2A (left), CB2 (centre) and NPM1 (right) base material specimens.

Already at lower magnification, differences in the appearance of the fracture surfaces can be observed between the cast steel variants and the forged material. All specimens show attributes of a ductile fracture with characteristic dimple structure. Whereas, in the cast steels, numerous particles are observed at the bottom of the dimples, in NPM1 only few and rather small particles within the dimples are detected (Figure 56).

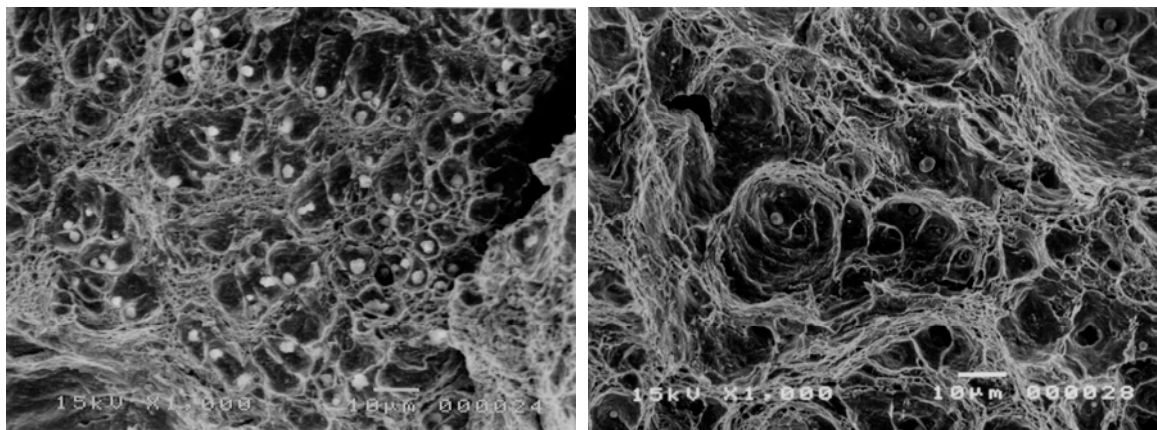


Figure 56: Different appearance of fracture surfaces. Base material CB2 (left) showing dimples with vast number of inclusions, NPM1 showing dimples with a small number of small inclusions (right).

Inclusions are identified by EDX point measurements. As the particles are located at the bottom of the dimples and sometimes very small in size, some background noise of the bulk material is also incorporated in the EDX spectra. Therefore, an EDX spectrum of a boron nitride can show additional peaks. Four different types of non-metallic inclusions are detected within the three steels. Boron nitrides (BN), silicon oxides ( $\text{SiO}_2$ ), aluminium oxides ( $\text{Al}_2\text{O}_3$ ) and manganese sulphides (MnS) are identified by their characteristic EDX spectra. Further images and EDX spectra of all detected inclusions are summarised in Appendix D. In Figure 57, representative boron nitride particles for each steel grade are shown.

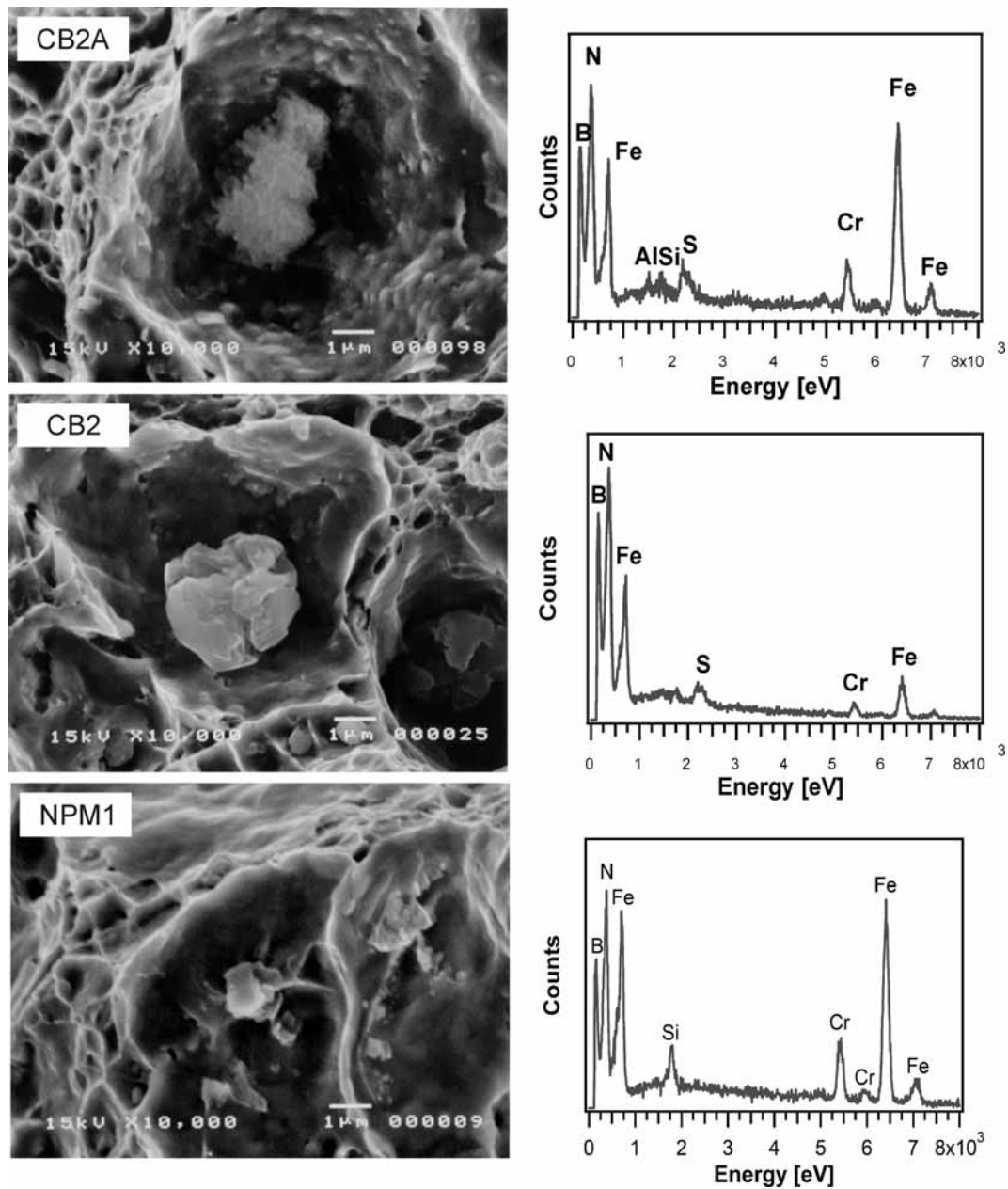


Figure 57: Boron nitrides observed in CB2A (top), CB2 (middle) and NPM1 (bottom) base material identified by EDX spot measurements.

In the cast variants CB2A and CB2, BN particles are relatively large with several micrometers in diameter. In NPM1, only boron nitrides with a maximum size of 1 μm are observed. All boron nitrides have a characteristic appearance with a rough surface structure compared to the smooth surface of the other types of non-metallic inclusions.

To characterise the distribution of boron nitride inclusions within the base materials, SEM images of representative areas of the fracture surfaces are taken at lower magnifica-

tion. Particles are identified by EDX spot measurements and manually coloured. CB2 shows the largest number of BN particles of all three steels closely followed by CB2A. In both steels, the fracture surface is almost covered with BN particles. EDX spectra of some particles show the characteristic peaks of a BN as well as of a MnS. These particles are coloured differently, although it is believed that these ambiguous spectra are caused by two different particles very close to each other. At the same level of magnification, no boron nitrides are observed in NPM1.

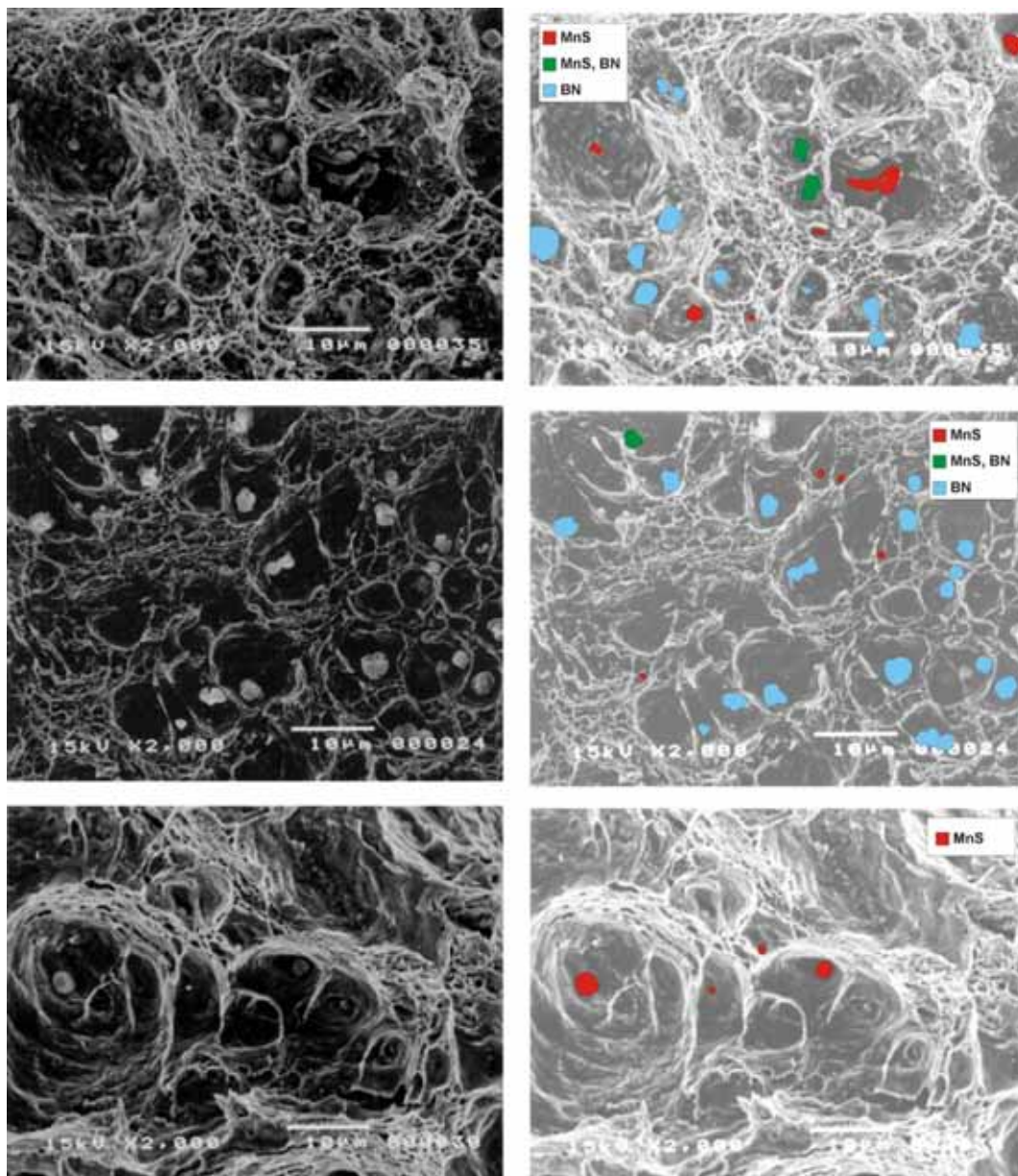


Figure 58: Distribution of non-metallic inclusions in base material of CB2A (top), CB2 (middle) and NPM1 (bottom).

Investigations at higher magnification reveal BN particles in NPM1 material, too. The size of these particles as well as the number density is significantly lower than the ones observed in the other steels. Figure 59 shows several small BN particles observed in NPM1 steel.

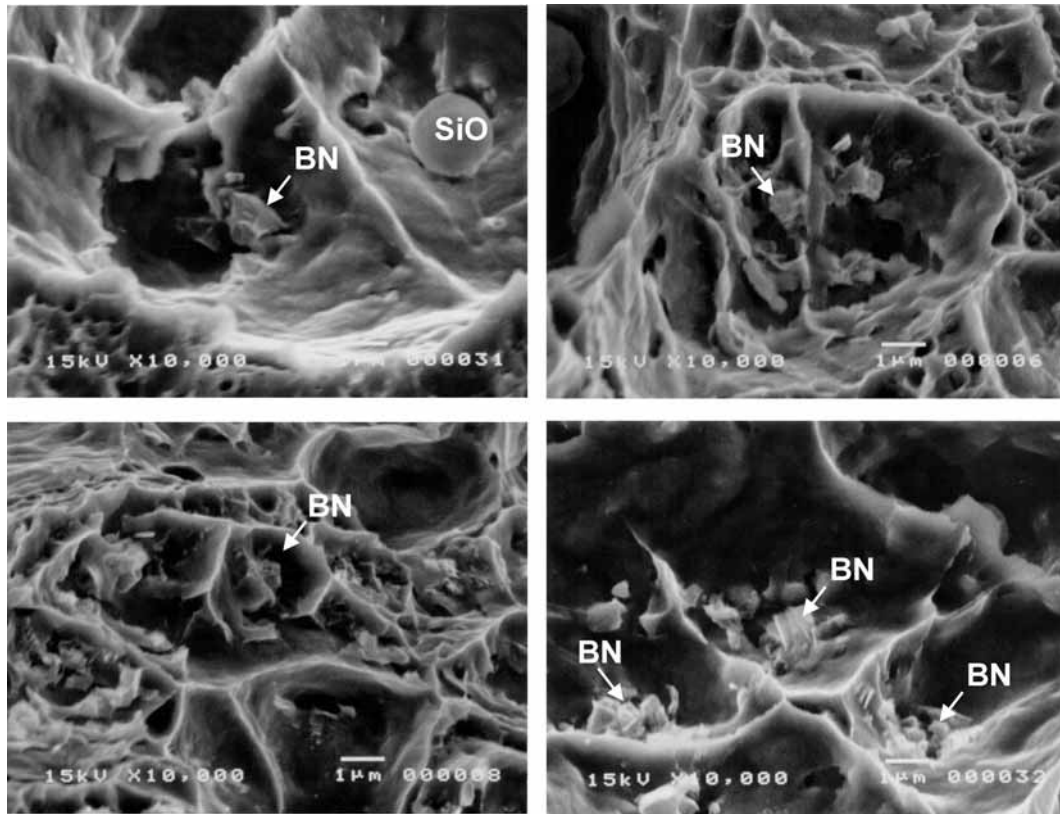


Figure 59: Small boron nitrides observed in NPM1 base material identified by EDX spot measurements.

A summary of the size and distribution of the non-metallic inclusions within the three different base materials is given in Table 30.

Table 30: Summary of detected non-metallic inclusions in CB2A, CB2 and NPM1 base material.

|                                    | CB2A                |                         | CB2                 |                                 | NPM1             |                                |
|------------------------------------|---------------------|-------------------------|---------------------|---------------------------------|------------------|--------------------------------|
|                                    | Size                | Distribution            | Size                | Distribution                    | Size             | Distribution                   |
| <b>BN</b>                          | 2 – 5 $\mu\text{m}$ | uniform<br>high density | 1 – 4 $\mu\text{m}$ | uniform<br>very high<br>density | <1 $\mu\text{m}$ | uniform<br>very low<br>density |
| <b>MnS, BN</b>                     | 2 – 5 $\mu\text{m}$ | uniform<br>low density  | ~3 $\mu\text{m}$    | isolated                        | not detected     |                                |
| <b>MnS</b>                         | < 4 $\mu\text{m}$   | uniform<br>high density | < 3 $\mu\text{m}$   | uniform<br>low density          | <2 $\mu\text{m}$ | uniform<br>low density         |
| <b>Al<sub>2</sub>O<sub>3</sub></b> | ~5 $\mu\text{m}$    | isolated                | ~5 $\mu\text{m}$    | isolated                        | <4 $\mu\text{m}$ | isolated                       |

## 1.4 X-ray diffraction

In advance to the in-situ synchrotron X-ray diffraction measurements during a weld thermal cycle, diffraction patterns of the base materials have been obtained (Figure 60).

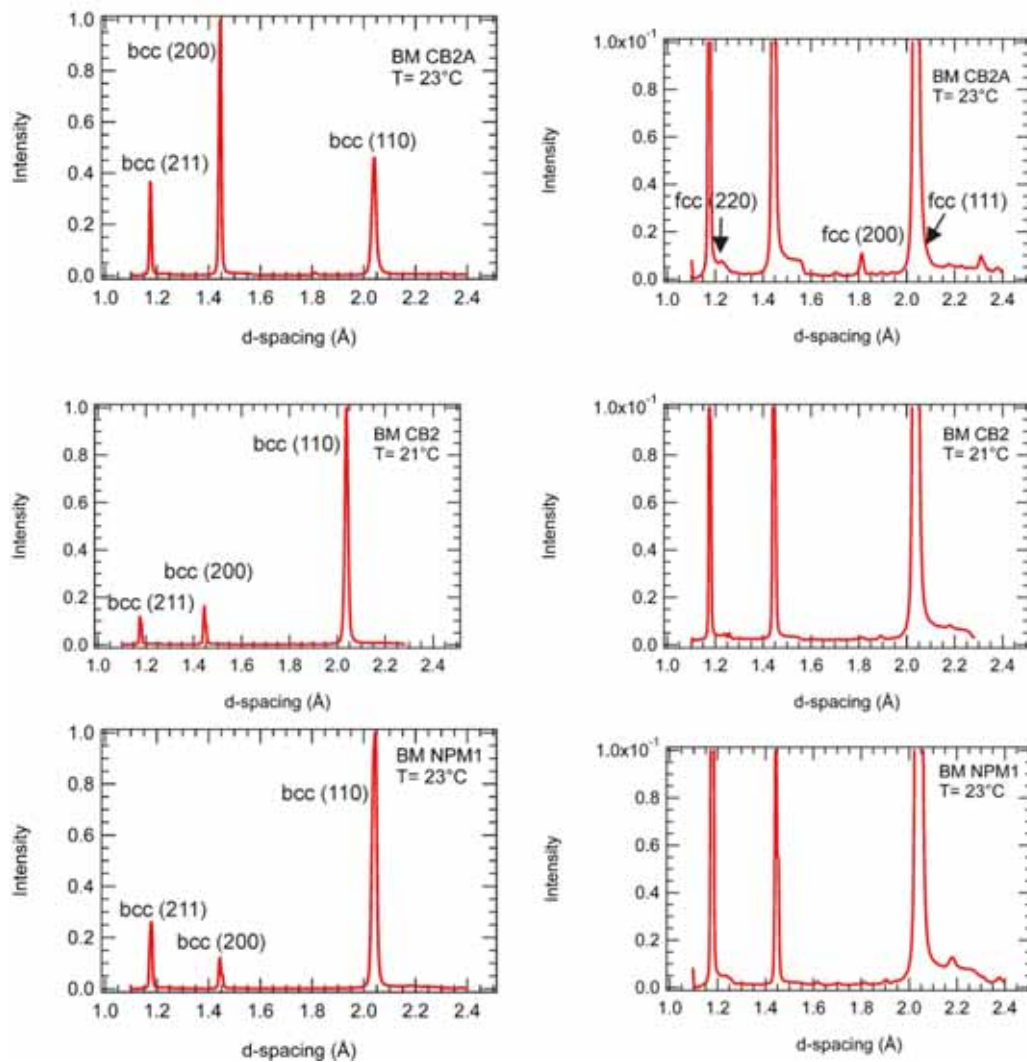


Figure 60: X-ray diffraction patterns of base materials CB2A (top), CB2 (middle) and NPM1 (bottom) obtained at room temperature.

In all specimens of CB2 and NPM1 base material, only bcc peaks characteristic for a tempered martensitic microstructure are detected. In some specimens of CB2A base material, also small fcc peaks are recorded whereas other CB2A base material specimens only show bcc peaks (see Appendix D). Calculation of the phase fraction of retained austenite in CB2A specimens showing fcc peaks indicates 1 % retained austenite.

## 1.5 Thermodynamic analysis

Equilibrium phase diagrams as a function of the chromium content have been calculated for all three steels using Matcalc. Contents of all other alloying elements have been set constant according to the chemical composition given in the experimental section of this work. In Figure 61 to 63, the calculated phase diagrams are shown in a simplified way displaying only the matrix phases austenite and ferrite. At the nominal chromium content of each alloy, a dotted line is drawn from top to bottom. Taking a look at the phase transformations from high to lower temperatures, all steels solidify primarily ferritic. They all have a similar solidus temperature around 1410°C. While CB2A and CB2 pass a dual phase region of austenite and delta ferrite during solidification, NPM1 solidifies completely ferritic and in the temperature range of 1410°C to 1388°C consists of 100% delta ferrite. On further cooling, also in NPM1, austenite starts to nucleate on the expense of delta ferrite. At temperatures below  $A_{c4}$  all steels are fully austenitic. This phase transformation is taking place at almost the same temperature of 1250°C in the cast alloys, while in NPM1 transformation takes place approximately 70 degrees lower at 1183°C.  $A_{e3}$  temperature is similar in CB2A and NPM1 material (880°C) and about 30°C lower for CB2 steel. This ratio is also similar for the  $A_{e1}$  transformation temperature. CB2 transforms at about 790°C and CB2A and NPM1 about 40 degrees higher at 830°C. An overview of the calculated equilibrium phase transformation temperatures is given in Table 31.

In all steels, delta ferrite is stable down to room temperature above a certain level of chromium. In steel NPM1, this threshold value is the lowest for the three alloys at 11.1 wt.% chromium followed by CB2A (11.6 wt.%) and CB2 (12.2 wt.%).

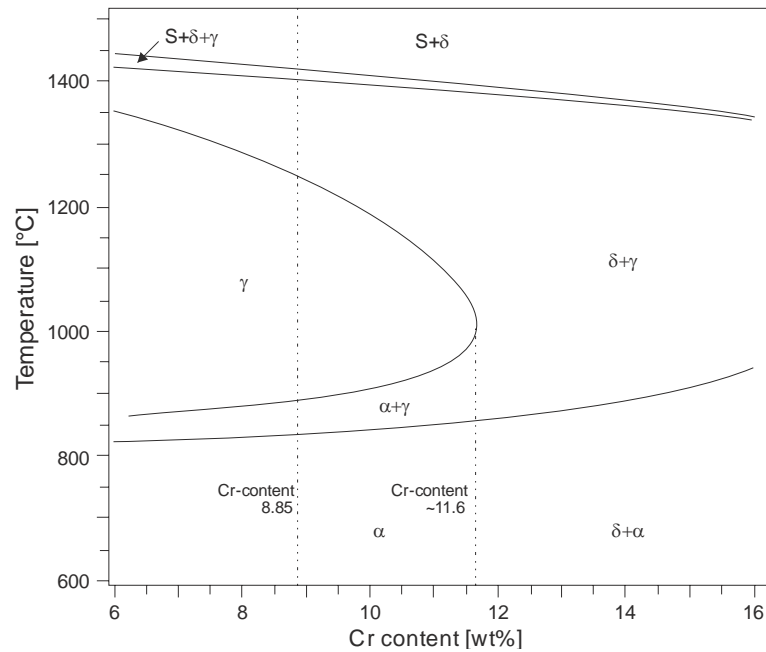


Figure 61: Calculated phase diagram of CB2A as a function of chromium content based on the chemical composition according to Table 5 using the software Matcalc.

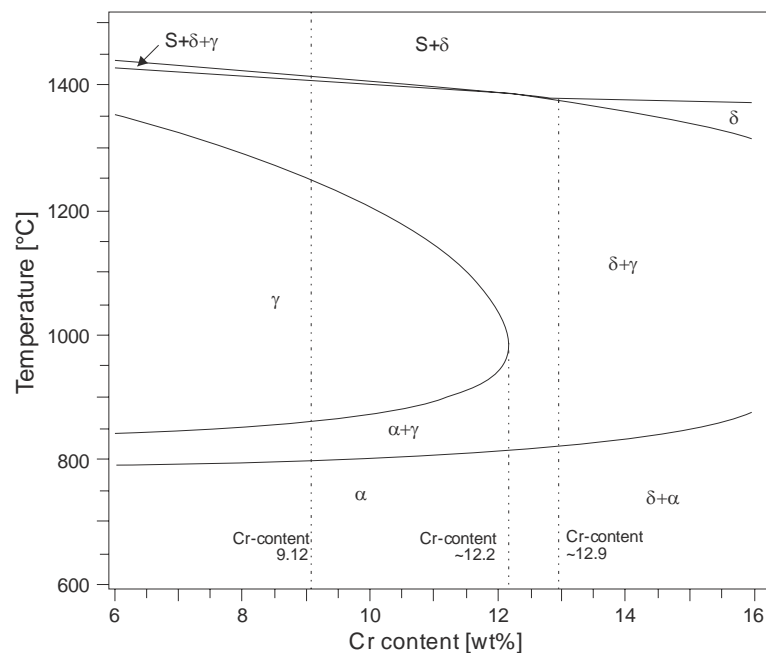


Figure 62: Calculated equilibrium phase diagram of CB2 using chemical composition according to Table 7 as a function of chromium content using the software Matcalc.

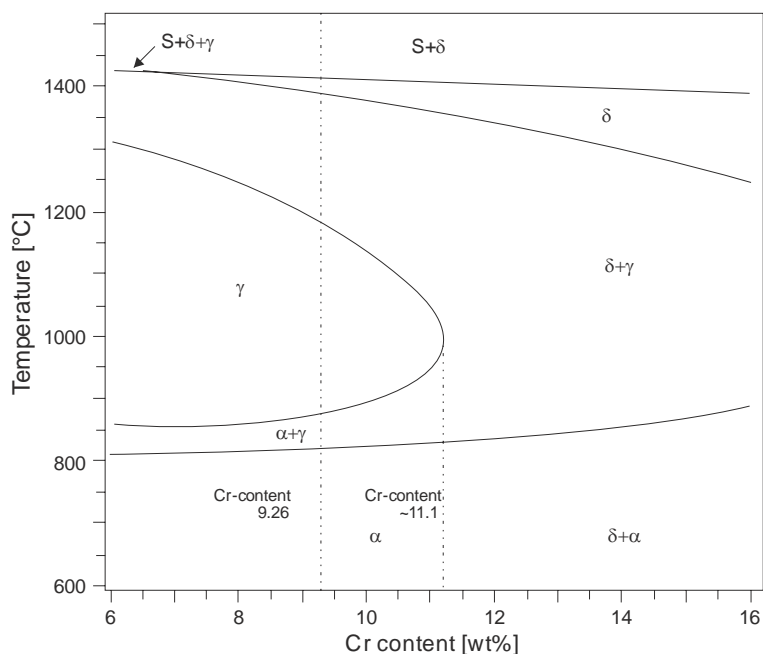


Figure 63: Calculated phase diagram of NPM1 using chemical composition according Table 9 carbon content using the software Matcalc.

Table 31: Calculated equilibrium phase transformation temperatures using the software Matcalc.

|                            | CB2A   | CB2    | NPM1   |
|----------------------------|--------|--------|--------|
| <b>Solidus temperature</b> | 1407°C | 1411°C | 1410°C |
| <b>A<sub>e1</sub></b>      | 835°C  | 792°C  | 828°C  |
| <b>A<sub>e3</sub></b>      | 887°C  | 854°C  | 881°C  |
| <b>A<sub>e4</sub></b>      | 1249°C | 1257°C | 1183°C |
| <b>A<sub>e5</sub></b>      | -      | -      | 1388°C |

Diagrams of the calculated phase fractions as a function of temperature are shown in Figure 64. For all three steels, NbC, VN, Laves phase,  $M_2B$ ,  $M_{23}C_6$  and Z-phase are calculated to be stable in certain temperature ranges. Additionally, in NPM1 steel,  $M_6C$  carbides are stable.  $M_2B$  borides start to precipitate at first at temperatures close or slightly above the solidus temperature and remain stable down to room temperature. A problem with predictions of phase stability of boron based phases is that, at the moment, boron is not well incorporated in the databases<sup>‡</sup> and results concerning boron in steels have to be treated with some care. The calculation also predicts boron nitrides as non-stable phases in these steels, which is also of great uncertainty for the same reason as for the borides. Niobium carbides are stable up to highest temperatures, similar to the second type of MX precipitates, the vanadium nitrides. Whereas NbC is stable down to room temperature, VN disappears close to a temperature around 800°C and is replaced by Z-phase. In all three steels,  $M_{23}C_6$  chromium carbides have the largest volume fraction and, once precipitated, they are stable also at lower temperatures.

---

<sup>‡</sup> At the time of completion of this work, a new thermodynamic database (Fe-data6.tdb) was released. In this database, boron based phases are incorporated based on the latest findings. Research on boron based phases will be continued in the work of I. Holzer at the IWS.

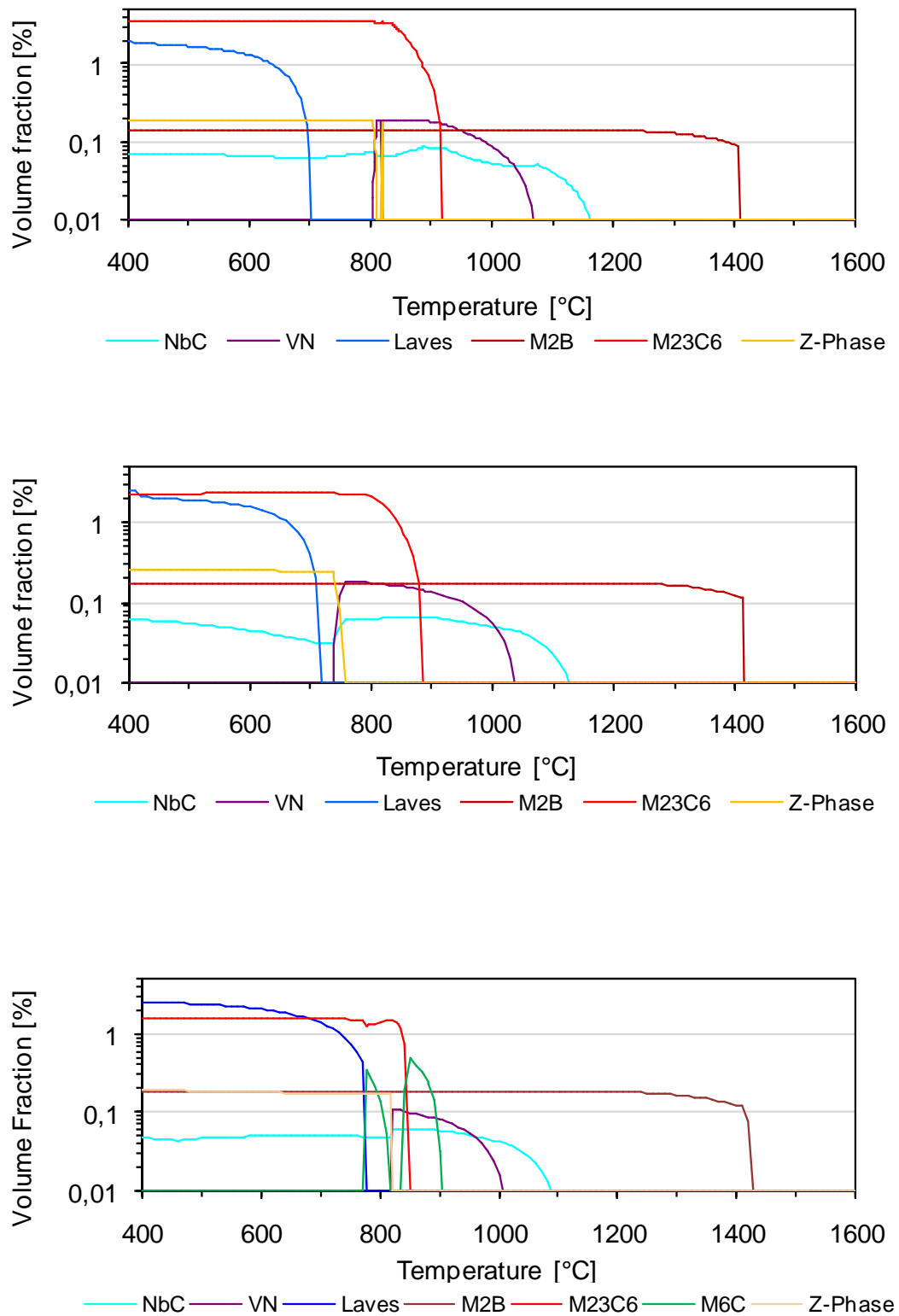


Figure 64: Calculated phase fraction diagrams for precipitate phases as a function of temperature of CB2A (top), CB2 (middle) and NPM1 (bottom) using Matcalc.

Equilibrium phase fractions of phases contributing to particle strengthening are calculated at two specific temperatures, 600°C and 650°C, representative for possible service temperatures (Figure 65). CB2A shows the largest volume fraction of precipitates close to 5 vol.%, slightly higher than in CB2 and NPM1 material. The levels of borides ( $M_2B$ ) and Z-phase are similar in all steels. NPM1 shows the largest volume fraction of Laves phase and CB2A the largest fraction of  $M_{23}C_6$ . The volume fractions of Laves phase and  $M_{23}C_6$  for CB2 material are in between the values of CB2A and NPM1. Whereas Laves phase in CB2A and CB2 contains molybdenum, in NPM1 it contains tungsten because of the different alloying concept.

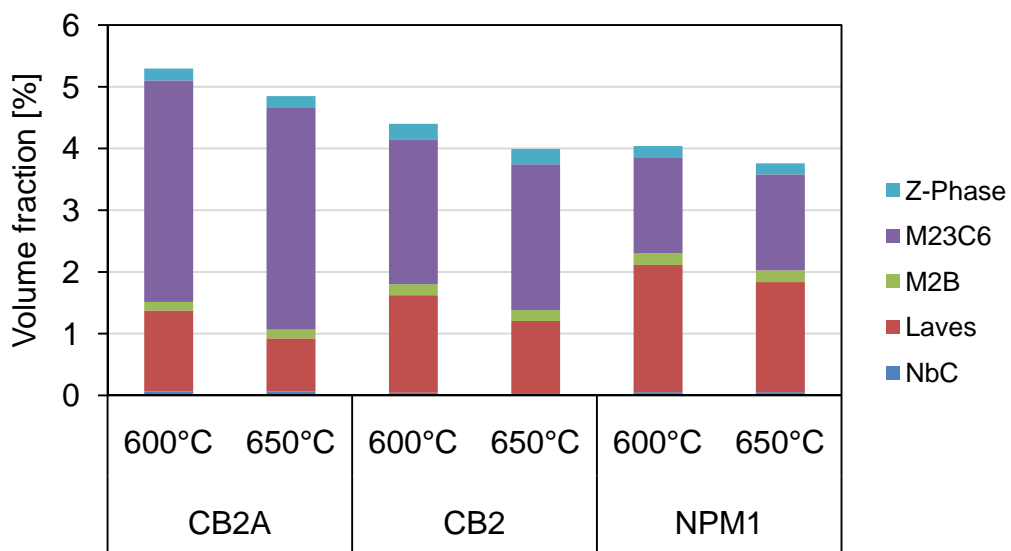


Figure 65: Calculated equilibrium volume phase fractions of phases contributing to particle strengthening at 600°C and 650°C.

Table 32 summarises the range of thermal stability of the individual domains of precipitates.

**Table 32: Calculated range of thermal stability for precipitates predicted in CB2A, CB2 and NPM1 steel.**

|             | NbC      | VN             | Laves   | M <sub>2</sub> B | M <sub>23</sub> C <sub>6</sub> | M <sub>6</sub> C               | Z-Phase |
|-------------|----------|----------------|---------|------------------|--------------------------------|--------------------------------|---------|
| <b>CB2A</b> | < 1179°C | 805°C - 1077°C | < 703°C | < 1410°C         | < 920°C                        | -                              | < 812°C |
| <b>CB2</b>  | < 1142°C | 737°C - 1046°C | < 719°C | < 1416°C         | < 887°C                        | -                              | < 759°C |
| <b>NPM1</b> | < 1104°C | 817°C - 1017°C | < 776°C | < 1431°C         | < 850°C                        | 833°C - 903°C<br>770°C - 816°C | < 819°C |

## 1.6 Mechanical properties

Basic information on the mechanical properties of the base materials have either been obtained by mechanical testing at IWS (CB2A, NPM1) or have been taken from the materials certificate provided by the steelmaker (CB2). Creep testing data for CB2 material has been obtained by partners within the European COST activities and is reported within Appendix B. NPM1 base material has been creep tested at the IWS and results are reported below.

Table 33 gives a summary of the mechanical properties for the three steel grades. The base material hardness is almost at the same level for all three steels. Fracture elongation (A) and reduction of area (Z) are higher for the forged material NPM1. The average impact energy of 27 Joule at ambient temperature for CB2 is low compared to the 69 Joule for CB2A material. Impact properties of NPM1 base material are not obtained because of lack of testing material.

**Table 33: Summary of the mechanical properties at ambient temperature.**

|   | CB2A     | CB2 <sup>1</sup> | NPM1          |
|---|----------|------------------|---------------|
| <b>Hardness (HV10)</b>                              | 243      | 229              | 238           |
| <b>Ultimate tensile strength (<math>R_m</math>)</b> | 676 MPa  | 726 MPa          | 649 MPa       |
| <b>0.2% proof strength (<math>R_{p0.2}</math>)</b>  | 478 MPa  | 590 MPa          | 504 MPa       |
| <b>Fracture Elongation (A)</b>                      | 14 %     | 19.2%            | 36 %          |
| <b>Reduction of area (Z)</b>                        | 47%      | 60%              | 73 %          |
| <b>Impact energy at ambient temperature</b>         | 69 Joule | 28, 29, 25 Joule | not evaluated |

<sup>1</sup> Data taken from material certificate Nr. 49.0840

For NPM1 material, tensile properties are obtained at elevated temperatures. Figure 66 shows the yield strength and tensile strength at different temperatures. With increasing testing temperature, the yield strength as well as the tensile strength decrease. At 650°C, the most desired service temperature for this material, the yield strength is 263 MPa and the tensile strength 275 MPa. With increasing testing temperature, fracture elongation and reduction of area increase (Figure 67).

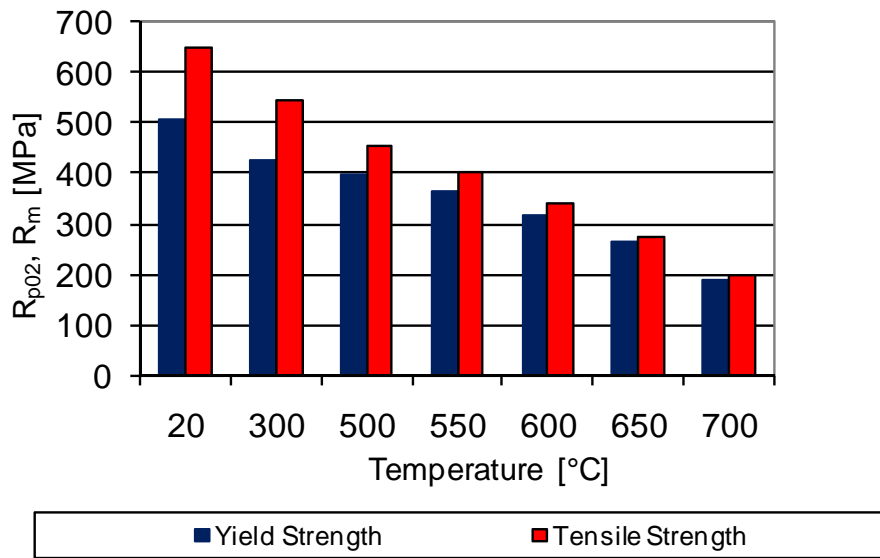


Figure 66: NPM1 base material tensile properties at ambient and elevated temperatures.

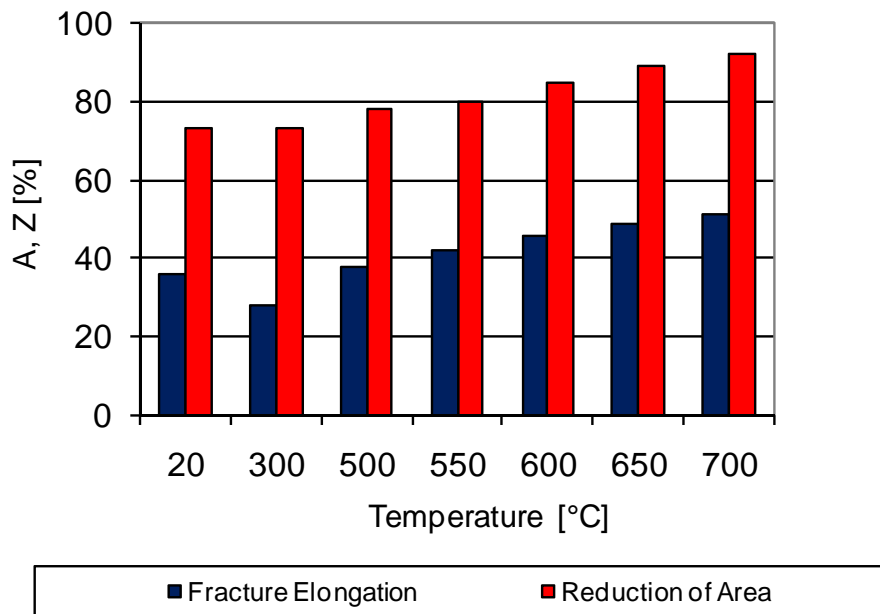


Figure 67: Fracture elongation and reduction of area for NPM1 base material obtained by tensile testing at ambient and elevated temperature.

### 1.6.1 Creep testing of NPM1 base material

Creep tests for material NPM1 at both stress levels, 130 and 100 MPa, are still running. When this thesis was completed, testing times of 8.600 hours at 130 MPa and 7.850 hours at 100 MPa have been achieved (Figure 68). The creep strain data indicates that the specimen tested at the higher stress level is already in the tertiary creep regime. The steady state creep region (secondary creep) with a constant strain rate is found between 1.000 hours and approximately 6.000 hours. After 8.600 hours of testing, a creep strain of 1.9% has accumulated. The lower stressed specimen is still in the steady-state creep regime and a creep strain of 0.48% is reported after 7.850 hours of testing.

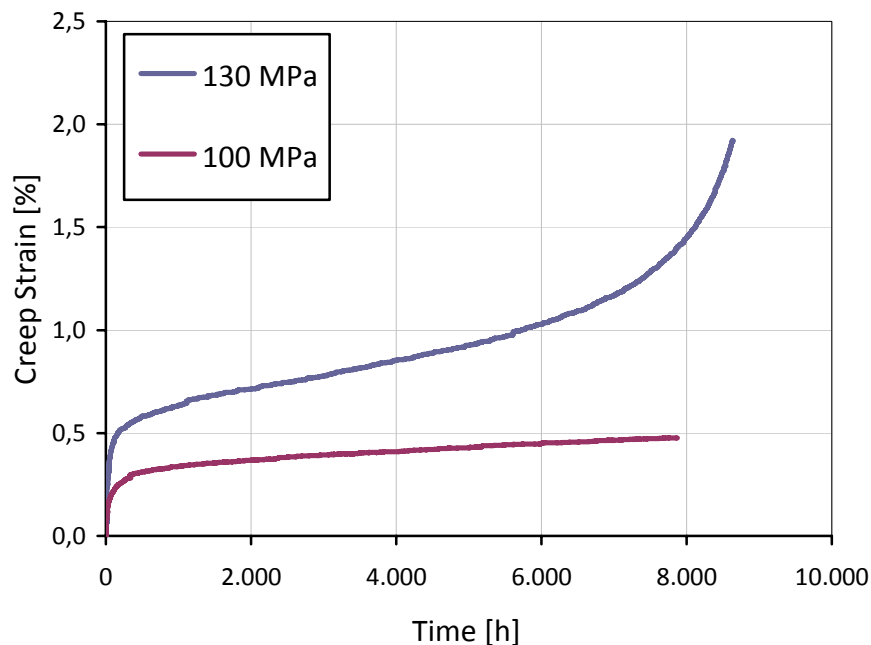
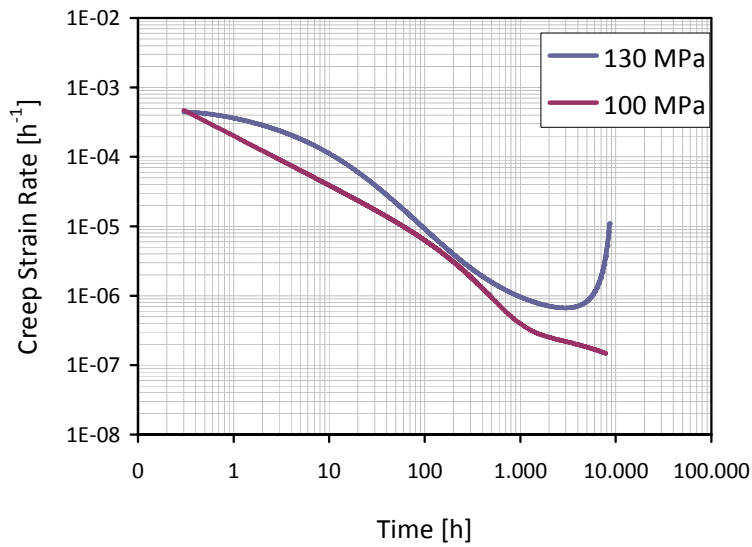


Figure 68: Creep strain versus testing time for NPM1 base material at 650°C and two different stress levels.

Creep strain rate for both specimens is calculated from the recorded strain data (Figure 69). In the primary creep region, the creep strain rate is decreasing down to the minimum creep rate reached after a certain testing time. The minimum creep rate for the specimen tested at 130 MPa is  $6.7 \times 10^{-7}$  and reached after 2.900 hours of testing. For the specimen tested at 100 MPa, the overall minimum creep rate has not been reached so far. After 7.850 hours of testing, a minimum creep rate of  $1.5 \times 10^{-7}$  is measured.



**Figure 69:** Creep strain rate as function of testing time for NPM1 base material at 650°C and two different stress levels.

Figure 70 shows the creep strain rate as function of the creep strain. For the specimen tested at 130 MPa the minimum creep rate is reached at a strain of 0.008. Creep rate of the lower stressed specimen is still decreasing. Therefore, the minimum creep strain rate could not yet be obtained.

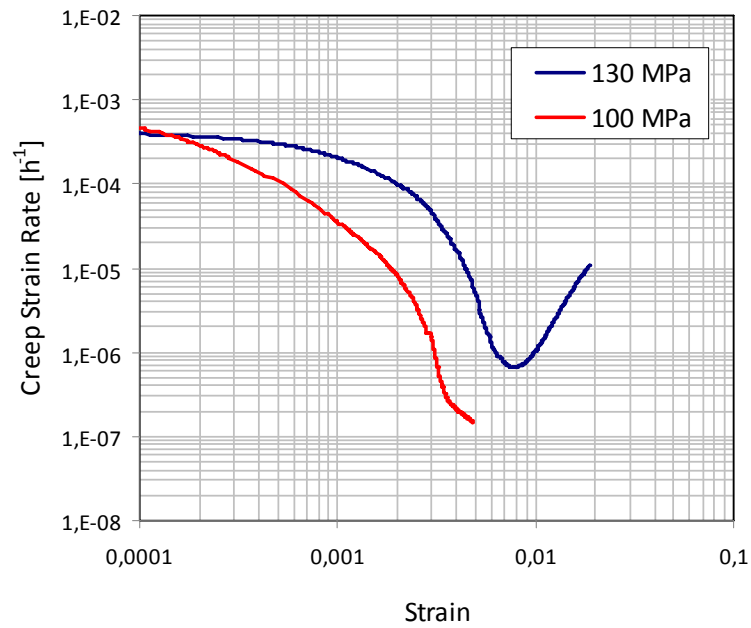


Figure 70: Creep strain rate versus strain for NPM1 base material tested at  $650^{\circ}\text{C}$  and two different stress levels.



## 2 Heat affected zone characterisation

The formation of the heat affected zone (HAZ) in the investigated three boron containing martensitic 9% chromium steels is studied by physical HAZ simulation. Phase transformations during characteristic weld thermal cycles are observed by dilatometry and in-situ X-ray diffraction. The influence of weld thermal cycles on the microstructure is investigated by optical and electron microscopy performed on HAZ simulated specimens. The formation of delta ferrite at highest peak temperature, its retention during cooling and the implications on the mechanical properties after a post-weld heat treatment are studied. Evolution of the grain structure in the HAZ is of special interest, as for example, the fine-grained region is susceptible to Type IV cracking during long-term creep exposure. NPM1 HAZ grain structure is of particular interest as in a similar 9Cr-3W-3Co alloy, suppression of the formation of a fine-grained HAZ region has been detected by Japanese researchers. Hence, for NPM1 steel, additionally to the weld-simulated heat affected zone, the HAZ of a multi-layer weld produced by gas tungsten arc welding is investigated.

### 2.1 Dilatometry

Dilatometry is used to observe phase transformations during characteristic weld thermal cycles. For CB2 and NPM1 material dilatometric data are obtained by an attached dilatometer during physical HAZ simulation using a Gleeble thermo-mechanical simulator. For CB2A a quenching dilatometer is used. This allows quenching specimens at designated temperatures and studying the obtained microstructure. The formation and retention of delta ferrite during weld thermal cycles is of particular interest.

#### 2.1.1 Phase transformations in CB2A

Phase transformations in steel CB2A are obtained using a quenching dilatometer applying a weld thermal cycle with a peak temperature of  $T_p=1300^\circ\text{C}$  and a characteristic cooling time of  $t_{8/5}=43$  s. Additionally the characteristic of delta ferrite is studied by holding at a peak temperature of  $1300^\circ\text{C}$  for 60 seconds.

*Phase transformations on heating*

The thermal cycle exhibits a heating rate of  $100\text{K s}^{-1}$ . The heating part of the dilation curve for steel CB2A is reported in Figure 71. The measured transformation temperatures are summarised in Table 34. The first transformation on heating at  $760^\circ\text{C}$  marks the transition of ferromagnetic to paramagnetic material state, the so called Curie temperature ( $A_{C2}$ ). The onset ( $A_{C1}$ ) and completion ( $A_{C3}$ ) of austenite formation take place at  $930^\circ\text{C}$  and  $1053^\circ\text{C}$ , respectively. This means that the austenite transformation stretches over a temperature interval of  $123^\circ\text{C}$ .

**Table 34: Measured phase transformation temperatures on heating in CB2A steel applying a heating rate of  $100\text{K s}^{-1}$ .**

| Steel grade | $A_{C1}$            | $A_{C3}$             | $A_{C1} - A_{C3}$   | $A_{C2}$            |
|-------------|---------------------|----------------------|---------------------|---------------------|
| CB2A        | $930^\circ\text{C}$ | $1053^\circ\text{C}$ | $123^\circ\text{C}$ | $760^\circ\text{C}$ |

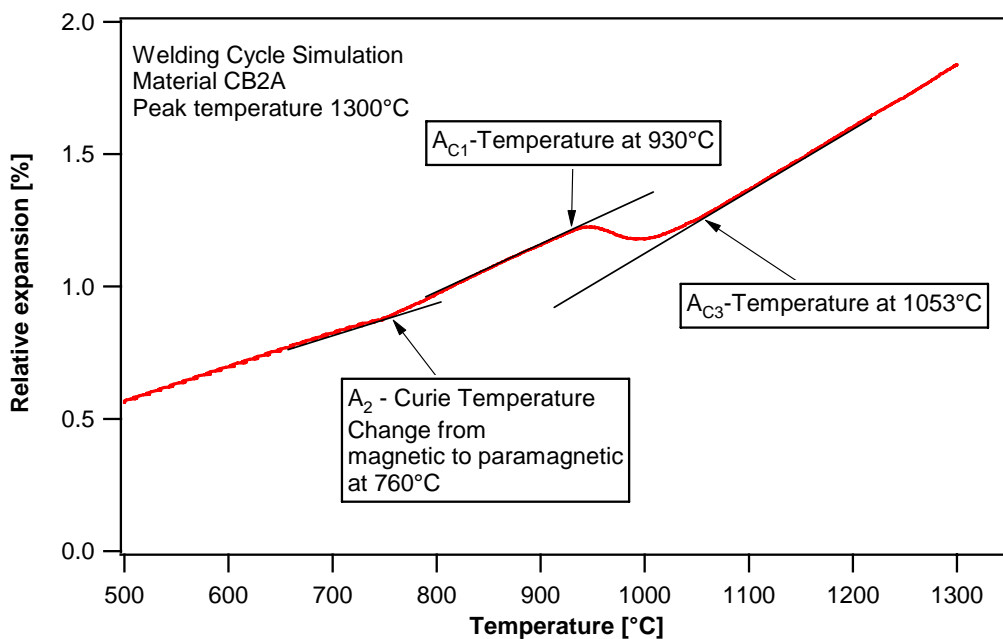


**Figure 71: Heating part of the dilation curve obtained for steel CB2A applying a heating rate of  $100^\circ\text{C s}^{-1}$ .**

As shown in Figure 72, completion of austenitisation is very fast and takes only about one second. The difference in austenite fcc and delta ferrite bcc lattice structure in the high temperature region is too small to be detected by dilatometry.

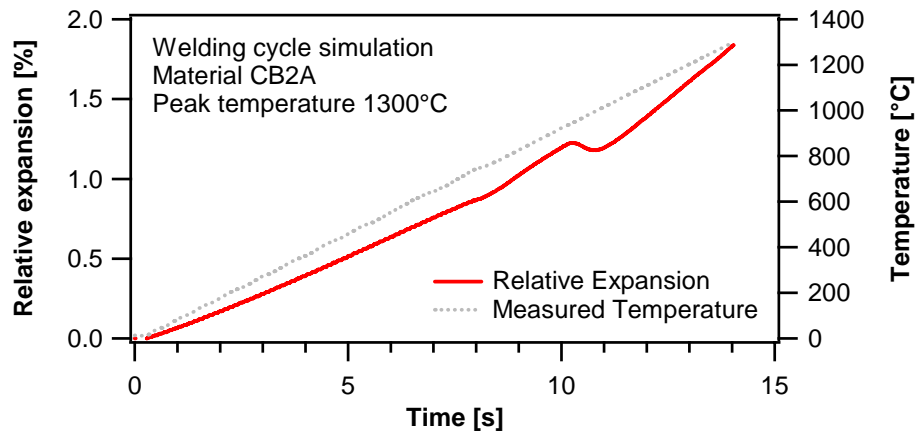


Figure 72: Heating part of the dilation curve versus time for steel CB2A applying a heating rate of  $100^{\circ}\text{C s}^{-1}$ .

### Phase transformations on cooling

The only observable phase transformation during cooling is the transformation of austenite to body-centred-tetragonal (bct) martensite. The corresponding dilation curve is shown in Figure 73. The measured martensite start ( $M_S$ ) and finish ( $M_F$ ) temperatures are  $375^{\circ}\text{C}$  and  $165^{\circ}\text{C}$  respectively.

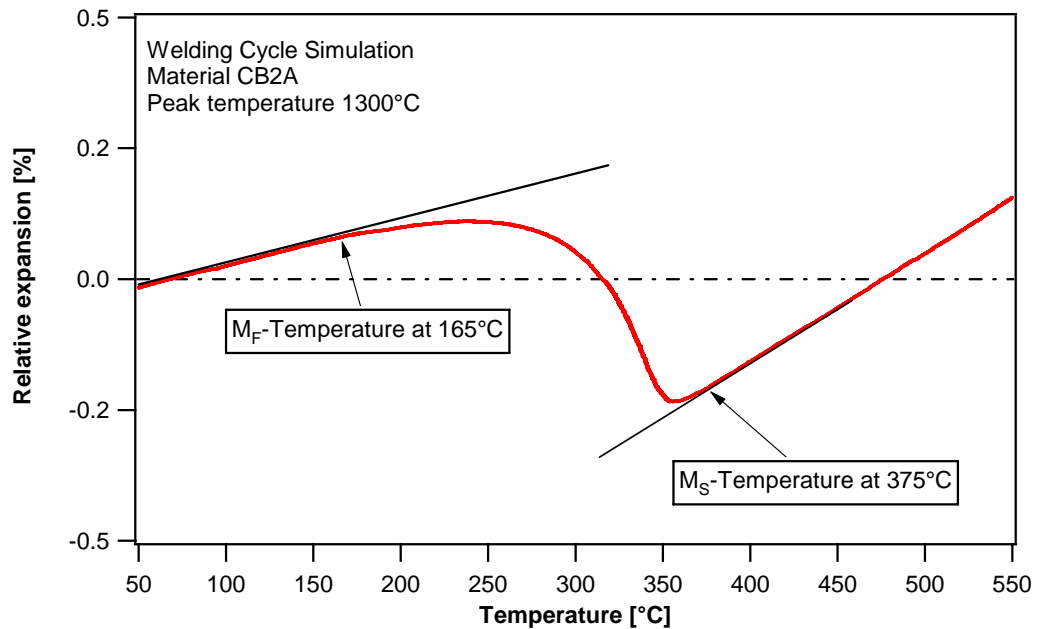


Figure 73: Martensitic transformation observed in CB2A during a simulated weld thermal cycle ( $T_P=1300^{\circ}\text{C}$ ,  $t_{8/5}=43\text{s}$ ).

### Phase transformations during special thermal cycle

Interesting results in dilation are obtained by heating a specimen to a peak temperature of 1300°C applying a heating rate of 100K s<sup>-1</sup> and holding at peak temperature for 60 seconds followed by rapid quenching of the sample.

Measured transformation temperatures are summarised in Table 35. During this thermal cycle, it has been possible to determine the re-transformation of delta ferrite to austenite ( $A_{r5}$  and  $A_{r4}$ ) on cooling (see Figure 74).

**Table 35: Measured transformation temperatures in steel CB2A during special temperature cycle.**

| Steel | $A_{c1}$ | $A_{c3}$ | $A_{c4}$ | $A_{r5}$ | $A_{r4}$ | $A_{r5} - A_{r4}$ | $M_s$ | $M_F$ |
|-------|----------|----------|----------|----------|----------|-------------------|-------|-------|
| CB2A  | 930°C    | 1050°C   | 1280°C   | 1076°C   | 1023°C   | 53°C              | 320°C | 90°C  |

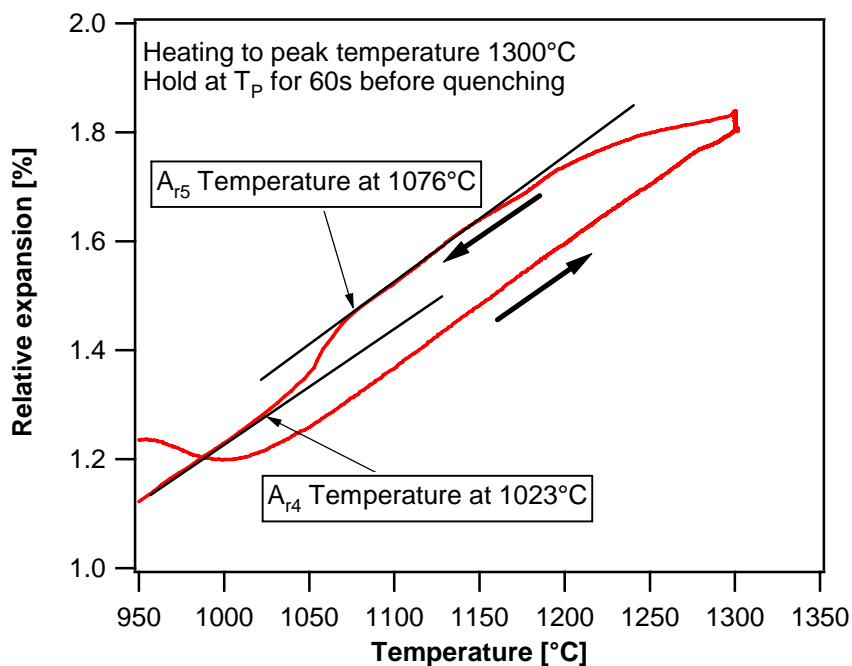


**Figure 74: High temperature part of dilatometer curve obtained by special temperature cycle.**

### 2.1.2 CB2

Phase transformations in CB2 are recorded directly during Gleeble weld simulation for all applied weld thermal cycles. All recorded phase transformation temperatures are summarised

in Table 36. On heating, the onset of austenite formation is in the range of 875°C to 950°C. Austenite formation is completed at temperatures between 970°C and 1060°C.

**Table 36: Transformation temperatures of CB2 obtained by dilatometry during different Gleeble weld simulations. Details of the weld thermal cycles are described in Table 18 and 19**

| Simulated Welding Process | T <sub>P</sub> [°C] | A <sub>C1</sub> [°C] | A <sub>C3</sub> [°C] | M <sub>S</sub> [°C] | M <sub>F</sub> [°C] |
|---------------------------|---------------------|----------------------|----------------------|---------------------|---------------------|
| <b>GTAW (1)</b>           | 1300                | 950                  | 1060                 | 360                 | 200                 |
|                           | 1100                | ∅                    | ∅                    | 375                 | 220                 |
|                           | 960                 | ∅                    | X                    | 400                 | 300                 |
| <b>GTAW (2)</b>           | 1300                | ∅                    | ∅                    | 350                 | 190                 |
|                           | 1100                | ∅                    | ∅                    | 376                 | 210                 |
|                           | 960                 | 890                  | X                    | 410                 | 285                 |
| <b>SMAW</b>               | 1300                | 930                  | 1030                 | 350                 | 215                 |
|                           | 1100                | 918                  | 975                  | 360                 | 195                 |
|                           | 950                 | 915                  | X                    | 400                 | 260                 |
| <b>MIG</b>                | 1300                | 925                  | 1025                 | 355                 | 220                 |
|                           | 1100                | 920                  | 980                  | 370                 | 205                 |
|                           | 950                 | 915                  | X                    | 410                 | 260                 |
| <b>SAW (1)</b>            | 1300                | 920                  | 1025                 | 350                 | 200                 |
|                           | 1100                | 900                  | 975                  | 370                 | 210                 |
|                           | 920                 | 900                  | X                    | 410                 | 275                 |
| <b>SAW (2)</b>            | 1300                | 920                  | 1015                 | 350                 | 230                 |
|                           | 1100                | 900                  | 970                  | 365                 | 210                 |
|                           | 920                 | 875                  | X                    | 400                 | 270                 |

X ... no transformation observed

∅ ... transformation temperature not measurable

Martensite start (M<sub>S</sub>) and finish (M<sub>F</sub>) temperatures are higher for HAZ simulations with lower peak temperatures. The onset of martensite formation is in the temperature range of

350°C to 410°C and martensite formation is completed between 300°C and 190°C (Figure 75 and Figure 76).

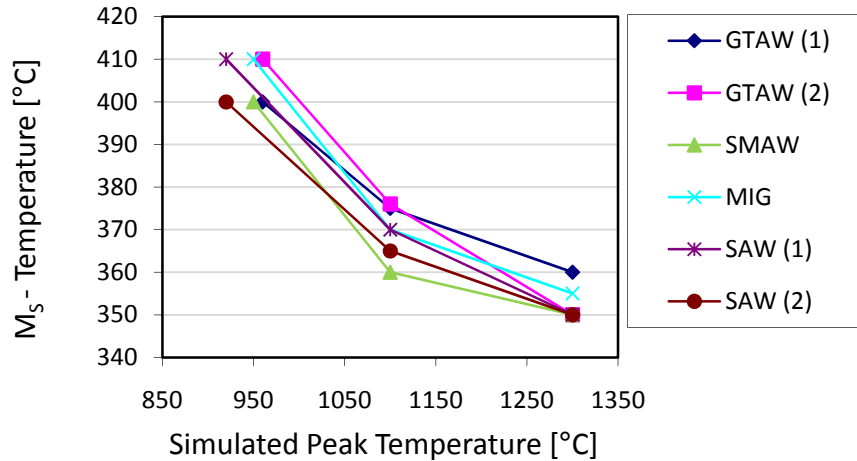


Figure 75:  $M_S$ -temperature as a function of simulated peak temperature for CB2.

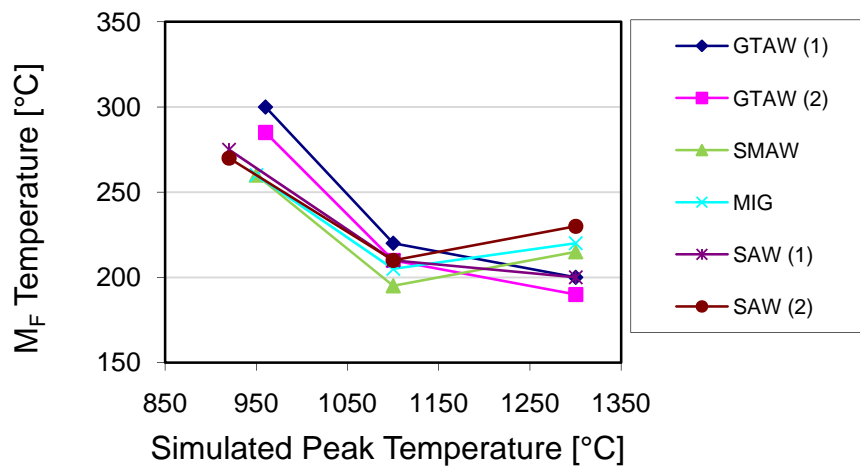


Figure 76:  $M_F$ -temperature as a function of simulated peak temperature for CB2.

### 2.1.3 NPM1

Phase transformations in NPM1 have been recorded directly during Gleeble weld simulation for all applied weld thermal cycles. Peak temperatures varied from 950°C to 1300°C whereas the heat input was set constant. With increasing peak temperature, increasing trans-

formation temperatures on heating are observed (see Figure 77). Austenite formation starts between 925°C and 970°C and is completed at temperatures between 1010°C and 1030°C.

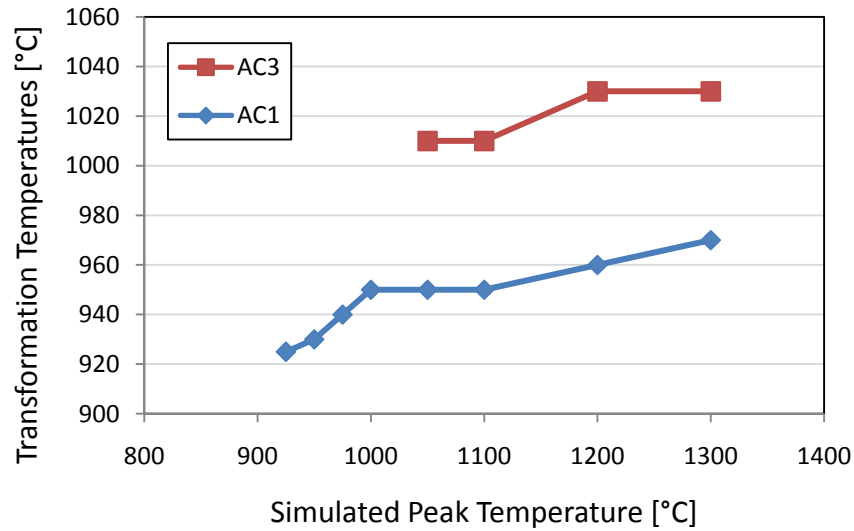


Figure 77: Transformation temperatures  $A_{C1}$  and  $A_{C3}$  for NPM1 as a function of simulated peak temperature.

On cooling, martensite start and finish temperatures decrease as the peak temperature of the applied thermal cycle is increased. The formation of martensite starts in the temperature range of 430°C to 400°C and martensite formation is completed between 320°C and 250°C.

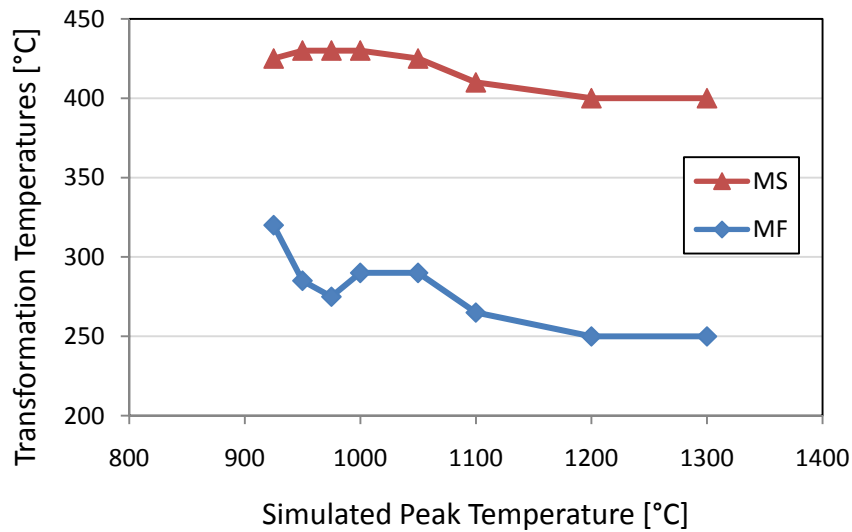


Figure 78: Martensite start and finish temperatures for NPM1 as a function of simulated peak temperature.

## 2.2 In-situ X-ray diffraction

The temperature cycles for in-situ X-ray diffraction are identical for all three steel variants. The thermal cycles are characterized by a peak temperature of 1300°C and a characteristic cooling time around 40 seconds. Phase transformations are studied during fast weld thermal cycles applying a heating rate of 100K s<sup>-1</sup> and during slow thermal cycles with a heating rate of 10K s<sup>-1</sup>. On the following pages the results are presented for each steel grade.

### 2.2.1 CB2A

Figure 79 shows the sequence of phase transformations during a weld thermal cycle applied on CB2A material. Starting from a tempered martensitic microstructure, the ferritic lattice expands to larger values of d-spacing before austenite is formed. When reaching  $A_{C1}$  temperature, austenite formation starts. After completion of austenitisation, only signals of austenite (fcc) are recorded for a short period of time. Reaching highest peak temperatures, the diffraction signal of ferrite re-appears. As the material has been fully austenitic just seconds before, this ferrite can be identified as high temperature delta ferrite.

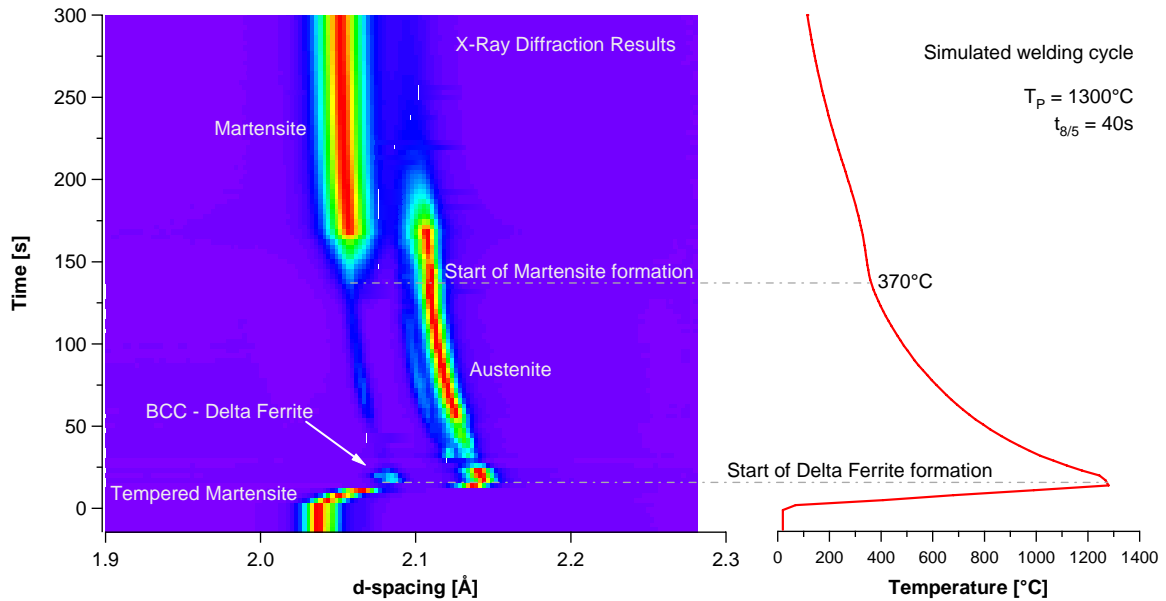


Figure 79: Phase transformations during HAZ simulation for CB2A recorded by in-situ X-ray diffraction.

On cooling, the signal of ferrite weakens again, as re-transformation of delta ferrite to austenite takes place. The remaining bcc signal during further cooling indicates some retained delta ferrite within the steel. Martensite formation starts around 370°C. The d-spacing of martensite is similar to that of ferrite, therefore, the peaks overlap. By the formation of martensite bcc peaks are amplified again and fcc peaks decrease.

The recorded diffraction data is converted into phase fraction versus time plots. Figure 80 shows the complete phase fraction diagram for a weld thermal cycle on CB2A steel. Austenitisation and formation of delta ferrite during the heating part of the thermal cycle are very rapid processes. The high-temperature part of the diagram is enlarged and discussed in a separate figure. Also the cooling part of the thermal cycle is shown in an additional diagram.

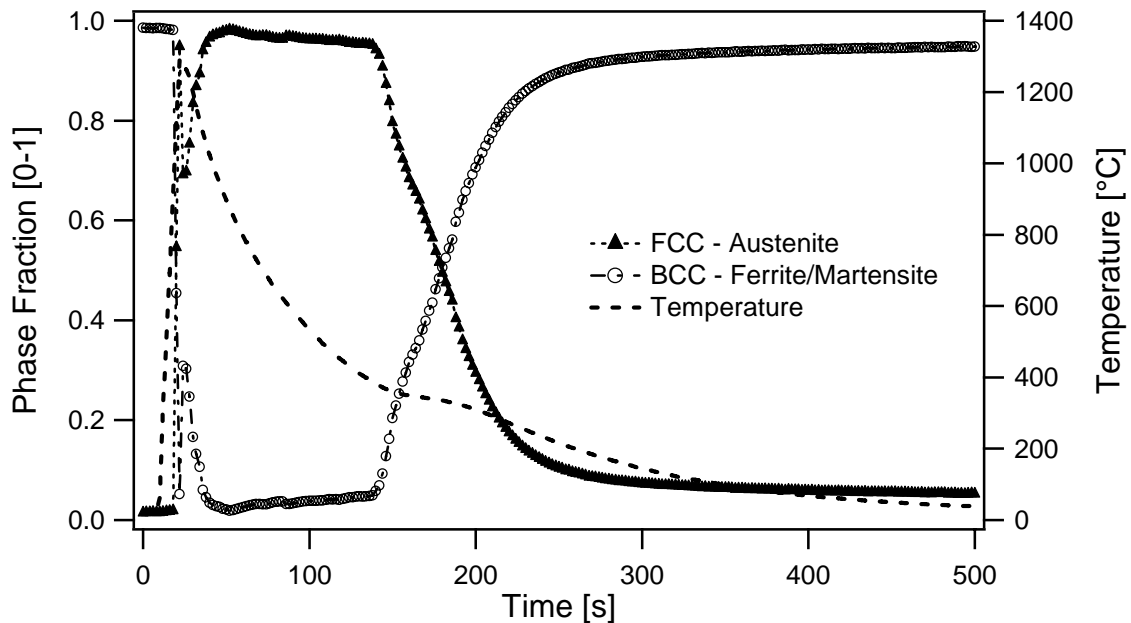


Figure 80: Austenite and ferrite/martensite phase fractions in CB2A material during HAZ simulation applying a heating rate of  $100\text{K s}^{-1}$  obtained by in-situ X-ray diffraction.

Figure 81 shows a magnification of the high-temperature part of the diagram shown in Figure 80. The diffraction pattern at  $1293^\circ\text{C}$  reveals 5% bcc phase fraction. Supported by microstructural investigations, this bcc phase fraction has been identified as newly formed delta ferrite. The maximum amount of delta ferrite of 31% is reached at  $1290^\circ\text{C}$ . On cooling, delta ferrite re-transforms to austenite and the bcc phase fraction decreases down to a certain minimum. Since it is assumed that the steel has been fully austenitic during heating, this minimum level of bcc corresponds to the level of retained delta ferrite. For CB2A, the level of retained delta ferrite is approximately 2%.

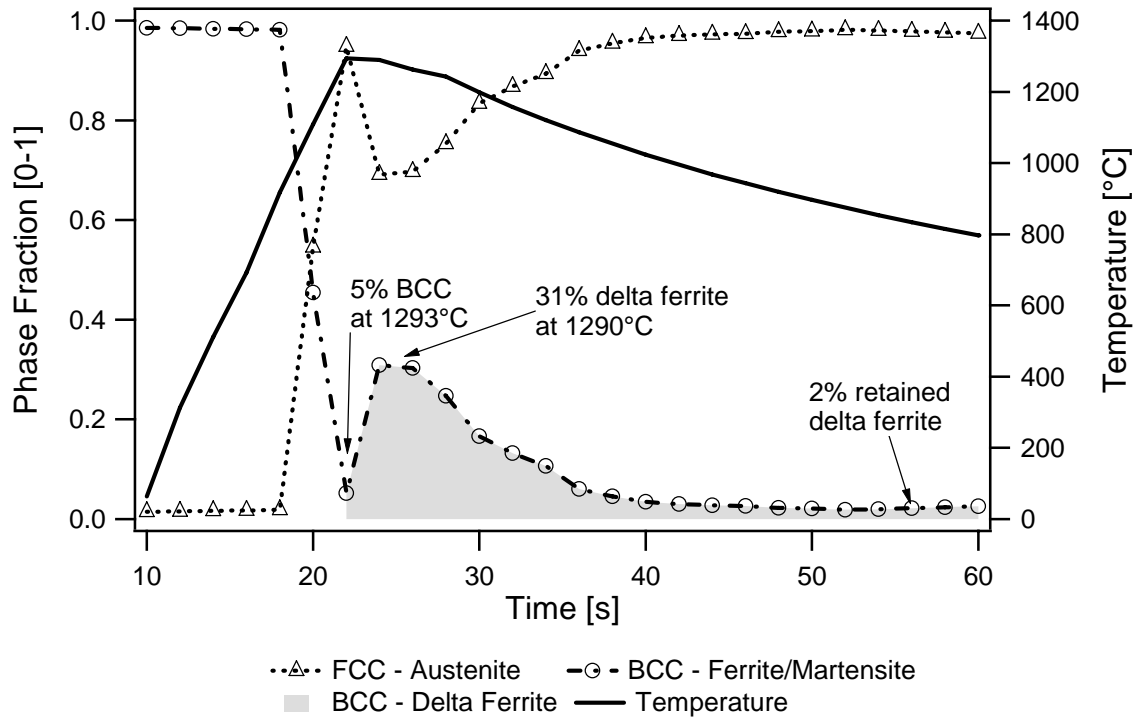


Figure 81: Magnification of the high temperature part of Figure 80.

On cooling, formation of martensite is observed. Transformation to martensite starts at 380°C and causes a decrease of the cooling speed due to the exothermic nature of the transformation. With increasing phase fraction of martensite, the austenite phase fraction simultaneously decreases. After completion of the weld thermal cycle, the austenite phase fraction has not decreased to zero, indicating approximately 5% of retained austenite. The final microstructure of CB2A after completion of the weld thermal cycle consists of martensite with 2% retained delta ferrite and 5% retained austenite.

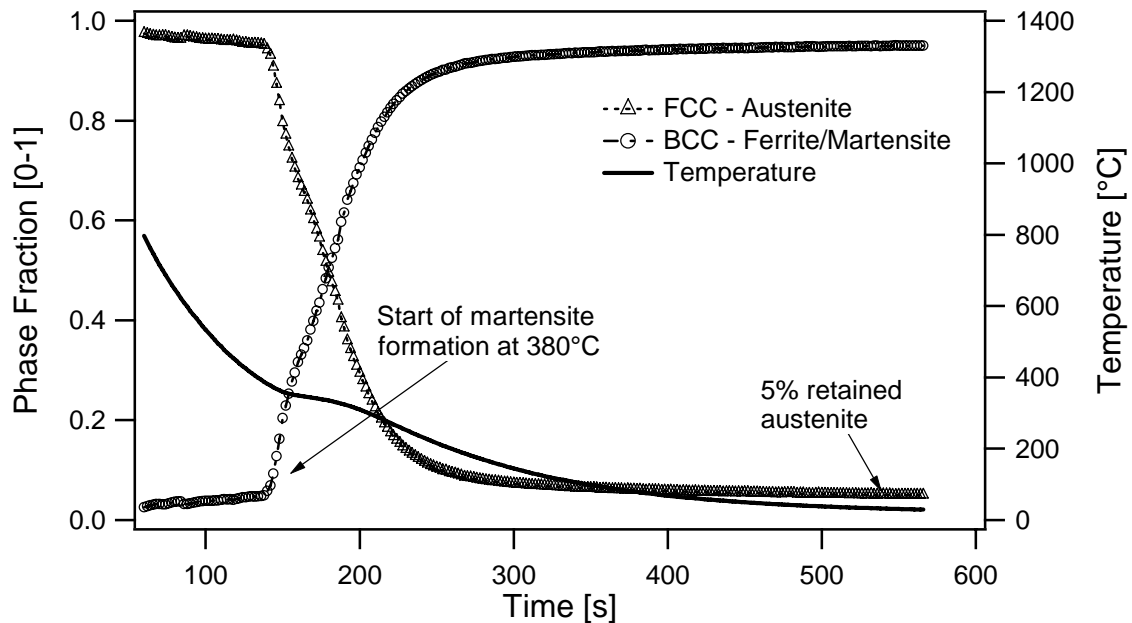


Figure 82: Magnification of the cooling part of Figure 80 showing the start of the martensite transformation at 380°C.

More information on the transformations during heating has been gathered by applying a reduced heating rate of  $10\text{K s}^{-1}$ . By this thermal cycle, completed austenitisation of the material is confirmed.  $A_{C1}$  and  $A_{C3}$  temperature are interpolated to be  $880^\circ\text{C}$  and  $1105^\circ\text{C}$ , respectively. Delta ferrite starts to form at  $1220^\circ\text{C}$  and reaches its maximum of 19% at a temperature of  $1268^\circ\text{C}$ . On cooling, the phase fraction of delta ferrite is reduced to 2%, the same level as observed during the fast weld thermal cycle. Martensite transformation starts at about  $407^\circ\text{C}$  but is not fully completed at room temperature. After completion of the slow thermal cycle, CB2A microstructure consists of martensite with 2% retained delta ferrite and 4% retained austenite. Results of further XRD measurements on material CB2A can be found in Appendix D.

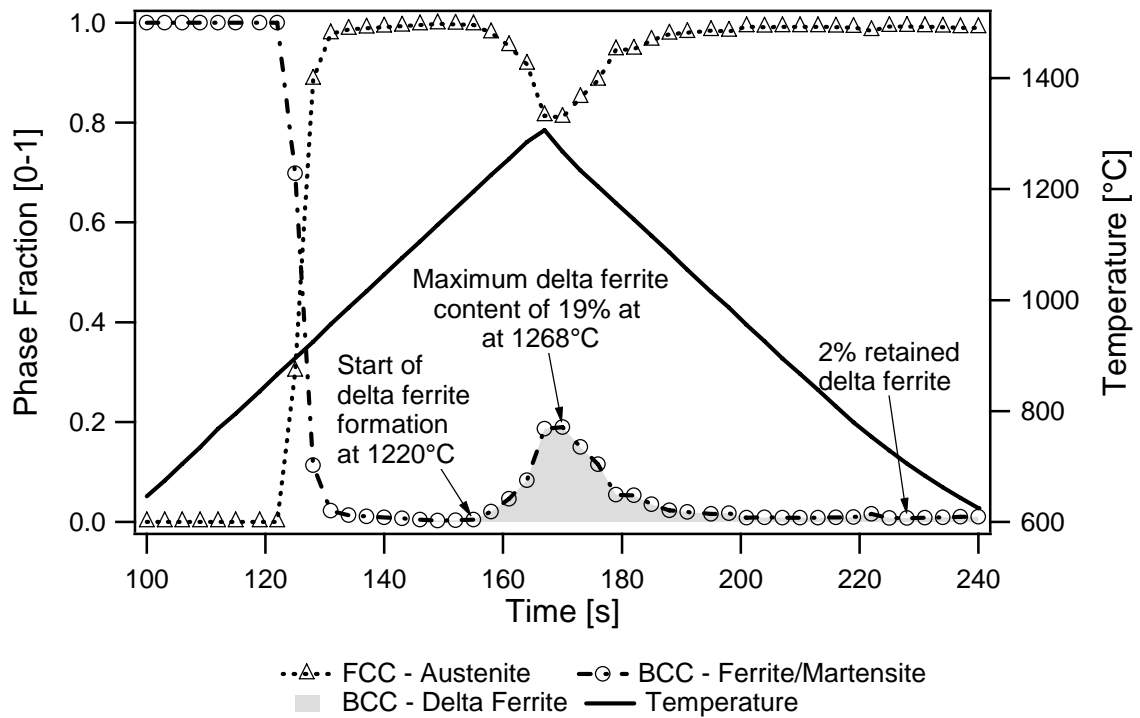


Figure 83: Phase fractions in steel CB2A obtained by in-situ X-ray diffraction during a thermal cycle with a heating rate of  $10\text{K s}^{-1}$ .

### 2.2.2 CB2

For steel grade CB2, a weld thermal cycle with a heating rate of  $100\text{K s}^{-1}$  is evaluated. At a temperature of  $1181^\circ\text{C}$ , 2.5% bcc phase fraction is evaluated. Supported by microstructural examinations, it can be assumed that this phase fraction is newly formed delta ferrite. The maximum content of 34% delta ferrite is reached at  $1275^\circ\text{C}$ . During cooling, 3% delta ferrite is retained within CB2. Martensite formation starts at  $394^\circ\text{C}$ . After completion of the weld thermal cycle, CB2 microstructure consists of martensite with 3% retained delta ferrite and 4% retained austenite (see also Appendix D).

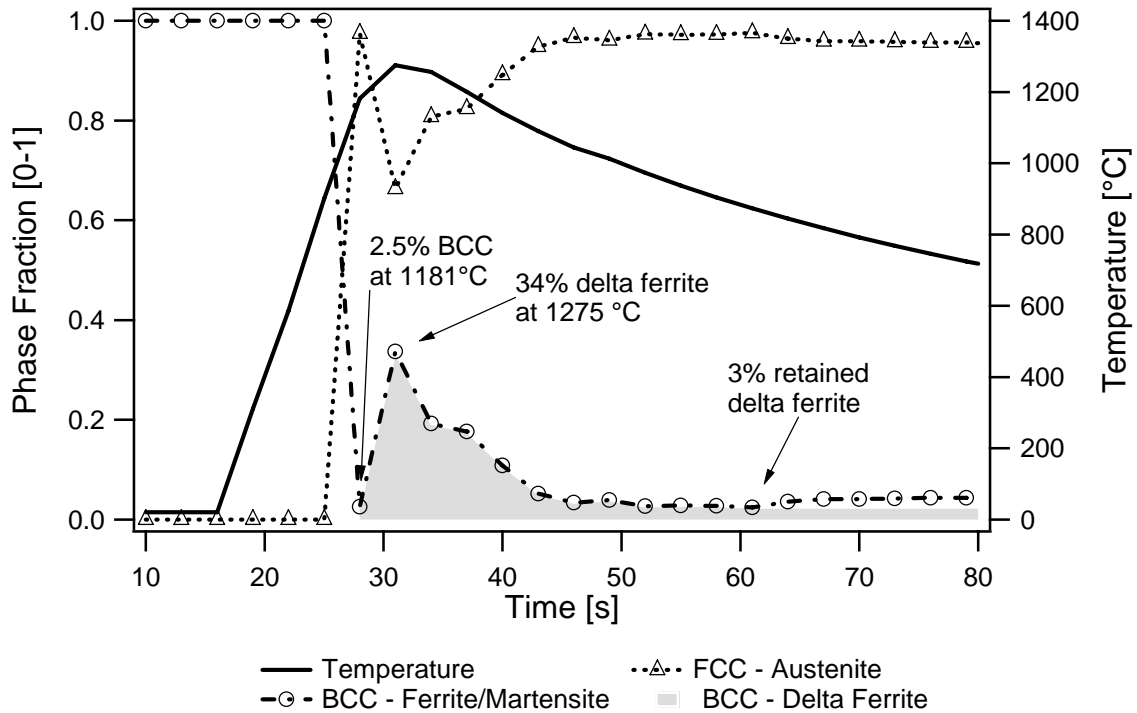


Figure 84: Phase fractions in steel CB2 during a weld thermal cycle applying a heating rate of  $100\text{K s}^{-1}$  obtained by in-situ XRD.

### 2.2.3 NPM1

During HAZ simulation applying a heating rate of  $100\text{K s}^{-1}$  on material NPM1, fully austenitisation is shown. The diffraction pattern recorded at  $1095^\circ\text{C}$  during heating reveals a fully austenitic microstructure. At higher temperatures, delta ferrite starts to form and reaches its maximum amount of 45% at  $1258^\circ\text{C}$  on cooling. Delta ferrite to an extent of 4% is retained within the NPM1 material. Martensite formation starts at  $419^\circ\text{C}$ , but is not completely finished at room temperature. The final microstructure of steel NPM1 after a completed weld thermal cycle consists of martensite with 4% retained delta ferrite and 4% retained austenite.

Quenching the same specimen in liquid nitrogen for 30 seconds and recording a diffraction pattern afterwards shows that the amount of retained austenite did not transform to martensite.

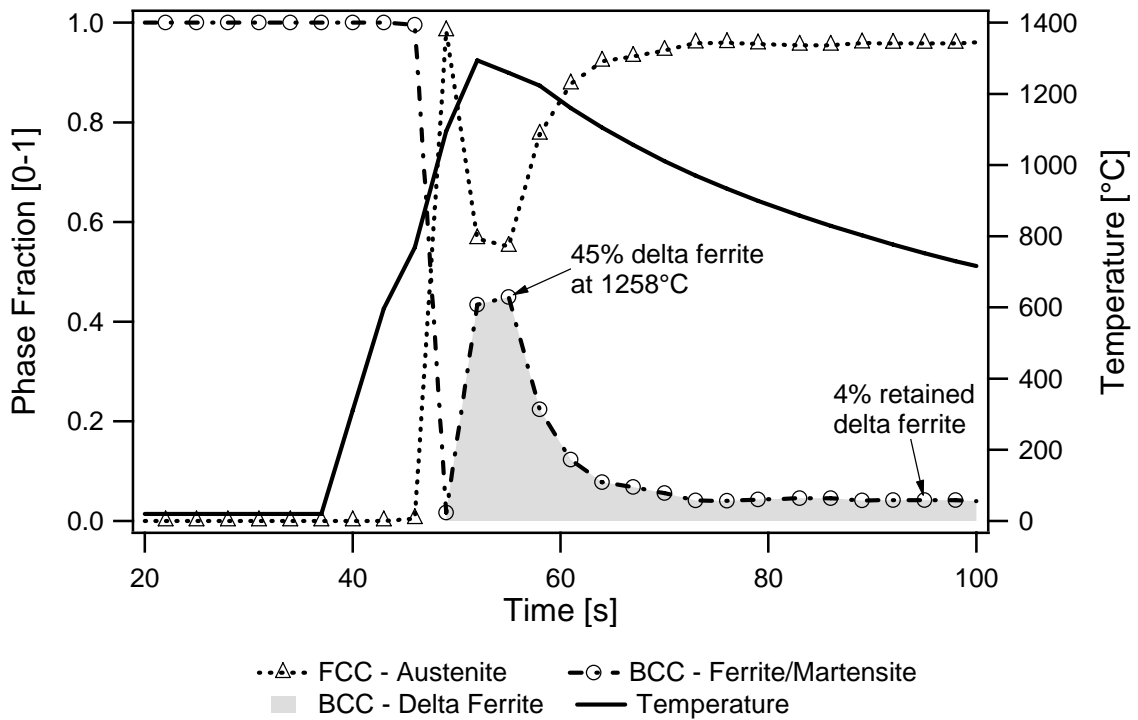


Figure 85: Phase fractions in steel NPM1 during a weld thermal cycle applying a heating rate of  $100\text{K s}^{-1}$  obtained by in-situ XRD.

More information on the transformations during heating could be gathered by applying a reduced heating rate of  $10\text{K s}^{-1}$ .  $A_{C1}$  and  $A_{C3}$  temperature are interpolated to be  $910^\circ\text{C}$  and  $1016^\circ\text{C}$  respectively. Delta ferrite starts to form at  $1220^\circ\text{C}$  and reaches its maximum of 65% at a temperature of  $1294^\circ\text{C}$ . On cooling, the phase fraction of delta ferrite is reduced to 4%, the same level as observed during the fast weld thermal cycle. Martensite formation starts at about  $440^\circ\text{C}$  but is not fully completed at room temperature. After completion of the slow thermal cycle, NPM1 microstructure consists of martensite with 4% retained delta ferrite and 3% retained austenite.

Results of further XRD measurements on material NPM1 can be found in Appendix D.

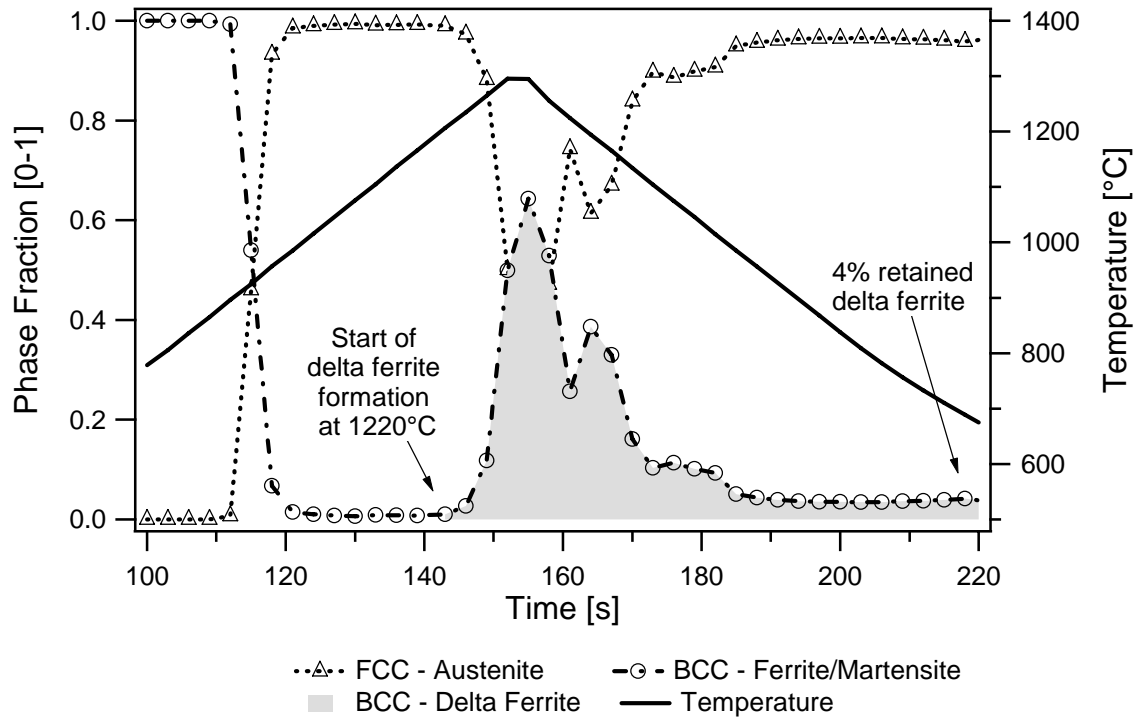


Figure 86: Phase fractions in steel NPM1 obtained by in-situ X-ray diffraction during a thermal cycle with a heating rate of  $10\text{K s}^{-1}$ .

#### 2.2.4 Comparison of XRD measurements

In Table 37, phase transformation temperatures and phase fractions obtained by in-situ X-ray diffraction during thermal cycle simulations are summarised. Figures for all analysed simulations are summarised in Appendix D.

Table 37: Summary of measured phase transformation temperatures and phase fractions from in-situ XRD.

| Specimen  | Heating rate<br>[K s <sup>-1</sup> ] | A <sub>C1</sub><br>[°C] | A <sub>C3</sub><br>[°C] | A <sub>C4</sub><br>[°C] | M <sub>s</sub><br>[°C] | Maximum<br>delta ferrite | Final<br>microstructure                    |
|-----------|--------------------------------------|-------------------------|-------------------------|-------------------------|------------------------|--------------------------|--|
| CB2A (A8) | 100                                  | x                       | x                       | x                       | 390                    | 20%                      | martensite<br>2% δ-ferrite<br>5% austenite |
| CB2A (A1) | 100                                  | x                       | x                       | x                       | 380                    | 31%                      | martensite<br>2% δ-ferrite<br>5% austenite |
| CB2A (A2) | 10                                   | 880                     | 1105                    | 1220                    | 420                    | 19%                      | martensite<br>2% δ-ferrite<br>4% austenite |
| CB2A (A4) | 10                                   | 903                     | 1001                    | 1143                    | 390                    | 29%                      | martensite<br>2% δ-ferrite<br>4% austenite |
| CB2 (C3)  | 100                                  | x                       | x                       | x                       | 394                    | 34%                      | martensite<br>3% δ-ferrite<br>4% austenite |
| NPM1 (N1) | 100                                  | x                       | x                       | x                       | 419                    | 45%                      | martensite<br>4% δ-ferrite<br>4% austenite |
| NPM1 (N7) | 100                                  | x                       | x                       | x                       | 420                    | 58%                      | martensite<br>5% δ-ferrite<br>3% austenite |
| NPM1 (N5) | 10                                   | 896                     | 1016                    | 1220                    | 435                    | 65%                      | martensite<br>4% δ-ferrite<br>3% austenite |

### 2.3 Heat affected zone microstructures

Creep properties of steel are directly coupled with the microstructure. In the heat affected zone, the weld thermal cycle causes the formation of an extremely complex microstructure, which differs from the initial base material microstructure. Physical weld simulation allows the generation of HAZ microstructures by the exact control of the main influencing factors of the thermal cycle, i.e. heating rate, peak temperature and cooling rate. Metallographic investigations and mechanical testing on HAZ microstructures provide insight into the changes during welding. This allows directly correlating microstructure and thermal history.

The formation and retention of delta ferrite as a function of the thermal cycle are studied in detail.

### 2.3.1 CB2A

The presence of delta ferrite during different stages of the simulated welding cycles is studied by optical microscopy of quenched samples. Samples have been quenched at several peak temperatures on heating, as well as at different temperatures on cooling. The applied temperature cycle is equal to the one used for dilatometry and in-situ X-ray diffraction on steel CB2A. By fast quenching of samples, a cooling rate of more than  $100\text{K s}^{-1}$  is realised. It is assumed that, with this heat treatment, the microstructure present at quenching temperature is frozen to a major extent. Only austenite is able to transform to martensite during quenching, but delta ferrite is retained down to room temperature.

The final microstructure after the entire weld thermal cycle is shown in Figure 87. It consists of martensite with approximately 1% retained delta ferrite.

In Figure 88, the complete sequence of micrographs on quenched samples during the heating part of the thermal cycle is shown. The sample quenched at  $1088^\circ\text{C}$  on heating shows no retained delta ferrite, revealing that this temperature is still below the  $A_{C4}$  temperature. On raising the quenching temperature by  $100^\circ\text{C}$  to  $1188^\circ\text{C}$ , the microstructure shows first changes close to the prior austenite grain boundaries. The dark etching response in some areas is attributed to first delta ferrite formation.

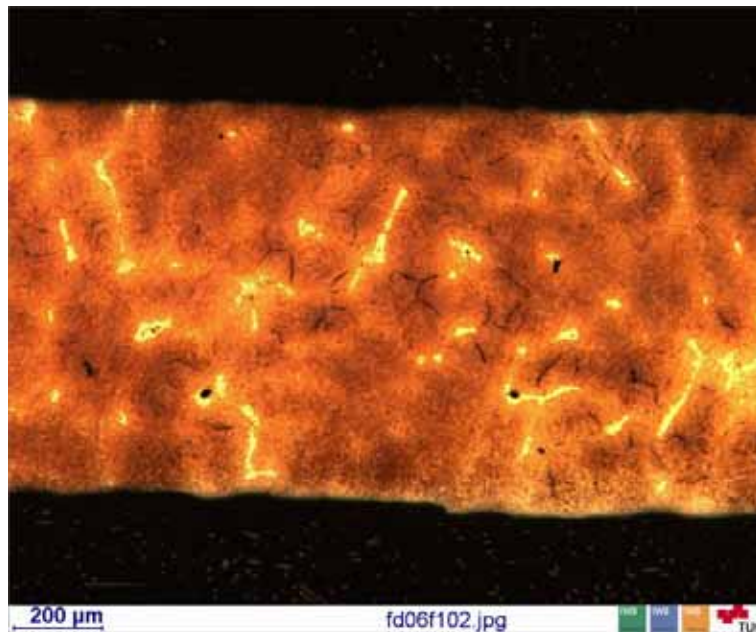


**Figure 87:** Optical micrograph of CB2A microstructure after completed simulated welding cycle.

The specimen quenched at 1279°C already shows a small amount of retained delta ferrite. A further increase in peak temperature to 1300°C only slightly increases the volume fraction of retained delta ferrite. The micrographs obtained on specimens quenched during the cooling part of the thermal cycle are shown in Figure 89.

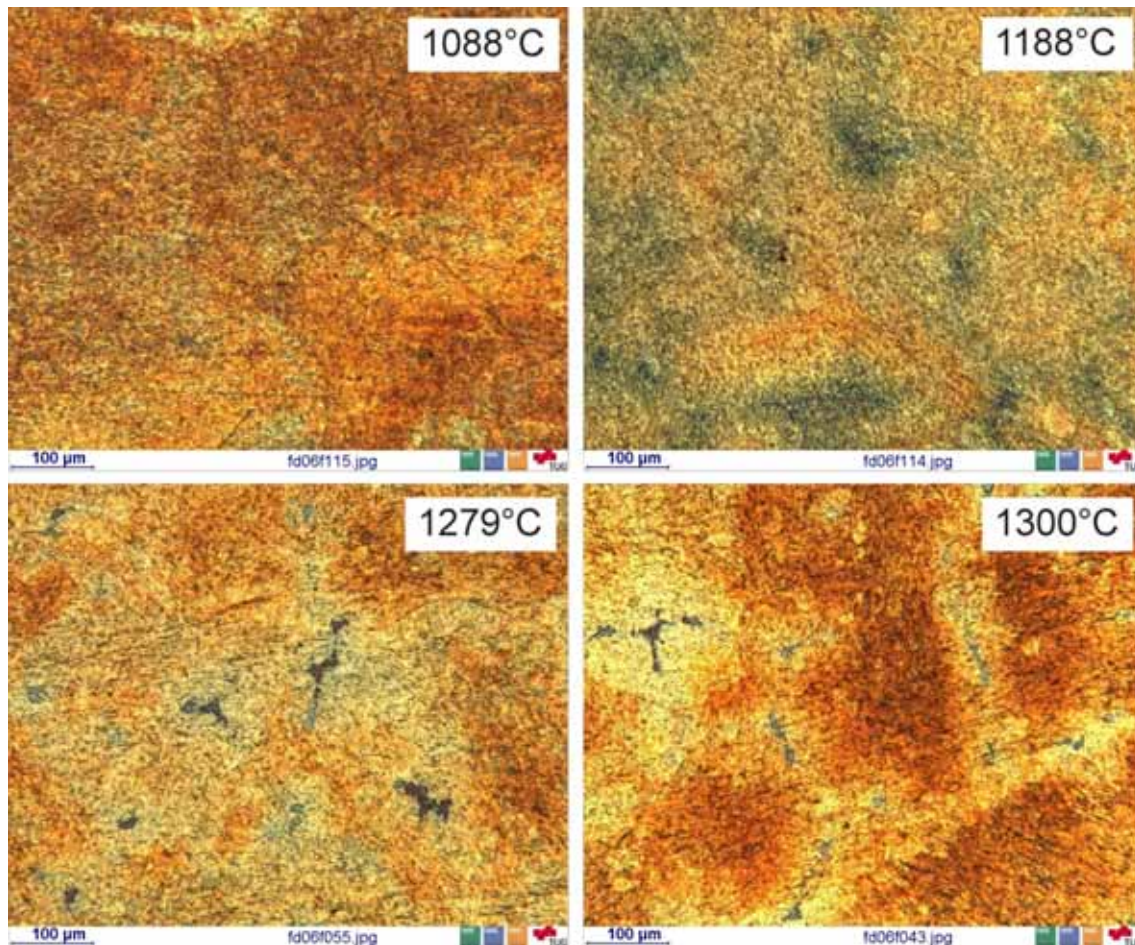


Figure 88: Microstructure of CB2A quenched on heating

The maximum amount of delta ferrite during the simulated welding cycle is reached when quenching the sample on cooling at about 1200°C. Delta ferrite starts to nucleate preferably at the prior austenite grain boundaries and grows until the complete grain boundary is covered. This leads to a meshed structure of retained delta ferrite. From 1200°C on, the content of retained delta ferrite decreases steadily with decreasing quenching temperature. At lower temperatures the meshed structure of retained delta ferrite breaks up into several single lines of delta ferrite along the prior austenite grain boundaries.

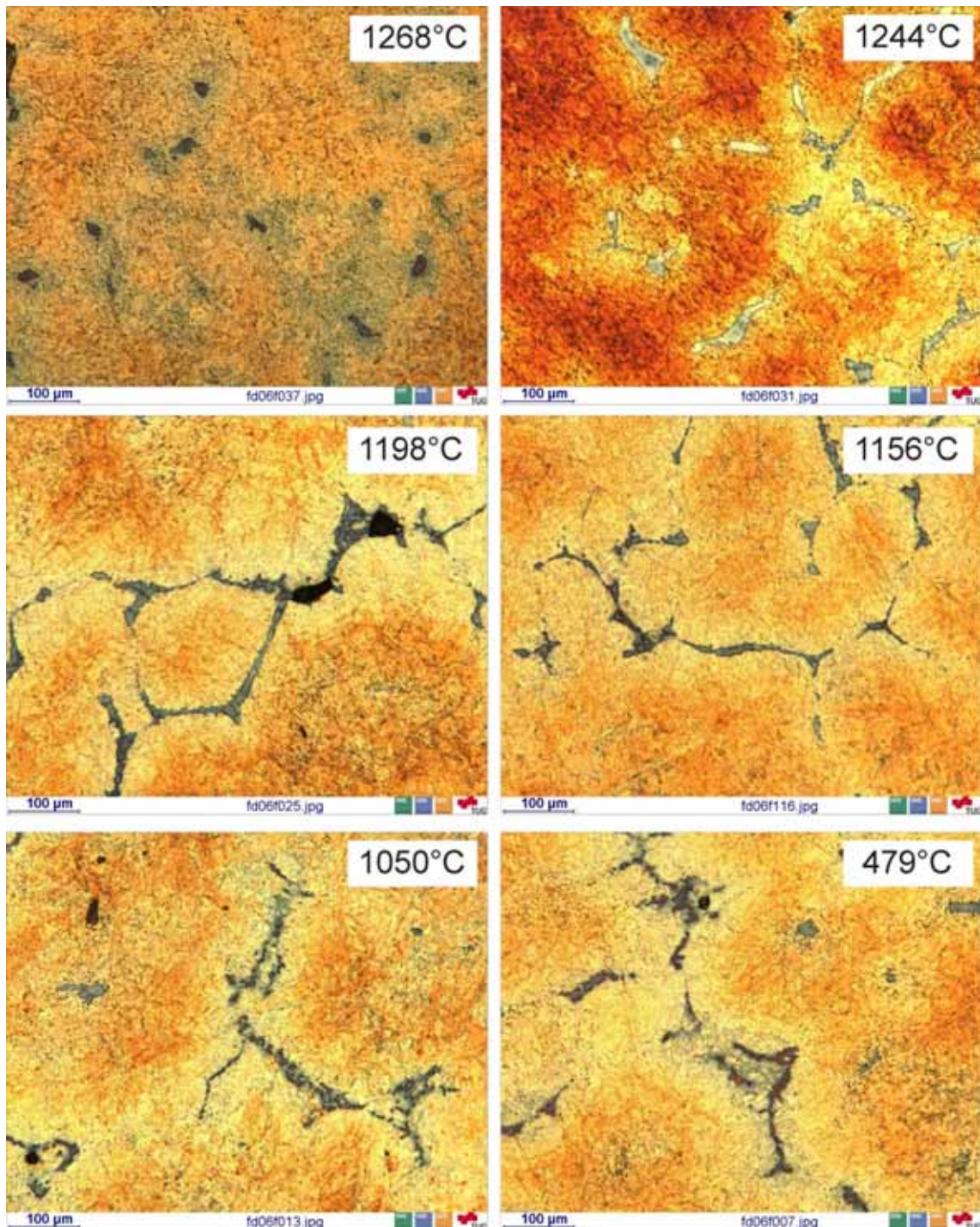


Figure 89: Microstructure of CB2A quenched on cooling.

Results of the quantification of retained delta ferrite using image analysis are shown in Figure 90.

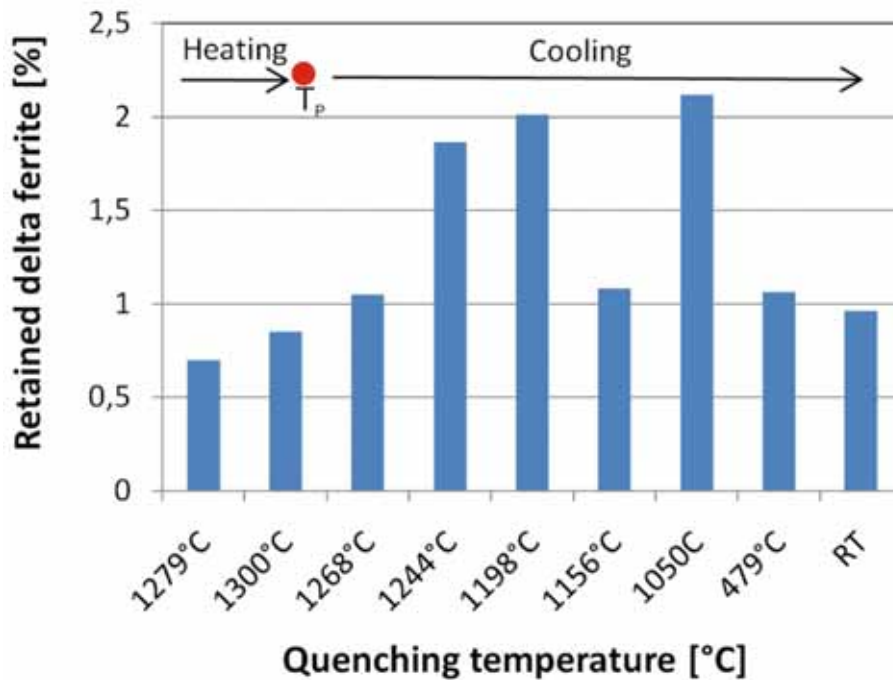


Figure 90: Area fraction of retained delta ferrite as a function of quenching temperature during applied weld thermal cycle.

Figure 91 shows a large grain of delta ferrite surrounded by martensite in CB2A steel after a weld simulation with a peak temperature of 1300°C. In polished and etched condition, the delta ferrite region is characterised by a smooth surface. No lath structure is observed compared to the surrounding martensite. The delta ferrite grain boundary is jagged and of irregular shape. An EDX line scan across the delta ferrite region in CB2A in as-welded condition reveals an enrichment of chromium and molybdenum at the grain boundary (Figure 92).

By SEM, neither precipitates in the delta ferrite nor in the martensite region are identified. By TEM investigation of a sample quenched at a peak temperature of 1300°C, some very small undissolved precipitates are found aligned along a lath boundary (Figure 93). They are identified by EELS as niobium carbides and their size ranges from 7 to 11 nm. After the completed weld thermal cycle, also the fine carbides are dissolved and instead carbon and iron rich precipitates have formed (Figure 94). Because of their small size, it is not possible to clearly identify these precipitates and, therefore, further research on these particles has already started which is outside the scope of this work.

Weld simulated CB2A microstructure after an additional post-weld heat treatment is discussed in Chapter V.2.6.

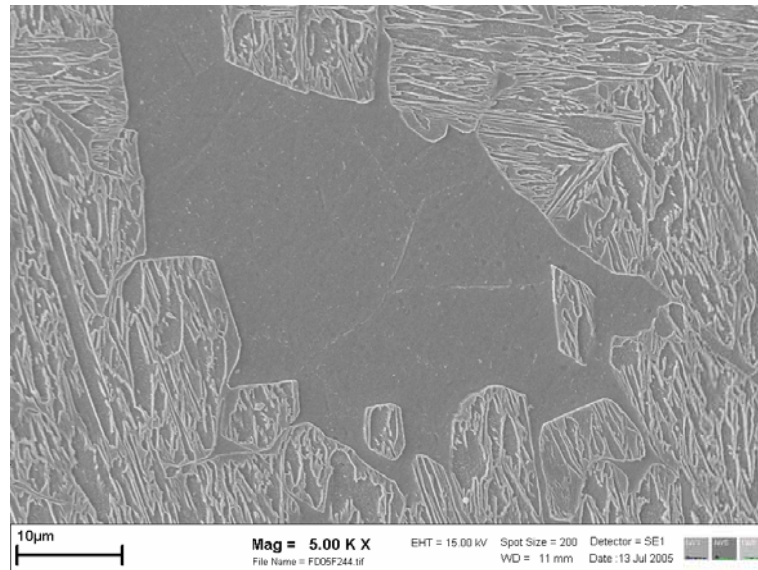


Figure 91: Microstructure of CB2A after weld simulation ( $T_p=1300^\circ\text{C}$ ,  $t_{8/5}=40$  s) showing a delta ferrite grain surrounded by martensitic lath structure.

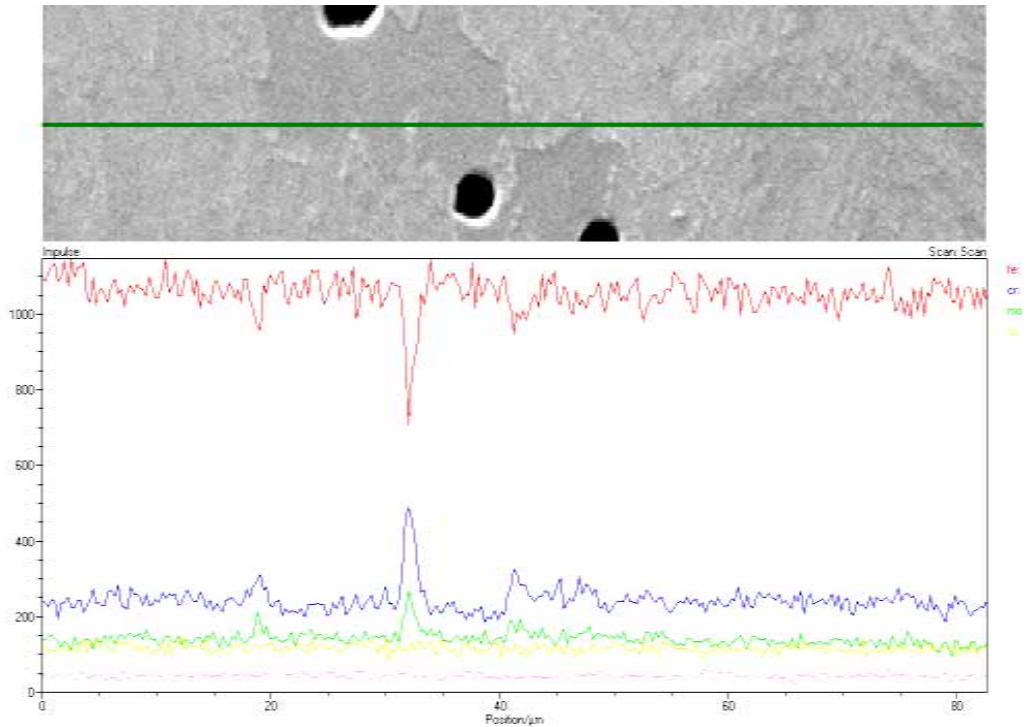


Figure 92: Line scan across a delta ferrite grain after HAZ simulation revealing enrichment in chromium and molybdenum at the grain boundaries.

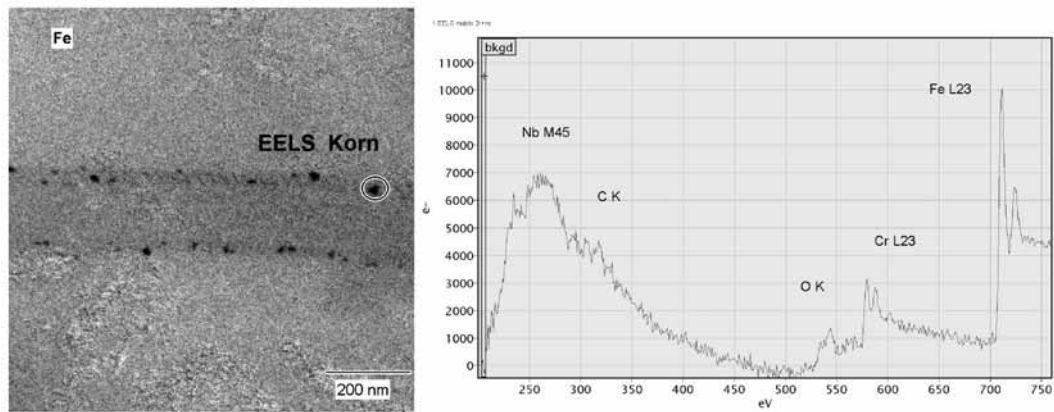


Figure 93: Undissolved particles in CB2A after quenching specimen at 1300°C identified by EELS as niobium carbides

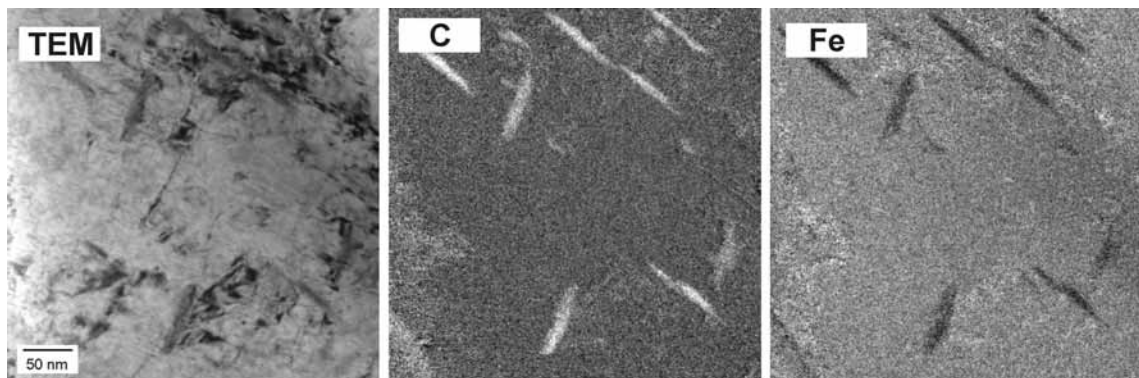


Figure 94: TEM image and EFTEM maps revealing carbon and iron rich precipitates in CB2A steel after a completed weld thermal cycle ( $T_P=1300^\circ\text{C}$ ,  $t_{8/5}=40$  s).

Specimen 11, heated to a peak temperature of 1300°C and held at this temperature for 60 seconds before quenching, reveals a much higher level of retained delta ferrite. Figure 95 shows an optical micrograph of the sample at lower magnification. The area fraction of retained delta ferrite fraction is evaluated by image analysis to be approximately 15%.



Figure 95: Optical micrograph of specimen 11 quenched after heating to 1300°C and holding for 60s revealing about 15% of retained delta ferrite (grey areas) in the microstructure.

### 2.3.2 CB2

#### *Influence of peak temperature*

Three regions of a characteristic heat affected zone of a weld have been simulated by applying three different peak temperatures (see Figure 96). The lowest peak temperature is in between the  $A_{C1}$  and  $A_{C3}$  transformation temperatures. As a result, the microstructure of the inter-critical HAZ consists of newly formed (virgin) martensite and tempered martensite in as-welded condition. Most of the precipitates are not affected by the weld thermal cycle. Therefore, numerous precipitates are still observed along the prior austenite grain and martensite lath boundaries. No delta ferrite is observed in the ICHAZ. Further images of weld-simulated CB2 HAZ simulated microstructures can be found in the Master Thesis of F. Mendez-Martin.<sup>118</sup>

After applying a peak temperature of 1100°C, most of the precipitates are dissolved. The initial tempered martensitic microstructure has fully transformed to virgin martensite. Regions of delta ferrite are visible for the first time. They are placed mainly along prior austenite grain boundaries and between initial martensite laths. As the peak temperature is increased to 1300°C, the microstructure appears to be coarser. Delta ferrite phase fraction increases. The delta ferrite is positioned along prior austenite grain boundaries as well as in between blocks

of martensite. Additionally, some large grains of delta ferrite are observed within the microstructure. No precipitates are found in as-welded condition.

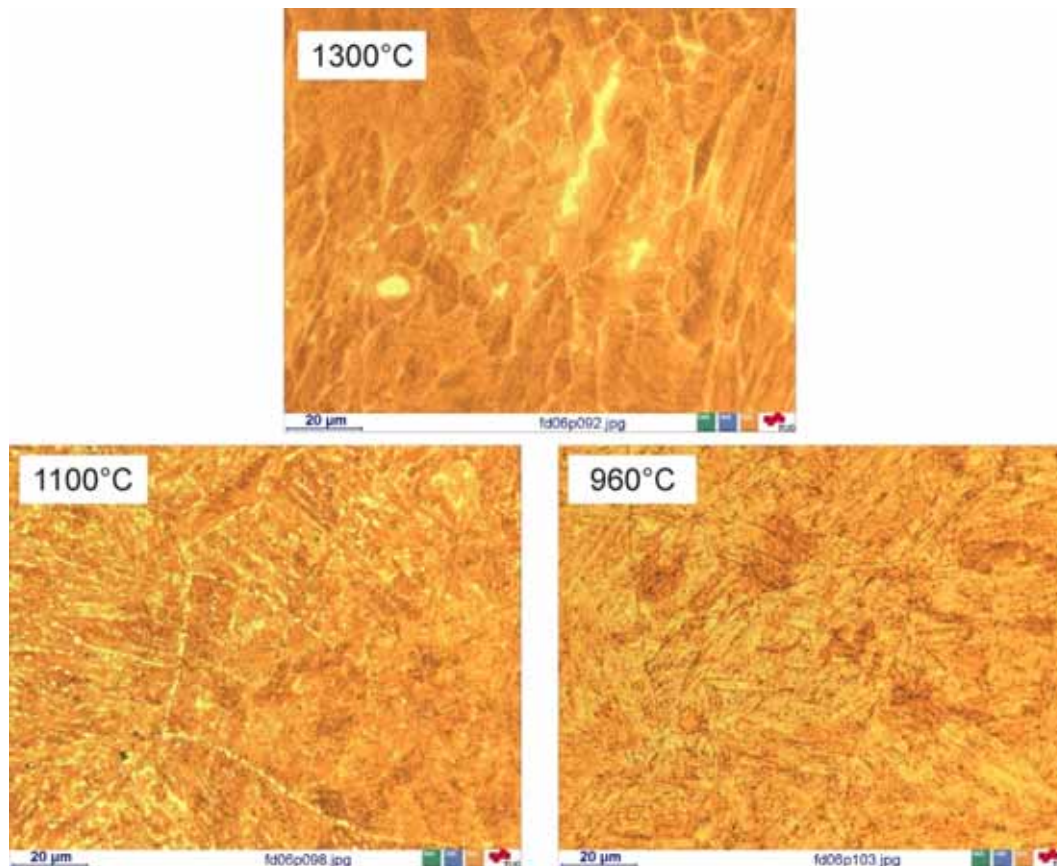


Figure 96: Influence of peak temperature – CB2 as-welded, GTAW(2), 1300°C, 1100°C, 960°C.

#### *Influence of heat input*

The influence of heat input (see Figure 97) on CB2 microstructure in as-welded condition is characterised as follows:

- The higher the heat input, the more the initial cast microstructure disappears.
- With increasing heat input the phase fraction of delta ferrite increases.
- At lower heat inputs, delta ferrite is present as blocks and laths, whereas at higher heat inputs, laths of delta ferrite dominate.
- Martensitic lath width increases with increasing heat input.

### *Influence of a post-weld heat treatment*

The PWHT results in an increase of precipitates in the simulated intercritical HAZ. Precipitates are mainly aligned along prior austenite grain boundaries as well as along martensite laths.

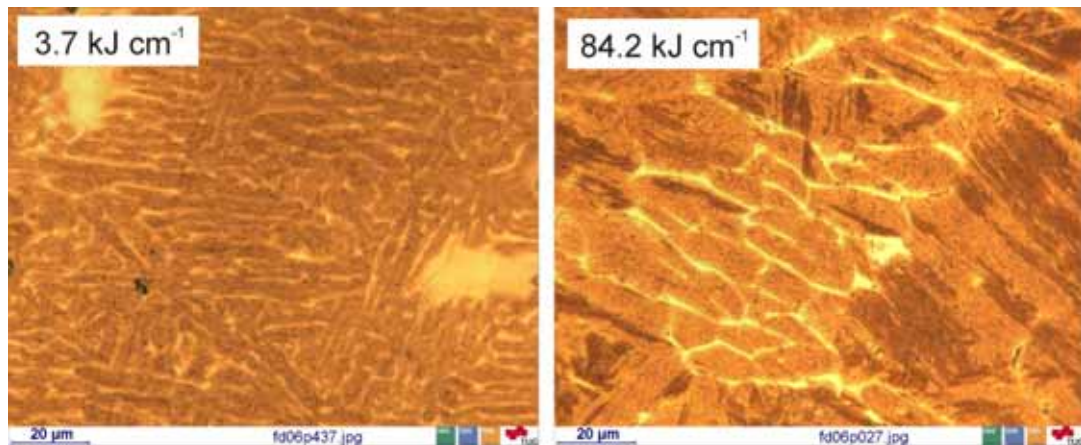


**Figure 97: Influence of heat input on CB2 -  $T_p=1300^\circ\text{C}$  - GTAW(1) (left) and SAW(2) (right) in the „as-welded“ condition.**

After the post-weld heat treatment, re-precipitation takes place in the fine-grained HAZ ( $T_p=1100^\circ\text{C}$ ). Precipitates are positioned along prior austenite and martensite lath boundaries. After post-weld heat treatment, it is difficult to identify delta ferrite regions within the microstructure. Optically, a uniform microstructure prevails.

The post-weld heat treatment of the simulated coarse grained HAZ ( $T_p=1300^\circ\text{C}$ ) also leads to re-precipitation.

Generally, after the post-weld heat treatment the microstructure has a uniform appearance. It consists of tempered martensite with precipitates along the prior austenite grain as well as martensite lath boundaries. Regions of delta ferrite, clearly visible in the as-welded condition, cannot be distinguished from the tempered martensite.

### 2.3.3 NPM1

#### *Influence of single weld thermal cycles*

Optical micrographs of NPM1 microstructures weld-simulated with different peak temperatures are shown in Figure 98. Up to a simulated peak temperature of 925°C, no changes compared to the initial base material microstructure are observed. Between peak temperatures of 950°C and 1000°C a first decrease in the number density of precipitates is visible. After the HAZ simulation with a peak temperature of 1100°C, most of the precipitates are dissolved. Delta ferrite is only visible in the specimen simulated with the highest peak temperature of 1300°C. The shape of delta ferrite is lath-like, positioned in-between packages of martensite.

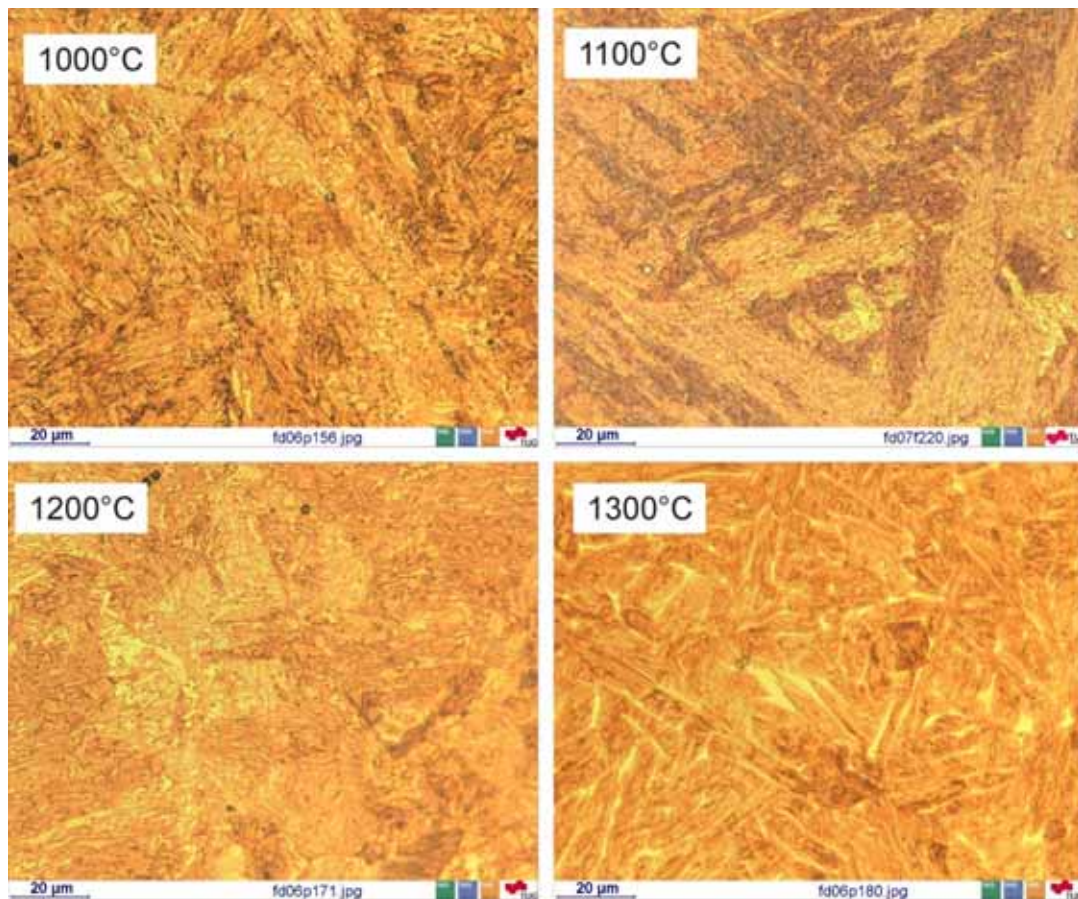


Figure 98: Micrographs of NPM1 steel after HAZ simulation with different peak temperatures in the as-welded condition.

### *Influence of a post-weld heat treatment*

Optical micrographs of the heat treated NPM1 microstructures can be found in Appendix D. Post-weld heat treatment after HAZ simulation with lower peak temperatures results in additional precipitation. For specimens simulated with higher peak temperatures, the post-weld heat treatment results in re-precipitation of dissolved precipitates. Favoured locations for precipitation are prior austenite and martensite lath boundaries.

### *Double weld thermal cycles*

The as-welded microstructure of specimens simulated with a double weld thermal cycle is investigated by light microscopy. Corresponding images can be found in Appendix D. Delta ferrite is only visible after a simulation applying a first peak temperature of 1300°C followed by 1100°C. The delta ferrite is positioned between laths of martensite. The phase fraction of delta ferrite in this sample is lower compared to the specimen simulated with a 1300°C single weld thermal cycle. After simulation with peak temperatures of 1300°C and 950°C there is no evidence of retained delta ferrite in the microstructure.

No precipitates are found in the specimens simulated with a first peak temperature of 1300°C independent of the peak temperature of the second thermal cycle. The specimen simulated with a first peak temperature of 1100°C shows some remaining isolated precipitates. Figure 99 shows the microstructure of double weld-simulated specimens after PWHT.

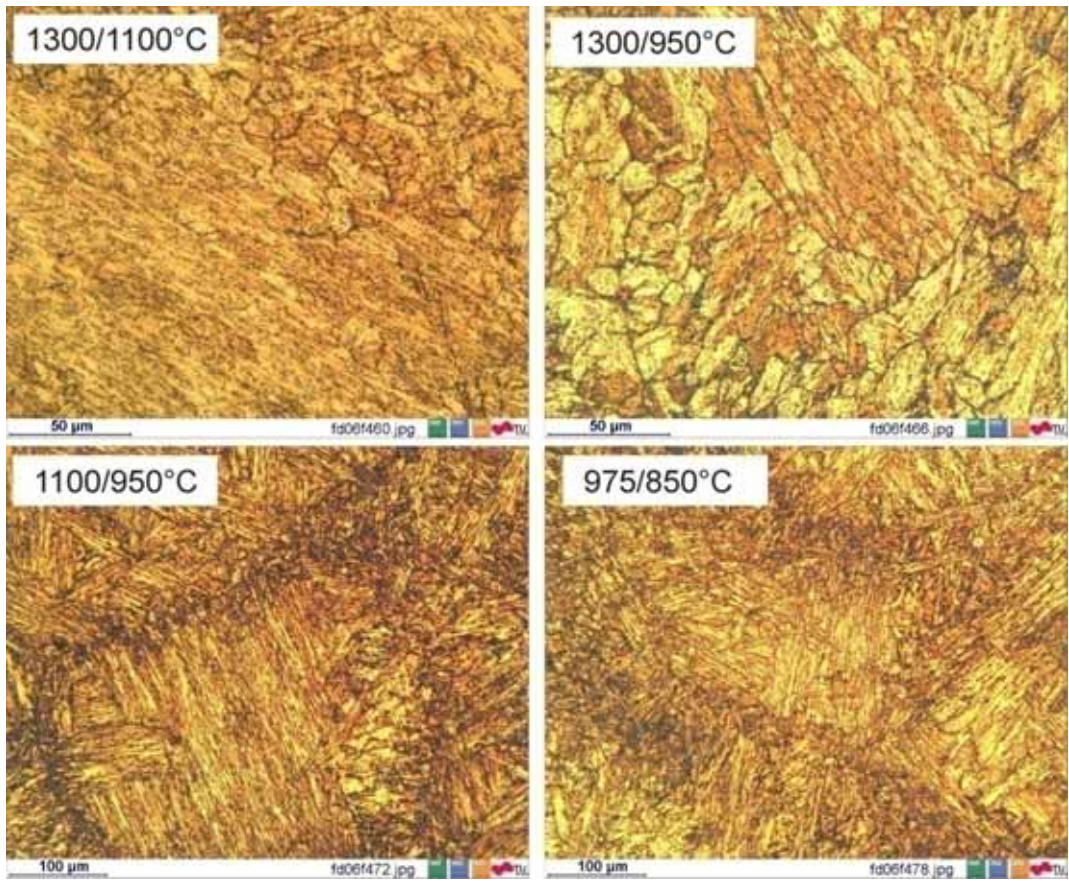


Figure 99: Microstructure of NPM1 steel after double cycle HAZ simulation using different peak temperatures and applying a PWHT.

## 2.4 Grain size evolution in the heat affected zone

The fine-grained region of the heat affected zone is regarded as the weakest part in creep exposed welded constructions. A Japanese steel with low nitrogen content and addition of boron showed no grain refinement in the HAZ. The cross-weld creep strength of this steel is similar to the base material creep strength (see Introduction and Appendix C). Within this chapter, the grain size in the HAZ of the 9Cr-3W-3Co steel, NPM1, with slightly higher addition of nitrogen is compared to the European cast steel variant CB2. The influence of an increased nitrogen addition on the suppression of a fine-grained zone in NPM1 is studied. Prior austenite grain size after HAZ simulation with different peak temperatures is analysed by optical microscopy.

### 2.4.1 CB2

After HAZ simulation with a peak temperature of 1100°C, the cast steel CB2 shows a complete refinement of its microstructure (see Figure 100), no matter which heat input has been simulated. The average diameter of grains is between 10 to 20 µm. Increasing the peak temperature to 1300°C results in significant coarsening of the prior austenite grains. A bimodal grain size distribution characterised by large grains up to a millimetre in diameter as well as some remaining small grains is observed.

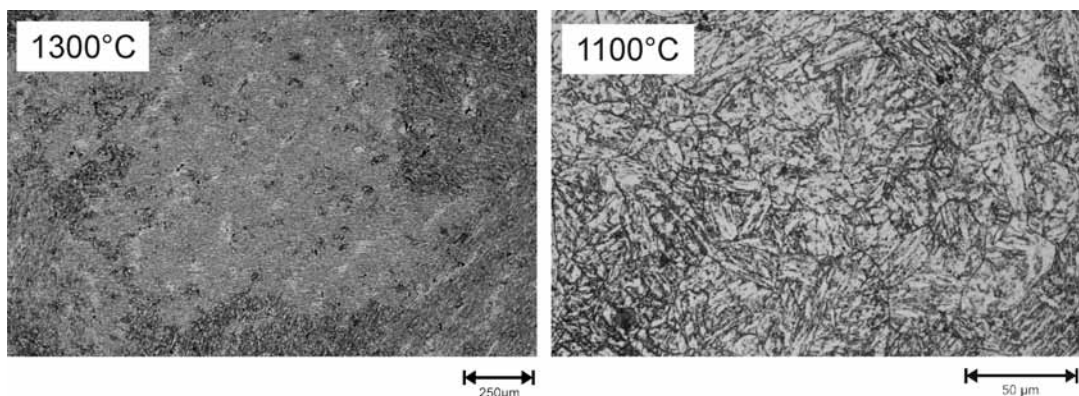


Figure 100: CB2 microstructure after SMAW simulation. Coarse grained microstructure  $T_P=1300^\circ\text{C}$  (left) and fine grained microstructure  $T_P=1100^\circ\text{C}$  (right)

### 2.4.2 NPM1

NPM1 microstructure after HAZ simulation is different to the one observed in CB2. Whereas in CB2, after simulation with a peak temperature of 1100°C, a fully refined micro-

structure is present, NPM1 shows the same prior austenite grain size as before simulation. Figure 101 shows micrographs of the same location in a specimen in the as-received condition (top) and after HAZ simulation applying a peak temperature of 1100°C (bottom). The prior austenite grain boundary is preserved throughout the weld thermal cycle. At the same time, close to the grain boundary, some small grains are newly formed (Figure 102). Especially in the interior of the large grains, similar martensitic structure is clearly visible before and after simulation. Even the orientation of the martensitic laths after HAZ simulation is still the same as observed in the base material.

Increasing the peak temperature of the HAZ simulation to 1200°C increases the refinement of the microstructure close to the prior austenite grain boundaries of the initial microstructure (Figure 103). Retained homogeneous martensitic lath packages in the grain interior become smaller. They still show the same macroscopic orientation as observed before weld simulation (Figure 104).

Even after simulation with a peak temperature of 1300°C some remaining homogeneous martensitic lath packages are visible in the grain interior. The initial prior austenite grain boundaries observed in the base material are blurred by numerous newly formed grains and not visible any longer (Figure 105).

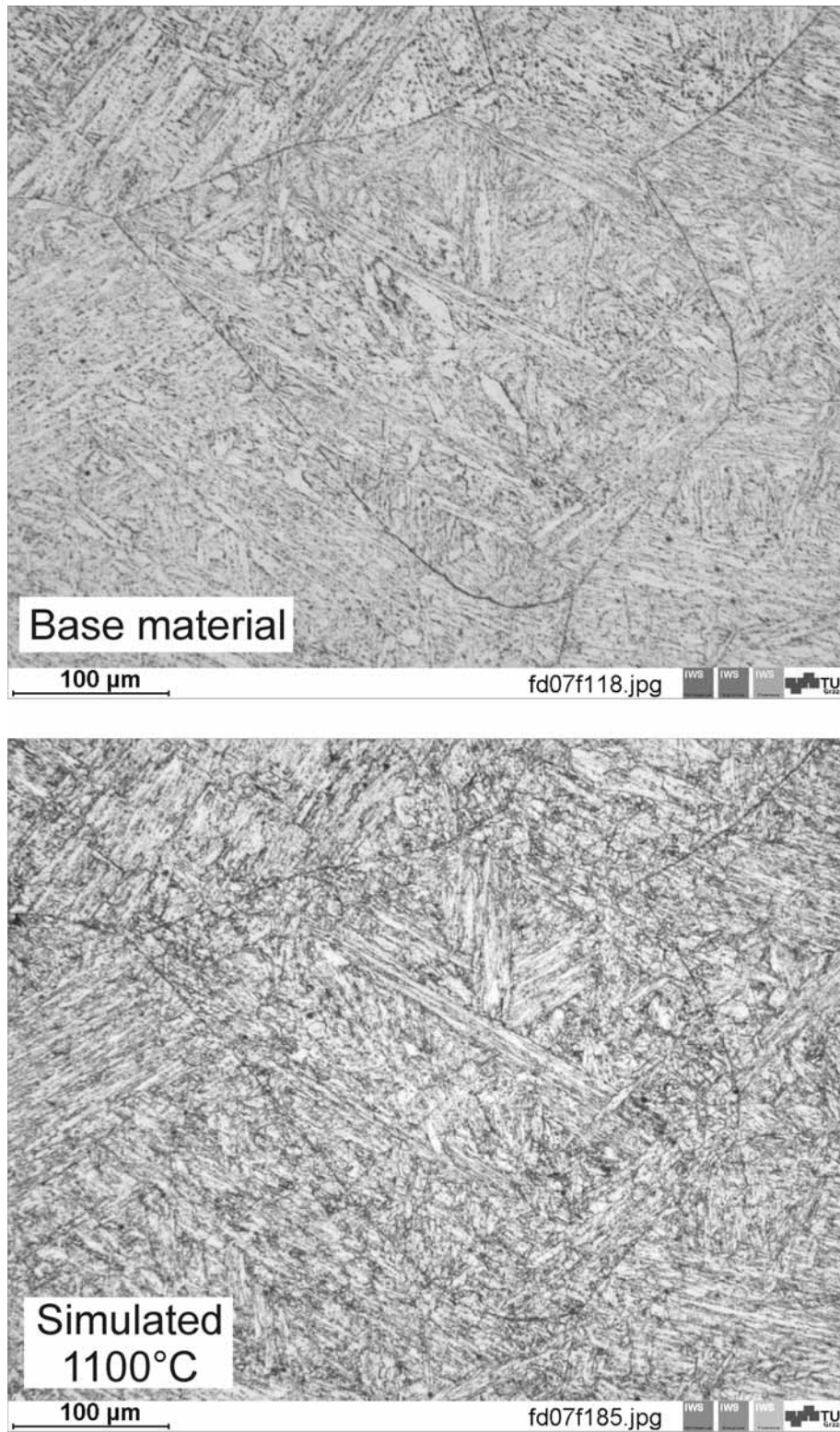


Figure 101: Preserved prior austenitic grain structure in NPM1 after Gleeble HAZ simulation applying a peak temperature of 1100°C.

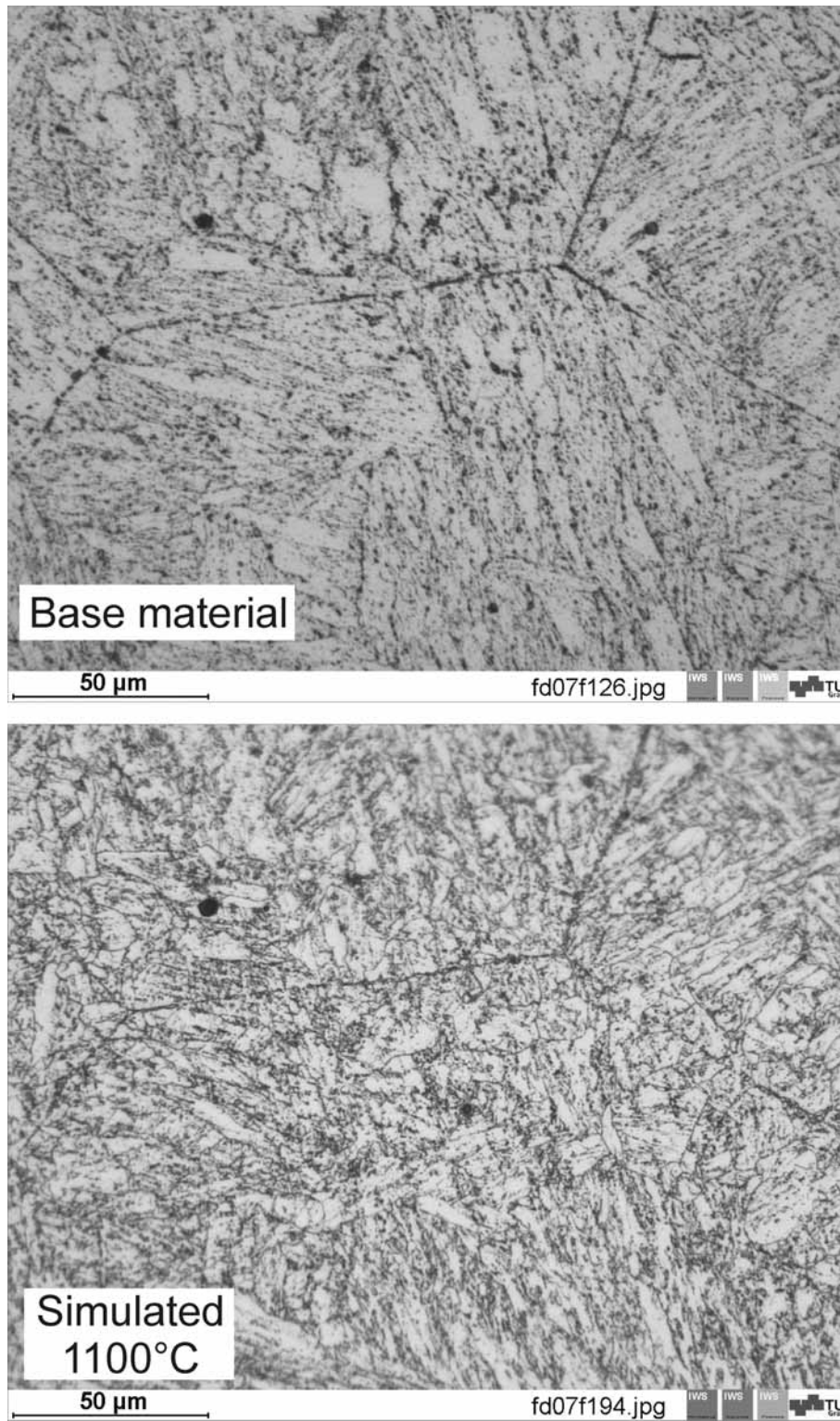


Figure 102: Preserved prior austenite grain boundary of the NPM1 base material with aligned newly nucleated fine grains.

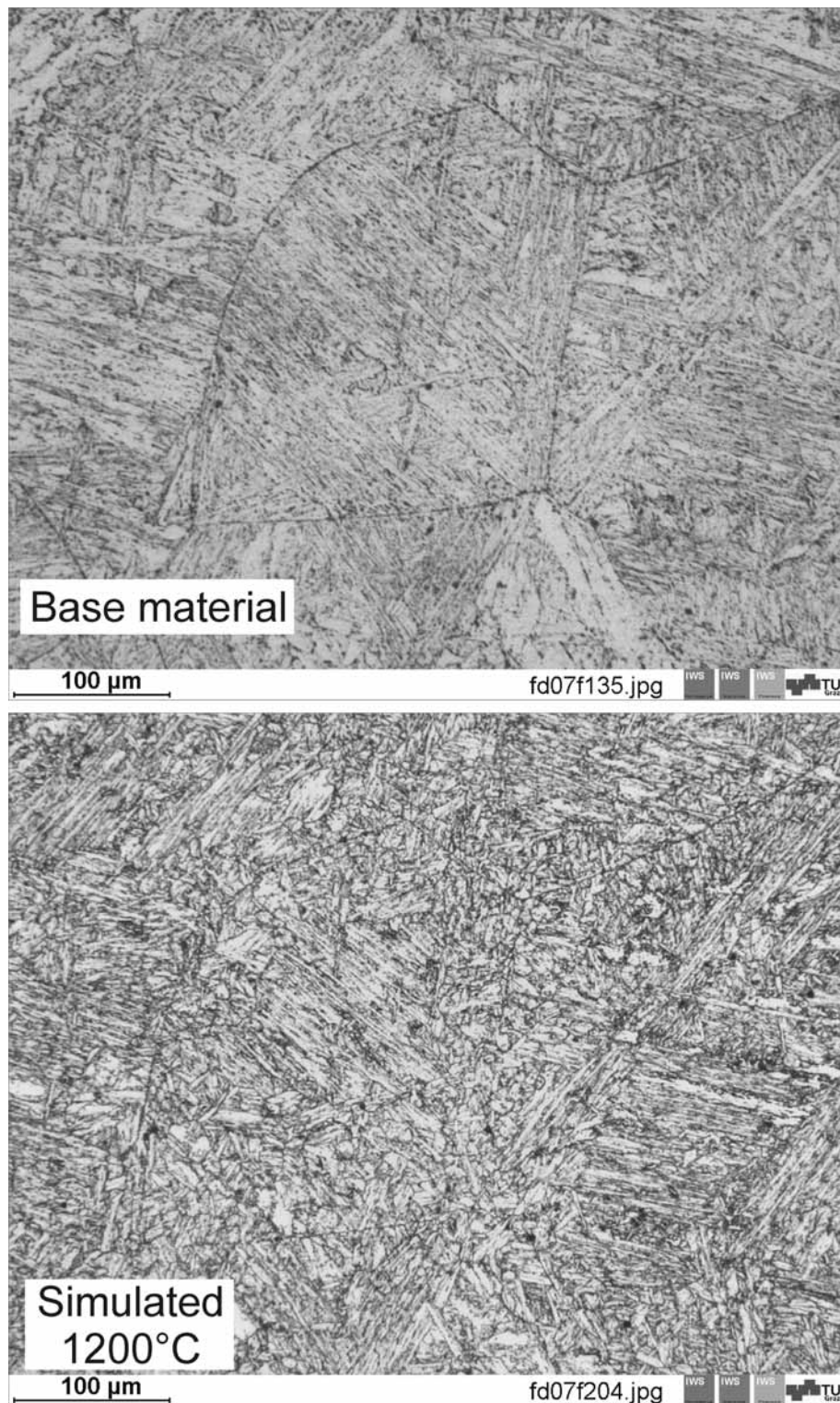


Figure 103: Preserved prior austenitic grain structure in NPM1 after Gleeble HAZ simulation applying a peak temperature of 1200°C.

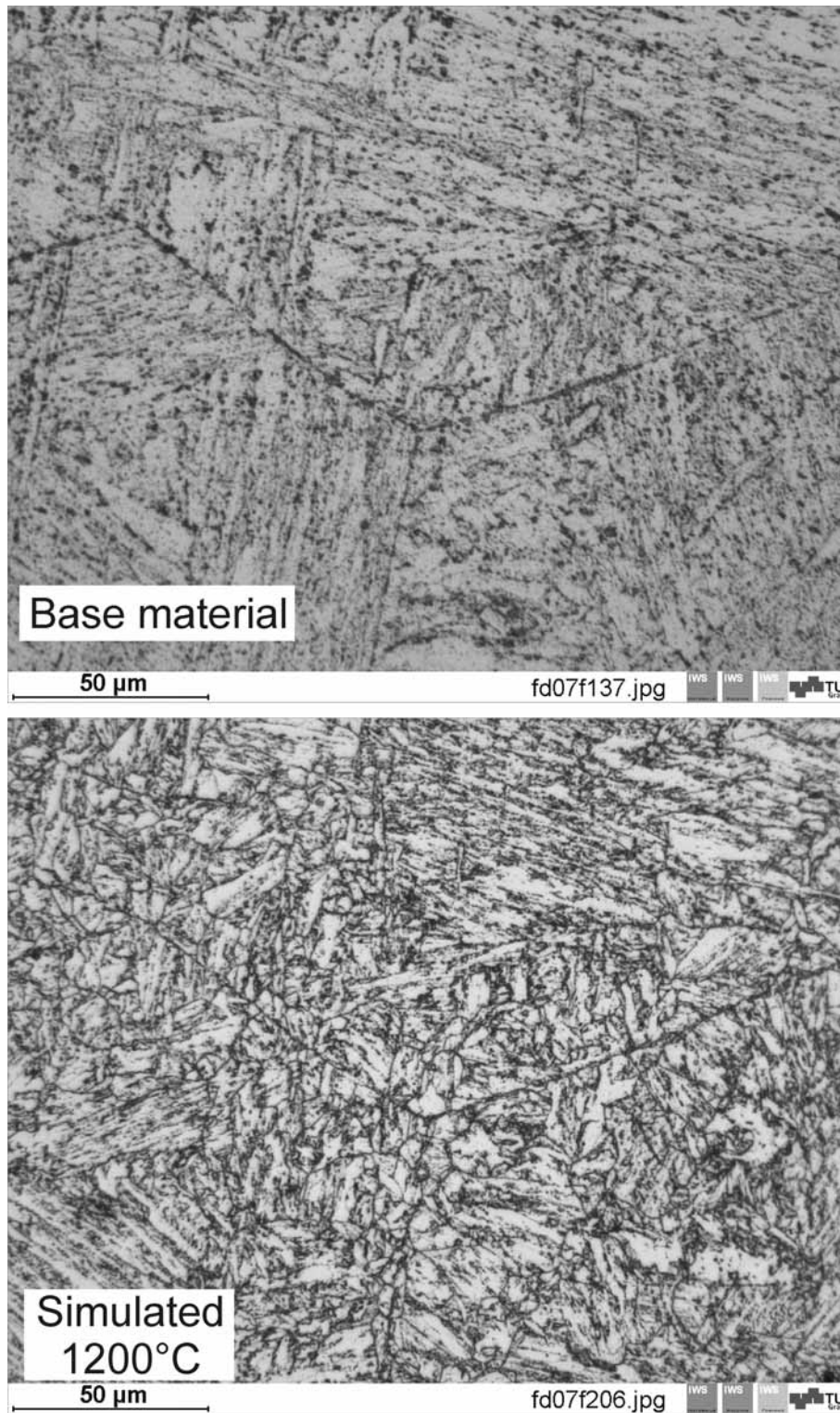


Figure 104: Detail of prior austenite grain boundary in NPM1 steel before (top) and after HAZ simulation applying a peak temperature of 1200°C.

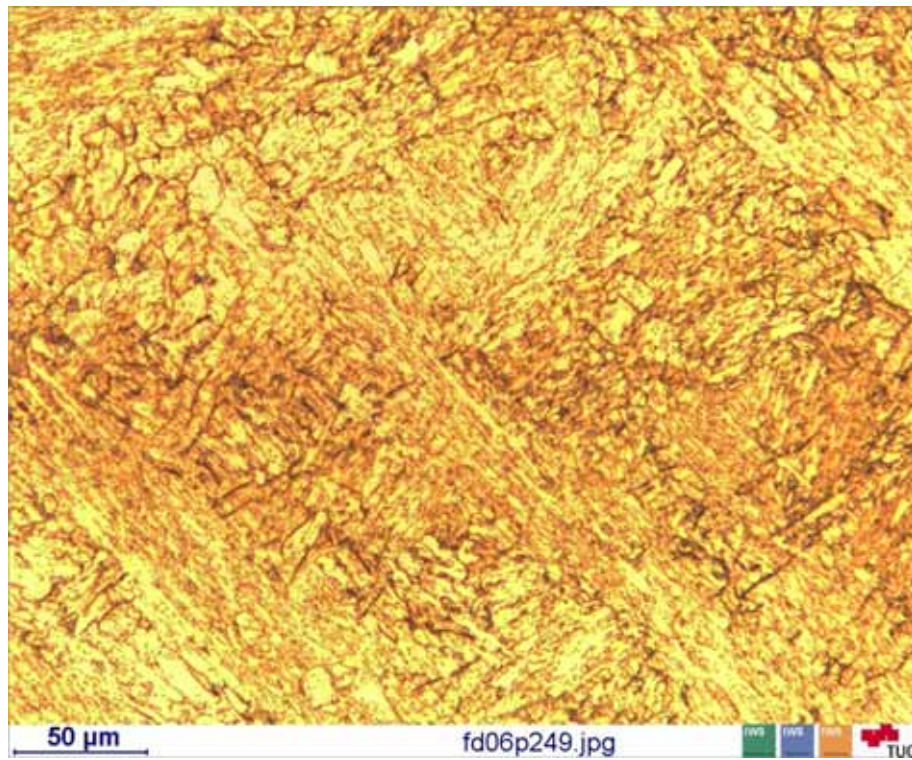


Figure 105: Optical micrograph of NPM1 steel after HAZ simulation applying a peak temperature of 1300°C and subsequent PWHT.

## 2.5 Hardness of heat affected zone microstructures

The micro hardness of matrix phases in the three HAZ simulated steels is compared. Macro hardness on weld simulated and heat treated microstructures are performed to detect possible soft-zones within the heat affected zone.

### 2.5.1 CB2A

After HAZ simulation, the microstructure of CB2A consists of newly formed martensite and areas of retained delta ferrite. Micro hardness of the virgin martensite is around 360 HV0.01 and the retained delta ferrite exhibits a much lower hardness below 200 HV0.01 (Figure 106).



**Figure 106: Micro hardness measurements of weld simulated CB2A microstructure ( $T_P=1300^{\circ}\text{C}$ ,  $t_{8/5}=40$  s) in the as-welded condition.**

### 2.5.2 CB2

Similar results are obtained for steel grade CB2. Micro hardness of virgin martensite is above 400 HV0.01 whereas delta ferrite regions exhibit a hardness of 200 HV0.01 or even below (Figure 107). The intercritical HAZ consist of tempered and virgin martensite. Therefore, the hardness ranges from 227 HV0.01 to above 400 HV0.01. For the delta ferrite re-

gions, post-weld heat treatment leads to a slight increase of the hardness to approximately 250 HV0.01. PWHT softens the martensitic microstructure to 250 HV0.01.

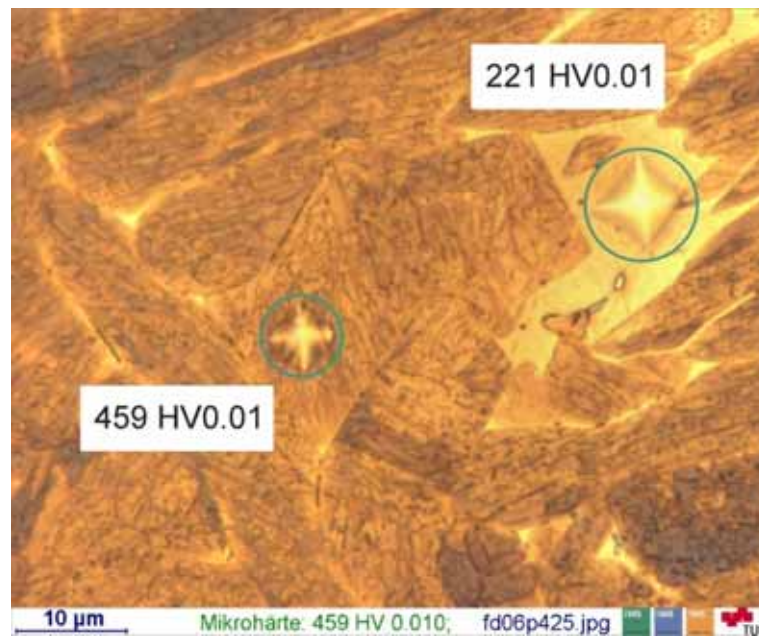


Figure 107: CB2 SMAW  $T_p=1300^\circ\text{C}$ , as-welded.

Figure 108 shows the macro hardness as a function of the applied peak temperature for all simulated microstructures of CB2 material in the as-welded condition.

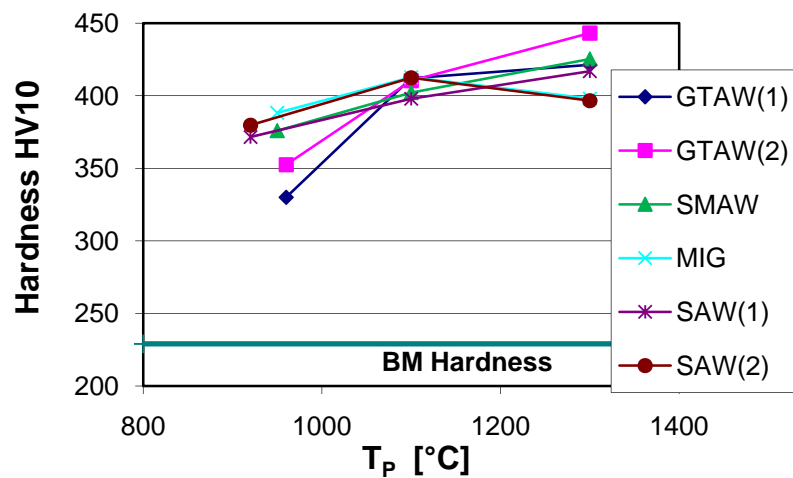


Figure 108: Hardness as a function of simulated peak temperature in as-welded condition for steel CB2.

Figure 109 shows the macro hardness of weld simulated CB2 microstructures after a post-weld heat treatment of 24 hours at 730°C. The hardness of the simulated coarse-grained and fine-grained microstructures is reduced significantly. Hardness produced by the intercritical thermal cycle is reduced by the PWHT to values below the hardness level of the base material of 229 HV10.

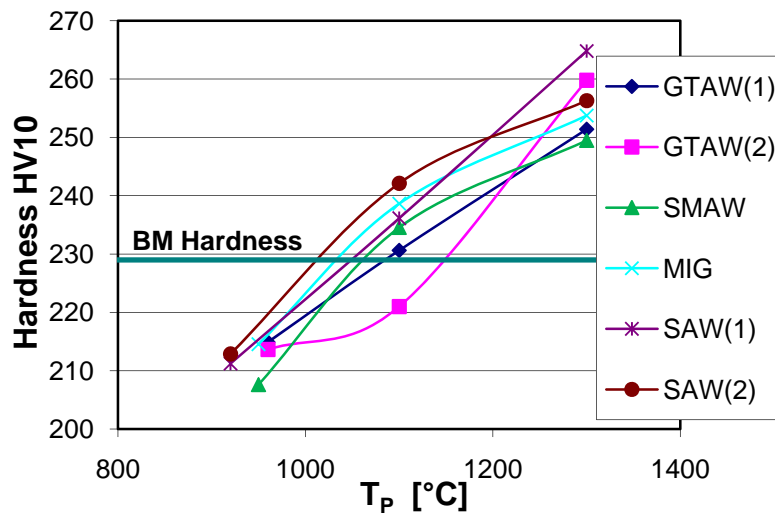


Figure 109: Hardness as a function of simulated peak temperature after PWHT for material CB2.

### 2.5.3 NPM1

Regions of retained delta ferrite in NPM1 steel in the as-welded condition exhibit a micro hardness of approximately 250 HV0.01. The hardness of the newly formed martensite is well above 400 HV0.01. A post-weld heat treatment at 740°C for 4 hours leaves the hardness of the delta ferrite regions unchanged whereas the martensite hardness is reduced to approximately 300 HV0.01.

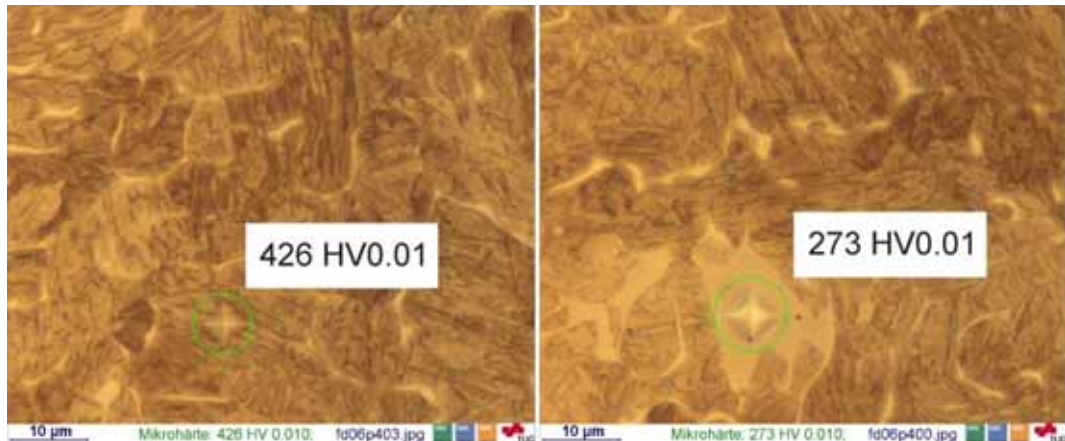


Figure 110: Micro hardness of NPM1  $T_p=1300^\circ\text{C}$ , as-welded.

Macro hardness of HAZ simulated NPM1 material as a function of the peak temperature is shown in Figure 111. Highest hardness of 400 HV10 in the as-welded condition is observed after simulation with a peak temperature of  $1100^\circ\text{C}$ . Applying higher peak temperatures results in a decrease in hardness values. Weld thermal cycles with a peak temperature below  $900^\circ\text{C}$  result in a hardness slightly below the base material hardness of 238 HV10.

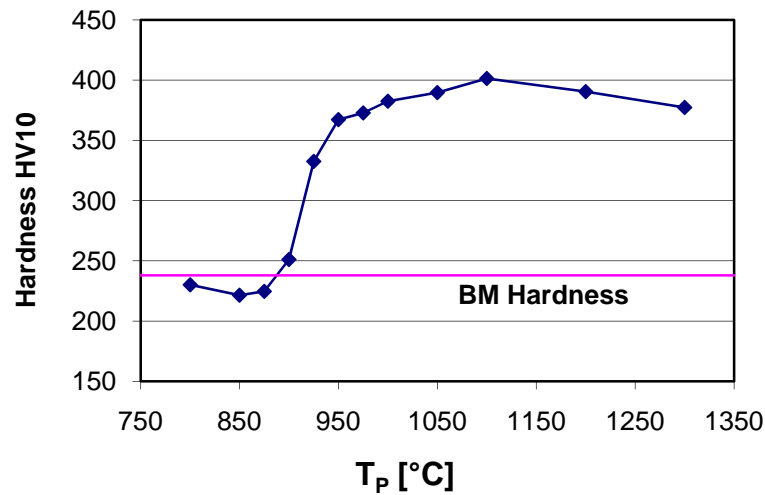


Figure 111: Hardness as a function of simulated peak temperature in as-welded condition for material NPM1.

A post-weld heat treatment at 740°C for 4 hours reduces the hardness significantly. The maximum hardness of 260 HV10 is measured for the microstructure produced by the 1200°C thermal cycle.

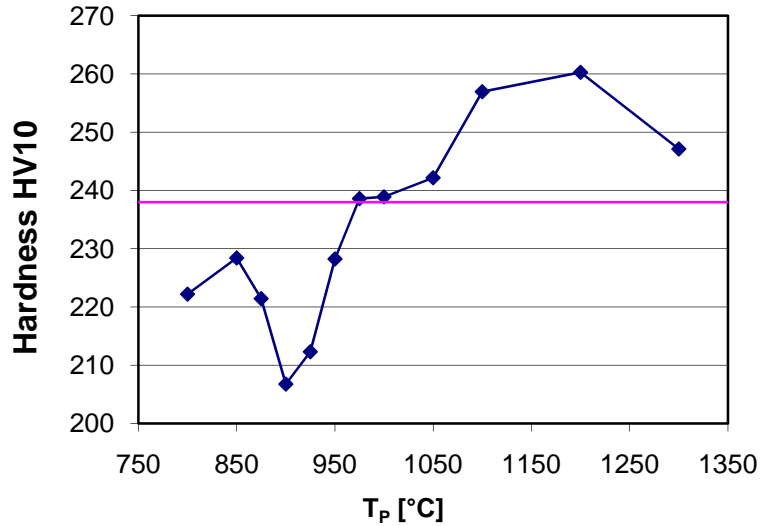


Figure 112: Hardness as a function of simulated peak temperature after PWHT - NPM1.

During PWHT, a pronounced softening of microstructures simulated with peak temperatures close to 900°C takes place. The hardness values are about 30 HV10 lower compared to the level of the base material.

Macro hardness values for the specimens after a double weld thermal cycle simulation before and after PWHT are given in Table 38.

Table 38: Hardness NPM1 – double weld thermal cycle simulation.

| Peak temperatures | as-welded<br>[HV10] | after PWHT<br>[HV10] |
|-------------------|---------------------|----------------------|
| 1300°C/1100°C     | 426                 | 251                  |
| 1300°C/950°C      | 336                 | 266                  |
| 1100°C/950°C      | 405                 | 238                  |
| 975°C/850°C       | 305                 | 229                  |

## 2.6 Behaviour of retained delta ferrite in the heat affected zone

It has been shown that the microstructure after HAZ simulation can contain a significant level of retained delta ferrite. The behaviour of retained delta ferrite in CB2A material during a PWHT is studied in more detail. Optical micrographs of the same locations show that the shape of the retained delta ferrite regions does not change during PWHT (Figure 113). Delta ferrite regions have the same shape after PWHT compared to the as-welded condition, no matter if they are lath-like or bulky. Optical micrographs reveal strong precipitation especially along the delta ferrite and martensite grain boundaries. A TEM sample of a phase boundary region of weld simulated and heat treated CB2A microstructure has been extracted by FIB technology (position is shown in Figure 113 – left - bottom).

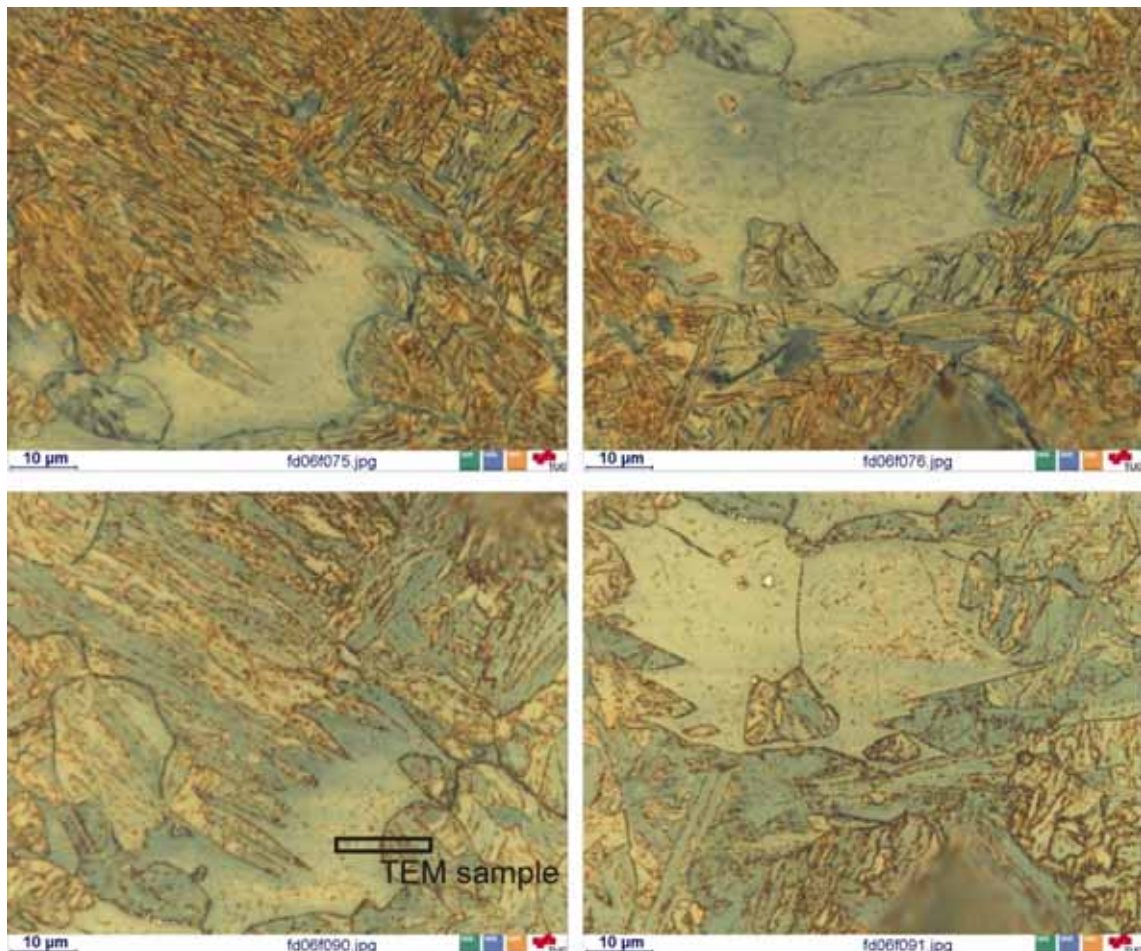


Figure 113: Delta ferrite in steel CB2A after weld simulation with  $T_P=1300^\circ\text{C}$ ,  $t_{8/5}=40$  s (top) and after subsequent PWHT of  $730^\circ\text{C}$  for 12 hours (bottom).

By TEM investigation, it is possible to clearly distinguish between delta ferrite and martensite regions. Delta ferrite appears as a homogeneous bright area within the specimen (Figure 114). At higher magnification, single strings of dislocations are visible within the delta ferrite. The number of dislocations in the delta ferrite is lower compared to the martensite. Therefore, the martensite appears in a diffuse grey structure and single strings of dislocations cannot be identified. Figure 115 shows a finger-like region of delta ferrite surrounded by martensite. Numerous precipitates encircle the delta ferrite region. By an EDX mapping of the image area, the precipitates are identified as chromium rich particles. An analysis of the particles at higher magnification shows that they are also rich in molybdenum and that they are flanked by small vanadium rich particles. It is presumed that the large particles rich in chromium are chromium carbides and the small vanadium rich particles are MX precipitates.

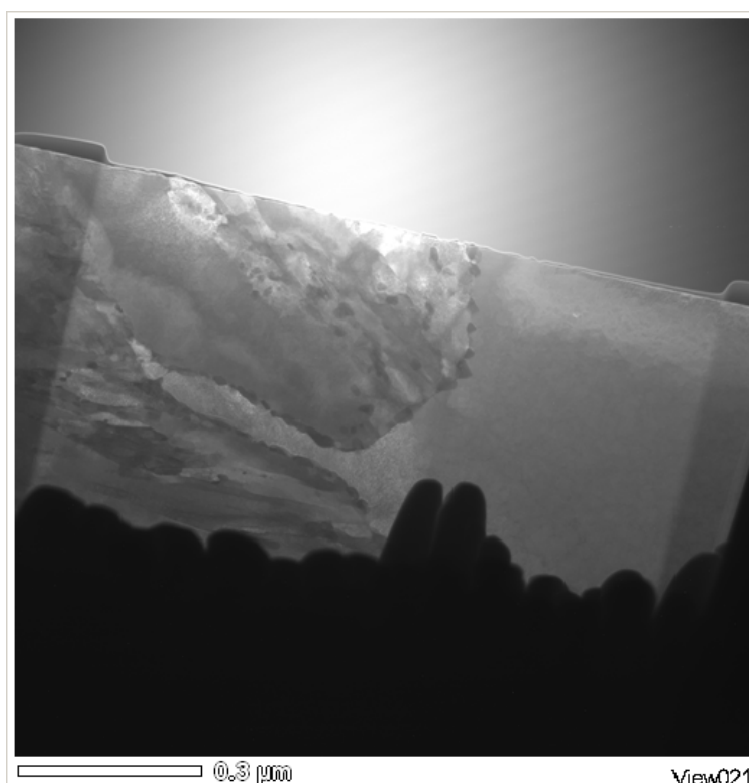


Figure 114: TEM image of CB2A specimen obtained by FIB preparation shown in Figure 113 revealing delta ferrite region on the right side and martensitic lath structure on the left side of the image.

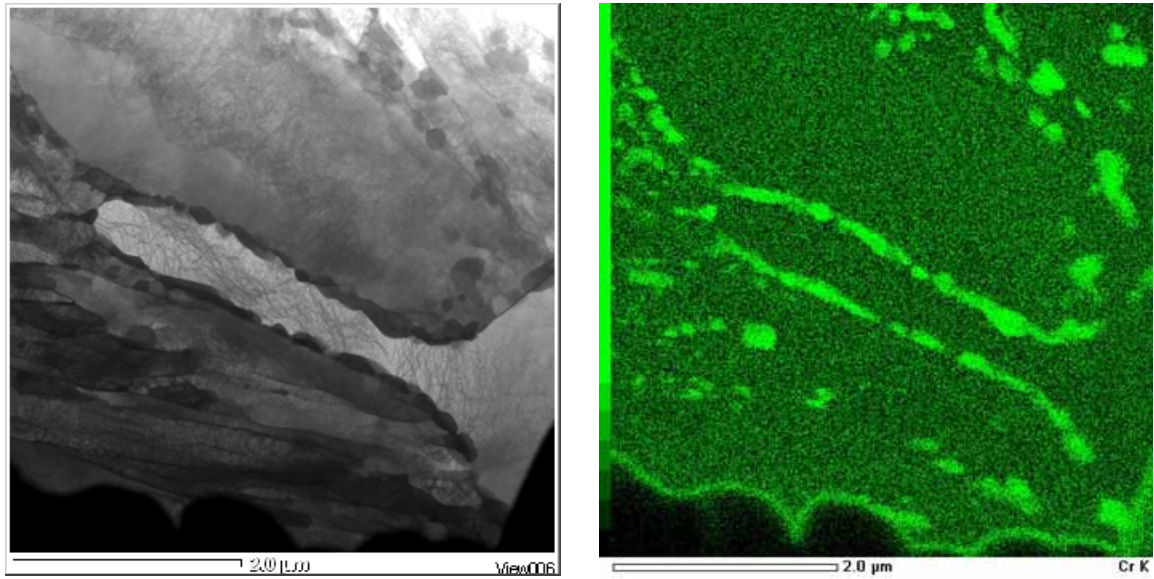


Figure 115: TEM image of finger-like delta ferrite region in CB2A and EDX chromium mapping revealing heavy precipitation along delta ferrite/martensite phase boundary.

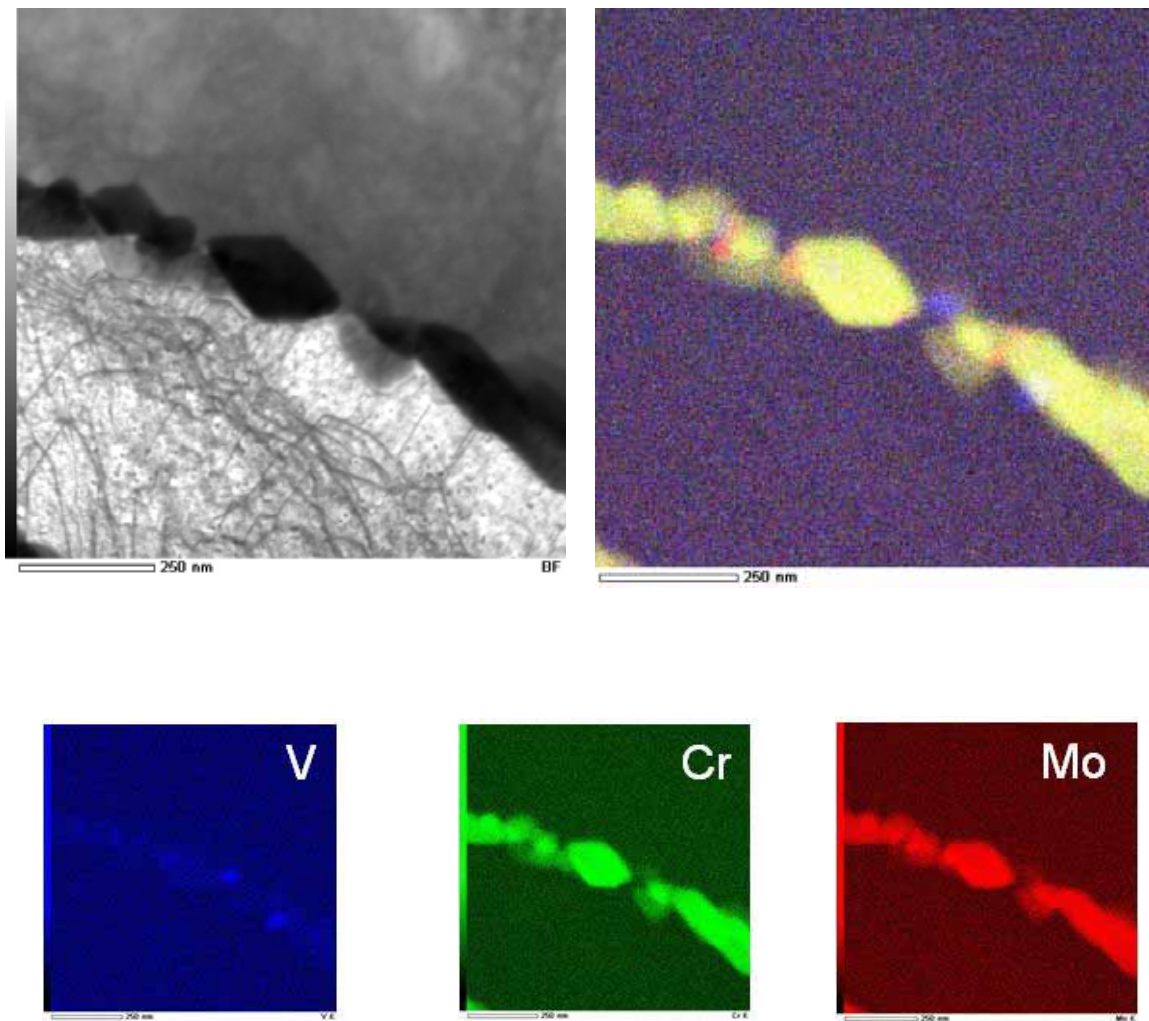


Figure 116: Precipitates along delta ferrite/martensite phase boundary and corresponding EDX elemental maps in steel CB2A.

The microstructure of fractured HAZ simulated and heat treated CB2A Charpy specimens has been studied by optical and electron microscopy. The higher the simulated peak temperature is, the lower are the measured impact toughness values. Figure 117 shows the fracture surfaces of the investigated impact specimens.

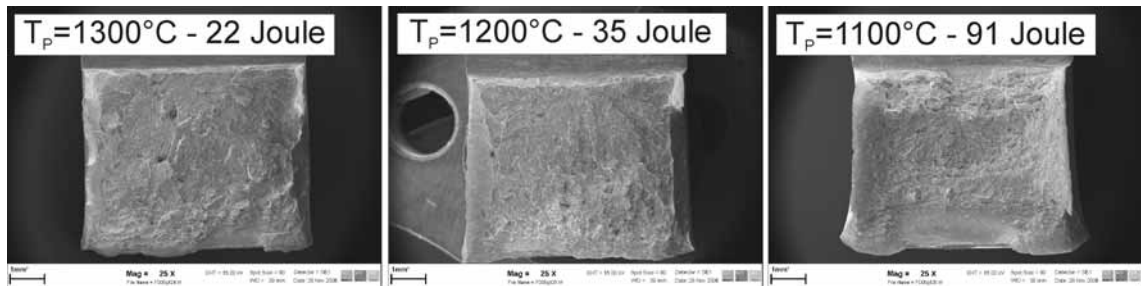


Figure 117: Fracture surface of HAZ simulated impact specimens of steel CB2A tested at room temperature.

The fracture mode of all three samples can be characterised as brittle transgranular cleavage (Figure 118). The specimen simulated with the lowest peak temperature of 1100°C shows some ductile areas on the fracture surface.

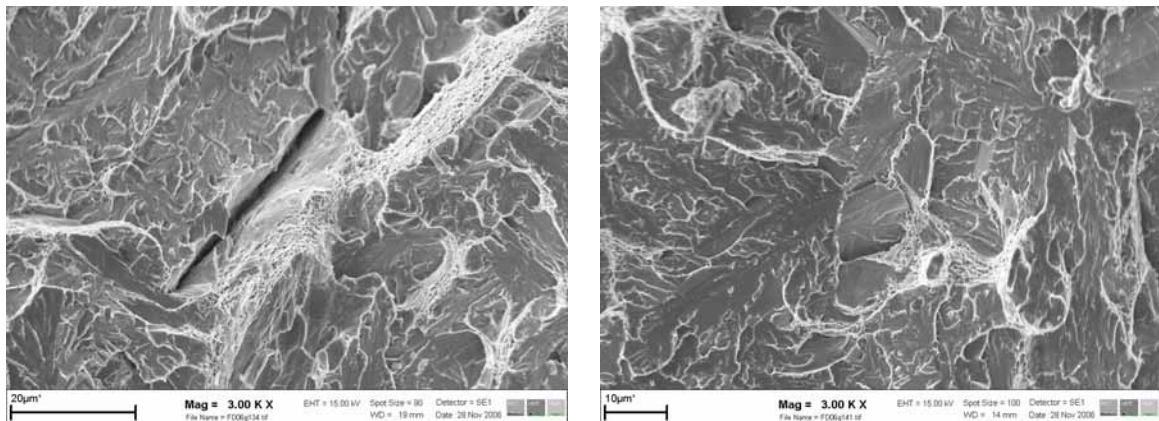


Figure 118: SEM images of fracture surfaces of CB2A impact specimens (shown in Figure 117)  $T_P=1300^\circ\text{C}$  (left) and  $T_P=1200^\circ\text{C}$  (right).

The microstructure of impact specimens simulated with peak temperatures of 1200°C and 1300°C contain a certain amount of retained delta ferrite, whereas the specimen simulated with a peak temperature of 1100°C consists of martensite only. Crosssectional optical micrographs of the fractured impact specimens reveal a smooth fracture through regions of retained delta ferrite (Figure 119). Again, heavy precipitation along delta ferrite/martensite boundaries is observed.

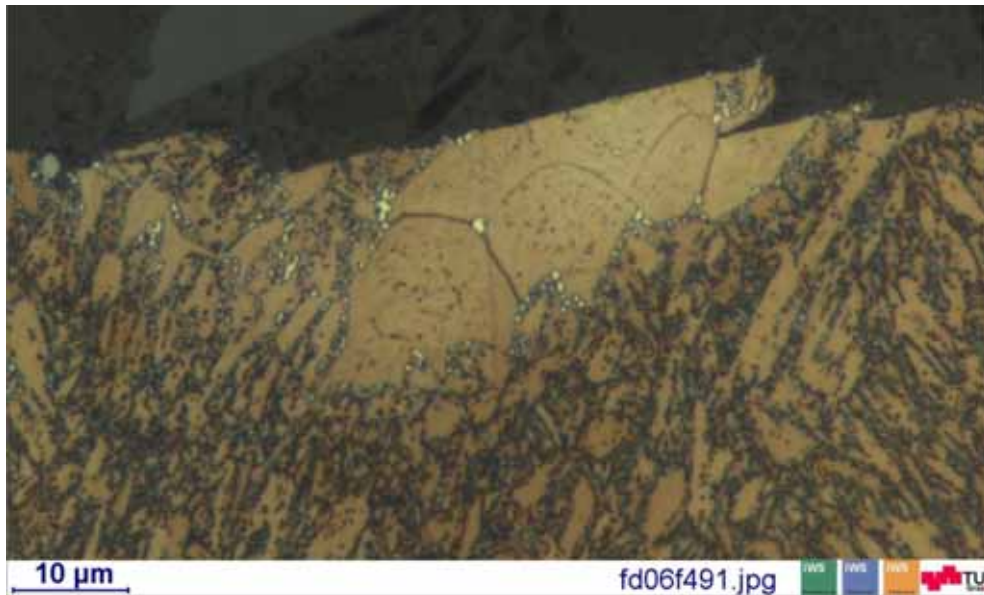


Figure 119: Crosssectional micrograph of fractured (room temperature) CB2A impact specimen simulated with a peak temperature of 1200°C. A smooth transgranular fracture through the delta ferrite grain can be observed.

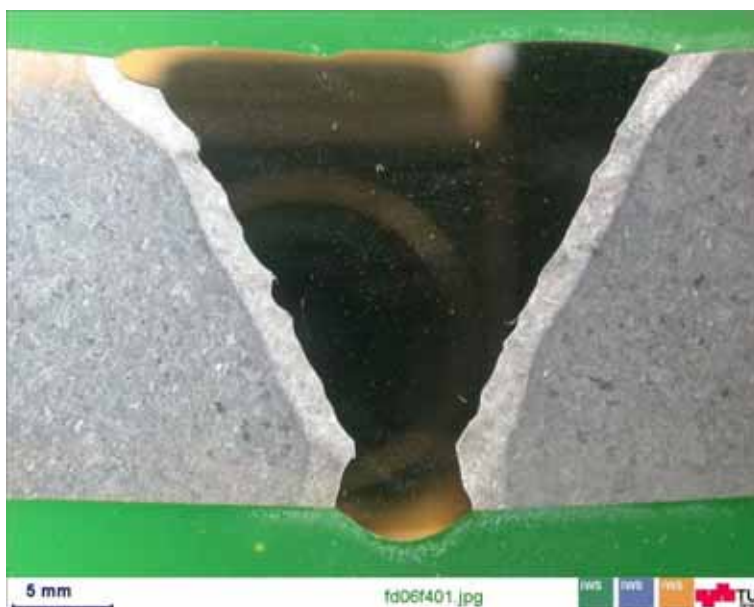


Figure 120: Secondary cracking close to the fracture surface in a delta ferrite grain observed in the impact specimen simulated with a peak temperature of 1300°C and tested at room temperature.

At a location close to the fracture surface, secondary cracking within a delta ferrite grain is observed (Figure 120). In addition to cracking in the grain interior, also, cracks along the grain boundary of the delta ferrite, which is heavily decorated with precipitates, are visible.

## 2.7 NPM1 test weld

To confirm results obtained by HAZ simulation, a test weld of NPM1 steel has been fabricated. No problems have occurred when welding plates of NPM1 base material using Nibas filler metal. As a result, a sound weld has been produced. Figure 121 shows a crosssectional macrograph of the welded joint with the reflective Ni base weld deposit flanked by the heat affected zone.



**Figure 121: Macrograph of NPM1 test weld with Nibas weld deposit and homogeneously formed heat affected zone.**

### 2.7.1 Microstructure

Gas tungsten arc welding with a calculated heat input of  $9.5 \text{ kJ cm}^{-1}$  leads to the formation of a heat affected zone with a total width of 1.8 mm. Figure 122 shows a micrograph of the HAZ in as-welded condition.

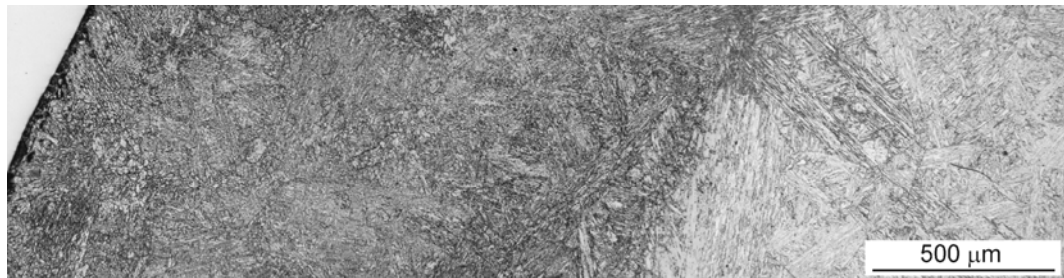


Figure 122: Micrograph of the HAZ of NPM1 test weld in as-welded condition with a total HAZ width of 1.8 mm.

The HAZ microstructure in the as-welded condition close to the weld fusion line and 1.5 mm off from this is shown in Figure 123. The region close to the weld fusion line is characterised by parallel martensite lath packages separated by a dark-etching, not yet identified phase. Single grains with a diameter of about 50 μm are observed directly adjacent to the fusion line. No delta ferrite is detected in the entire HAZ. The region 1.5 mm off the fusion line, where usually the fine grained region is located, shows the same prior austenite grain size as observed in the initial base material microstructure.

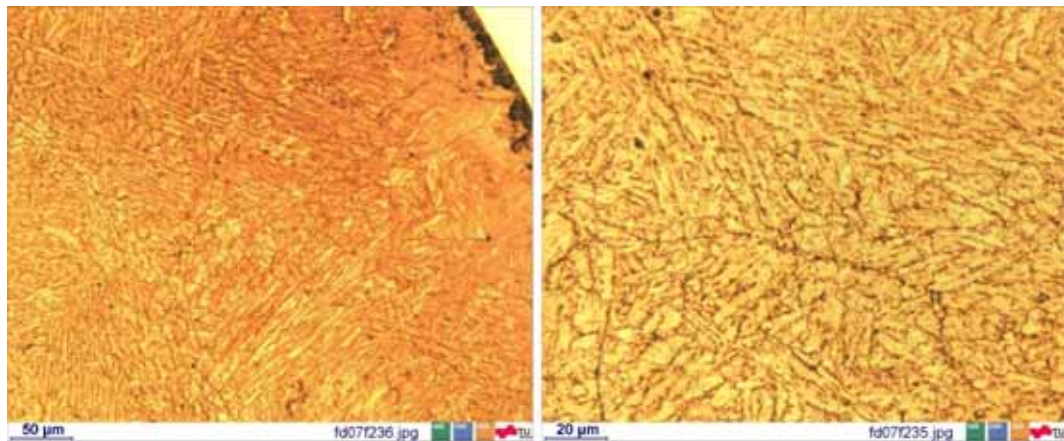
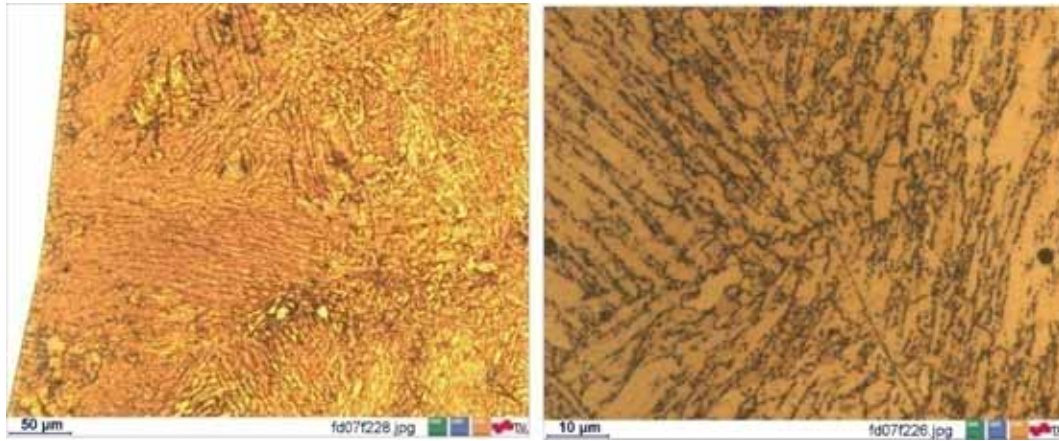


Figure 123: HAZ microstructure of NPM1 test weld in as-welded condition close to the fusion line (left) and 1.5 mm off from the fusion line (right).

Post-weld heat treatment results in re-precipitation of dissolved precipitates. The microstructure close to the weld fusion line after PWHT looks similar to the as-welded microstructure. Dark lines, separating packages of martensite laths, are identified as dense seams of precipitates. 1.5 mm off the fusion line, where the initial grain size of the base material is pre-

served throughout the welding process, PWHT reveals fine newly formed grains close to the initial grain boundary (Figure 124).



**Figure 124: HAZ microstructure of NPM1 test weld after PWHT close to the fusion line (left) and 1.5 mm away from the fusion line (right).**

The results of optical microscopy are supported by EBSD investigations of the HAZ microstructure. Figure 125 shows the microstructure of the heat affected zone 1.5 off the fusion line. Small grains surround homogeneous packages of martensite laths in the interior of prior austenite grains. A grain mapping performed on EBSD data clearly shows the small grains located at the initial prior austenite grain boundary.

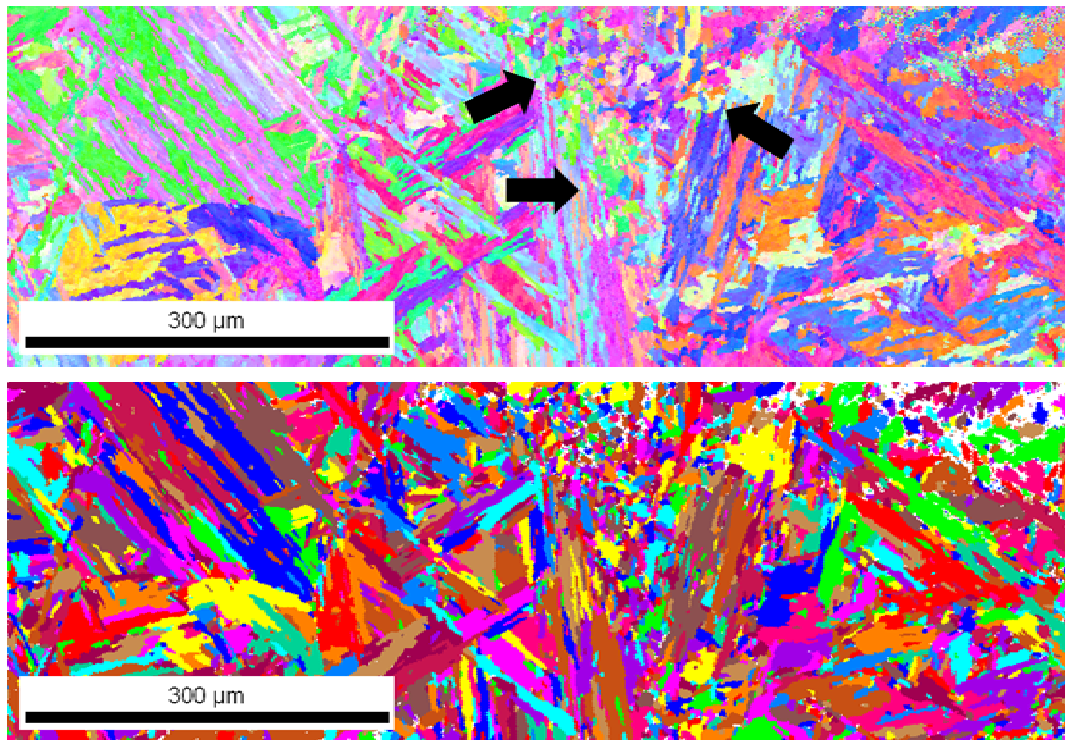
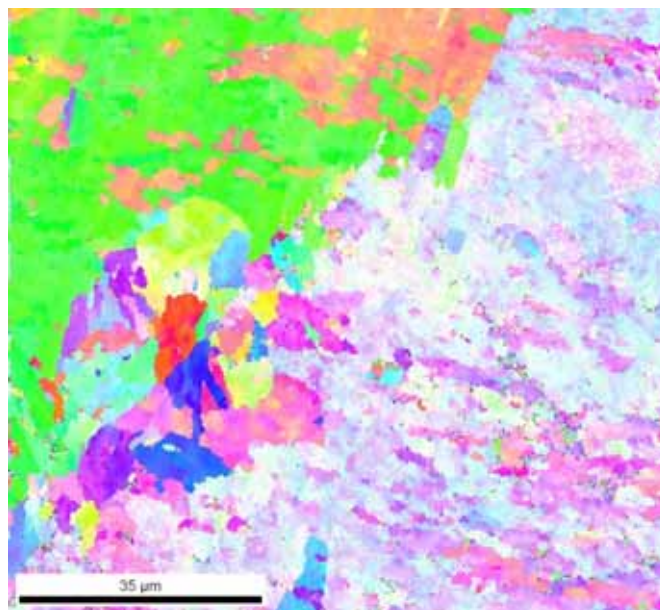


Figure 125: EBSD images of NPM1 test weld HAZ microstructure - Large prior austenite grains with martensitic lath structure and newly formed small grains along prior austenite grain boundary located 1.5 mm off from the weld fusion line. Inverse pole figure (top) and grain mapping (bottom).

At higher magnification, new grains are visible directly adjacent to the initial grain boundary of the base material. The average grain size of the new grains is below 10 μm (Figure 126).



**Figure 126: Details of prior austenite grain boundary with newly formed small grains located 0.5 mm off the weld fusion line.**

### 2.7.2 HAZ hardness

A hardness traverse across the heat affected zone of NPM1 test weld in as-welded condition reveals the highest hardness of 340 HV0.1 close to the weld fusion line. Two millimetres off the fusion line, a minimum in hardness with 210 HV0.1 is measured. In superposition with the optical micrograph it is apparent that this minimum is outside the part of the heat affected zone which has transformed during welding (Figure 127). In this region of the HAZ, simply over-tempering of the base material has taken place.

Post-weld heat treatment results in a reduction of the maximum hardness of about 60 HV0.1 hardness points. Tempering of the transformed microstructure of the HAZ results in a softening of the material. The magnitude of the hardness minimum (210 HV0.1) is not influenced by the PWHT and is still located 2.1 mm off the fusion line in the over-tempered region. In superposition with the optical micrograph of the heat treated HAZ, still large prior austenite grains prevail in a region close to the unaffected base material, where, in conventional 9% Cr steels, the fine grained region is located (Figure 128).

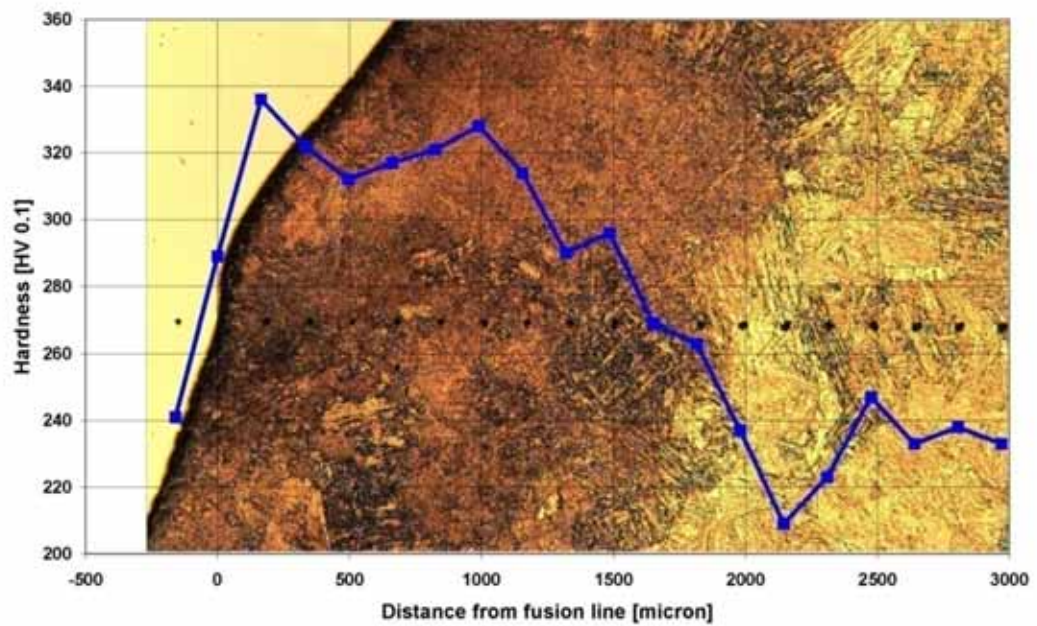


Figure 127: Micro hardness along HAZ of NPM1 test weld in as-welded condition.

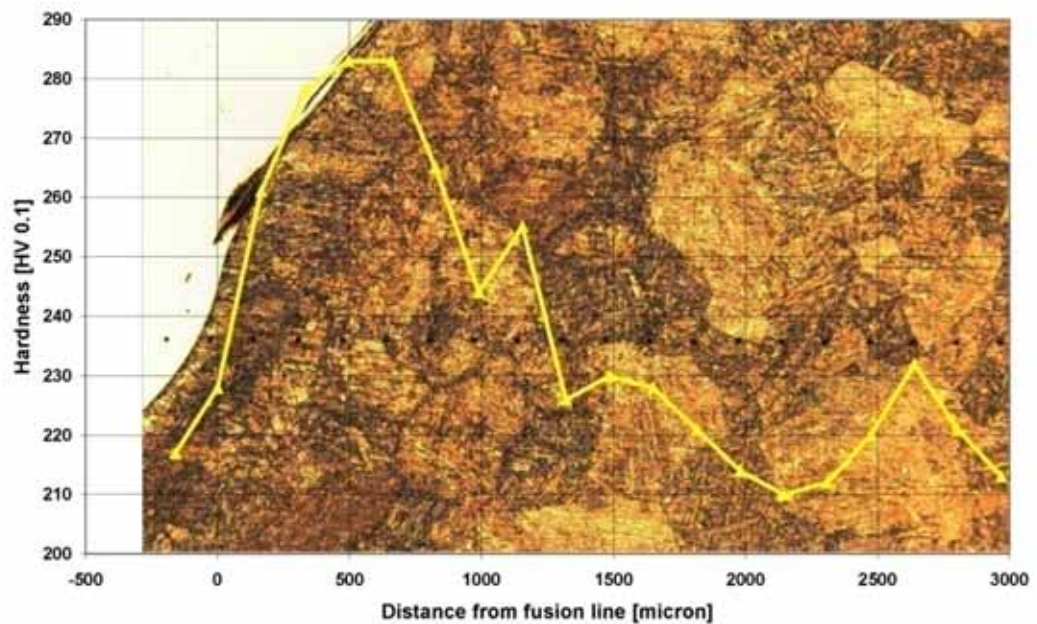


Figure 128: Micro hardness along HAZ of NPM1 test weld after a PWHT of 4 hours at 740°C.

### 3 Results of the Matching Program

Creep tests of E911 cross-welds in the creep laboratory of the IWS have reached a maximum duration of almost 30.000 hours. Although some specimens, especially those tested at lower stress levels are still running, interesting information on the influence of weld metal creep strength on the overall creep strength of cross-welds could be gathered. Microstructural investigations of fractured specimens give insight into the predominant failure mechanisms, which are weld metal failures and Type IV cracking.

#### 3.1 Cross-weld creep strength

Results of creep tests at 600°C reveal similar behaviour for all three cross-welds. In Figure 129, creep rupture data is shown in comparison to the mean line of E911 base material creep strength and the  $\pm 20\%$  scatter band evaluated by the ECCC in 2005. Up to a testing duration of 10.000 hours, the creep strength of the cross-welds is almost aligned to the mean line of the base material. Only the creep rupture strength of the under-matching weld is in the lower part of the scatter band from the beginning on. Significant deviation from the base material creep strength starts close to a testing time of 10.000 hours and the -20% line of the scatter band is crossed after about 20.000 hours. The specimen of the under-matching series tested at a stress level of 80 MPa failed after 28.000 hours, which corresponds to a reduction of creep strength compared to the base material of 30% and results in a weld strength factor of 0.7.

At the highest stress level of 150 MPa, improvement of the creep rupture strength can be achieved by selection of a weld metal with increased creep strength. The specimen of the over-matching series, with P92 grade weld metal, failed after 2.300 hours of testing, which is 1.000 hours later than the specimen of the under-matching series, and 400 hours later than the matching specimen. At lower stress levels and longer testing durations, time to rupture converges for specimens of the matching and the over-matching series. Specimens of these series tested at 120 MPa and 110 MPa failed almost after identical testing times. Similar results are found for the specimens of the under- and over-matching series tested at a stress level of 90 MPa. They show almost the same time to rupture close to 26.000 hours. The matching specimen tested at this stress level is still running and has reached a testing time of 29.000 hours with a current creep strain of 1 %.

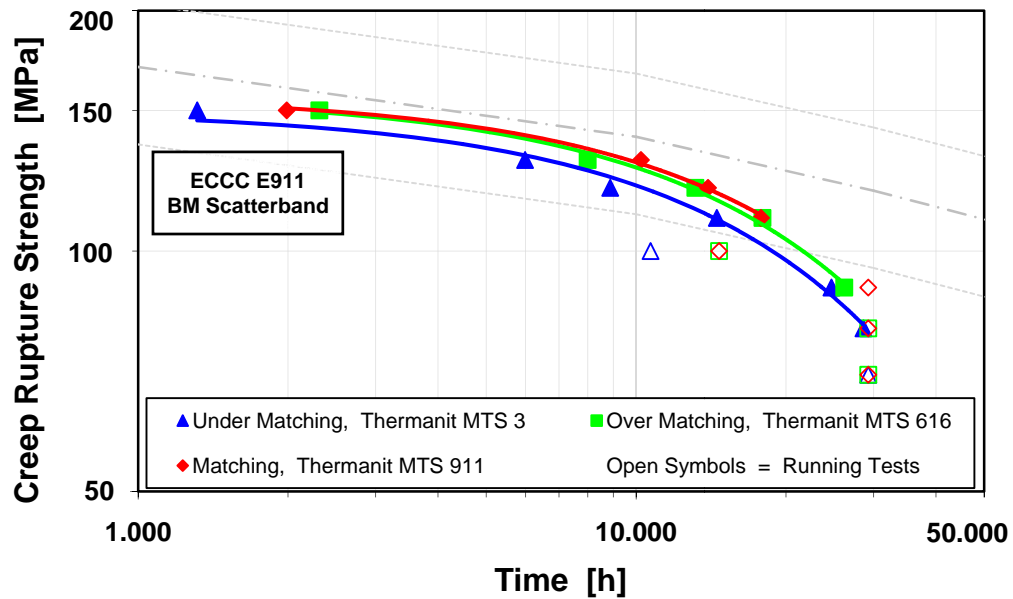


Figure 129: Creep rupture strength at 600°C of cross-weld samples of the under-, over- and matching weld compared to the E911 base material scatter band.

Recorded creep strain data for all three welds are summarised in Figure 130. Analysis of the strain data reveals that the specimens tested at 150 MPa show no distinct stages of creep. For all other specimens, the recorded strain data can be categorized according to a characteristic creep curve in primary, secondary and tertiary creep region. The time period in the secondary creep regime, characterised by a constant creep rate, is increasing with decreasing stress level. The final creep strain at the time of fracture is decreasing with decreasing stress level. Creep strain after fracture is highest for the specimens of the under-matching weld (<10%) and lowest for the over-matching weld (<4%).

A detailed compilation of the time to rupture, the failure location, the reduction of area and the rupture elongation for each specimen is given in Table 39.

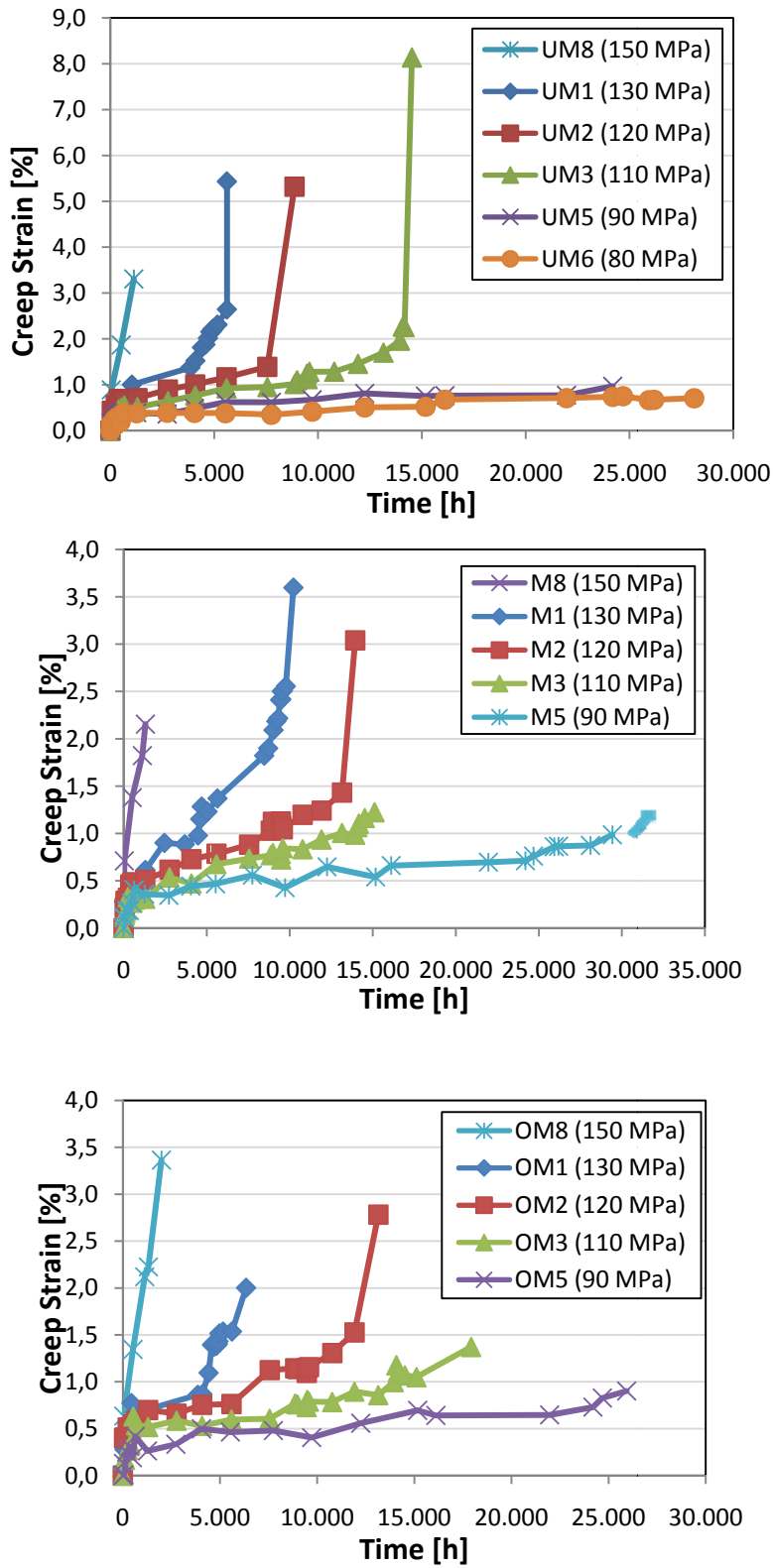


Figure 130: Creep strain data for cross-weld specimens of the under-matching (top), matching (middle) and over-matching (bottom) series tested at 600°C.

**Table 39: Compilation of results of the creep rupture tests of E911 cross-welds with three different weld metals evaluated at 600°C.**

|                       | Spec. | Stress Level<br>[MPa] | Time to<br>rupture<br>[h] | FL  | RA<br>[%] | RE<br>[%] |
|-----------------------|-------|-----------------------|---------------------------|-----|-----------|-----------|
| <b>Under-Matching</b> | UM8   | 150                   | 1.314                     | WM  | 18.4      | 7.3       |
|                       | UM1   | 130                   | 5.982                     | WM  | 9.0       | 5.4       |
|                       | UM2   | 120                   | 8.869                     | WM  | 11.0      | 5.3       |
|                       | UM3   | 110                   | 14.519                    | WM  | 13.9      | 8.1       |
|                       | UM4   | 100                   | R                         | -   | -         | -         |
|                       | UM5   | 90                    | 24.680                    | HAZ | 11.0      | 1.0       |
|                       | UM6   | 80                    | 28.613                    | HAZ | 1.1       | 2.6       |
|                       | UM7   | 70                    | R                         | -   | -         | -         |
| <b>Matching</b>       | M8    | 150                   | 1.988                     | WM  | 13.0      | 5.8       |
|                       | M1    | 130                   | 10.226                    | HAZ | 9.3       | 3.6       |
|                       | M2    | 120                   | 13.945                    | HAZ | 9.8       | 3.0       |
|                       | M3    | 110                   | 17.819                    | HAZ | 8.4       | 1.4       |
|                       | M4    | 100                   | R                         | -   | -         | -         |
|                       | M5    | 90                    | R                         | -   | -         | -         |
|                       | M6    | 80                    | R                         | -   | -         | -         |
|                       | M7    | 70                    | R                         | -   | -         | -         |
| <b>Over-Matching</b>  | OM8   | 150                   | 2.311                     | HAZ | 9.0       | 27.9      |
|                       | OM1   | 130                   | 7.992                     | HAZ | 10.4      | 2.9       |
|                       | OM2   | 120                   | 13.150                    | HAZ | 11.8      | 2.8       |
|                       | OM3   | 110                   | 17.931                    | HAZ | 9.2       | 1.4       |
|                       | OM4   | 100                   | R                         | -   | -         | -         |
|                       | OM5   | 90                    | 26.185                    | HAZ | 6.1       | 2.8       |
|                       | OM6   | 80                    | R                         | -   | -         | -         |
|                       | OM7   | 70                    | R                         | -   | -         | -         |

FL ... Fracture Location  
RA ... Reduction of area  
WM...Weld metal

R ... Running Tests  
RE ... Rupture elongation  
HAZ.. Heat affected zone

### 3.2 Investigation of failure locations

All fractured creep specimens have been investigated with regard to their location of failure. Two different fracture locations are observed throughout all specimens. Some have failed within the weld metal by a relatively low deformation fracture. The other failures have occurred within the heat affected zone (HAZ) of the welds and are also characterised by low deformation. A representative crosssectional macro image of a weld metal failure is shown in Figure 131. An image of a characteristic low deformation HAZ fracture is shown in Figure 132.

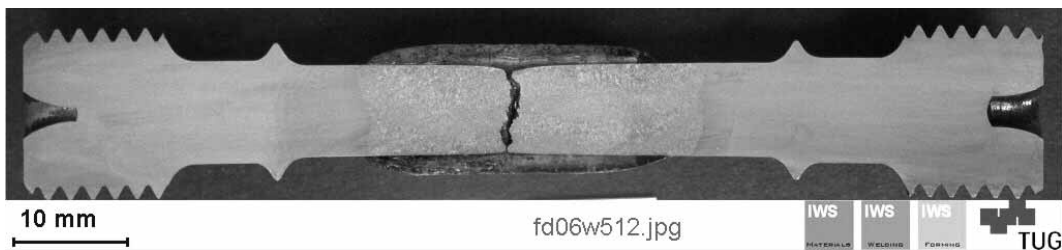


Figure 131: Specimen UM1 with characteristic weld metal failure in the center of the specimen.

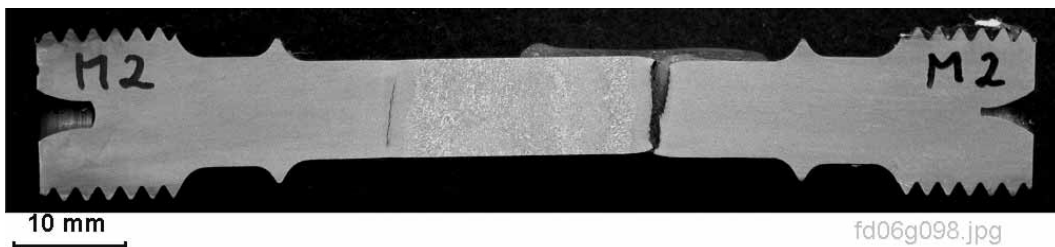


Figure 132: Specimen M2 as reference for a low deformation failure within the heat affected zone.

Figure 133 shows a macrograph at higher magnification of specimen UM2 of the under-matching series which has failed after 8.869 hours at a stress level of 120 MPa. The fracture has occurred right in the middle of the deposited weld metal. Several secondary cracks, which follow the grain boundaries of the columnar solidified weld metal, can be seen. In the middle of the specimen, the refinement of the microstructure by subsequently deposited weld beads can be seen. The mechanism of weld metal failures observed in this program is described in more detail in Chapter V.3.3.

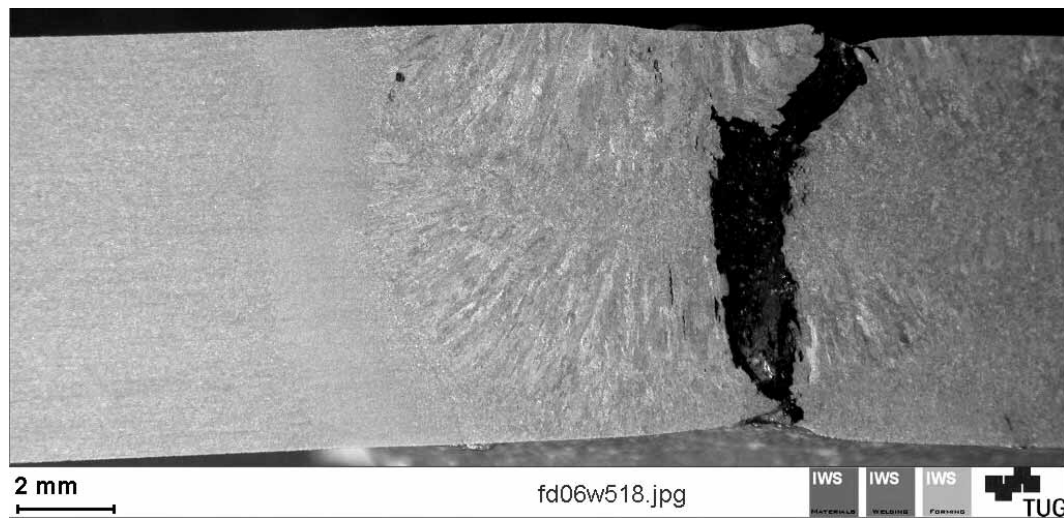


Figure 133: Specimen UM2 – The final fracture occurred within the center of the deposited weld metal. Secondary cracks follow the grain boundaries of columnar solidified grains.

A macrograph of a representative failure in the HAZ is shown in Figure 134. The final fracture is completely parallel to the weld fusion line. The total width of the HAZ in this specimen is approximately 2 mm.

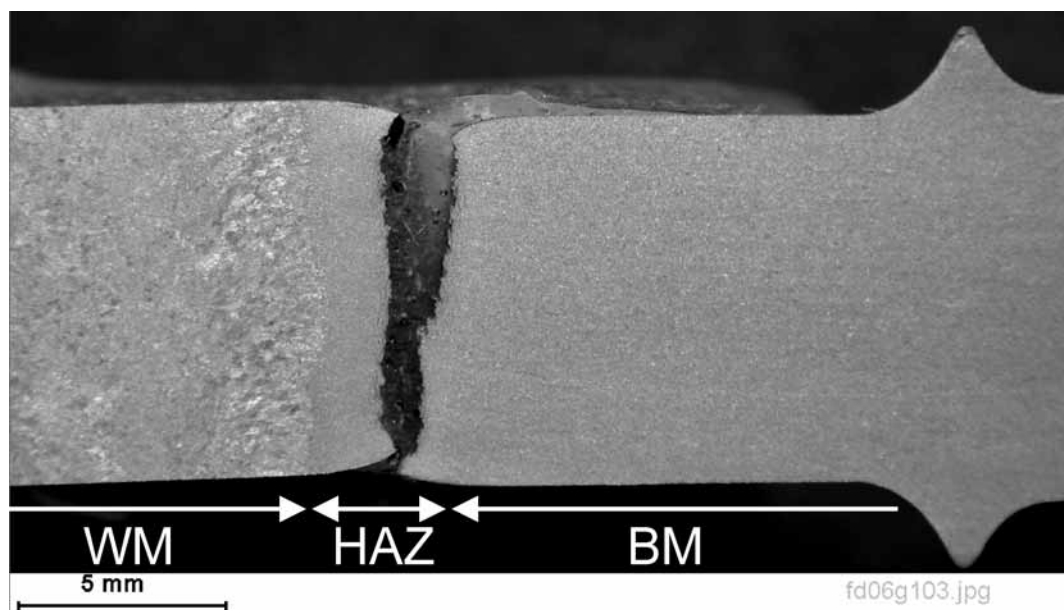


Figure 134: Specimen M2 – Characteristic HAZ failure parallel to the weld fusion line close to the unaffected base material.

The distance of the fracture is approximately 1.5 mm off the weld fusion line close to the unaffected base material. For this specimen of the matching series, which has failed after 13.945 hours at a stress level of 120 MPa, the reduction of area is about 10%. A detailed reflection on HAZ failures within this program is given in Chapter V.3.4.

Macrographs of all specimens, which have fractured within the Matching Program so far, are shown in Figure 135.

### **Under-Matching Series**

At testing stresses higher than 100 MPa, creep specimens of the under-matching series fractured in the weld metal. The fracture appearance of these specimens is similar, and characterised by only a small reduction of area. The fracture is not branched and in some specimens a correlation between the fracture path and the layer structure of the weld beads can be drawn. For the specimens tested at 90 MPa and 80 MPa a shift in failure location is observed. They failed by Type IV mechanism in the outer region of the HAZ. Similar to the weld metal failures, no significant reduction of area is measured for these specimens.

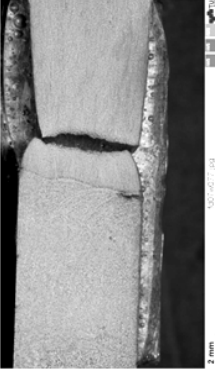
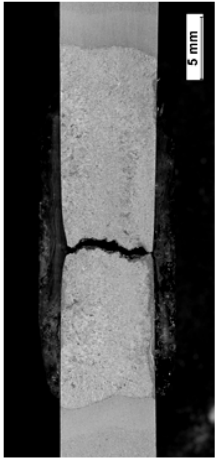
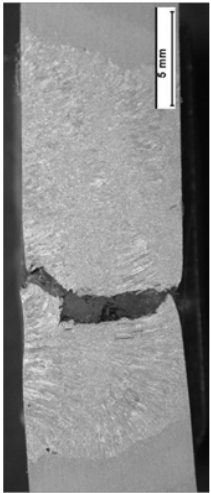
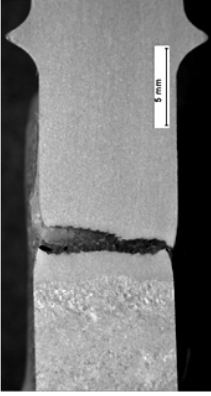
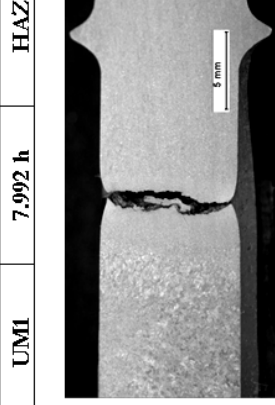
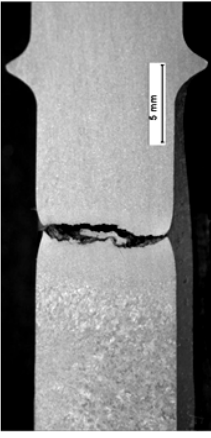
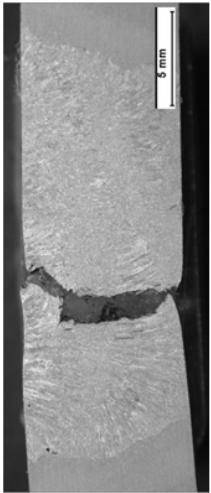
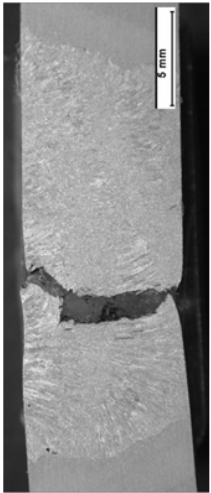
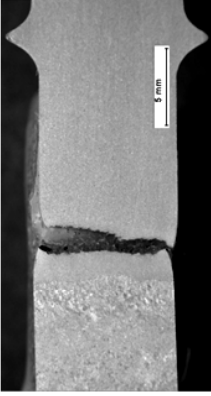
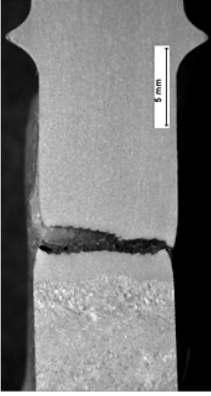
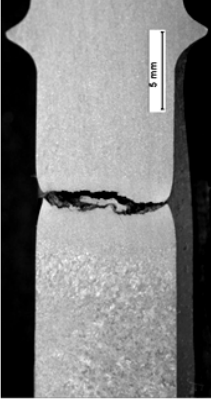
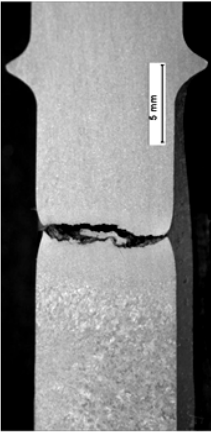
### **Matching Series**

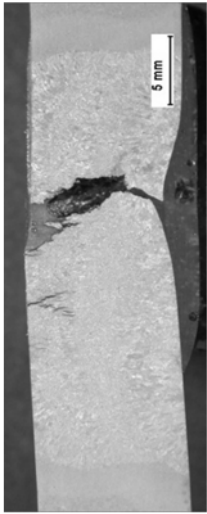
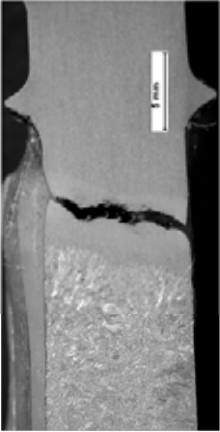
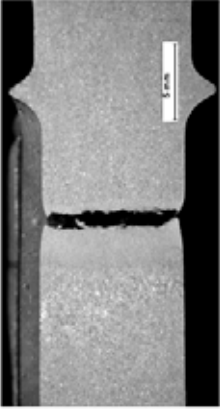
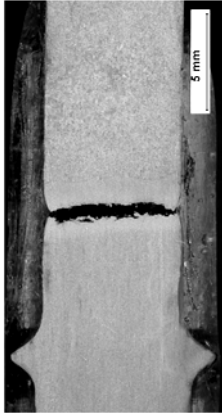
The investigation on the fracture locations on specimens of the matching series reveals similar findings. At the highest stress level of 150 MPa the creep specimen failed after 2.000 hours in the weld metal. At lower stress levels failure location is shifted again into the HAZ of the weldment. More precisely, the specimens failed close to the outer part of the HAZ adjacent to the unaffected base material. The final cracks are completely parallel to the weld fusion line. For example, the weld fusion line of specimen M3, which failed after 17.819 hours, is inclined with respect to the specimen longitudinal axis. Therefore, the final fracture is inclined to the same extent as the fusion line.

### **Over-Matching Series**

The characteristic fracture path parallel to the weld fusion line is also observed on specimens of the over-matching series. Contrary to the under-matching and matching series, all specimens of the over-matching series fractured within the HAZ, so far. Specimen OM8 tested at the highest stress level of 150 MPa failed in the HAZ but also secondary failures are visible close to the fusion line and in the weld metal.

Figure 135: Compilation of macrographs of fractured specimens tested at 600°C.

| Stress Level [MPa] | Under-Matching P91-type   |   | Matching E911-type   |  | Over-Matching P92-type  |   |
|--------------------|---|---|--|--|---|---|
|                    | UM8   | WM  | M8   | WM   | UM8   | HAZ   |
| 150                |    |     |    |    |    |   |
|                    | 1.314 h   | 5.982 h   | 1.988 h  | 10.226 h   | 2.311 h   | 7.992 h   |
| 130                |   |  |   |  |  |  |
|                    | 5.982 h   | 8.869 h   | 10.226 h   | 13.945 h   | 7.992 h   | 13.150 h  |
| 120                |  |  |  |  |  |  |
|                    | 8.869 h   | 8.869 h   | 13.945 h   | 13.945 h   | 13.150 h  | 13.150 h  |

| Stress Level [MPa] | Under-Matching P91-type   |          |    | Matching E911-type   |          |     | Over-Matching P92-type  |          |     |
|--------------------|---|----------|----|--|----------|-----|---|----------|-----|
|                    | UM3   | 14.519 h | WM | M3   | 17.819 h | HAZ | OM3   | 17.931 h | HAZ |
| 110                |    |          |    |  |          |     |  |          |     |
|                    |    |          |    | <p>running</p>   |          |     |  |          |     |
| 90                 |  |          |    | <p>running</p>   |          |     | <p>running</p>  |          |     |
|                    | <p>UM6</p>  |          |    | <p>M6</p>  |          |     | <p>OM6</p>  |          |     |
| 80                 | <p>UM6</p>  |          |    | <p>M6</p>  |          |     | <p>OM6</p>  |          |     |
|                    | <p>28.613 h</p>   |          |    | <p>HAZ</p>   |          |     | <p>HAZ</p>  |          |     |

A shift of failure location from the weld metal into the HAZ is predominant. The stress level at which this shift takes place is depending on the weld metal. For the under-matching welds, shifting takes place at a threshold stress of about 100 MPa. A shift of failure location for the matching weld is observed close to 140 MPa. Although all specimens of the over-matching series fractured in the HAZ, secondary cracking within the weld metal of the specimen tested at 150 MPa indicates possible weld metal fractures at higher stress levels. The stress dependency of the shift in failure location is shown graphically in Figure 136. For all specimens, so far investigated, no base material failures or any significant damage within the base material has been observed.

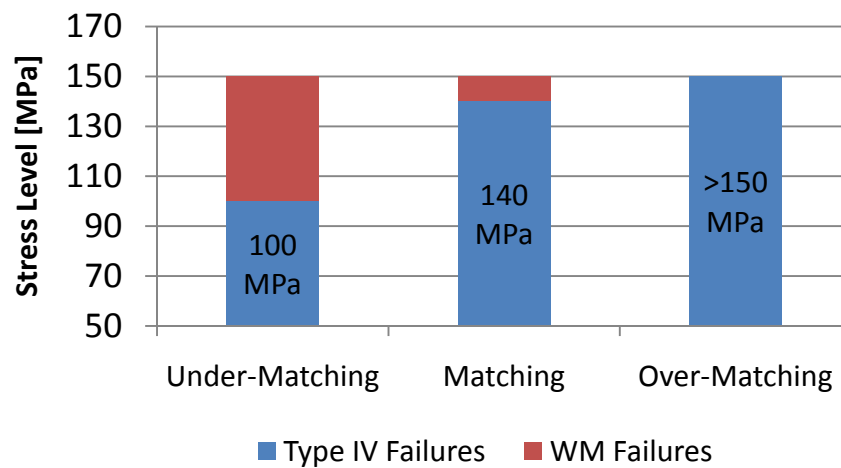
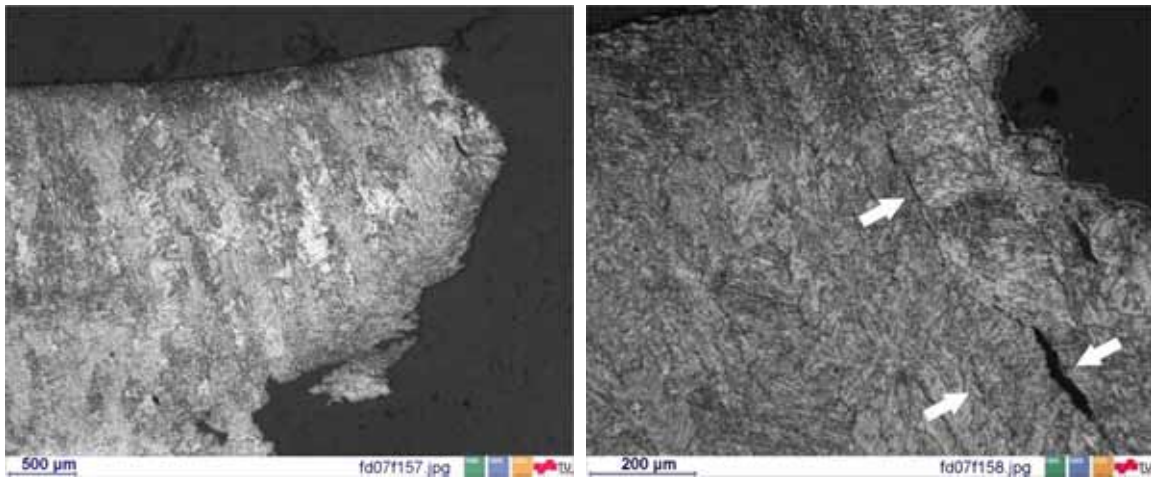


Figure 136: Threshold stress for shift of failure location as a function of the weld metal.

### 3.3 Weld metal failures

Weld metal failures observed in the Matching Program appear in two manifestations. When the primary solidified weld metal has not been affected by the subsequently deposited weld beads and a columnar grain structure persists, failures are observed along the grain boundaries of the columnar grains (see Figure 137).



**Figure 137:** Fracture line in specimen UM2 following the fusion line of a weld bead (left) and secondary inter-granular cracking along columnar grains in the weld metal (right).

If the weld metal microstructure has been almost completely refined by the subsequent weld beads, damage initiates primarily along prior austenite grain boundaries within the weld metal. Formation of creep voids is observed preferentially along prior austenite grain boundaries but also to a lesser extent along martensite lath and packet boundaries. Figure 138 shows a micrograph of weld metal microstructure with creep cavities along a prior austenite grain boundary in specimen UM1.

When creep cavitation is already in an advanced stage, coalescence of voids results in the formation of micro-cracks. These micro-cracks form predominantly along prior austenite grain boundaries oriented perpendicular to the load direction. Figure 139 shows a representative micrograph of creep damage along grain boundaries in the weld metal. Creep voids can be seen in the entire area but micro-crack formation is limited to the prior austenite grain boundaries. In the final creep stage, micro-cracks in turn, coalesce to macro-cracks.

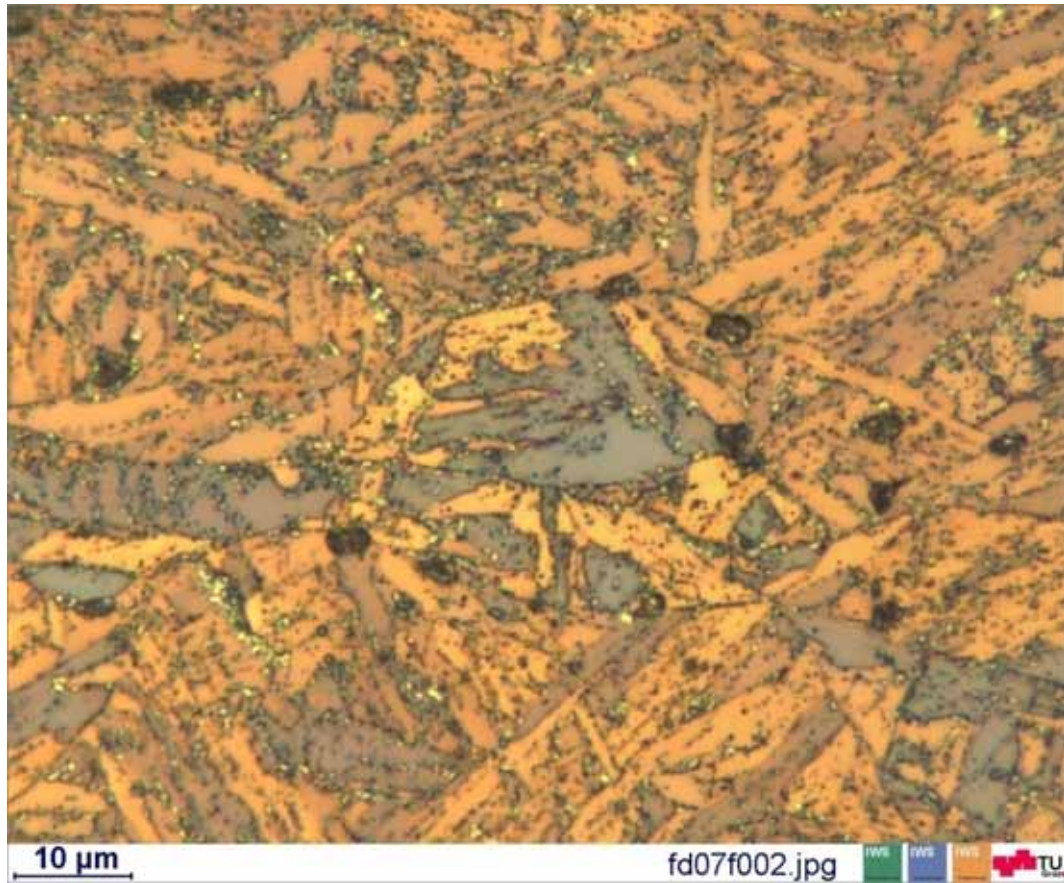
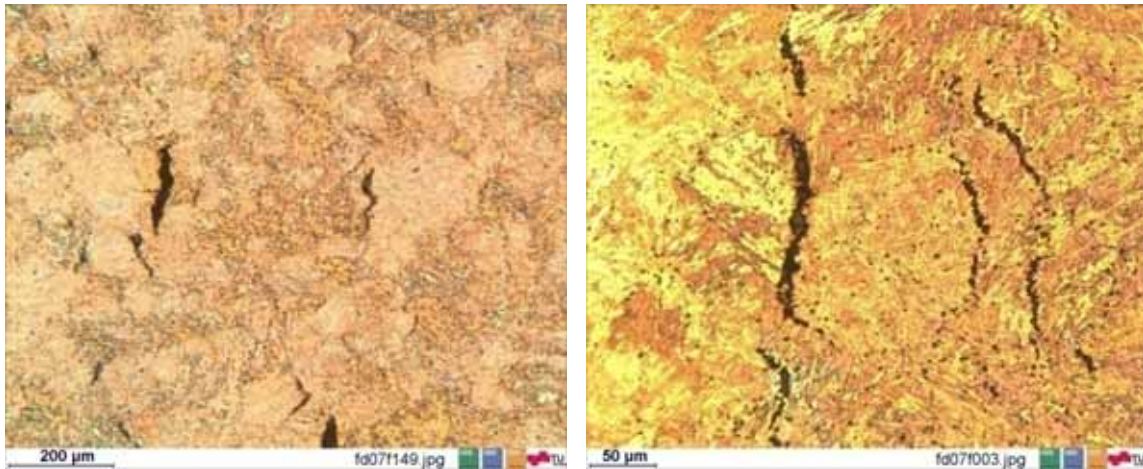


Figure 138: Creep cavitation along prior austenite grain boundaries in the weld deposit of specimen UM1 fractured after 5.982 hours at 130 MPa.



**Figure 139: Weld metal failures in specimens UM8 (left) and UM1 (right) by formation of creep voids and micro-cracks preferentially along prior austenite grain boundaries perpendicular to the load direction.**

### 3.4 Type IV failures

The failure mechanism prevailing at lower stress levels in all three welds is identified as Type IV cracking. As mentioned before, the location of failure is in the outer region of the HAZ, close to the unaffected base material. Type IV failures are characterised by a macroscopically low deformation. Figure 140 shows a cross-sectional macrograph of specimen M2 of the matching series fractured after about 14.000 hours. The final fracture has taken place in the right HAZ of the weld. Significant damage is also observed in the left HAZ. By using scanning electron microscopy in QBSD mode it is possible to visualise creep voids and their distribution within the HAZ. A slag inclusion at the fusion line did not have any effect on the overall creep behaviour of this specimen. The total HAZ width is about 2 mm. Only very localised creep damage is observed. Void formation is limited to a 1 mm wide band approximately 1 mm off the weld fusion line in the direction of the base material. The band of voids is completely parallel to the weld fusion line. Damage in this region has advanced to a degree that already macro-cracks have formed. Therefore, single voids, micro-cracks as well as macro-cracks are present.

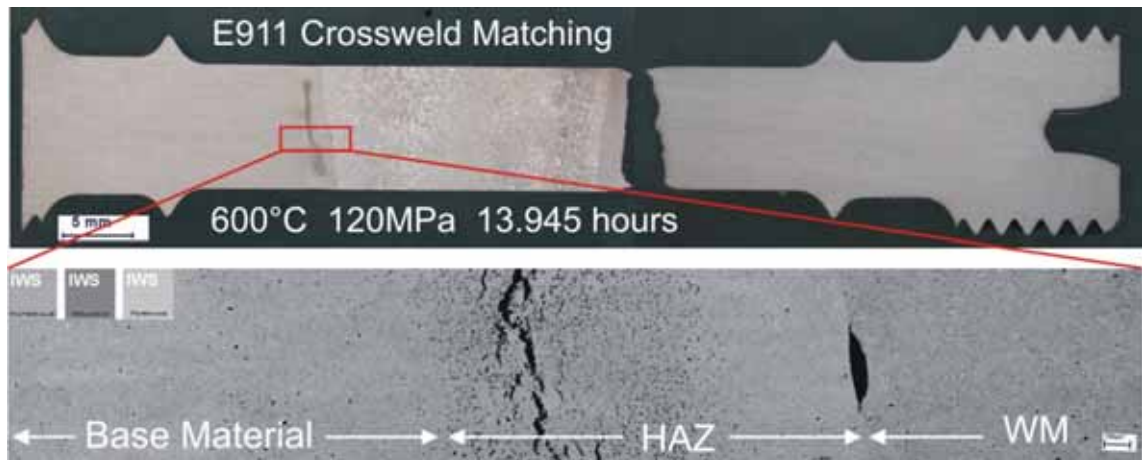


Figure 140: Cross-sectional macrograph of specimen M2 (top) and detail of the damage distribution within the HAZ.

Grain structure in the damaged region in the left HAZ of specimen M2 is analysed using EBSD method. Figure 141 shows the distribution of grains close to the location of failure. The grain size in the failed region is very small.

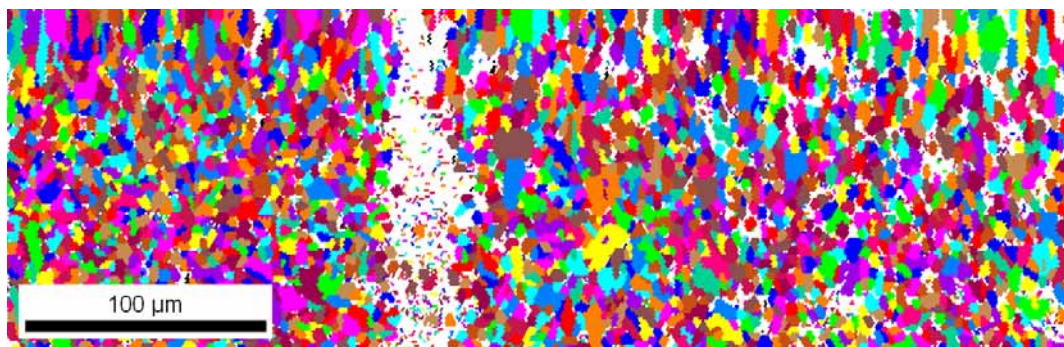
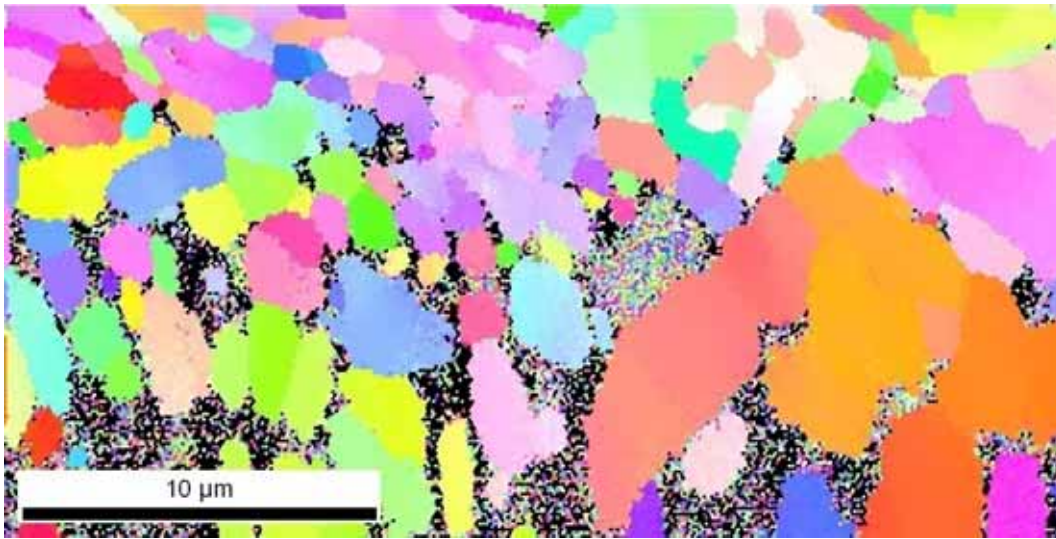


Figure 141: EBSD grain mapping at the location of fracture in specimen M2. Crack and creep voids are represented by white areas within the image.

A second image taken at the same location at a higher magnification is shown in Figure 142. Most of the equiaxed grains are far smaller than  $10\ \mu\text{m}$ . A martensitic lath structure as seen in the weld metal and the base material is not observed in this region.



**Figure 142: Detail of grain distribution close to the failure location in specimen M2.**

Although optical microscopy is reaching its limit with such fine microstructures, Figure 143 gives an impression of cavitation in the fine-grained region of the HAZ of specimen OM1. Bright spots at prior austenite grain boundaries indicate large coarsened precipitates.

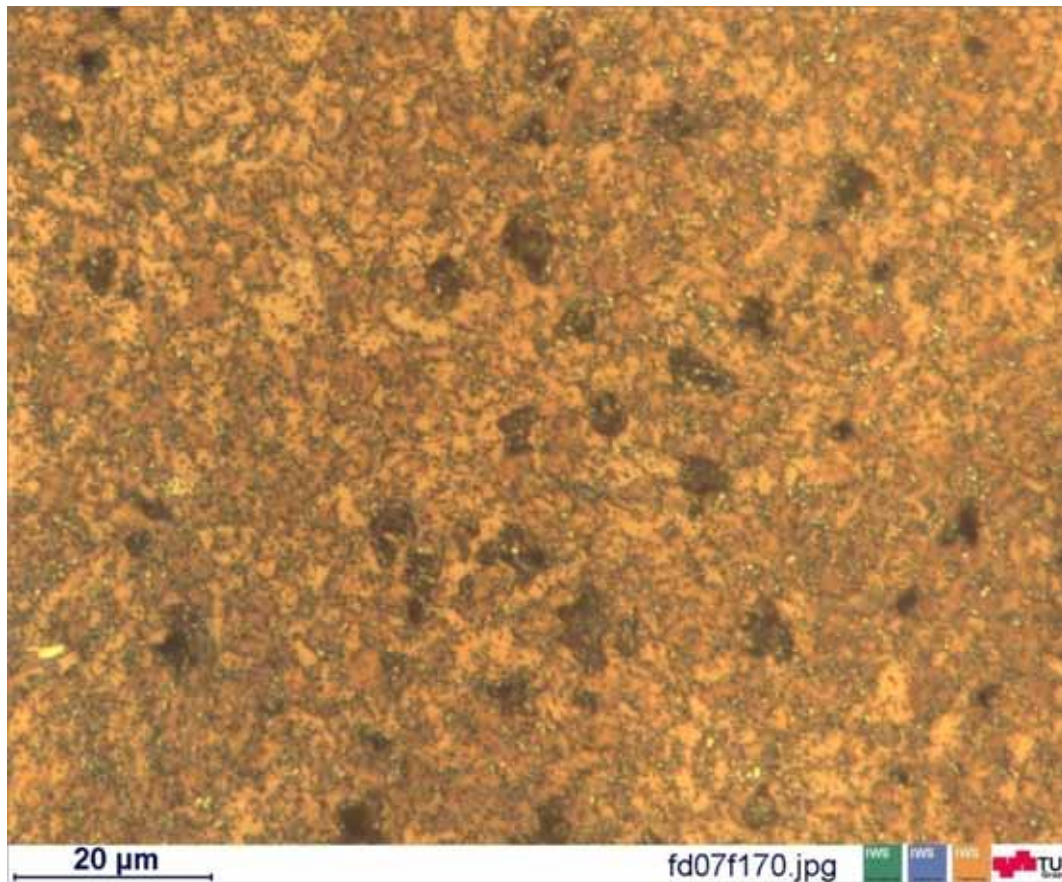


**Figure 143: Optical micrograph of the microstructure close to the location of failure in specimen OM1. Creep cavitation in the fine-grained heat affected zone.**

Looking at base material and fine-grained HAZ microstructure at higher magnification using SEM in QBSD mode, significant differences can be shown (Figure 144). In the FGHAZ, prior austenite grain boundaries are clearly visible but already in the as-received condition no martensite laths can be seen. After about 14.000 hours of creep testing, coarsening of precipitates has taken place. In the creep exposed base material, this coarsening occurs to a lesser extent than in the FGHAZ region. In the fine-grained HAZ region, only few small precipitates are preserved. Large precipitates in the range of 1 μm are predominant and positioned mainly along the prior austenite grain boundaries. In the creep exposed base material, still martensite laths and packet boundaries are observed.

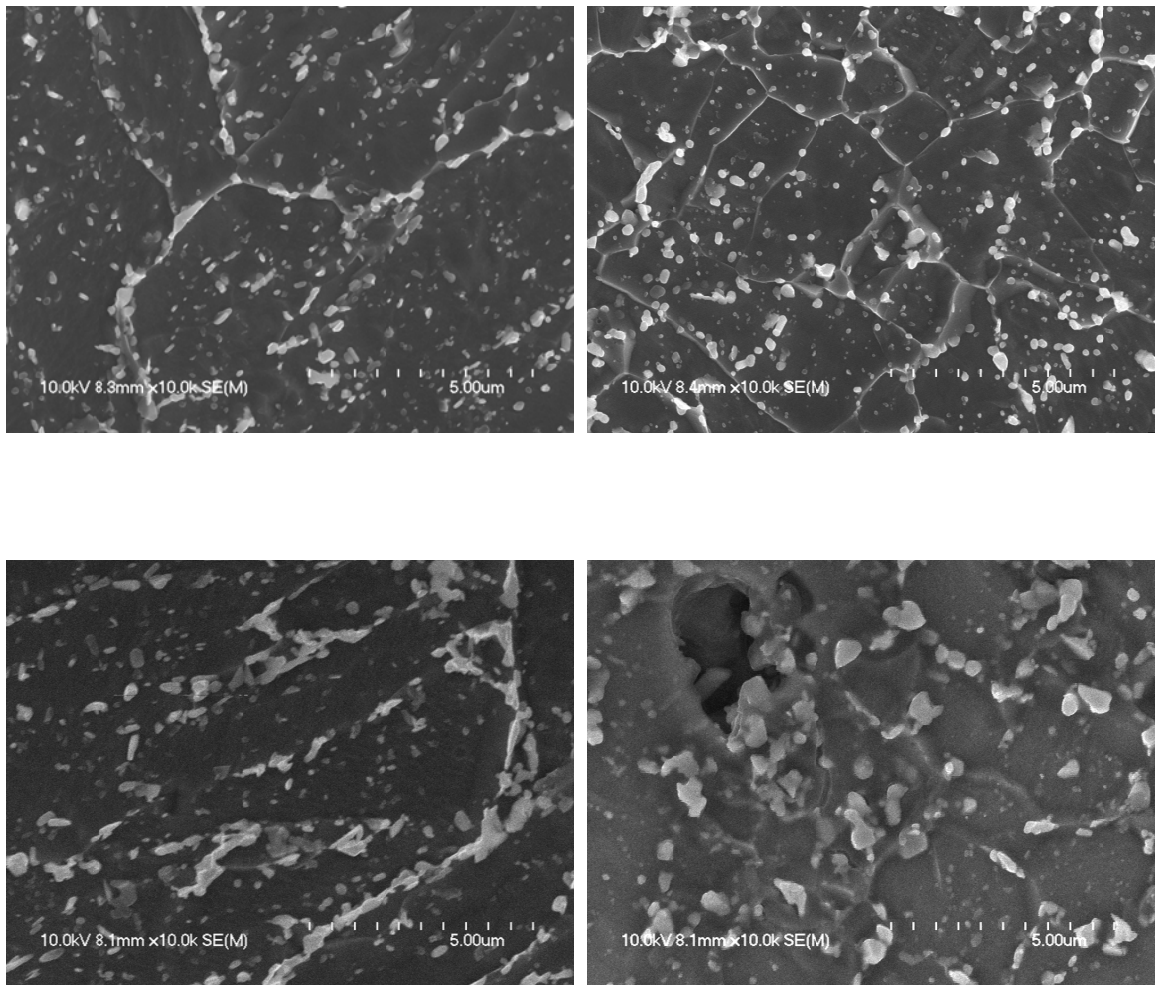


Figure 144: SEM micrographs of base material (left) and fine-grained HAZ region (right) after PWHT (top) and after 13.945 hours of creep exposure (bottom).

## VI. Discussion

On the following pages the results obtained within this work are discussed referring to results of other authors published in literature. The base material microstructures and properties of the three 9% Cr steels are compared among each other and to most advanced European and Japanese candidate materials.

The influence of different weld thermal cycles on the HAZ microstructure and its consequences for the mechanical properties are discussed in the second sub-section.

Finally, the effect of weld metal selection on the long-term creep behaviour of cross-welds is discussed in the third sub-section on the basis of the results of the Matching Program.

### 1 Base material properties

In the as-received condition, which is the normalised and tempered condition, all three steels exhibit a tempered martensitic microstructure. Evidence of retained austenite in CB2A, given by X-ray diffraction measurements could not be verified by optical microscopy. This is attributed to the low volume fraction of 1%.

The cast steel variants CB2A and CB2 feature an inhomogeneous shape of the prior austenite grains. The diameter ranges from several hundred micrometers to millimetres. The forged steel NPM1 is characterised by a uniform grain size with an average diameter of 255  $\mu\text{m}$ .

In all three steels, precipitates are mainly positioned along prior austenite and martensite lath boundaries. Similar domains of precipitates are detected in all three steels. They are identified by electron microscopy as chromium carbides, vanadium nitrides or (V,Nb)(C,N) carbonitrides. In NPM1 base material, optical and electron microscopy reveal a precipitate free zone of several microns in width adjacent to the prior austenite grain boundaries. This effect is not observed in the cast steel variants, CB2A and CB2.

Thermodynamic analysis of equilibrium phases predicts almost the same types of precipitates for the three steels. These are:  $\text{M}_{23}\text{C}_6$ , NbC, VN, Laves phase,  $\text{M}_2\text{B}$  and Z-phase. Additionally,  $\text{M}_6\text{C}$  carbides are supposed to be stable in NPM1 material. At the desired service temperatures of 600°C or 650°C, Z-phase is stable in all three steels and forms on

the expense of VN particles. At service temperature, NPM1 features the highest equilibrium phase fraction of Laves phase. This can be attributed to the increased tungsten content of 3%. In CB2A and CB2, Laves phase is based on molybdenum, whereas it is tungsten-based in NPM1 as a consequence of the different alloying concept.

Calculated equilibrium transformation temperatures slightly differ for the three materials. Whereas  $A_{e1}$  and  $A_{e3}$  are similar for all three steels, NPM1 is the first to form delta ferrite at around 1180°C. This is about 70°C lower as predicted for CB2A and CB2. NPM1 is also the only steel amongst the materials investigated that can become fully ferritic at highest temperatures.

With a chromium content close to 9%, all three steels are prone to contain some level of delta ferrite. Calculated phase diagrams show that the actual chromium content is very close to the threshold value of chromium where delta ferrite becomes a stable phase down to room temperature. This can be relevant when precipitates dissolve and cause a local enrichment of ferrite stabilising elements. Local enrichment is most probable during weld thermal cycles characterised by a high peak temperature and fast cooling. Interstitial elements such as carbon have a high diffusivity and can easily diffuse away from enriched regions. For substitutional elements, such as chromium or molybdenum, local enrichment cannot be levelled out by diffusion because of the lower diffusional mobility.

All base materials have been investigated concerning the possible precipitation of boron nitrides. CB2 shows the largest and also highest number density of boron nitrides closely followed by CB2A. In NPM1 base material, only small and widely spaced BN particles can be found. Inserting the three steel variants into the boron nitride diagram developed by Sakuraya,<sup>119, 120</sup> the tendency observed by electron microscopy is confirmed. Whereas, right of the experimentally determined line, BN particles have been observed, left of it, no BN particles have been found. In the diagram, CB2 is positioned farthest right of the predicted BN solubility line indicating precipitation of large boron nitrides. NPM1 is very close to the line where, in other steels, only small BN particles have been observed.

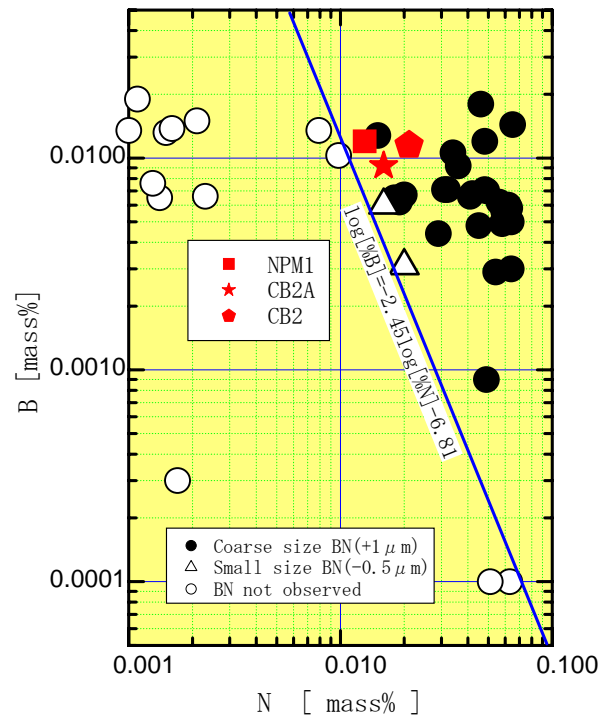


Figure 145: Tendency of CB2A, CB2 and NPM1 to contain boron nitrides based on experimental results obtained by Sakuraya at NIMS.<sup>119</sup>

Many researchers claim a beneficial effect of boron on the creep properties of martensitic steels.<sup>121, 122</sup> However, boron can only improve the creep behaviour if it is either enriched in other precipitates or dissolved in the matrix. Boron dissolved in  $M_{23}C_6$  carbides is said to retard their coarsening and, therefore, improve the long-term stability of the microstructure during creep exposure.<sup>123-126</sup> If the boron is bound in coarse BN particles, it is considered as ineffective. Since only few and very small BN particles are found in NPM1 base material, a beneficial effect of the remaining boron on the long-term creep properties is expected.

Base metal creep properties for NPM1 have been evaluated up to a duration of almost 9.000 hours. When comparing creep properties of forged and cast materials, the different initial microstructural constitution, e.g. grain size, has to be taken into account. At 650°C, CB2 base material of the same melt as investigated within this work exhibited a creep rupture strength of 90 MPa or below (see Appendix B). Compared to the 130 MPa of steel

NPM1, further progress can also be expected for cast steel variants based on a sound alloying concept.

In comparison to the promising European rotor steel B2, NPM1 also exhibits improved creep strength. An improvement in the long-term creep behaviour of NPM1 base material has to be verified by creep tests at lower stress levels.

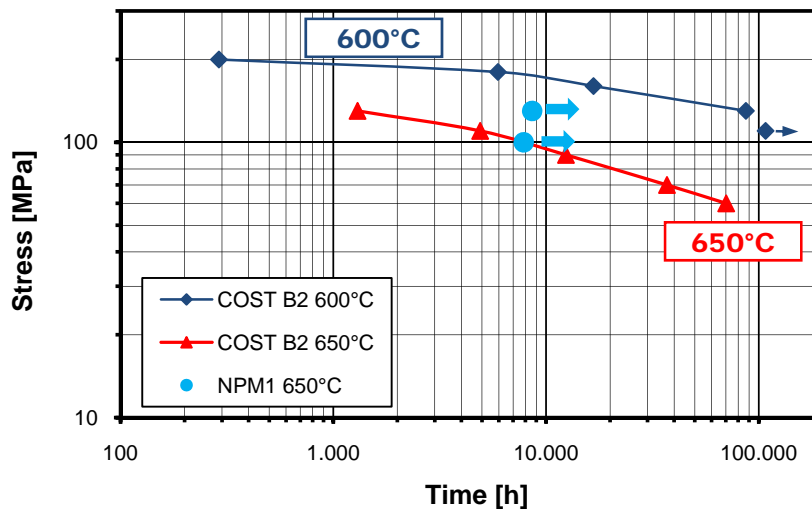


Figure 146: Comparison of creep rupture strength of the promising European B2 rotor steel and NPM1 base material.<sup>127</sup>

The minimum creep rate for the European rotor steel variants B2 and FB2 at 650°C and 80 MPa have been evaluated at the Austrian Research Center.<sup>128</sup> B2 exhibits a minimum creep rate of  $1 \times 10^{-6} \text{ h}^{-1}$  and FB2 base material  $5.4 \times 10^{-7} \text{ h}^{-1}$ . Although tested at a higher stress level of 130 MPa, NPM1 base material features a value of  $6.7 \times 10^{-7} \text{ h}^{-1}$ , which is clearly below the value for B2.

Compared to the Japanese prototype of NPM1, with additions of 38 ppm nitrogen and 139 ppm boron, the increased nitrogen content of 130 ppm leads to improved creep behaviour in the short term range up to 10,000 hours. Precipitation of fine nitrides can give additional creep strength to the material.<sup>129</sup> Again, these beneficial effects have to be confirmed also at lower stress levels and longer testing times. This is especially necessary, since the equilibrium calculation predicts a complete dissolution of VN by Z-phase precipitation at long times. The minimum creep rate for NPM1 base material is similar to the one ob-

tained at NIMS for a 9Cr-3W-3Co-VNb steel with addition of 140 ppm boron and 80 ppm nitrogen tested at 120 MPa.<sup>130</sup>

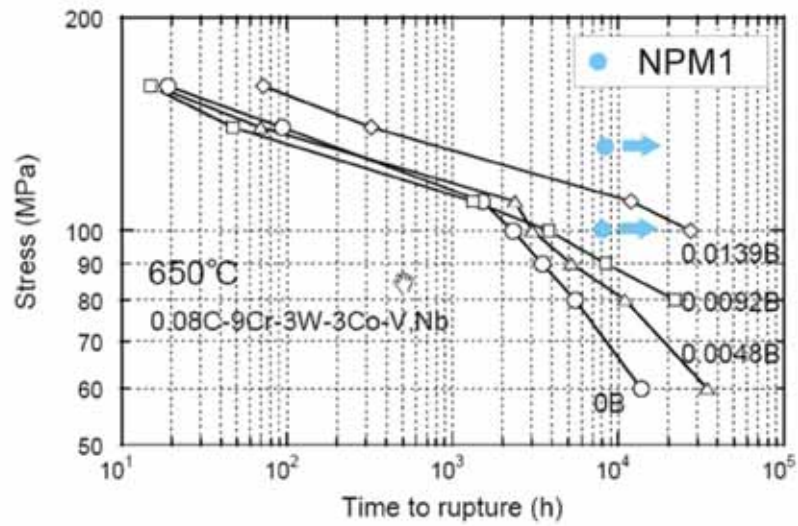


Figure 147: Comparison of creep rupture strength of boron containing 9Cr-3W-3Co-VNb test alloys and NPM1 steel at 650°C.

## 2 Heat Affected Zone

### *Phase transformations*

Phase transformations during characteristic weld thermal cycles have been observed by dilatometry and in-situ X-ray diffraction. All three steels show similar phase transformation temperatures for comparable weld thermal cycles. The onset ( $A_{C1}$ ) and completion ( $A_{C3}$ ) of austenite formation are strongly influenced by the heating rate of the thermal cycle. The calculated thermal cycles are characterised by an increasing heating rate with increasing peak temperatures. Increasing heating rate leads to a superheating of the tempered martensite before transformation to austenite starts. For NPM1, the equilibrium calculation predicts the onset of austenite formation at  $A_{C1}=828^{\circ}\text{C}$ . Analysis of dilatometric data shows the  $A_{C1}$  temperature to be at  $920^{\circ}\text{C}$  for the  $T_p=925^{\circ}\text{C}$  and  $970^{\circ}\text{C}$  for the  $T_p=1300^{\circ}\text{C}$  simulated thermal cycle.

The start of martensite formation is directly related to the experienced peak temperature. Higher peak temperatures lead to lower  $M_s$ -temperatures. In CB2 steel, martensite formation during a GTAW cycle starts at  $410^{\circ}\text{C}$  for a simulated peak temperature of  $T_p=950^{\circ}\text{C}$ . Increasing the peak temperature to  $1300^{\circ}\text{C}$  shifts the onset of martensite formation to a temperature of  $M_s=355^{\circ}\text{C}$ . Dissolution of precipitates during high temperature thermal cycles causes an enrichment of alloying elements, especially carbon, within the matrix. Increased carbon content in the austenite matrix is known to lower the  $M_s$ -temperature in steels. The martensite-finish temperature ( $M_f$ ) behaves similarly.

### *Formation of delta ferrite and its implications on toughness*

Formation of delta ferrite at highest peak temperatures has been directly observed by in-situ X-ray diffraction during characteristic weld thermal cycles. In all three steel variants, the formation of delta ferrite is observed at temperatures above  $1250^{\circ}\text{C}$ . The maximum amount of delta ferrite as well as the level of retained delta ferrite is strongly influenced by the chemical composition of the steels and by the heating and cooling rates of the thermal cycle. In NPM1, a volume fraction of 65% delta ferrite is formed in the high temperature region ( $>1200^{\circ}\text{C}$ ) for the thermal cycle with a lower heating rate ( $10\text{K s}^{-1}$ ) compared to 45% delta ferrite for the faster thermal cycle with a heating rate of  $100\text{K s}^{-1}$ . Fast weld thermal cycles as well as thermal cycles with a reduced heating rate lead to a retention of a

certain amount of retained delta ferrite down to room temperature. The highest level of retained delta ferrite at room temperature is observed in NPM1 (4%) followed by CB2 (3%) and CB2A (2%). In addition to delta ferrite, also austenite, which does not transform to martensite on cooling, is retained in all three steels.

Formation of delta ferrite in CB2A is also observed by a series of experiments using a quenching dilatometer. This investigation reveals that only a little amount of delta ferrite is formed during the heating part of the weld thermal cycle up to a peak temperature of 1300°C. The main proportion of delta ferrite forms during cooling above a temperature of approximately 1200°C. Below this temperature, re-transformation of delta ferrite to austenite takes place and the level of delta ferrite again decreases. Similar to the results of the X-ray diffraction experiments, a certain level of delta ferrite is retained down to room temperature.

The retained delta ferrite appears in two manifestations. In the two cast steel variants CB2A and CB2, bulky grains of delta ferrite are visible. Fine, lath-like grains of delta ferrite along prior austenite grain boundaries or embedded in-between martensite laths are observed in all three steels. These two appearances of delta ferrite are attributed to the production route of the individual steels. The casting process produces local segregations resulting in a non-homogeneous distribution of alloying elements. Areas enriched in ferrite-stabilising elements can transform uniformly to delta ferrite and these large grains can be retained down to room temperature. In steel NPM1, homogenisation of the elemental distribution is achieved by the forging process. Above a temperature of 1100°C, precipitates, especially chromium carbides, along prior austenite grain and martensite lath boundaries dissolve. Dissolution of precipitates leads to a local enrichment in alloying elements in the adjacent areas. The local enrichment in interstitial elements (C, N) is easily levelled out due to their high diffusivity at these high temperatures. In contrast, the relatively fast weld thermal cycle and the low diffusivity inhibit a uniform elemental distribution of substitutional elements (Cr, Mo). Local enrichment in ferrite stabilising elements promotes the formation and retention of delta ferrite along prior austenite grain and martensite lath boundaries. Metallography on samples quenched during simulated thermal cycles support the proposed mechanism.

The hardness of the retained delta ferrite ( $\sim 200\text{HV}_{0.01}$ ) is significantly lower compared to the newly formed martensite ( $\sim 400\text{HV}_{0.01}$ ). Therefore, the reduction of macro-

hardness observed in specimens simulated with peak temperatures higher than 1200°C is attributed to a certain level of soft retained delta ferrite within the hard martensitic matrix.

During post-weld heat treatment, extensive precipitation takes place at the phase boundaries of delta ferrite. TEM investigations on weld-simulated and heat-treated specimens of CB2A show the precipitation of chromium- and molybdenum-rich carbides as well as vanadium nitrides. Especially carbides form a dense seam around the grains of retained delta ferrite. The shape of delta ferrite grains is not altered by the PWHT. At highest peak temperatures, when delta ferrite starts to form, partitioning of alloying elements can be observed. It is shown by EDX line-scans that the delta ferrite is enriched in ferrite stabilising elements, especially chromium and molybdenum, at the grain boundaries. In return, the carbon is forced into the adjacent austenitic regions because of the low solubility of carbon in the bcc lattice. The retained delta ferrite at room temperature is still enriched in chromium and molybdenum.

During post-weld heat treatment, partial homogenisation of the microstructure occurs. The martensite is tempered and re-precipitation takes place. At the grain boundaries of delta ferrite, the increased chromium and molybdenum content leads to increased precipitation of carbides. Fracture investigations on impact specimens with weld simulated microstructure show a preferred formation of cracks along the delta ferrite – martensite phase boundary. The drop in toughness at a peak temperature of about 1200°C corresponds to the first appearance of delta ferrite in CB2A (see Figure 148). The dense seam of carbides surrounding the retained delta ferrite regions is the preferred location for the initiation of cracks. Retained delta ferrite in combination with a dense seam of carbides along its grain boundaries as well as an increased prior austenite grain size in general produced by high temperature weld cycles can explain the reduced impact toughness values of microstructures exposed to high temperature thermal cycles and subsequent tempering.

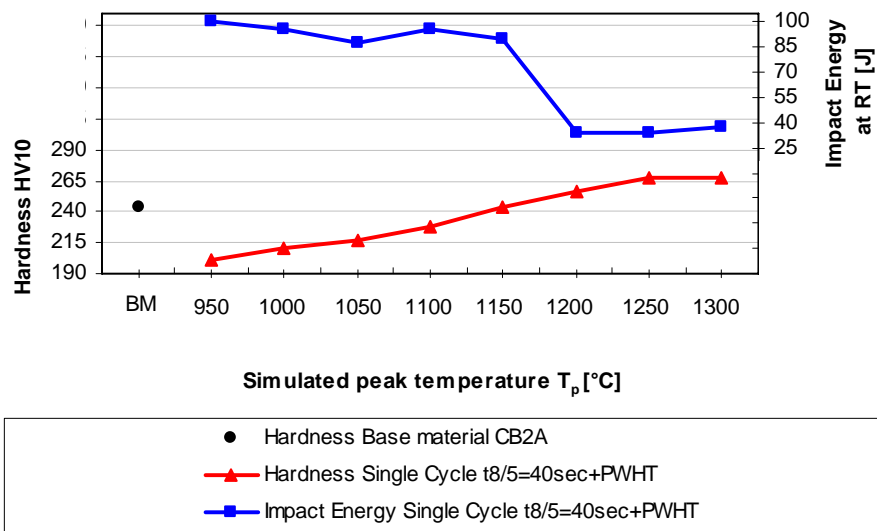


Figure 148: Hardness and impact toughness of weld simulated CB2A material as a function of peak temperature obtained by A. Schalber.<sup>113</sup>

### *Suppression of grain refinement in the HAZ of NPM1*

The grain size in the heat affected zone is generally a function of the weld cycle peak temperature. CB2 shows a heat affected zone, which is typical for these ferritic steel grades. At highest peak temperatures ( $\gg A_{C3}$ ), a coarse-grained microstructure is formed. Specimens exposed to temperatures in the range of the  $A_{C1}$  temperature show a complete refinement of the microstructure, and the grain size is in the range of 10  $\mu\text{m}$ .

NPM1 shows a completely different grain structure in the HAZ. Specimens exposed to a peak temperature of 1100°C show almost the same microstructure as observed in the base material before weld simulation. Although the steel has fully transformed to austenite on heating and to martensite on cooling, the initial grain size and even the orientation and the macroscopic appearance of the martensitic laths is retained. Martensite laths observed in the base material look identically after the weld simulation. Additionally, some newly formed small grains can be observed close to the prior austenite grain boundaries. On increasing the peak temperature to 1200°C, the fraction of fine grains also increases. The interior of the prior austenite grains still shows the same martensitic lath structure as observed in the base material. Initial austenite grains with an average size of 255  $\mu\text{m}$  are still recognisable. Further increase in peak temperature to 1300°C leads to a blurred appearance of the microstructure. Close to the prior austenite grain boundaries, the microstructure is

almost fully refined. The prior austenite grain boundaries of the base material cannot be detected any longer, although the initial grain interior still shows some areas with homogeneous packages of martensite laths. Similar behaviour is observed in the HAZ of the multi-layer welded joint. No distinct fine-grained zone formation is observed. Throughout the entire HAZ, some large packages of martensite laths prevail next to newly formed fine grains. Therefore, the HAZ microstructure formed in NPM1 is not uniform and cannot be categorised in coarse- and fine-grained areas. These results show that, although the nitrogen content of the present NPM1 melt is increased compared to the Japanese prototype alloy, still the suppression of a fine-grained zone formation is maintained. As shown in the results section of the base material characterisation, NPM1 shows improved creep strength compared to the European steel grades B2, FB2, CB2 and the 9Cr-3W-3Co-VNbB steel with reduced nitrogen content. Additionally, the HAZ microstructure formed in NPM1 has a high potential for the suppression of Type IV cracking since Type IV cracking occurs per definition only in a microstructure with small ferritic grains. Therefore, NPM1 is a very promising candidate material for components in thermal power generation.

### 3 Matching Program

#### *Cross-weld creep strength*

Up to 10.000 hours of creep testing, the creep strength of cross-welds is within the scatter-band of E911 base material. At longer testing times, results of creep tests indicate a significant reduction of creep strength of cross-welds compared to the base material. After 30.000 hours, the reduction in cross-weld creep strength increases already to approximately 30%. This is almost the same reduction of creep strength as observed in weldments of P91 and P122 after 100.000 hours at 600°C.<sup>17, 18</sup> The abrupt decrease in creep strength takes place close to 20.000 hours of testing. Therefore, extrapolation from results of short-term test up to a duration of 20.000 hours, to longer times can result in significant over-estimation of the cross-weld creep strength. This is even more crucial as the discrepancy between base material and cross-weld creep strength is known to increase further, with increasing test duration. These results emphasise the importance of long-term testing data, not only for base and weld metals, but also for welded joints.

Results of the Matching Program indicate that the location of failure of cross-welds is influenced by the applied testing stress. For the under-matching (P91-type) and matching (E911-type) weld metals, final fractures at higher testing stresses occur in the weld metal. At these stress levels, the creep strength of the base material and of the HAZ are superior to that of the weld metals. Cross-welds with over-matching, P92-type, weld metal show best performance at highest stress levels. Therefore, no weld metal failures are observed for all over-matching cross-welds.

Improved creep behaviour of welds fabricated with high creep resistant weld metal is limited to high stress levels and short test durations. This advantage diminishes as the applied testing stress is lowered and the testing time increases. Below 100 MPa, no improvement in cross-weld creep strength can be achieved by the selection of a weld metal of higher creep strength. At lower stress levels, the discrepancy in base material and cross-weld creep strength is almost independent of the selected weld metal. Analysis of failure locations shows that at lower stress levels the heat affected zone is the weakest region. Time to rupture and fracture location are only weakly influenced by the selected weld metal. Therefore, a restraining effect of high strength weld metal on the heat affected zone is not expected to be present after long testing times.

### *Weld metal failures*

Weld metal failures observed in E911 cross-welds are characterised by low macroscopic deformation independent of the used weld metal. If the solidified weld metal microstructure is not altered by subsequently deposited weld beads, cracking is observed mainly along the grain boundaries of the primary solidified columnar weld metal grains. Grain boundaries oriented perpendicular to the load direction show enhanced crack formation.

Weld metal microstructure, refined by multi-layer welding, shows formation of creep voids mainly along prior austenite grain boundaries.

Whether the weld metal microstructure is characterised by larger columnar grains or a fully refined structure, damage is mainly observed along the prior austenite grain boundaries.

### *Type IV failures*

Type IV cracking in the heat affected zone is the predominant failure mode in specimens tested below 100 MPa. These stress levels are more relevant in practice, since the design stress of welded power plant components is below 100 MPa. The selected weld metal is only of minor influence on the overall cross-weld creep strength, as the failures are located in the heat affected zone of the base material. A possible restraining effect of the weak HAZ areas by the adjacent stronger weld and base metal is not detected for long-running tests, so far. Restraining might be active at highest stresses but at lower stress levels and longer testing times, time to rupture is almost similar for all three welds. This is well in line with research work of Kimmins and Smith<sup>92</sup> who concluded that material weak in creep deforms independently of adjacent stronger material. Specimens of the matching series slightly tend to show longer time to rupture, superior to the under- and over-matching welds.

Type IV cracking can be defined as the life-limiting failure mode in E911 cross-welds. It is a problem of the refined microstructure in the heat affected zone of the base material. The fine-grained HAZ region is characterised by a grain size lower than 5  $\mu\text{m}$ . No martensitic lath structure is observed in this region. Only partial dissolution of precipitates during the weld thermal cycle possibly leads to enhanced coarsening of the undissolved particles during PWHT. Coarsening continues during creep exposure. In this part of the HAZ, the strengthening effect of a martensitic microstructure with finely dispersed precipitates is

inferior from the beginning of creep exposure. Additionally, diffusion in the FGHAZ is enhanced by the high density of prior austenite grain boundaries. Therefore, creep at lower stress levels, as a diffusive process, is enhanced in this region. It is evident that all processes governed by diffusion can proceed faster in the FGHAZ compared to the base metal, weld metal or other regions of the HAZ. These processes are, for example, annihilation of dislocations, coarsening of precipitates, and precipitation of unfavoured phases (e.g. Z-phase). To conclude, the problematic with the microstructure in the fine-grained HAZ is that it is already recovered to a major extent before creep exposure starts and, additionally, recovery during creep proceeds faster compared to other regions within the cross-welds. Failure is literally forced to the fine-grained heat affected zone.

A crucial feature of Type IV cracking in practice is that it is very difficult to detect in components during service. Damage initiates by the subsurface formation of creep voids. Surface inspection methods, such as replication techniques, penetration testing or eddy current testing, are not able to detect Type IV damage until very late in life. Low deformation fractures, characteristic for Type IV failures, mean low visibility of damage by optical inspections of components. Therefore, final fracture of components takes place without or only very limited signs of warning by deformation of the damaged area. Only the application of advanced volumetric inspection methods allows the identification of Type IV damage already in the initial stage.



## VII. Summary

The work presented in this thesis is concerned with the evolution of the microstructure in the heat affected zone of boron containing martensitic 9% chromium steels. Special focus is put on the relationship between microstructure and mechanical properties, especially the creep behaviour.

Long-term creep testing of E911 cross-welds shows that, at lower stress levels and longer testing times, the heat affected zone (HAZ) of the base material is the weakest point. HAZ creep failures are predominant irrespective of the creep strength of the weld filler metal. Type IV cracking in the fine-grained HAZ (FGHAZ) region is the only failure mechanism observed at stresses below 100 MPa and testing durations up to 30.000 hours, so far. The location of failure is characterised by equiaxed grains with an average size below 10  $\mu\text{m}$ . No martensitic lath structure is observed in this region and precipitates in this region tend to be coarser from the beginning of testing on. Therefore, the FGHAZ enters service already in a weaker condition compared to other regions of a cross-weld. Additionally, coarsening of precipitates during creep exposure, recovery, as well as other diffusion-driven processes are enhanced in the FGHAZ by the high density of prior austenite grain boundaries. Finally, Type IV cracking leads to a reduced cross-weld creep strength compared to the base material of 30% already after 30.000 hours of testing. This discrepancy in creep strength level is known for other martensitic steels to increase with increasing testing duration. Type IV cracking in the fine-grained HAZ is identified as the major end-of-life failure mechanism at service stresses in E911 cross-welds independently of the used weld metal.

The evolution of the HAZ microstructure during weld thermal simulation is studied in detail for three 9% chromium steels with controlled additions of boron. In as-received condition, which is the quenched and tempered condition, all three steels show almost similar microstructural features. They all exhibit a tempered martensitic microstructure with finely dispersed precipitates mainly aligned along prior austenite and martensite lath boundaries. The two cast steel variants CB2A and CB2 are characterised by large irregular shaped grains, whereas the forged material NPM1 has a homogeneous polygonal grain structure. In CB2A and CB2, numerous large boron nitride particles with a diameter of several microns are found. The boron-nitrogen balanced 9Cr-3W-3CoVNb steel NPM1

shows only very small ( $< 1 \mu\text{m}$ ) and scarcely distributed BN particles. Therefore, it is assumed that, in this steel most of the boron is either incorporated in other precipitates or dissolved in the matrix.

Screening creep tests of NPM1 material indicate excellent creep properties. The creep rupture strength at 130 and 100 MPa and 650°C up to the duration of 10,000 hours so far is well above the creep strength of the most promising European candidate materials B2, FB2 and CB2, as well as above the creep strength of the Japanese low nitrogen reference steel.

In-situ X-ray diffraction using synchrotron radiation gives insight into phase transformations during thermal weld simulation. For all three steels, the formation and retention of delta ferrite is observed. Dense precipitation of mainly chromium carbides along the phase boundaries of retained delta ferrite during PWHT contributes to the reduced impact toughness of coarse-grained HAZ simulated microstructure.

HAZ grain structure in NPM1 steel exhibits high potential to prevent Type IV cracking in cross-welds. The cast steels, CB2A and CB2 show a fully refinement of the grain structure in regions exposed close to the  $A_{C3}$  transformation temperature. In NPM1, no refinement of the microstructure is observed up to highest peak temperatures. The initial microstructure is preserved throughout the weld thermal cycles although the steel experiences multiple phase transformations. At highest peak temperatures, some smaller grains nucleate close to the initial grain boundaries but a complete refinement of the microstructure is not observed. Although the exact mechanism for this behaviour is not fully understood yet, the prevention of a complete fine-grained HAZ can result in the elimination of the susceptibility to Type IV cracking. This improvement can lead to similar creep strength levels of cross-welds and base material and render a weld strength factor unnecessary. Further confirmation applying long-term creep tests of cross-welds are necessary.

## VIII. Outlook

The promising improved creep behaviour of the boron-nitrogen balanced 9Cr-3W-3Co-VNb base material assessed by short-term tests up to 10.000 hours has to be approved by long-term tests at lower stress levels. Therefore, additional melts of NPM1 will be produced and investigated.

The formation and retention of delta ferrite during characteristic weld thermal cycles has been observed within this work. The underlying mechanism of the very localised formation of delta ferrite will be studied in detail in continuative work using a new quenching dilatometer at the institute and kinetic simulation.

The determination of the exact mechanism of the suppression of the formation of a fine-grained heat affected zone in NPM1 steel emerged to exceed the scope of this work. The evolution of grain structure during characteristic weld thermal cycles will be investigated in future work. The creep strength of cross-weld specimens of the NPM1 test melt fabricated within this work will be evaluated by creep testing at 650°C and several stress levels. The location of failure as well as the failure mechanism will be investigated extensively.

The Matching Program will be continued. Interesting results of the specimens creep tested at lower stress levels can be expected within the next years.



## IX. References

- <sup>1</sup> Armor A F and Viswanathan R, “Supercritical fossil steam plants: Operational issues and design needs for advanced plants”, in 4<sup>th</sup> int conf *Advances in Materials Technology for Fossil Power Plants*, Hilton Head Island, ASM International, 2005.
- <sup>2</sup> Viswanathan R, Henry J F, Tanzosh J, Stanko G, Shingledecker J and Vitalis V, “U.S. Program on materials technology for USC power plants”, in 4<sup>th</sup> int conf *Advances in Materials Technology for Fossil Power Plants*, Hilton Head Island, ASM International, 2005.
- <sup>3</sup> Kern T U, Wieghardt K and Kirchner H, „Material and design solutions for advanced steam power plants”, in 4<sup>th</sup> int conf *Advances in Materials Technology for Fossil Power Plants*, Hilton Head Island, ASM International, 2005.
- <sup>4</sup> Masuyama F, “Alloy development and material issues with increasing steam temperature”, in 4<sup>th</sup> int conf *Advances in Materials Technology for Fossil Power Plants*, Hilton Head Island, ASM International, 2005.
- <sup>5</sup> Blum R, Vanstone R W and Messelier-Gouze C, “Materials development for boilers and steam turbines operating at 700°C”, in 4<sup>th</sup> int conf *Advances in Materials Technology for Fossil Power Plants*, Hilton Head Island, ASM International, 2005.
- <sup>6</sup> Staubli M, Bendick W, Orr J, Deshayes F and Henry C, „European collaborative evaluation of advanced boiler materials”, in int conf *Materials for advanced power engineering 1998*, Liege, Forschungszentrum Jülich, 1998.
- <sup>7</sup> Cerjak H, “*Welding of steam turbine components*”, Study report of the COST 505 Welding Group, Directorate General Science, Research and Development, Brussels, 1992.

- <sup>8</sup> Easterling K, “*Introduction to the physical metallurgy of welding*”, Butterworths, 1983.
- <sup>9</sup> Masuyama F, Matsui M and Komai N, “Creep rupture behaviour of advanced 9-12%Cr steel weldment”, *Key Engineering Materials*, 2000 **171-174** 99-108.
- <sup>10</sup> Letofsky E, „Das Verhalten von Schweißverbindungen moderner Kraftwerkswerkstoffe“, *Doctoral Thesis*, Graz University of Technology, 2001.
- <sup>11</sup> Morris P F, “Terms and Terminology for weld creep testing”, *ECCC Recommendations*, 2001 2(IIb).
- <sup>12</sup> Allen D J, Harvey B and Brett S J, “Fourcrack – An investigation of the creep performance of advanced high alloy steel welds”, in int conf *Creep & Fracture in High Temperature Components – Design & Life Assessment Issues*, London, DEStech Publications, 2005.
- <sup>13</sup> Tu S T, Segle P and Gong J M, “Strength design and life assessment of welded structures subjected to high temperature creep”, *Int J Pres Ves & Piping*, 1996 **66** 171-86.
- <sup>14</sup> AD 2000-Merkblatt B 0, Ausgabe 01.2003, VdTÜV, 2003.
- <sup>15</sup> Masuyama F, “Creep rupture life and design factors for high strength ferritic steels”, in int conf *Creep & Fracture in High Temperature Components – Design & Life Assessment Issues*, London, DEStech Publications, 2005.
- <sup>16</sup> Sandstrom R and Tu S T, “The effect of multiaxiality on the evaluation of weldment strength reduction factors in high-temperature creep”, *Transactions of the ASME*, 1994 **116** 76-80.

- <sup>17</sup> Tabuchi M and Takahashi Y, “Evaluation of creep strength reduction factors for welded joints of modified 9Cr-1Mo steel (P91)”, *2006 ASME Pressure Vessels and Piping Division Conference*, Vancouver, ASME, 2006.
- <sup>18</sup> Takahashi Y and Tabuchi M, “Evaluation of creep strength reduction factors for welded joints of HCM12A (P122)”, in *2006 ASME Pressure Vessels and Piping Division Conference*, Vancouver, ASME, 2006.
- <sup>19</sup> Schubert J, Klenk A and Maile K, “Determination of weld strength factors for the creep rupture strength of welded joints”, in int conf *Creep and Fracture in High Temperature Components – Design & Life Assessment Issues*, London, DEStech Publications, 2005.
- <sup>20</sup> Francis J A, Mazur W and Bhadeshia H K D H, “Type IV cracking in ferritic power plant steels”, *Mater Sci Technol*, 2006 **22(12)** 1387-95.
- <sup>21</sup> Abe F, “Ultra-steel R&D in NIMS for 650°C USC plant”, in *8<sup>th</sup> Ultra-Steel Workshop*, Steel Research Center, NIMS, Tsukuba, 2004.
- <sup>22</sup> Granjon H (1991), *Fundamentals of Welding Metallurgy*, Cambridge, Abington Publishing.
- <sup>23</sup> Schulze G (2004), *Die Metallurgie des Schweißens*, Berlin, Springer
- <sup>24</sup> Vekeman J, Dhooge A, Huysmans S, Vandenberghe B and Jochum C, „Weldability and high temperature behaviour of 12% Cr-steel for tubes and pipes in power plants with steam temperatures up to 650°C”, *IIW Report XI-863-06*, 2006.
- <sup>25</sup> Reed R and Bhadeshia H K D H, „A simple model for multipass steel welds“, *Acta Metal Mater*, 1994 **42(11)** 3663-3678.

- <sup>26</sup> Cerjak H, Nagel G and Prader R, „Quantifizierung der Zähigkeitsverteilung in einer dickwandigen RDB-UP-Viellagenschweißung, in *MPA-Seminar Sicherheit und Verfügbarkeit in der Anlagentechnik mit dem Schwerpunkt Komponenten nuklearer und konventioneller Kraftwerke*, 1996
- <sup>27</sup> Lundin C D, „Weld performance in high energy piping“, in 5th int conf *Trends in Welding Research*, Pine Mountain, ASM, 1999.
- <sup>28</sup> Faulkner R G, Williams J A, Gonzales Sanchez and Marshall A W, Influence of Co, Cu and W on the microstructure of 9%Cr steel weld metals, *Materials Science and Technology*, 2003 **19** 347-354.
- <sup>29</sup> Fidler R S and Gooch D J, The hot tensile properties of simulated heat affected zone structures in 9CrMo and 12CrMoV steels, in int conf *Ferritic Steels for Fast Reactor Steam Generators*, London, 1978.
- <sup>30</sup> Chandravathi K S, Laha K, Rao B S and Mannan S L, Microstructure and tensile properties of modified 9Cr-1Mo steel (grade 91), *Materials Science and Technology*, 2001 **17** 559-565.
- <sup>31</sup> Laha K, Chandravathi K S, Rao K B S and Mannan S L, Hot tensile properties of simulated heat-affected zone microstructures of 9Cr-1Mo weldment, *International Journal of Pressure Vessels and Piping*, 1995 **62** 303-311.
- <sup>32</sup> Kumar A, Laha K, Jayakumar T, Bhanu Sakara Rao K and Raj B, Comprehensive microstructural characterisation in modified 9Cr-1Mo ferritic steel by ultrasonic measurements, *Metallurgical and Materials Transactions A*, 2002 **33A** 1617-1626.
- <sup>33</sup> Soo J N, Creep crack growth in 9Cr1Mo, in int conf *Ferritic Steels for Fast Reactor Steam Generators*, London, BNES, 1978.

- <sup>34</sup> Yamada K, Igarashi M, Muneki S and Abe F, Effect of Co addition on microstructure in high Cr ferritic steels, *ISIJ International*, 2003 **43(9)** 1438-1443.
- <sup>35</sup> Mannan S L and Laha K, Creep behaviour of Cr-Mo steel weldments, *Transactions of the Indian Institute of Metals*, 1996 **49(4)** 303-320.
- <sup>36</sup> Totemeier T C, Simpson J A and Tian H, Effect of weld intercooling temperature on the structure and impact strength of ferritic-martensitic steels, *Materials Science and Engineering A*, 2006 **A426** 323-331.
- <sup>37</sup> Moustafa I M, El Bagoury N, Ammar M I, Ibrahim S A and Nofal A A, Solidification mechanism of martensitic stainless steel, *Ironmaking and Steelmaking*, 2001 **28(5)** 404-411.
- <sup>38</sup> Park J S, Kim S J and Lee C S, Effect of W addition on the low cycle fatigue behaviour of high Cr ferritic steels, *Materials Science and Engineering A*, 2001 **A298** 127-136.
- <sup>39</sup> Schäfer L, Influence of delta ferrite and dendritic carbides on the impact and tensile properties of a martensitic chromium steel, *Journal of Nuclear Materials*, 1998 **258-263** 1336-1339.
- <sup>40</sup> Carrouge D, Bhadeshia H K D H and Woolin P, Effect of delta ferrite on the impact properties of supermartensitic stainless steel heat affected zone, *Science and Technology of Welding and Joining*, 2004 **9(5)** 377-389.
- <sup>41</sup> Grobner P J and Hagel W C, The effect of molybdenum on high-temperature properties of 9 pct Cr steels, *Metallurgical Transactions A*, 1980 **11A** 633-642.
- <sup>42</sup> Sawada K, Kushima H and Kimura K, Z-phase formation during creep and aging in 9-12% Cr heat resistant steels, *ISIJ International*, 2006 **46(5)** 769-775.

- <sup>43</sup> Igarashi M and Yoshizawa M, Long-term creep deformation characteristics of advanced ferritic steels for USC power plants, in 4<sup>th</sup> int conf *Advances in Materials Technology for Fossil Power Plants*, Hilton Head Island, ASM International, 2005.
- <sup>44</sup> Liu X Y and Fujita T, Effect of chromium content on creep rupture properties of a high chromium ferritic heat resisting steels, *ISIJ International*, 1989 **29(8)** 680-686.
- <sup>45</sup> Kimura K, Sawada K, Kushima H and Toda Y, „Degradation behaviour and long-term creep strength of 12Cr ferritic creep resistant steels”, in 8th int conf *Materials for Advanced Power Engineering 2006*, Liege, Forschungszentrum Jülich GmbH, 2006.
- <sup>46</sup> Baek J W, Nam S W, Kong B O and Ryu S H, The effect of delta-ferrite in P92 steel on the formation of Laves phase and cavities for the reduction of low cycle fatigue and creep fatigue life, *Key Engineering Materials*, 2005 **297-300** 463-468.
- <sup>47</sup> Hara T and Asahi H, Effect of delta ferrite on sulphide stress cracking in a low carbon 13mass% chromium steel, *ISIJ International*, 2000 **40(11)** 1134-1141.
- <sup>48</sup> Schüller H J, Hagn L and Woitscheck A, “Risse im Schweißnahtbereich von Formstücken aus Heißdampfleitungen - Werkstoffuntersuchungen “, *Der Maschinenschaden*, 1974 **47(1)** 1-13.
- <sup>49</sup> Brett S J, “Type IIIa cracking in ½CrMoV steam pipework systems”, *Science and Technology of Welding and Joining*, 2004 **9(1)** 41-45.
- <sup>50</sup> Viswanathan R and Foulds J, “Failure Experience with seam-welded hot reheat pipes in the USA”, in conf *VGB Conference – Materials and Welding Technology in Power Plants 1994*, Essen, VGB, 1994.

- <sup>51</sup> Lundin C D, Khan K K, Yang D, Hilton S and Zielke W (1990), *Failure analysis of a service-exposed hot reheat steam line in a utility steam plant – WRC Bulletin 354*, New York, Welding Research Council.
- <sup>52</sup> Dhooge A and Vinckier A, “Reheat cracking – A review of recent studies”, *Welding in the World*, 1986 **24(5/6)** 2-17.
- <sup>53</sup> Dix A W and Savage W F, “Factors influencing strain-age cracking in INCONEL X-750”, *Welding Journal*, 1971 **50(6)** 247-252.
- <sup>54</sup> Lundin C D and Khan K K, “Fundamental studies of the metallurgical causes and mitigation of reheat cracking in 1¼-Cr-½Mo and 2¼Cr-1Mo steels”, *Welding Research Council Bulletin 409*, 1996.
- <sup>55</sup> Mayr P, “Charakterisierung und Überprüfung der Schweißbeignung des neu entwickelten hochwarmfesten Werkstoffs P23”, *Master Thesis*, Graz University of Technology, 2004.
- <sup>56</sup> Nevasmaa P, Salonen J, Holmström S and Caminada S, “Heat affected zone toughness behaviour and reheat cracking susceptibility of thermally simulated microstructures in new P23 (7CrWVMoNb9-6) steel”, *IIW Doc. IX-A-08-06*, 2006
- <sup>57</sup> Brett S J, “Cracking experience in steam pipework welds in national power“, in conf *VGB Conference – Materials and Welding Technology in Power Plants 1994*, Essen, VGB, 1994.
- <sup>58</sup> Gooch D J and Kimmins S T, “Type IV cracking in 1/2Cr1/2Mo1/4V / 2 1/4Cr1Mo weldments”, in 3rd int conf *Creep and Fracture of Engineering Materials and Structures*, Swansea, Maney Pub, 1987.
- <sup>59</sup> Smith D J, Walker N S and Kimmins S T, “Type IV creep cavity accumulation and failure in steel welds”, *Int J Pres Ves & Piping*, 2003 **80** 617-27.

- <sup>60</sup> Brear J M, Fairman A, Middleton C J and Polding L, “Predicting the creep life and failure location of weldments”, *Key Engineering Materials*, 2000 **171-174** 35-42.
- <sup>61</sup> Fujibayashi S and Endo T, “Creep behaviour of a low alloy ferritic steel weldment”, in 9th int conf *Creep and Fracture of Engineering Materials and Structures*, Cambridge, Maney Pub, 2001.
- <sup>62</sup> Middleton C J, Metcalfe E, „A review of laboratory Type IV cracking data in high chromium ferritic steels”, in int conf *Steam Plants for the 1990's*, London, IMechE, 1990.
- <sup>63</sup> Brühl F, Cerjak H, Schwaab P and Weber H, “Metallurgical investigation on the base material and weldments of the 9% chromium X10CrMoVNb91”, *Steel Research*, 1991 **62(2)** 75-82.
- <sup>64</sup> Parker J D and Stratford G C, “Strain localisation in creep testing of samples with heterogeneous microstructures”, *Int J Pres Ves & Piping*, 1996 **68** 135-43.
- <sup>65</sup> Tezuka H and Sakurai T, “A trigger of Type IV damage and a new heat treatment procedure to suppress it. Microstructural investigations of long-term ex-service Cr-Mo steel pipe elbows”, *Int J Pres Ves & Piping* 2005 **82** 165-174.
- <sup>66</sup> Shibli I A and Le Mat Hamata N, “Creep and fatigue crack growth in P91 weldments”, in 9th int conf *Creep and Fracture of Engineering Materials and Structures*, Cambridge, Woodhead Publishing, 2001.
- <sup>67</sup> Ennis P J, “The mechanical properties and microstructures of 9% chromium steel P92 weldments”, *OMMI*, 2002 **1(2)** 1-23.

- <sup>68</sup> Takemasa F et al, “Type IV creep damage analysis for full size component test on welded P91 boiler hot reheat piping”, in int conf *Elevated Temperature Design and Analysis, Nonlinear Analysis and Plastic Components*, San Diego, ASME, 2004.
- <sup>69</sup> Lundin C D and Prager M, “A new approach to investigation into Type IV cracking susceptibility”, in int conf *Fitness-for Service Evaluations in Petroleum and Fossil Power Plants*, ASME, 1998.
- <sup>70</sup> Ellis F V and Viswanathan R, “Review of Type IV cracking in piping welds”, in 1st int conf *Integrity of High Temperature Welds*, London, IOM, 1998.
- <sup>71</sup> Brett S J, Oates D L and Johnston C, “In-service Type IV Cracking in a Modified 9Cr (Grade 91) Header”, in int conf *ECCC Creep Conference*, London, 2005.
- <sup>72</sup> Masuyama F, Komai N and Sasada A, “Creep failure experience in welds of advanced steel boiler components”, *IIW Doc. XI-795-04*, International Institute of Welding, 2004.
- <sup>73</sup> Komai N and Masuyama F, “Microstructural degradation of the HAZ in 11Cr-0.4Mo-2W-V-Nb-Cu steel (P122) during creep”, *ISIJ International*, 2002 **42(12)** 1364-1370.
- <sup>74</sup> Shinozaki K, Li D, Kuroki H, Harada H and Ohishi K, “Analysis of degradation of creep strength in heat affected zone of weldment of high Cr heat-resisting steels based on void observation”, *ISIJ International*, 2002 **42(12)** 1578-84.
- <sup>75</sup> Hasegawa Y, Muraki T and Ohgami M, “Metallurgical investigation of a Type IV damage at the heat affected zone of weld for tungsten containing martensitic heat resistant steels”, in conf *Experience with creep-strength enhanced ferritic steels and new and emerging computational methods*, San Diego, ASME, 2004.

- <sup>76</sup> Letofsky E, “Microstructure aspects of creep resistant welded joints”, *IIW Doc. IX-2055-03*, 2003.
- <sup>77</sup> Abe F, Tabuchi M, Kondo M and Tsukamoto S, “Improvement of creep strength of advanced ferritic steel welded joints”, *IIW Report XI-794-04*, 2004.
- <sup>78</sup> Albert S K et al, “Microstructural investigations on Type IV cracking in a high Cr steel”, *ISIJ International*, 2002 **42(12)** 1497-1504.
- <sup>79</sup> Kondo M et al, “Suppression of Type IV failure in high-B low-N 9Cr-3W-3Co-NbV steel welded joint”, in 4th int conf *Advances in Materials Technology for Fossil Power Plants*, Ohio, ASM International, 2004.
- <sup>80</sup> Watanabe T et al, “Creep damage evaluation of 9Cr-1Mo-V-Nb steel welded joints showing Type IV fracture”, *Int J Pres Ves & Piping*, 2006 **83** 63-71.
- <sup>81</sup> Tabuchi M et al, “Creep crack growth behaviour in the HAZ of weldments of W containing high Cr steel”, *Int J Pres Ves & Piping*, 2001 **78** 779-84.
- <sup>82</sup> Letofsky E and Cerjak H, “New quantitative microstructural characterisation on creep tested welded joints”, in 6th int conf *Trends in Welding Research*, Pine Mountain, ASM, 2002.
- <sup>83</sup> Abe F, and Tabuchi M, “Microstructure and creep strength of welds in advanced ferritic power plant steels, *Science Technology of Welding and Joining*, 2004 **9(1)** 22-30.
- <sup>84</sup> Eggeler G et al, “Analysis of creep in a welded P91 pressure vessel”, *Int J Pres Ves & Piping*, 1994 **60** 237-57.

- <sup>85</sup> Masuyama F, Komai N and Sasada A, “Creep failure experience in welds of advanced steel boiler components”, *IIW Doc. XI-795-04*, 2004.
- <sup>86</sup> Kimmins S T, Coleman M C and Smith D J, “An overview of creep failure associated with heat affected zones of ferritic weldments”, in 5th int conf *Creep and Fracture of Engineering Materials and Structures*, London, IOM, 1993.
- <sup>87</sup> Li D, Shinozaki K and Kuroki H, “Stress-strain analysis of creep deterioration in heat affected weld zone in high Cr ferritic heat resistant steel”, *Mater Sci Technol*, 2003 **19** 1253-1260.
- <sup>88</sup> Tabuchi M et al, “Study on the creep fracture of advanced high Cr steel weldment”, *Ultra-Steel conference: Requirements from new Design of Constructions*, Tsukuba, 2003.
- <sup>89</sup> Abe F and Tabuchi M, “Microstructure and creep strength of welds in advanced ferritic power plant steels”, *Science and Technology of Welding and Joining*, 2004 **9(1)** 22-30.
- <sup>90</sup> Perrin I J and Hayhurst D R, „Continuum damage mechanics analyses of type IV creep failure in ferritic steel crossweld specimens”, *Int J Pres Ves & Piping*, 1999 **76(9)** 599-617.
- <sup>91</sup> Abe F, Tabuchi M, Kondo M and Tsukamoto S, “Improvement of creep strength of advanced ferritic steel welded joints”, *IIW-Report XI-794-04*, International Institute of Welding, 2004.
- <sup>92</sup> Kimmins S T and Smith D J, “On the relaxation of interface stresses during creep of ferritic steel weldments”, *Journal of Strain Analysis*, 1998 **33(3)** 195-206.
- <sup>93</sup> Ito T, Nonaka I and Takemasa F, “Full size internal pressure creep test and life evaluation for welded Gr.91 hot reheat piping”, *IIW Doc. XI-796-04*, 2004.

- <sup>94</sup> Parker J and Bisbee L, “Girth weld cracking in high temperature headers”, in int conf *Creep & Fracture in High Temperature Components – Design & Life Assessment Issues*, London, DEStech Publications, 2005.
- <sup>95</sup> Brett S J, “The management of weld cracking in high-temperature CrMoV pipework systems”, in int conf *Assuring it's safe: Integrating Structural Integrity, Inspection and Monitoring into Safety and Risk Assessment*, IMEchE, 1998.
- <sup>96</sup> Kondo M et al, “Suppressing type IV failure via modification of heat affected zone microstructures using high boron content in 9Cr heat resistant steel welded joints”, *Science and Technology of Welding and Joining*, 2006 **11(2)** 216-223.
- <sup>97</sup> Kimmins S T and Gooch D J, “Austenite memory effect in 1Cr-1Mo-0.75V(Ti, B) steel”, *Metal Science*, 1983 **17** 519-532.
- <sup>98</sup> Abe F, “Metallurgy for long-term stabilization of ferritic steels for thick section boiler components in USC power plant at 650°C”, in 8<sup>th</sup> in conf *Materials for Advanced Power Engineering 2006*, Liege, Forschungszentrum Jülich, 2006.
- <sup>99</sup> Buchmayr B, Cerjak H, Witwer M, Maile K, Theofel H and Eckert W, “Experimental and numerical investigations of the creep behaviour of the dissimilar weldment GS-17CrMoV5-11 and X20CrMoV12-1”, *Steel Research*, 1990 **61(6)** 268-273.
- <sup>100</sup> Helander T Z, Andersson H C M and Oskarsson M, “Structural changes in 12-2.25%Cr weldments – an experimental and theoretical approach”, *Materials at High Temperature*, 2000 **17(3)** 389-96.
- <sup>101</sup> Witwer M, “Untersuchungen an Mischschweisverbindungen warmfester CrMoV-Stähle”, *Doctoral Thesis*, Graz University of Technology, 1989.

- <sup>102</sup> Buchmayr B, Cerjak H, Kirkaldy J S and Witwer M, “Carbon diffusion and microstructure in dissimilar Cr-Mo-V-welds and their influence on the mechanical properties”, in 2nd int conf *Trends in Welding Research*, Gatlinburg, ASM International, 1989.
- <sup>103</sup> Rosenthal D, „Mathematical theory of heat distribution during welding and cutting“, *Welding Journal*, 1941 **20(5)** 220-234.
- <sup>104</sup> Rykalin N N (1957), *Berechnung der Wärmevorgänge beim Schweißen*, Berlin, VEB Verlag Technik Berlin.
- <sup>105</sup> Goldak J, Chakravarti A and Bibby M, “A new finite element model for welding heat source”, *Metall. Trans. B*, 1984 **15B** 299–305.
- <sup>106</sup> Buchmayr B, “Characterisation of the creep behaviour of weldments by HAZ-simulation”, *ECCC Recommendations*, 2005 3(II) Appendix 2.
- <sup>107</sup> Palmer T A, Elmer J W and Wong J, In situ observations of ferrite – austenite transformations in duplex stainless steel weldments using synchrotron radiation, *Science and Technology of Welding and Joining*, 2002 **7(3)** 159-171.
- <sup>108</sup> Babu S S, Elmer J W, Vitek J M and David S A, Time-resolved X-ray diffraction investigation of primary weld solidification in Fe-C-Al-Mn steel welds, *Acta Materialia*, 2002 **50** 4763-4781.
- <sup>109</sup> Sonderegger B, „Charakterisierung der Substruktur in modernen 9-12% Cr Stählen mittels der EBSD Methode“, *Doctoral Thesis*, Graz University of Technology, 2005.
- <sup>110</sup> Sonderegger B, Mitsche S and Cerjak H, „Microstructural analysis on a creep resistant martensitic 9-12% Cr steel using the EBSD method“, *Materials Science and Engineering A*, 2007, in print.

- <sup>111</sup> Sonderegger B, Mitsche S and Cerjak H, „Martensite laths in creep resistant martensitic 9-12% Cr steels - Calculation and measurement of misorientations“, *Materials Characterisation*, 2006, in print.
- <sup>112</sup> Sonderegger B, TU Graz, *Private Communications*, 2007.
- <sup>113</sup> Schalber A, „Charakterisierung der Schweißbeignung des Bor-modifizierten 9% Chromstahles CB2A“, *Master Thesis*, TU Graz, 1998.
- <sup>114</sup> Kozeschnik E and Buchmayr B, *“Mathematical Modelling of Weld Phenomena 5”*, (London, Institute of Materials, 2001), 349-361.
- <sup>115</sup> Svoboda J, Fischer F D, Fratzl P and Kozeschnik E, “Modelling of kinetics in multi-component multi-phase systems with spherical precipitates I. – Theory”, *Mater. Sci. Eng. A*, 2004 **385(1-2)** 166-174.
- <sup>116</sup> Kozeschnik E, Svoboda S, Fratzl P and Fischer F D, “Modelling of kinetics in multi-component multi-phase systems with spherical precipitates II. – Numerical solution and application”, *Mater. Sci. Eng. A*, 2004 **385 (1-2)** 157-165.
- <sup>117</sup> Kozeschnik E, Svoboda J and Fischer F D, “Modified evolution equations for the precipitation kinetics of complex phases in multi-component systems”, *CALPHAD*, 2005 **28(4)** 379-382.
- <sup>118</sup> Mendez-Martin F, “Microstructural characterisation of the HAZ of new creep resistant 9% chromium steels using weld simulation technique”, *Master Thesis*, Graz University of Technology, 2006.
- <sup>119</sup> Sakuraya K, Okada H and Abe F, „BN type inclusions formed in high Cr ferritic heat resistant steel“, *Energy Materials*, 2006 **1(3)** 158-166.

- <sup>120</sup> Sakuraya K, Okada H and Abe F, „Influence of heat treatment on formation behavior of boron nitride inclusions in P122 heat resistant steel”, *ISIJ International*, 2006 **46(11)** 1712-1719.
- <sup>121</sup> Albert S K, Kondo M, Tabuchi M, Yin F, Sawada K and Abe F, “Improving the creep properties of 9Cr-3W-3Co-NbV steels and their weld joints by the addition of boron”, *Metallurgical and Materials Transactions A*, 2005 **36A** 333-343.
- <sup>122</sup> Czyrska-Filemonowicz A, Spiradek K, Bryla K, Firganek H, Zielinska-Lipiec A and Ennis P J, “Transmission electron microscopy and boron trace autoradiography investigation of precipitates in creep deformed 9% chromium steels”, in *4<sup>th</sup> int conf Advances in Materials Technology for Fossil Power Plants*, Hilton Head Island, ASM International, 2005.
- <sup>123</sup> Abe F, “Alloy design of creep and oxidation resistant 9Cr steels for thick section boiler components operating at 650°C” in *4<sup>th</sup> int conf Advances in Materials Technology for Fossil Power Plants*, Hilton Head Island, SC, EPRI, 2004.
- <sup>124</sup> El-Kashif, Asakura K and Shibata K, “Effects of nitrogen in 9Cr-3W-3Co ferritic heat resistant steels containing boron”, *ISIJ International*, 2002 **42(12)** 1468-1476.
- <sup>125</sup> Hättestrand M and Andréén H O, „Boron distribution in 9-12% chromium steels”, *Materials Science and Engineering*, 1999 **A270** 33-37.
- <sup>126</sup> Hofer P, Miller M K, Babu S S, David S A and Cerjak H, “Atom probe field ion microscopy investigation of boron containing martensitic 9 pct chromium steel”, *Metallurgical and Materials Transactions A*, 2000 **31A** 975-984.
- <sup>127</sup> Spiradek K, Austrian Research Centers, *Private Communications*, 2006.

<sup>128</sup> Kager F, Böck N, Spiradek-Hahn K, Höfingger S, Brabetz M and Zeiler G, „Superior long-term creep behaviour and microstructural evolution of 9%Cr-steels with boron”, in int conf *Materials for Advanced Power Engineering 2006*, Liege, Forschungszentrum Jülich, 2006.

<sup>129</sup> Semba H and Abe F, “ Creep deformation behavior and microstructure in high boron containing 9%Cr ferritic heat resistant steels”, in 4<sup>th</sup> int conf *Advances in Materials Technology for Fossil Power Plants*, Hilton Head Island, SC, EPRI, 2004.

<sup>130</sup> Abe F, “Metallurgy for long-term stabilization of ferritic steels for thick section boiler components in USC power plant at 650°C”, in 8<sup>th</sup> int conf *Materials for Advanced Power Engineering 2006*, Liege, Forschungszentrum Jülich, 2006.